UNIVERSITÀ DI PARMA

UNIVERSITA' DEGLI STUDI DI PARMA

DOTTORATO DI RICERCA IN

Scienza e Tecnologia dei Materiali

CICLO XXXV

Fabrication and characterization of UHTCMCs for tribological applications

Coordinatore:
Chiar.mo Prof. Enrico Dalcanale

Tutore:
Chiar.ma Dott.ssa Diletta Sciti

Co-tutore:
Chiar.mo Dott. Antonio Vinci

Dottorando: Matteo Mor

Anni Accademici 2019/2020 – 2021/2022

A chi mi ha aiutato in questo percorso.

A me stesso, per averlo finito.

Abstract

The interest in the Ultra-High Temperature Ceramic Matrix Composites (UHTCMCs) increased over the last years due to their combination of toughness typical of CMCs with the high temperature stability of ultra-high temperature ceramics. The demand of UHTCMCs with better properties produced through more sustainable processes had led to the investigation of different approaches. This thesis deals with the fabrication and characterization of short pitch-based carbon fibres reinforced UHTCMCs for extreme applications, using a slurry impregnation process that avoids the problems related to the processes reported in literature. This work can be divided into four parts:

In the first part, a new technique for the manufacturing of short fibre reinforced ultra-refractory ceramics via slurry casting is presented. This technique - based on the use of natural thickeners and planetary mixer - allowed the fabrication of a free to organic solvent, thin (~100 μm), flexible and easy to handle sheets suitable for the fabrication of homogeneous structures by overlapping and Hot-Pressing sintering. A large range of compositions - in terms of matrix and fibre volumetric content - from 0-100% was possible with this method. The short carbon fibre amount incorporated in the sheets ranged from 20-50 vol. % and the fibre length ranged from 3 to 5 mm. The matrix composition investigated with this technique consisted of ZrB_2 90 vol. % - SiC 10 vol. %. Microstructure and mechanical properties of different samples were investigated. The microstructure observed with SEM showed a homogeneous fibre distribution, low interaction between fibre and matrix and no damage in the fibre surface due to the mixing process. From mechanical tests, increasing the fibre amount from 35 to 50 vol.% led to an improvement of the mechanical properties. In fact, the 4-point flexural strength ranged from 107 to 140 MPa, depending on the amount of carbon fibres. The same behaviour was observed during the works of fracture tests (WOF). The WOF ranged from 108 to 253 J/m^2.

The second part was focused on the processing and oxidation resistance study of graded materials composed with three different layers, with an amount of 0-20-50 vol. % of short carbon fibres respectively. Three different samples were fabricated: 1) ZrB_2- 85 vol %, SiC- 10 vol %, Y_2O_3- 5 vol %, 2) ZrB_2- 85 vol %, $MoSi_2$- 15 vol %, 3) SiC- 95 vol %, Y_2O_3- 5 vol %. The analysis of the morphology showed that all samples presented a homogeneous fibre distribution and a good interaction between the layers without the

presence of defects. The same samples were subjected to oxidation at 1650 °C in air and the behaviour of each layer composition was evaluated. SEM and EDS analysis were carried out to investigate the oxidation grade and the oxygen diffusion. The sample containing $MoSi_2$ resulted the most interesting with a mass loss of – 0.56 mg/cm^2 lower than the -4.51 mg/cm^2 and -7.05 mg/cm^2 of the others.

In the third part, the preparation and properties of complex structures with changing matrix compositions and complex shapes starting from the new slurry casting process presented in this thesis were investigated. In detail, four different structures were analyzed. The first sample was obtained hot pressing the sheets with the pressure applied perpendicularly to the pile-up direction. The sheets with a vertical orientation sintered by Hot-Pressing and composed by a matrix of ZrB_2-85 vol.%, SiC- 10 vol.%, reinforced with 40 vol.% of 3 mm long pitch-based carbon fibers (Z3-40-Z). It was characterized by a good fiber distribution and an interesting sheet bending that improved the mechanical properties with a value of flexural strength of 130 MPa. The second sample was a square plate composed by an external part of ZrB_2-35 vol. %, SiC- 60 vol. %, Y_2O_3-5 vol. % reinforced with 40 vol. % of short pitch-based carbon fibres with a length of 3 mm (ZSY605) and an internal square part composed by a matrix of ZrB_2-85 vol. %, SiC- 10 vol. %, Y_2O_3-5 vol. % reinforced with 40 vol. % of short pitch-based carbon fibres with a length of 3 mm (ZSY105). The two joined interfaces displayed good interaction, but defects originating from different stress distribution during sintering resulted in a low flexural strength of 45 MPa. To investigate the possibility to produce samples with a non-square shape, a cylindrical shape was fabricated (Z3-40-C). It was made by vertical sheets of UHTCMCs and sintered by Hot pressing, resulting in a final sample composed by a core of ZrB_2-35 vol.%, SiC- 60 vol.%, Y_2O_3-5 vol.% reinforced with 40 vol. % of short pitch-based carbon fibres with a length of 3 mm and an external shell of ZrB_2-85 vol.%, SiC- 10 vol. %, Y_2O_3-5 vol.% reinforced with 40 vol. % of short pitch-based carbon fibres with a length of 3 mm. In this case, the sample resulted with a good fibre distribution and good matrix interaction at the interface between the compositions. Finally, a cone was obtained by pressure-less sintering from the bending of a UHTCMC sheets composed by ZrB_2-85 vol.%, SiC- 10 vol.%, Y_2O_3-5 vol.% reinforced with 40 vol. % of short pitch-based carbon fibres with a length of 3 mm, which demonstrated the feasibility to obtain complex shapes with different techniques.

In the fourth part, the tribological properties of Ultra-high-temperature ceramic matrix composites (UHTCMCs) have been examined to give a better understanding of this material class for friction applications. Two pads consisting of pitch-based carbon fiber (Cf) reinforced ZrB_2-10 vol. % SiC were prepared with long fibers arranged in 0°/90° orientation (ZL) and randomly oriented chopped fibers (ZS). Microstructure, mechanical properties and tribological behavior on a self-designed dynamometer were tested, and the friction film was analyzed to examine relevant wear mechanisms. As disc, three different compositions were used: a carbon fiber reinforced carbon−silicon carbide disc (C/C-SiC), a Steel disc and a carbon fiber reinforced carbon disc (C/C). Tests conducted against a C/C-SiC disc showed a promising stable braking performance. However, wear and mechanical stress were high and could be tolerated only with long carbon fiber reinforcement. In the case of the test conducted against the Steel disc - most specifically for the ZS material, it was observed that abraded material from the disc formed a stable friction film by fusing together harder pad particles with abraded steel dust. This reduced wear and stabilized the braking performance. Finally, the interaction between the UHTCMCs materials and the C/C disc showed an interesting low coefficient of friction without pads damage and with an operating temperature of ≈ 550 °C.

Keywords

- Ultra-High-Temperature Ceramic Matrix Composites
- Short carbon fibre
- Friction properties
- Complex shapes
- Microstructure
- Mechanical properties
- Oxidation resistance

List of publications

- Matteo Mor, Antonio Vinci, Simone Failla, Pietro Galizia, Luca Zoli, Diletta Sciti. A novel approach for manufacturing of layered, ultra-refractory composites using pliable, short fibre-reinforced ceramic sheets. *Journal of Advanced Ceramics*, 2023, 12(1): 155-168. https://doi.org/10.26599/JAC.2023.9220674

Table of contents

1. Aim of the work

The most important requirements for braking material are high and stable coefficient of friction (COF), low wear rate for increased life, low weight and vibration and harshness properties (NVH) [1]. Common disc materials include steel, carbon-carbon (C/C) and carbon fibre reinforced carbon-silicon carbide (C/C-SiC). Each of them presents some problem, such as low operating temperature [2], low oxidation resistance graphite [3], [4] and high wear rate [5], [6]. According to literature, Ultra-High Temperature Ceramics (UHTCs) have been considered for tribological applications to overcome the common disc problems and a number of papers have analyzed their wear behavior in different pin-on-disc configurations [7]–[11]. However, tests which reproduce real application environments were not carried out. For these reasons, new applications (such as automotive) for Ultra-High Temperature Ceramic Matrix Composites (UHTCMCs) were investigated in this work. Moreover, thanks to their high melting point, high oxidation resistance and good strength, the UHTCMCs materials are of great interest for different fields, especially the aerospace. Moreover, these materials are used in extreme environments associated with hypersonic flight, atmospheric re-entry, rocket propulsion, plasma arc electrodes and heating elements [12]–[14].

The fibres reinforcement of UHTCMCs materials can be made with continuous carbon fibres/fabric - which allows to obtain good mechanical properties [14]–[16] - or with short fibres - which are more interesting for industries, especially due to their convenient manufacturing process/low fabrication costs [17]. Moreover, short fibres are easy to adapt to conventional and new manufacturing techniques [18]. In literature, several ways have been explored to incorporate short fibres into a ceramic matrix such as ball milling, colloidal process, and tape casting. However, all of them have some disadvantages. The ball milling causes damage on the fibre surface, reduces the fibre length from millimetres to 100-300 μm due to fibre fracture and forms debris [19]. The colloidal process avoids the fibre damage but requires the use of organic solvents (e.g.: ethanol) that make the process less sustainable [20]. The tape casting process presents the same problem, as mixtures of ethanol and butanol are used as a solvent and the non-ionic Triton X-100 as a surfactant. In addition, only a low amount of fibre can be added as reinforcement with tape casting, thus reducing the improvement in mechanical properties [21]. For these reasons, the aim of this PhD thesis is developing a new process route for

the incorporation of high-volume fraction of short fibres into UHTC matrices that overcome some limitations of already known techniques.

This work can be divided in four different parts:

1) In the first part, the focus was on the development of a new process route for the fabrication of UHTCMCs using uncoated short pitch-based carbon fibres as a reinforcement. This process was based on slurry casting using water as medium that avoided the main problems of the commonly used processes for the fabrication of UHTCMCs. Moreover, the use of different amounts of fibre reinforcement or fibre length was studied and tested to obtain some indications about the mechanical properties.
2) In the second part, thanks to the versatility of the new process that allowed to obtain UHTCMCs sheets with variable fibre amount, graded structures were produced and studied. More in detail, three graded samples with the same matrix composition and different volumetric amounts of carbon fibres (0, 20, 50 %) were fabricated and their oxidation resistance was evaluated through tests at 1650 °C in air in order to investigate the effect of matrix composition and fibre volumetric amount.
3) In the third part, the flexibility of the UHTCMCs sheets was used to produce samples with non-planar shapes (such as cones or wedges) or samples with double matrix compositions, such as rings and squares, with different inner and outer compositions.
4) The fourth part proposes a new application for the UHTCMCs as braking materials. The use of UHTC materials reinforced with short and long carbon fibres as pads for braking application was evaluated with a testing machine at the University of Bayreuth, Germany. To identify the best conditions, three different discs composed by different materials were used.

This work was carried out at the Institute of Science, Technology and Sustainability for Ceramics (CNR-ISSMC former ISTEC) in Faenza (Ravenna, Italy), with a period abroad at the Ceramic Materials Engineering group (CME) at the Bayreuth Universität (Bayreuth, Germany).

1.1 References

[1] P. Kumar and V. K. Srivastava, “Tribological behaviour of C/C–SiC composites—A review,” *J. Adv. Ceram.*, vol. 5, no. 1, pp. 1–12, 2016, doi: 10.1007/s40145-015-0171-z.

[2] Ralph Renz, *Entwicklung eines Werkstoff- und Bauweisenkonzepts für keramische Verbundbremsscheiben (Band 14)*. 2018.

[3] G.Savage, *Savage 1993 - Carbon-carbon composites.pdf*. Chapman & Hall, 1993.

[4] P. Kumar and V. K. Srivastava, “A Review on Wear and Friction Performance of Carbon–Carbon Composites at High Temperature,” *Int. J. Appl. Ceram. Technol.*, vol. 13, no. 4, pp. 702–710, 2016, doi: 10.1111/ijac.12538.

[5] S. Fouquet, M. Rollin, R. Pailler, and X. Bourrat, “Tribological behaviour of composites made of carbon fibres and ceramic matrix in the Si–C system,” *Wear*, vol. 264, no. 9–10, pp. 850–856, Apr. 2008, doi: 10.1016/j.wear.2006.12.081.

[6] P. Fournier, P. Reynaud, F. Platon, and J. Absi, “Tribological behaviour of carbon-fibre-reinforced SiC matrix composites,” *Proc. IMechE Part J J Eng. Tribol.*, vol. 214, no. 3, pp. 291–306, 2000, doi: 10.1243/1350650001543188.

[7] D. Sciti, S. Guicciardi, L. Zoli, S. Failla, and C. Melandri, “Dry sliding wear behaviour of ZrB2-based ceramics: Self-mated and cross coupling with alumina,” *J. Eur. Ceram. Soc.*, vol. 42, no. 14, pp. 6335–6346, 2022, doi: 10.1016/j.jeurceramsoc.2022.07.022.

[8] J. He, Y. Cao, Z. Li, and Y. Wang, “Study of tribological properties of polymer derived ZrB2-SiC ceramics,” *Ceram. Int.*, vol. 44, no. 13, pp. 15627–15630, 2018, doi: 10.1016/j.ceramint.2018.05.231.

[9] J. K. Sonber *et al.*, “Friction and wear properties of zirconium diboride in sliding against WC ball,” *Int. J. Refract. Met. Hard Mater.*, vol. 76, no. March, pp. 41–48, 2018, doi: 10.1016/j.ijrmhm.2018.05.009.

[10] M. Ivor, D. Medved, M. Vojtko, A. Naughton-Duszova, L. Marciniak, and J. Dusza, “Nanoindentation and tribology of ZrB2 based luminescent ceramics,” *J.*

Eur. Ceram. Soc., vol. 40, no. 14, pp. 4901–4908, 2020, doi: 10.1016/j.jeurceramsoc.2020.03.021.

[11] M. Mallik *et al.*, "Abrasive wear performance of zirconium diboride based ceramic composite," *Int. J. Refract. Met. Hard Mater.*, vol. 79, no. December 2018, pp. 224–232, 2019, doi: 10.1016/j.ijrmhm.2018.12.008.

[12] K. Upadhya, J. M. Yang, and W. P. Hoffman, "Materials for ultrahigh temperature structural applications," *Am. Ceram. Soc. Bull.*, vol. 76, no. 12, 1997.

[13] F. Monteverde, A. Bellosi, and L. Scatteia, "Processing and properties of ultra-high temperature ceramics for space applications," *Mater. Sci. Eng. A*, vol. 485, no. 1–2, pp. 415–421, Jun. 2008, doi: 10.1016/j.msea.2007.08.054.

[14] P. Hu *et al.*, "Rolling compacted fabrication of carbon fiber reinforced ultra-high temperature ceramics with highly oriented architectures and exceptional mechanical feedback," *Ceram. Int.*, vol. 44, no. 12, pp. 14907–14912, 2018, doi: 10.1016/j.ceramint.2018.04.249.

[15] D. Sciti, L. Pienti, A. Natali Murri, E. Landi, V. Medri, and L. Zoli, "From random chopped to oriented continuous SiC fibers-ZrB2 composites," *Mater. Des.*, vol. 63, pp. 464–470, Nov. 2014, doi: 10.1016/j.matdes.2014.06.037.

[16] L. Zoli and D. Sciti, "Efficacy of a ZrB2–SiC matrix in protecting C fibres from oxidation in novel UHTCMC materials," *Mater. Des.*, vol. 113, pp. 207–213, 2017, doi: 10.1016/j.matdes.2016.09.104.

[17] F. De Bianchi, S. A. Ponnusami, L. Silvestroni, and A. M. Grande, "Thermo-elastic properties in short fibre reinforced ultra-high temperature ceramic matrix composites: Characterisation and numerical assessment," *Mater. Today Commun.*, vol. 29, no. May, p. 102754, 2021, doi: 10.1016/j.mtcomm.2021.102754.

[18] X. He, Y. Zhou, D. Jia, and Y. Guo, "Effect of sintering additives on microstructures and mechanical properties of short-carbon-fiber-reinforced SiC composites prepared by precursor pyrolysis–hot pressing," *Ceram. Int.*, vol. 32, no. 8, pp. 929–934, Dec. 2006, doi: 10.1016/J.CERAMINT.2005.07.007.

[19] L. Pienti, D. Sciti, L. Silvestroni, and S. Guicciardi, “Effect of milling on the mechanical properties of chopped SiC fiber-reinforced ZrB2,” *Materials (Basel).*, vol. 6, no. 5, pp. 1980–1993, 2013, doi: 10.3390/ma6051980.

[20] J. J. Sha *et al.*, “Improved microstructure and fracture properties of short carbon fiber-toughened ZrB2-based UHTC composites via colloidal process,” *Int. J. Refract. Met. Hard Mater.*, vol. 60, pp. 68–74, 2016, doi: 10.1016/j.ijrmhm.2016.07.010.

[21] W. S. Yang *et al.*, “Microstructure and mechanical properties of short carbon fibre/SiC multilayer composites prepared by tape casting,” *Compos. Sci. Technol.*, vol. 72, no. 6, pp. 675–680, Mar. 2012, doi: 10.1016/j.compscitech.2012.01.014.

2. State of the art

2.1 Ultra-high temperature ceramics

2.1.1 Introduction

Ceramic materials generally can be defined as inorganic, non-metallic solids [1]. However, the definition still leaves some grey areas. So, the definition is expanded to include other characteristics such as melting temperature, bonding type, or electrical properties [2]. Ultra-high-temperature-ceramics (UHTCs) are a class of ceramic materials with melting points of 3000 °C or above. Most of the materials that have melting point above 3000 °C are carbides, borides or nitrides of early transition metals. Moreover, only few metals (W, Re and Ta) and one oxide ceramics (ThO_2) have such high melting points. For these reasons, the most studied UHTC compounds are ZrB_2, HfB_2, TaC, TaB_2, ZrC and HfC [3]. Another definition of UHTCs is that they are materials capable of being used in air at temperatures above the limiting temperature for high-temperature ceramics. [4], [5]. Materials such as Al_2O_3, SiC, and Si_3N_4 can be used in air at temperatures higher than 1600 °C so, the minimum use temperature for the ultra-high temperature regime should be above that level. However, recent hypersonic applications required higher temperatures, so 2000 °C have been cited as the cut-off of the ultra-high temperature regime [6], [7]. Finally – as for the chemical definition / UHTCs are borides, carbides or nitrides of early transition metals. So, any compounds such as Zr, Hf, Ta, W or Nb along with B, C or N can be a UHTC [5]. Moreover, the chemical definition allows to identify the characteristics of the material. In fact, borides/diborides present varying density, high thermal conductivity, moderate coefficient of thermal expansion (CTE), low electrical resistivity, good mechanical properties and oxidation resistance. Compared to them, carbide-based UHTCs presents similar CTE but lower mechanical properties, higher electrical resistivity and lower oxidation resistance. Compared with the previous ones, nitride-based UHTCs present lower mechanical properties, low thermal conductivity but high CTE [8]. For these reasons, among UHTCs the diborides are the most investigated. In particular, ZrB_2 and HfB_2 are the main candidates for the application in harsh environments, for the fabrication of nose cones, sharp leading edges, scramjet engines and components for the use in supersonic flight [4], [9], [10]. Historically, the first reports of synthesis of UHTC were published in the 1800s [11]. Subsequently, new research on UHTCs was conducted in the 1950s when HfB_2 and ZrB_2 were being used as nuclear reactor materials thanks to their high-temperature corrosion resistance [12]–[14]. The

interest in UHTCs significantly increased from 1960s due to the space race between NASA and the Soviet Union where a material capable to be used in the extreme environments was required [15]–[17]. In the last years, the interest in UHTCs were focused on their use in aerospace applications such as hypersonic vehicles [18]–[20].

2.1.2 Crystal structure

The chemical, physical and thermal properties of the materials are determined by the crystal structure. The strong covalent bond between transition metals and boron, carbon or nitrogen result in unique properties in the UHTC materials typical of both metals and ceramics, such as high melting temperature, hardness, stiffness, electrical and thermal conductivity [5], [10], [21]–[23].

Carbides present very high strength and hardness but suffer oxidation at relatively low temperature according to the following reaction [21], [22]:

$2MeC + 3O_2 \rightarrow 2MeO_2 + 2CO$ (Me= Ta, Zr or Hf)

Between the carbides, Ta and Hf (TaC and HfC) are particularly interesting because they possess the highest melting points known (3980 °C and 3928°C, respectively) [4]. These extremely high melting points can be attributed to the combination of the covalent, metallic and ionic nature of the bonding. The strong covalent bond comes from the interaction between the *d*-band of the metal and *p*-bond of the carbon which produce a sp^3 ibridization [24]. The group IV and V monocarbides adopt the face-centred cubic (FCC) structure during crystallization, with carbon atoms in the octahedral sites (Fig. 2.1) [25].

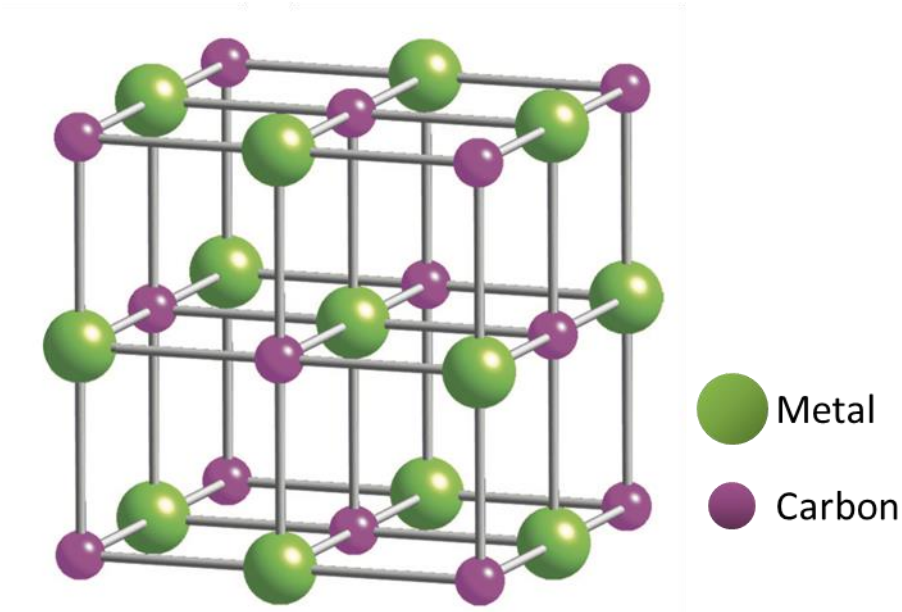

Fig. 2.1: Face-centred cubic (FCC) structure of metal carbides. Carbon atoms are in the octahedral sites of the lattice.

The general formula for the carbides is MeC (Me= Ti, Zr, Hf, V, Nb or Ta). However, monocarbides are often found in sub-stochiometric mixture where the formula is MeC_x ($_x$ is the C/Me ratio) [3].

Borides are characterized by strong bonds between the transition metal and boron. The crystal structure is a primitive hexagonal with alternating graphite-like boron layers and hexagonal metal layers (Fig. 2.2) [24], [26], [27]. The unit cell contains one MB_2 formula unit. The structure is composed by layers of B atoms in 2D graphite-like rings which alternate with hexagonally close-packed M layers. Due to the donor-acceptor interactions, the M-B bonds present ionic characteristics. However, the partial excitation of *d* electrons and the formation of *spd* hybrid configuration provides covalent characteristics. Despite these characteristics, hardness and brittleness are lower than the corresponding carbides because the B structure combines sp^3 hybridization with sp^2 configuration at lower-strength, whereas the carbon atoms present only sp^2 hybridization [24]. An interesting case is the one constituted by the borides of Zr and Hf: since the metals are chemically similar, the borides are also similar. Both are characterized by high hardness and temperature stability [4].

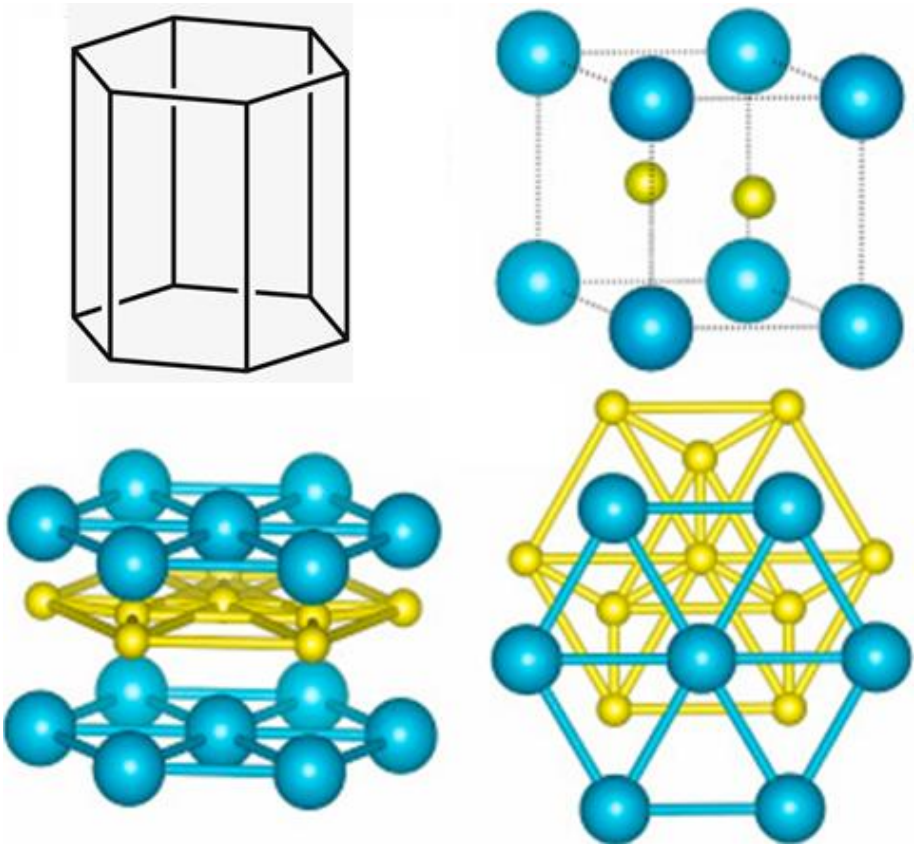

Fig. 2.2: Crystal structure of metal diborides.

Similar structure and composition of carbides are visible in nitrides (groups IV-VI). Between the nitrides in the UHTCs, the most interesting are ZrN, HfN and TaN. These mononitrides present an FCC structure [28]. The weaker bonding compared to the carbides results in lower refractory properties, but the combination of metallic, covalent, and ionic bonding leads to high hardness, high melting point and chemical inertness [21], [22].

2.1.3 Synthesis

During the fabrication of diborides-based UHTCs, transition metal oxides (MeO_2) or elemental metals (Me) are combined with boron sources (like B, B_2O_3, B_4C, etc.) to synthesize transition metal diboride (MeB_2) powders. Then, MeB_2 powders are densified using different methods such as pressure-less sintering, hot pressing, or spark plasma sintering, to obtain the final UHTC material. In some cases, powder synthesis and densification can be combined to obtain the final material in one step by using the reactive sintering which included different techniques such as reactive hot pressing and reactive spark plasma sintering. Borides and diborides can be synthetized by different methods

like elemental reaction between Me and B and reduction process using MeO_2 [3] (Fig. 2.3).

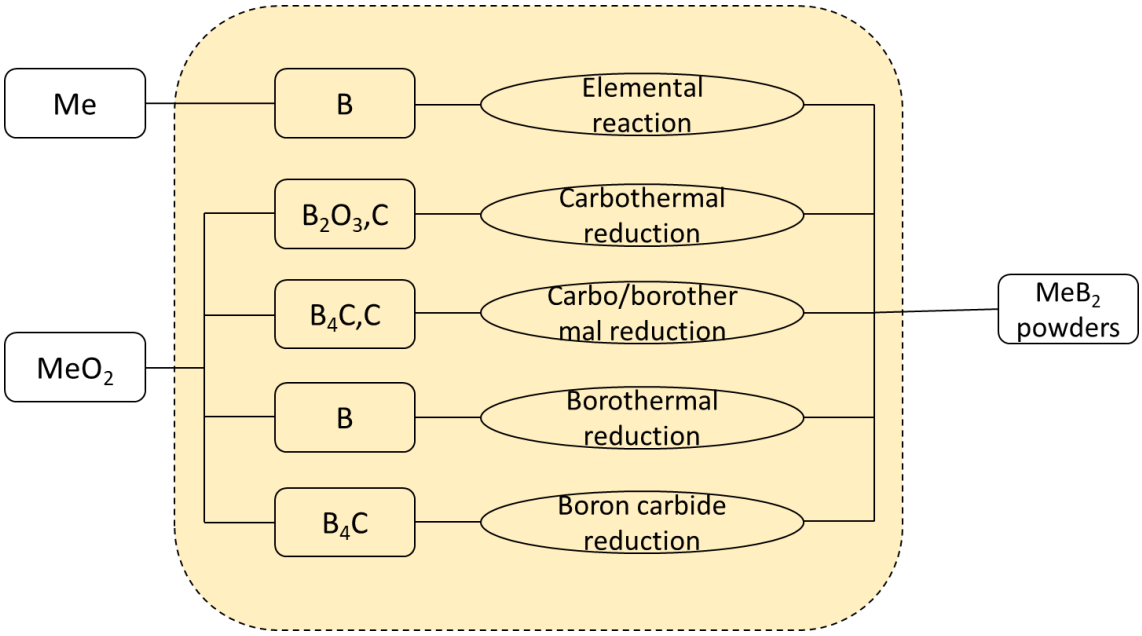

Fig. 2.3: Roadmap of fabrication process of MeB_2 by reactive synthesis of powders.

The simplest process for the synthesis of MeB_2 powder is the elemental reaction where diboride powders are obtained from metals (Me) or metal hydrides (MeH_2) and boron (reaction 2.1)

$$Me + 2B \rightarrow MeB_2 \quad (2.1)$$

These reactions are highly exothermal ($\Delta G°$=-318 kJ for ZrB_2), so it can auto-sustain itself after initiation. Moreover, the heat generated can promote local melting of transition metal, which further accelerates the reaction. Due to the high oxygen affinity of transition metals (such as Zr, Hf, etc) to avoid the formation of oxide impurities, the synthesis is carried out in reduced or inert atmosphere.

Other methods that can be used to produce diborides are reduction processes, where transition metal oxides, MeO_2, are used as metal source and boron materials (B, B_4C, B_2O_3) are used as boron source. In some cases, boron sources like B and B_4C can act as reducing agent.

The carbothermal reduction (reaction 2.2) is a reduction process commonly used to synthetize MeB_2 powders, in particular for ZrB_2 and HfB_2.

$$MeO_2 + B_2O_3 + 5C \rightarrow MeB_2 + 5CO_{(g)} \quad (2.2)$$

This process requires an excess of B_2O_3 due to its volatility that can result into a loss of reagents.

Another method used to synthetize MeB_2 powders is the carbo/borothermal reduction which uses MeO_x as transition metal source and B_4C as boron source (reaction 2.3).

$$2MeO_x + B_4C + (2x-1)C \rightarrow 2MeB_2 + 2xCO_{(g)} \quad (2.3)$$

This reaction does not take place in one step, but due to thermodynamics some intermediate reaction may be favourable. Due to the use of the ZrB_2 in this thesis, following are reported its intermediate reactions (reaction 2.4-2.5).

$$ZrO_2 + \frac{5}{6}B_4C \rightarrow ZrB_2 + \frac{2}{3}B_2O_3 + \frac{5}{6}C \quad (2.4)$$

$$ZrO_2 + \frac{5}{7}B_4C \rightarrow ZrB_2 + \frac{3}{7}B_2O_3 + \frac{5}{7}CO_{(g)} \quad (2.5)$$

During the synthesis of ZrB_2 the loss of B_2O_3 can lead to the formation of ZrC in the final product (reaction 2.6).

$$ZrO_2 + 3C \rightarrow ZrC + 2CO_{(g)} \quad (2.6)$$

Using an excess of B_2O_3 allows to decrease the formation of ZrC (reaction 2.7).

$$ZrC + B_2O_3 + 2C \rightarrow ZrB_2 + 3CO_{(g)} \quad (2.7)$$

In the carbothermal and carbo/borothermal reduction, carbon is used as reagent, but it may remain in the final products as an impurity. The borothermal reduction could minimize the carbon impurities by the use of elemental B as raw material to synthetize MeB_2 (reaction 2.8).

$$3MeO_2 + 10B \rightarrow 3MeB_2 + 2B_2O_{3(g)} \quad (2.8)$$

The excess of B can be removed by reaction with B_2O_3 forming gaseous species such as B_2O_2 and BO (reaction 2.9-2.10).

$$2B_2O_{3(l)} + 2B \rightarrow 3B_2O_{2(g)} \quad (2.9)$$

$B_2O_{3(l)} + B \rightarrow 3BO_{(g)}$ (2.10)

However, B_2O_3 is a source of oxygen impurities. To remove it, washing or vaporization with hot water at temperature above 1500 °C could be applied.

At the same time, the carbides can be synthetized by reaction of elemental precursor powders (reaction 2.11) where there is the direct carburization of the metal. Another possibility, and the most used due to the low production costs, is the carbothermal reduction of the corresponding oxide (reaction 2.12) [3], [29].

$Me + C \rightarrow MeC$ (2.11)

$MeO_2 + 3C \rightarrow MeC + 2CO_{(g)}$ (2.12)

2.1.4 Densification

The densification of ceramics is usually made by sintering. During this process, the powders are consolidated by heating at high temperature through diffusion mechanism. The sintering allows to obtain a dense material by forming bonds between particles and removing the porosity. It is affected by several parameters like gas atmosphere, pressure, temperature, time and particle size [1]. The diffusion process is promoted at high temperatures where the grains move along each other, filling the voids and reducing the porosity. The driving force is the decrease of Gibbs energy with the volume decrease. Two different sintering method can happen:

- Solid state sintering: in this process, the green body is heated at a temperature which is 70 – 90 % of its melting point. The high temperature promotes the atoms diffusivity at the interface between grains, resulting in the bonding between them. With the grain boundaries growth, the porosity decreases not leaving significant interconnected pores. In this mechanism, the glassy phase is not required so, an increase in properties such as thermal and electrical conductivity or strength are visible.

-Liquid phase sintering: is a sintering technique that uses a liquid phase to accelerate the interparticle bonding of the solid phase. The liquid phase can be obtained either through mixing different powders -melting one component or forming a eutectic- or by sintering at a temperature between the liquid and solid phases. Moreover, since the softer phase is generally the first to melt, the resulting microstructure typically consists of hard particles

in a ductile matrix, increasing the toughness of an otherwise brittle component [30]. The liquid phase sintering can be divided in three steps [1]: In the first step, the particles rearrange due to the capillary forces and fill all the porosity with the liquid phase. The second step is the Ostwald ripening [31], which consists in the dissolution of smaller grains in the liquid phase, followed by re-precipitation on the larger grains. This re-precipitation process is responsible for the development of microstructure, shape and grain growth. Finally, in the last step, there is a slow densification accompanied by grain coarsening due to the solid skeleton previously formed that hindered the rearrangement.

Thanks to its characteristics, the liquid phase sintering allows to obtain ceramics with good density at lower temperature than other mechanisms. However, the high temperature performance of the material is compromised so the creep resistance is lower. This happens because the low melting phase between grains tend to soften at high temperature.

The sintering of UHTCs materials presents some difficulties due to the strong covalent bond between atoms and low self-diffusivity [32]. To obtain a full densification in UHTCs, the sintering is usually carried out at temperature above 2000 °C. Unfortunately, at high temperature the grain coarsening prevails on densification, which leads to a decrease in mechanical properties. So, some mechanism has been developed to obtain a better densification:

- the use of pure and ultrafine powders, because the presence of oxide impurities on the particle surface promote the grain coarsening [33];

-the increasing of defect concentration by mechanical mechanisms such as high-energy milling [34];

-the reactive sintering at high temperature of solid precursors [35].

-the use of sintering additives that generate a liquid phase at the sintering temperature [36].

The use of additives is the most used method. To improve the sintering of borides, several additives have been tested such as silicon carbide [37]–[41]. SiC is the most used additive for these compounds and acts both as sintering aid and as oxidation resistant additive, also preventing grain growth [42]–[46].

Different techniques used for various ceramic materials can be adopted for the consolidation of UHTCs materials [47]:

-Hot pressing (HP): the green sample is heated under uniaxial pressure in order to accelerate the sintering process. The process is carried out in a vacuum or inert atmosphere. During the sintering, the shrinkage of the material is recorded as function of the temperature and time. By this way, it is possible to control sintering parameters during the hot pressing. Moreover, the data collected during the process can be used for kinetic studies. The HP is the most common method for the fabrication of dense UHTC bodies [28], [38], [48]. The application of pressure allows to lower the sintering temperature by a few hundred degrees.

-Reactive sintering: the sintering and synthesis of the material occur simultaneously during the heating step. An example is the sintering of nitrides where the metal reacts with nitrogen gas to obtain metal nitride in- situ.

-Self-propagating high-temperature synthesis: the sintering and synthesis of the material occur simultaneously during the heat treatment. In this process, an arc furnace is used to start an exothermic reaction that sustains itself. For this reason, this process is relatively economical compared to other processes.

-Hot isostatic pressing: the green sample is contained in a metallic or glassy casing. A uniform pressure is applied in all the directions and is generated by inert gases, such as argon or nitrogen.

-Spark plasma sintering (SPS): the green sample is subjected to a pressure in the range of 10 – 100 MPa and it is crossed by a direct current with a very high intensity. This technique allows to obtain high rating rates and large samples in a few minutes, with a final fully sintered body [49]–[51].

-Microwave sintering: the green sample is exposed to a radiation which heats the samples from the inside. With this method, it is possible to obtain high rating rates, but it is not uniform through the samples.

-Pressure-less sintering: the green sample is heated at a target temperature for a determinate time in an inert or reactive atmosphere. With this technique, high temperature and holding time are required to obtain high density but they promote grain growth which

decreases the mechanical properties. To minimize the grain growth, sintering aids such as SiC or B_4C are used. The pressure-less sintering is very simple and economic compared to the other techniques. It is usually chosen to fabricate near-net shape components [37], [39], [44], [46], [52].

Between the different sintering techniques, the most commonly used are hot pressing and spark plasma sintering, thanks to benefits associated to mechanical pressure application and fast heating, and pressure-less sintering for being cheaper and allowing the consolidation of complex preforms pressure-less sintering.

2.1.5 Mechanical properties

In Table. 2.1 the mechanical properties of the most used UHTCs are reported [53]–[55]. The characteristics of this material are due to their chemical composition. In fact, the strong covalent bonding in UHTCs provides a high value of elastic modulus that range from 350-540 GPa and a good value of flexural strength at room temperature, 300-570 MPa. The value of the mechanical properties of the UHTCs materials are quite scattered due to different problems such as the difficulty to obtain a full density material, the presence of impurities, structural defects, presence of different phases or the grain size and orientation. A way to change the mechanical behaviour of this materials is the addition of secondary phases. For example, the ZrB_2 based ceramics added with SiC possess a strength above 1000 MPa, fracture toughness higher than 5.5 $MPa \cdot m^{0.5}$ and hardness up to 22 GPa [24]. It was found that the room temperature strength of the ZrB_2 based ceramics was affected by SiC particle agglomerates [56]. So, since SiC particle size controls the strength, a uniform dispersion of SiC is required to maximize this property.

Table 2.1: Mechanical properties of different UHTCs [53-55].

Material	Temperature (°C)	Elastic modulus (GPa)	Flexural strength (MPa)	Hardness (GPa)
ZrB_2	23	500	380	25.3 – 28.0
	800	480	430	-
	1400	360	150	-
	1800	-	200	-
ZrC	23	348	-	27.0
TiB_2	23	551	300 – 370	25 – 33
TiC	23	451	-	30
HfB_2	23	530	480	21.2 – 28.4
	800	485	570	-
	1400	300	170	-
	1800	-	280	-
HfB_2/SiC	23	540	520	-
	800	530	380	-
	1400	410	180	-
	1800	-	280	-
HfC	23	352	-	26.0
TaB_2	23	257 – 570	-	19 – 25
TaC	23	285	-	18.2
ZrN	23	460	-	15
HfN	23	380	-	18

In Table. 2.2 the mechanical properties of ZrB_2 based ceramics with different amount of SiC are reported. The strength of ZrB2 increased with the increase of SiC content from

560 to 1090 MPa [57]. However, for SiC contents above 30 vol. %, SiC particles start aggregating, forming clusters that act as critical flaws and reduce the strength [58].

Table 2.2: Different mechanical properties at room temperature of ZrB_2- based UHTC with SiC as secondary phase [3], [59].

Material (vol. %)	**Elastic modulus (GPa)**	**Hardness (GPa)**	**Fracture toughness (MPa · $m^{0.5}$)**	**Flexural strength (MPa)**
ZrB_2	346 – 498	9 - 23	1.9 – 4.8	300 - 565
ZrB_2 + 10 SiC	450 – 507	18 – 24	3.8 – 5.7	393 - 835
ZrB_2 + 20 SiC	466 – 506	21 – 24	3.9 – 5.7	485 - 1009
ZrB_2 + 30 SiC	487 - 541	20 – 27	4.4 – 5.9	425 - 1150

The mechanical properties of UHTC materials are strongly affected by temperature. For example, the elastic modulus decreases with the temperature increase due to the weakening of the covalent bond. As reported in literature, the elastic modulus of ZrB_2 bulk ceramics decrease from 525 GPa at room temperature to 490 GPa at 1100 °C [10]. However, after 1200 °C the elastic modulus decreases rapidly due to the grain boundary sliding and diffusional creep mechanisms [58]. A similar behaviour is show by ZrB_2/SiC ceramics [60].

The strength at elevated temperature shows a different trend. For example, bulk ZrB_2 ceramics showed an increase from 325 MPa at room temperature to 420 MPa at 800°C due to thermal stress relief. Then, it decreased to 145 MPa at 1400°C and increased again to 200 MPa at 1900°C due to stress relief coupled with creep mechanisms. Finally, at 2200°C creep phenomena were more marked, and strength fell down to 50 MPa [61]. A similar trend was found for ZrB_2/SiC ceramics [58], [62].

The mechanical properties of carbides in literature are usually incomplete or not clearly reported [10]. The plastic deformation of carbides was observed only at very high temperatures and were found to be strongly dependent on stoichiometry [10].

2.1.6 Thermal properties

The thermal properties of a material refer to the response of materials to temperature changes and to the application of heat. Heat capacity, thermal expansion and thermal conductivity are properties that are often critical when evaluating applications requiring high temperature jumps.

In Table 2.3 the values of thermal expansion (CTE) and thermal conductivity of common UHTCs are reported [10], [54], [63]. These properties depend on temperature, and its variation should be considered during their design.

Table 2.3: Different values of thermal expansion (CTE) and thermal conductivity of common UHTCs [10], [54], [63].

Material	Temperature (°C)	CTE (10^{-6}/K)	Temperature (°C)	Thermal Conductivity (W/mK)
ZrB_2	20 – 1027	5.9	10	83.8
	1027 – 2027	6.5	-	81.8
ZrB_2/SiC	400 - 1600	5 – 7.8	100	98.7
	-	-	500	84.5
	-	-	1000	78
ZrC	20 – 1500	6.7	20	20.5
TiB_2	20 – 1027	4.6	-	-
	20 – 2205	5.2	-	-
	1027 – 2027	8.6	-	-
TiC	20 - 1500	7.7	-	-
HfB_2	20 – 1027	6.3	20	105
	1027 – 2027	6.8	400	75
	20 – 2205	7.6	800	70
HfB_2/SiC	-	-	100	79
	-	-	500	74
	-	-	1000	62
HfC	20 – 1500	6.6	20	20
	-	-	400	23
	-	-	800	30
TaB_2	20 – 1027	8.2	20	16
	1027 – 2027	8.4	1027	16.1
	20 – 1650	8.4	2027	36.2
TaC	20 - 1500	6.3	20	22

Due to their crystal structure, borides such as ZrB_2 and HfB_2 possess higher thermal conductivity compared to carbide or nitrides [64]. Even though the conductivity of borides decreases with the temperature increase, they tend to remain higher than those of nitrides and carbides. For example, ZrB_2 has a drop-off up to 2500 °C [59]. A high thermal conductivity provides a smaller thermal gradient, allowing to reduce thermal stresses within the material. Moreover, it allows heat to dissipated more quickly and radiate away from the surface reducing the temperature on the surface for a specific incident heat flux.

2.1.7 Oxidation resistance

Despite the unique combination of properties, bulk UHTCs possess rather poor oxidation resistance under 1000 °C compared with SiC. The oxidation behaviour of diborides has been studied over a wide range of temperature. The low oxidation resistance is due to the lack of the formation of a stable scale during the heating [24], [65]. Bulk ZrB_2 during oxidation forms porous ZrO_2 and B_2O_3 phases according to the following reaction:

$$ZrB_2 + \frac{5}{2}O_2 \rightarrow ZrO_{2(s)} + B_2O_{3(l/g)} \quad (2.13)$$

The B_2O_3 at temperature above 450 °C is liquid and surrounds the ZrO_2 grains providing a protection. At temperature around 1100 °C it volatilizes and leaves the porous scale susceptible to oxygen attack. For these reasons, the UHTCs are usually enriched with phases that improve the oxidation characteristics, such as SiC or metal silicides [10], [66], [67]. The combination of SiC phase with the ZrB_2 leads to the formation of a borosilicate glass (reaction 2.14), which is more viscous and less volatile than pure B_2O_3 and inhibits the oxygen diffusion inside the material up to 1600 °C (Fig. 2.4). At temperature above 1600 °C, the borosilicate has enhanced durability because the ZrO_2 particles are embedded into the glassy phase and induce a physical modification, while their partial dissolution promotes a chemical modification in the Si-O bonds [68].

$$ZrB_2 + SiC + 4O_2 \rightarrow ZrO_{2(s)} + SiO_2{\cdot}B_2O_{3(l)} + CO_{(g)} \quad (2.14)$$

Between the metal silicides, one of the most effective to improve the oxidation resistance of UHTC-based ceramics is $MoSi_2$ [66], [69], [70]. In fact, the presence of $MoSi_2$ during the oxidation leads to the formation of a SiO_2 glassy layer on the surface that acts as oxygen barrier and a stable condensed phase in the subsurface layer that suppresses the formation of volatile species. This factor has been considered the responsible for

hindering the ZrO_2 grain evolution, which decreases the oxygen diffusion rate inside the matrix. The oxidation mechanism of ZrB_2 based ceramic doped with $MoSi_2$ is reported in reaction 2.15,2.16 and 2.17.

$$2ZrB_2 + 5O_2 \rightarrow 2ZrO_2 + 2B_2O_3 \quad (2.15)$$

$$2MoSi_2 + 7O_2 \rightarrow MoO_3 + 4SiO_2 \quad (2.16)$$

$$2MoSi_2 + B_2O_3 + \frac{5}{2}O_2 \rightarrow 4SiO_2 + 2\,MoB \quad (2.17)$$

For the carbides, the oxidation mechanism is different. In fact, they are usually resistant to oxidation below 800 °C and above 1800 °C. At temperature over 800 °C a crystalline oxide is formed as shown in the reaction 2.18.

$$MeC + O_2 \rightarrow MeO_{2(s)} + C \quad (2.18)$$

For these reasons, usually carbides are used for applications where a rapid heating or temperature above 1800 °C are present. Even in this case, the addition of SiC or metal silicides can improve the oxidation resistance due to the formation of a dense SiO_2 protective layer between 1300 – 1500 °C [71], [72].

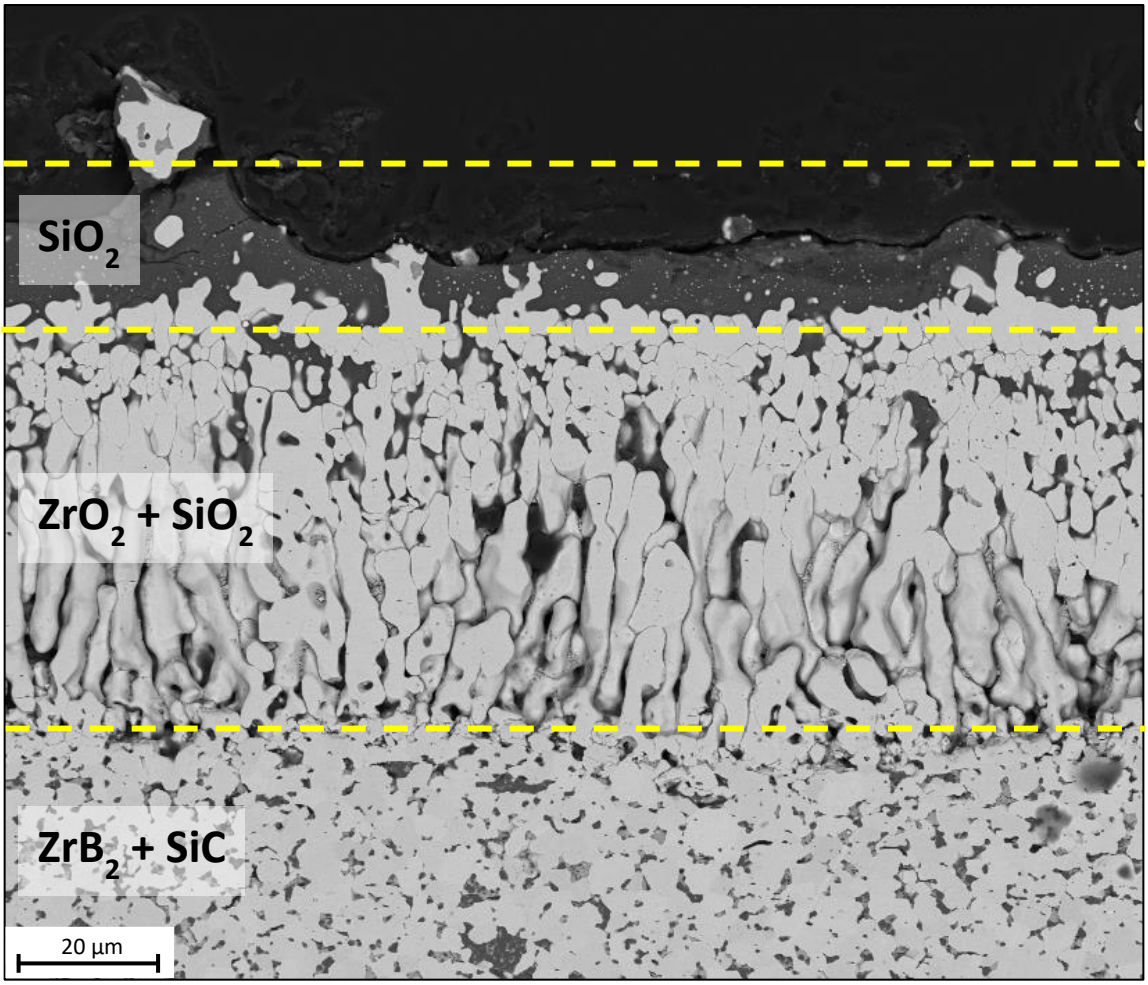

Fig. 2.4: Image of a cross section of ZrB_2-SiC material after 1' at 1650 °C in air. It is possible to identify from the surface: the glass layer, ZrO_2-based interlayer, SiC depleted zone and unreacted bulk ceramic.

2.1.8 Applications

Thanks to their properties - such as high melting point, high thermal conductivity, oxidation and erosion resistance - UHTCs applications can span from commercial industry to aerospace field. More in detail, due to the oxidation resistance required for aerospace application (above 2000 °C), UHTCs have been investigated for application as Thermal Protection System (TPSs) [73], sharp-leading edges [74], [75] and rocket motor nozzles [76], [77].

Due to their high thermal conductivity, borides can rapidly dissipate the heat by reducing thermal gradient and thermal stress [78]. Moreover, ZrB_2 and HfB_2 are being

investigated as potential materials for neutron shield, electrodes for metal refining or microelectronics [79]–[81].

Nitrides and carbides possess a very high melting point, high hardness, and chemical inertness. For these reasons, possible applications are nozzle throats, control thrusters and cutting tools [77], [82]. All these applications are characterized by high thermal and mechanical loads.

Unfortunately, UHTC bulk materials possess low fracture toughness, which limits their application where thermal shocks and vibrations are present. For these reasons, exposure to extreme temperature may lead to catastrophic failure. To avoid these problems and improve the fracture properties, short and long carbon or silicon fibres were introduced into UHTC matrices as reinforcement. Amount, orientation and type of fibres is still under investigation, as well as, the identification of the best technology to densify them.

2.2 Ceramic matrix composites

2.2.1 Introduction

Ceramic Matrix Composites (CMCs) are a class of ceramic materials constituted by carbon or ceramic fibres embedded in ceramic matrices (oxide or non-oxide). These materials have been investigated to improve the monolithic ceramic properties, mainly their brittleness. Indeed, the bonding forces present between the fibres and the matrix are relatively low, resulting in an improvement of the fracture toughness and resistance to crack propagation. Thanks to these characteristics, it is possible to prevent the catastrophic failures typical of bulk ceramics [83]. Moreover, CMCs present excellent properties such as high-temperature strength, high thermal conductivity, low coefficient of thermal expansion, good thermal shock resistance and low density. Finally, they are more resistant to high temperature oxidation compared to superalloys [84], [85].

Usually, CMCs labels indicate the type of fibre and the type of matrix (e.g.: carbon/silicon carbide, C/SiC, stands for carbon fibre reinforced silicon carbide). The most used CMCs are based on non-oxides matrices such as carbon or silicon carbide. They are carbon/carbon (C/C), carbon/silicon carbides (C/SiC), and silicon carbide/silicon carbide (SiC/SiC) [86].

C/C composites retain their properties at temperature around 2000 °C in an inert atmosphere or vacuum. However, they undergo oxidation at 500 °C [83] already. A different behaviour is visible for C/SiC or SiC/SiC that have a good oxidation and ablation resistance thanks to a silica film originating at 1100 °C due to the SiC oxidation. Above 1650 °C, SiO_2 will react with SiC at the interface to form volatile SiO, which turns to be limiting for their application to temperature below 1600 °C [87], [88]. Regarding the mechanical properties, a typical value of strength for C/SiC or SiC/SiC composites are between 160 – 410 MPa while fracture toughness between 5 – 25 $MPa \cdot m^{0.5}$ [89]–[91].

2.2.2 Processing

The main routes for the fabrication of CMCs are Chemical Vapour Infiltration (CVI), Polymer Infiltration and Pyrolysis (PIP) and Liquid Silicon Infiltration (LSI) (Fig. 2.5) [83], [92].

- Chemical Vapour Infiltration (CVI): this technique was developed for the production of C/C composites and is based on the deposition of the ceramic matrix from the gas phase. The porous carbon fibre preform is exposed to a mixture of argon and light hydrocarbons at 1000 °C and under a pressure of 1000 kPa. The gas decomposes on the surface of the fibres, depositing the carbon matrix around the fibres. This process can also be used for the deposition of SiC matrix. CVI process allows to obtain highly pure matrix, leading to excellent mechanical properties. However, several cycles should be repeated until full density is reached, requiring several weeks [93]–[95].

- Polymer Infiltration and Pyrolysis (PIP): this technique is based on the infiltration of a carbon fibre preform with a liquid precursor which is than pyrolyzed to form a graphitic matrix reinforced with fibres. This step can be repeated several times until near full density composites are obtained [90], [96].

- Liquid Silicon infiltration (LSI): This technique is based on the preliminary infiltration of a carbon preform with phenolic resin, followed by a pyrolysis and a melt silicon infiltration that reacts with solid carbon to form SiC in situ. With this process, fully dense composites are obtained but the molten silicon can damage the carbon fibres due to their high reactivity. Silicon can be substituted with other elements to form in-situ carbides [97]–[100].

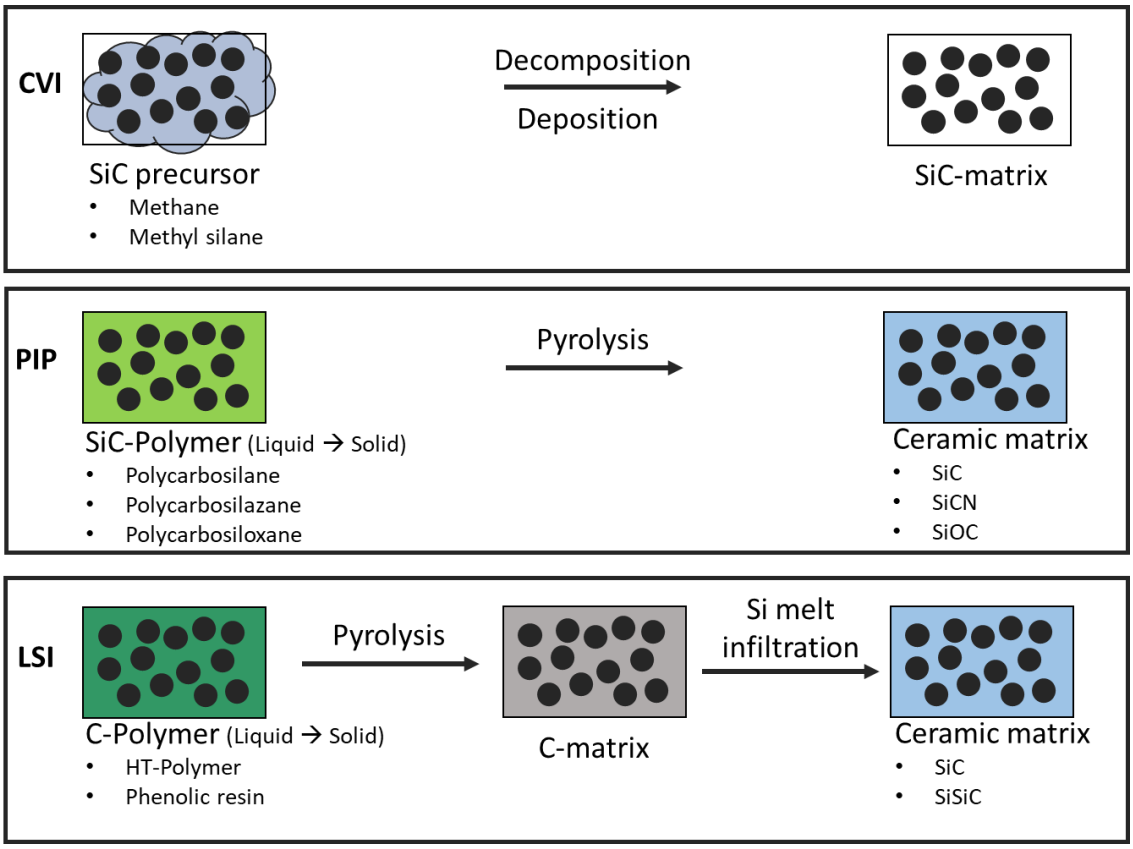

Fig. 2.5: Schematic representation for the fabrication of CMCs: Chemical Vapour Infiltration (CVI), Polymer Infiltration and Pyrolysis (PIP), and Liquid Silicon Infiltration (LSI).

2.2.3 Applications

The study of CMCs begun about 40 years ago for space applications. However, in recent years, civil requirements became the driving forces. Due to their high thermal stability and good corrosion and wear resistance, these materials are interesting for long term and damage tolerant applications in different industries sectors like ground transportation (e.g.: brake and clutch systems), mechanical engineering (e.g.: bearings, ballistic protections), and power generation (e.g.: burners, heat exchangers) [83]. For example, LSI-based C/SiC and C/C show unique properties for friction applications, like high wear rate resistance, high temperature resistance, thermal shock resistance and coefficient of friction, which can be tailored in a brake as well as in gliding systems. High performance brakes are one of the most important application areas for C/C materials. However, due to high wear and unstable coefficient of friction at low temperature, C/C is limited to applications in aircrafts and racing cars. These drawbacks could be overcome by C/SiC materials. Another promising application for C/SiC is ballistic protection

against high velocity projectiles. In fact, known monolithic armour ceramics, such as Al_2O_3, SiC, and B_4C, offer high protection against single hits but not multiple hits due to high brittleness of bulk ceramics. C/SiC materials, overcome these problems by reducing crack propagation and improving multiple hit performance, as well as reducing weight compared to monolithic Al_2O_3 and SiC [83].

2.3 Ultra-high temperature ceramic matrix composites

2.3.1 Introduction

The request of materials capable to resist in extreme conditions where a temperature above 2000 °C is reached - such as hypersonic flight and rocket propulsion- , has led to the development of a new class of ultra-high temperatures materials. UHTCs possess a high melting point and ablation resistance but are brittle. Vice versa CMCs possess excellent mechanical properties but are limited to a work temperature below 1600 °C [101]. For these reasons, many approaches have been investigated to combine the good mechanical properties of CMCs with the refractoriness of UHTCs. The most common approaches are listed below:

- CMCs with a UHTC coating: one of the easiest approaches for the protection of C/C composites is the use of a UHTC coating. The main issue of this method is obtaining a good adhesion between the C/C composite and the UHTC phase due to the different chemistry and thermal expansion coefficient of the materials [102]–[105].

- CMCs with UHTC particles: Another approach to improve the properties of the materials is by embedding UHTC particles in the ceramic matrix of C/C or C/SiC composites. In this way, the synergy created between the formation of B_2O_3 and SiO_2 results in the increase of the oxidation resistance [91], [106].

- UHTCs with continuous carbon fibres: the reinforcement of UHTC-rich matrix composites with continuous fibres improve toughness, damage tolerance and thermal shock resistance but presents the problem of the difficult infiltration of long carbon fibres. The most important parameter for this process is the rheology and chemical activity of the slurry. To obtain a good degree of infiltration, the powders loading in the suspension should be the highest possible. However, increasing the solid loading leads to an increase of viscosity which hinders the infiltration. So, some compromises have to be done to obtain the required result [107]–[109]

- UHTCs with carbon particles or short fibres: to increase the toughness of UHTCs, a way is to reinforce the matrix with the addition of carbon particles or short fibres. The process is quite simple and usually adopts a sintering technique. The final composites are typically characterized by lower strength compared to the bulk material due to the generation of internal stresses. However, the presence of short fibres improves the fracture toughness [110]–[115].

The high-performance composites are generally made from continuous fibres, but there are many applications where the requirements are less demanding or where the manufacturing route cannot be fabricated with continuous fibres. In this case, it is more appropriate to consider the use of short fibres. Moreover, some reinforcing fibres are available only in the form of short filaments, e.g. recycled carbon fibres. There are different ways to incorporate short fibres into a ceramic matrix. The most common are ball milling, colloidal process, and tape casting. Ball milling allows incorporation of high volumetric amount of fibres, but milling causes surface damage, fibre fracture with reduction of the fibre length from millimetres to 100-300 μm and debris formation [116]. Fibres with a rough surface are more reactive with the matrix phase during sintering, leading to a strong fibre-matrix interfacial bonding which limits fibre pull-out resulting in a lower toughening effect [46], [117], [118]. The colloidal process avoids the fibre damage but requires the use of organic solvents (e.g., ethanol) [119]. The same occurs for the tape casting process, where a mixture of ethanol and butanol are used as a solvent and the non-ionic Triton X-100 as a surfactant. Moreover, with tape casting only a low amount of fibre can be added, 10-15 vol. %. [120]. Recently, inks based on ZrB_2, and short fibres have been prepared via 3D printing. This technique offers the possibility of creating near net shaped components with controlled fibre alignment. However, one major drawback of this process is still represented by the low amount of fibres that can be incorporated ranging between 5-10 vol. %. Also, another problem of this process is the matrix cracking due to the presence of fibres [121]–[123]. In this work, a new process for the incorporation of short carbon fibres as reinforcement was investigated. This new method allows to incorporate high fraction of fibres into the matrix limiting the damaging during the mixing with ceramic powders. Moreover, in this way, graded structures and complex shape can be realized.

2.3.2 Processing method

The fabrication methods for the production of UHTCMCs are often a combination of the processes used for CMCs and UHTCs. In Fig. 2.6 the main methods are reported. For any composite, the selection of a matrix and second phase are very important in order to obtain the desired properties. Materials chosen for UHTCMCs matrices can be many, but the most used are transition metal borides - such as zirconium or hafnium - due to their properties [10]. The second phase can be constituted by different reinforcements such as particulate, chopped fibre, continuous fibre or preforms that are chosen in order to obtain the required properties. At the same time, the fibres used as reinforcements can be composed by different materials such as SiC fibres, carbon fibres or UHTC fibres. Carbon fibres are the most used due to anisotropic thermo-mechanical properties, low density that offers the highest specific modulus, highest specific strength of all reinforced fibres, and low price [124]. To produce UHTCMCs, an important step is the preparation of the interface between the matrix and the secondary phase. In literature, several works report the fabrication of UHTCMCs by the introduction of UHTC phases into the fibre matrix using techniques re-adapted from the CMC technologies such as:

- Chemical Vapour Infiltration (CVI): it is a layer-by-layer technique, versatile and conducted at low temperature. In this way, the fibre is not damaged thus resulting in excellent mechanical and anti-ablation properties. However, this process requires a very long processing time (months) to obtain a fully dense composite and a lot of energy is needed [124]–[126].

- Polymer Infiltration and Pyrolysis (PIP): this technique consists in the infiltration of one preform with SiC preceramic polymer doped with UHTC powders followed by pyrolysis. It allows to have a large versatility due to chemistry precursor and as a liquid precursor, the penetration into the fibre tow is easy due to the capillary pressure. However, many cycles of infiltration and pyrolysis are required to obtain a good densification due to low yields of ceramic. Moreover, the matrix can be porous and can contain micro-cracks due to the escape of gaseous by-products. Finally, the reactive chemicals and heat treatments can cause fibre degradation, leading to a loss of mechanical properties [124], [127], [128].

- Reactive Melt Infiltration (RMI): in this technique, a porous CMC is infiltrated with a molten metal in order to obtain a near fully dense matrix. The processing time for this technique is very short, resulting in a relatively cheap process. However, for fibre

composites the high temperature required for reactive metal infiltration (≥ 1400 °C) can damage the fibres. Moreover, residual metal phases which have relatively low oxidation resistance, and a low melting point can lead to accelerate cracks propagation when the material is operating at high temperature [124], [129], [130].

- Slurry Impregnation Process (SIP): this process consists in the fibre/woven fabric impregnation by introducing a slurry made of matrix powder. The slurry is usually prepared by ball milling the powder with a binder and dispersant in a solvent (aqueous or non-aqueous). The process is cheap, quick and easy, and the properties of the slurry are easily tuneable. However, the homogeneous penetration of large preforms is difficult [124].

In the case of short fibre, a slurry impregnation process is still used with some difference. In fact, in this case the short fibre and the ceramic powders are mixed with the help of a organic solvent and grinding media to obtain a homogeneous product. This process is called ball milling.

An essential step for the consolidation of bulk ceramics is the sintering, that is rarely applied to the manufacturing of CMCs due to the applied pressure combined with the high temperature that may cause fibre damage. Nevertheless, sintering processes have been used for UHTCMC manufacturing [131]. The sintering route is characterized by short process time and allows to create a fully dense UHTC matrix. However, an accurate setting is required to avoid cracks and a strong fibre-matrix interface. Moreover, the use of pressure in the sintering route limited the production to the fabrication of a simple shape. The main sintering techniques, as reported in the previously paragraphs are:

- Hot Pressing (HP): this method allows to sinter composites with a high amount of carbon fibres and a high density. However, due to the high temperature and pressures involved in the process, the fibres can be damaged and their interaction with the matrix can be too strong. Moreover, near-net shape components are not easily achievable [124].

- Pressure-less Sintering (PS): it allows to work with a high amount of fibres and low pressure, reducing the matrix-fibre interaction and fibre degradation. In addition, near-net shapes are possible. Unfortunately, the final density is lower than the other sintering techniques and the temperature and time required for the sintering are high due to the low pressure used [124].

- Spark Plasma Sintering (SPS): this process allows to work with a high volume of fibre and to obtain a high densification. Since the manufacturing time is short, the sintering temperature and time were reduced. Despite of the low sintering temperature and time, a strong matrix-fibre interaction is visible. Moreover, the equipment is more expensive than conventional HP furnaces and near-net shapes components are not achievable [124].

- Hot Isostatic Processing (HIP): It allows to use a high fibre volume fraction and to obtain near-net shaped components. Nonetheless, the equipment is expensive and high pressure is required [124].

In this work, a similar slurry impregnation process was used to prepare the "green" with pitch-based short carbon fibres as a reinforcement. The sintering of the "green" was carried out by hot pressing, with a focus on the reduction of the fibre damage and to obtain complex shapes.

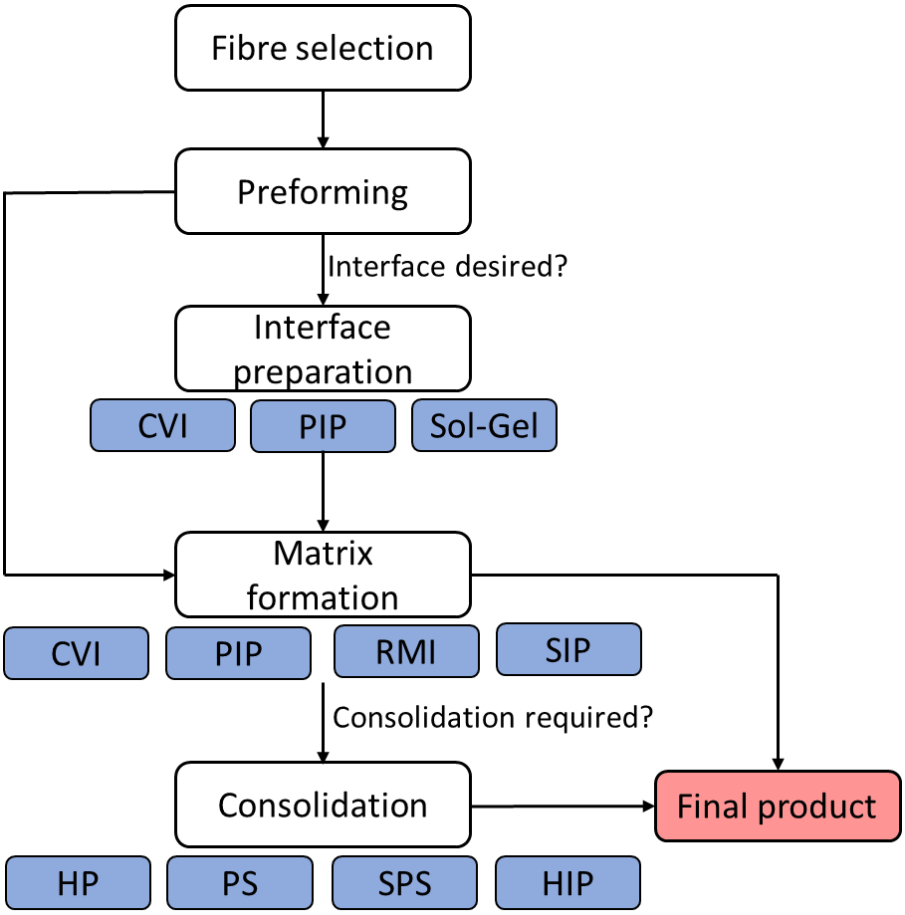

Fig. 2.6: process flow sheet summarises the different methods of process for obtaining the UHTCMCs

2.3.3 Mechanical properties of UHTCMCs

Despite the high number of publications on UHTCMCs, it is difficult to make a true comparison on mechanical properties across the board of UHTCMC processing techniques. This happens because each technique results in a variation of fibre volume fraction and orientation, composition of matrix and fibre phases, and overall porosity in the composite, all of which greatly influence the final mechanical properties. Moreover, the mechanical properties reported for UHTCMCs are also difficult to compare across studies as they can vary depending on testing procedure.

Generally, the addition of fibres has been found to decrease the strength of the bulk UHTCs due to the higher porosities or internal stress originating from the different CTE between fibre and matrix. However, the presence of fibre as a reinforcement has been shown to promote graceful failure and a higher ultimate failure strain that is important for applications where a high damage tolerance is required. So, in general UHTCMCs exhibit enhanced mechanical behaviour over current materials. In Table. 2.4 some mechanical properties of different UHTCMCs are reported.

Table. 2.4: Properties of carbon fibre reinforced ultra-high temperature ceramic matrix composites prepared with different approaches.

Materials	General characteristic	Density (g/cm^3)	Open porosity (%)	Flexural strength (MPa)	Reference
C_f/HfB_2-C	Injection + CVI + 2D preform	3.20	16.0	121.4	[125]
C_f/ZrC	PIP + 3D preform	1.98	12.4	107.6	[132]
C_f/ZrC	CVI + MRI + 3D preform	2.46	5.0	240.0	[133]
C_f/ZrC-SiC	HP + PIP + 2D preform	2.47	6.6	178.0	[134]
C_f/ZrC-SiC	CVI + PIP + 2D preform	2.18	4.9	748.0	[134]
C_f/ZrC-SiC	RMI + 3D needled preform	2.52	1.7	380.0	[135]
C_f/ZrC-SiC	RMI + 3D braided preform	2.94	5.3	101.5	[133]
C_f/ZrB_2-ZrC-SiC	RMI + 3D needled preform	2.42	9.4	185.0	[136]
C_f/ZrB_2	Vacuum bagging + HP + 1D fabric	3.30	/	90.0	[109]
C_f/ZrB_2-SiC-Si_3N_4	SI + HP + 1D fabric	/	Small	355.0 (//) 63.0 ($\perp$)	[137]
C_f/ZrB_2	HP + ball milled chopped fibre	3.40	15.0	103.0	[138]

2.3.4 Oxidation resistance

One of the main advantages of UHTCMCs materials is the introduction of the self-protection capability of UHTCs into conventional CMCs. In fact, carbon is one of the materials with the highest temperature stability because at atmospheric pressure it sublimate rather than melt and it can be used in application up to 2800 °C if kept in non-oxidising environment. However, in environment rich of oxygen the oxidation begins at 450 °C [139]. For this reason, the improvement of resistance due to the UHTCs matrices is required. To protect the carbon fibre from oxidation, different approaches were investigated. A first mechanism is the application of an environmental barrier coating (EBC), made of UHTCs, on CMC material [102], [103]. In this case, the interface points between the UHTC and CMC layer is a critical point. In fact, the adhesion between the composite and the coating could be compromised due to the different chemistry and thermal expansion of the materials. Another way is to introduce ZrB_2 powders into fibre preforms via slurry impregnation. In this case, a different route can be used such as chemical vapour infiltration (CVI) [89], polymer infiltration and pyrolysis (PIP) [140], pack cementation (PC) [103] and hot pressing (HP) [141]. In the case of UHTCMC fabricated by HP - where the UHTC is the main phase - the ZrB_2-SiC matrix with a high content of $SiC \geq 10\%$, can effectively protect the fibres from oxidation [142]. In this way, UHTCMs possess the CMCs damage tolerance thanks to the fraction of fibres and the ablation resistance of UHTC [138], [143], [144].

In literature studies, the oxide layer thickness was measured to compare the oxidation behaviour of different composites. The oxidised layer thickness obviously increases with increasing the oxidation temperature and is affected by the amount of fibre reinforcement and matrix composition. The oxide layers thickness of the ZrB_2 based UHTCMCs presented values from 18 μm to 170 μm due to the different oxidation conditions and samples composition (Table. 2.5). All the composites were damaged by the oxidation of the most vulnerable phase - the C – which led to the formation of pores and channels. However, the presence of a UHTC matrix that covers the fibres improves the oxidation resistance of the carbon fibre [145].

Table. 2.5: Oxide layer thickness of different ZrB_2 based UHTCMCs samples after oxidation tests in air.

Composition (vol. %)	Oxidation Temperature (°C)	Oxide layer thickness (μm)	Ref.
$54ZrB_2 + 3SiC + 3Y_2O_3 + 40Cf$	2000	170	[145]
$48ZrB_2 + 3SiC + 3Y_2O_3 + 46Cf$	2000	100	[145]
$50ZrB_2 + 3SiC + 47Cf$	1500	18	[146]
$46ZrB_2 + 1SiC + 3Y_2O_3 + 50Cf$	1500	24	[146]
$50ZrB_2 + 3SiC + 47Cf$	1650	43	[146]
$46ZrB_2 + 1SiC + 3Y_2O_3 + 50Cf$	1650	53	[146]
$57.5ZrB_2 + 2.5SiC + 40Cf$	1500	64	[147]
$55ZrB_2 + 5SiC + 40Cf$	1500	50	[147]
$52.5ZrB_2 + 7.5SiC + 40Cf$	1500	45	[147]
$50ZrB_2 + 10SiC + 40Cf$	1500	36	[147]
$57.5ZrB_2 + 2.5SiC + 40Cf$	1650	85	[147]
$55ZrB_2 + 5SiC + 40Cf$	1650	57	[147]
$52.5ZrB_2 + 7.5\ SiC + 40Cf$	1650	50	[147]
$50ZrB_2 + 10SiC + 40Cf$	1650	35	[147]

The dominant reactions in the oxidation of Cf reinforced UHTCMCs are:

$$C_{(s)} + \frac{1}{2}O_{2(g)} \rightarrow CO_{(g)} \quad (2.19)$$

$$C_{(s)} + O_{2(g)} \rightarrow CO_{2(g)} \quad (2.20)$$

$$ZrB_{2(s)} + 5O_{2(g)} \rightarrow ZrO_{2(s)} + B_2O_{3(l,g)} \quad (2.21)$$

$$SiC_{(s)} + \frac{3}{2}O_{2(g)} \rightarrow SiO_{2(l)} + CO_{(g)} \quad (2.22)$$

$$ZrB_{2(s)} + SiC_{(s)} + 4O_{2(g)} \rightarrow ZrO_{2(s)} + \rightarrow SiO_2 \cdot B_2O_{3(l)} + CO_{(g)} \quad (2.23)$$

The borosilicate glass can partially fill the holes left by vaporization of the carbon fibres, until its temperature limit is reached.

Some research also revealed that there is a trade-off between oxidation resistance and fracture toughness if matrix porosity is retained to promote poor adhesion to the fibre. On the one hand, a dense UHTC matrix is accompanied by a relatively strong matrix-carbon fibres interface offering a good oxidation protection but implying a lower value of fracture toughness. On the other hand, a partially porous UHTC leads to high values of fracture toughness due to the decrease of matrix Young's modulus and weak fibre/matrix interface. However, the porosity jeopardizes the resistance to oxidation/erosion [139]. In literature, it is reported that the short fibre reinforced composites showed a retained strength higher than ≈ 80% of its original value after an oxidation for 2 min in air at 2005 °C. The continuous fibre reinforced composites, after the oxidation at the same conditions maintained a ≈ 70% of the original shape [145].

A few papers studied the oxidation resistance of short and continuous fibre reinforced UHTCMCs [148]. Most of these tests conducted at temperature above 2200 °C demonstrated that UHTCMCs samples reinforced with long or short carbon fibres presented excellent oxidation resistance performance compared to the graphite samples in the same conditions, with an erosion rate ≈ 0.45 mm/s versus 0.15 mm/s of a ZrB_2 based UHTCMC.

2.4 Braking materials

For vehicles, brakes are commonly used in a pad on disc configuration. The most important requirements are high and stable coefficient of friction (COF) under multiple braking conditions, low wear rate for increased life, low life cycle cost, low weight, good noise, vibration and harshness properties (NVH) and a high degree of freedom in the structural design [149]. Common disc materials include steel, carbon-carbon (C/C) and carbon fibre reinforced carbon-silicon carbide (C/C-SiC) (Fig. 2.7). Steel is used for standard automotive braking systems. This material is cheap, possesses a relatively high and stable coefficient of friction and low wear rate [150]. Paired with organic or metallic

pads, they suit all but high-performance applications, where low operating temperature (≈ 400 °C [151]) and high steel density would cause sudden breaks. Therefore, C/Cs have been developed in the 1970s and used ever since in aircrafts and racing vehicles like formula 1 and formula E. A density of <2 g/cm³, high maximum operating temperatures (2000 °C) combined with high heat capacity and thermal shock resistance makes light brakes capable of absorbing huge amounts of energy in a short time [152]. However, C/C possess low oxidation resistance and low COF in wet or cold conditions due to the inherent lubrication ability of graphite [153], [154]. This makes them unusable for standard road vehicles and limits their application to racing cars. The C/C-SiC composites were developed since the 1990s and used for high performance cars [155]. These CMCs exhibit exceptional wear resistance, little to no oxidation and a high COF in different weather conditions with the price of more weight and limited operating temperature [154].

Fig. 2.7: Representation of three brake discs constituted by different materials.

2.4.1 C/C-SiC

C/C-SiC are a lightweight and thermally stable materials manufactured by LSI process. They overcome the drawbacks of C/C materials (influence of temperature and humidity on the coefficient of friction) and grey cast iron (high weight and low thermal stability), the two main materials for brake discs in cars and aircraft. C/C-SiC shows excellent tribological properties, especially a high and quite stable COF and high wear resistance. These properties allow to use these materials in emergency brake systems of elevator or cranes where sintered metallic and C/C brake pads have reached their thermal limits [156]–[158]. In fact, the oxidation of carbon starts at a temperature about 400 °C

in air and leads to destruction of the brake disc at higher temperature. This limits the use of C/C brakes on racing cars. One of the main problems for the brake materials is unstable COF. This is due to the low transverse thermal conductivity, especially in the 2D composites. To improve the transverse conductivities, different modifications can be achieved [83]:

- Use of carbon fibres with high thermal conductivity, like graphite fibres

- Increase the amount of fibres oriented perpendicular to the friction surface

- Increase the ceramic friction

The amount of ceramic can be easily increased by reducing the fibre content, resulting in a higher silicon uptake and consequently a higher density of the final material. So, the lower is the fibre volume content and higher the density, the higher the transverse thermal conductivity of the CMC material (Fig. 2.8). However, a higher density coincides with a decrease in strength and fracture toughness. So, the CMC composites must be designed according to the individual properties requirements of the brake system as a compromise between thermal and mechanical properties.

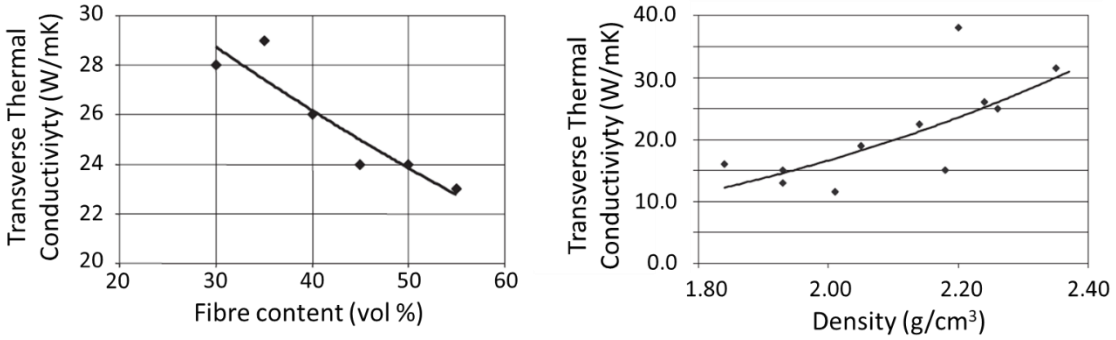

Fig. 2.8: Behaviour of thermal conductivity at 50 °C with different fibre volume (left) and with density (right) of reinforced C/SiC composites [157].

As for other materials, the thermal conductivity of C/SiC composites decreases with temperature increase. The average decrease of transverse conductivity between 300 °C and 900 °C is round 30%. These temperatures represent the temperature on the disc surface during a high-performance braking. Consequently, one important criteria for the choice of C/SiC materials for brake pads is their thermal conductivity at high temperature

[83]. For example, the drive units of elevators are designed for building of up to 500 m in height and can accelerate high mass. If the speed exceeds a determinate speed, the elevator is automatically brought to a controlled emergency stop when the brake pads can reach temperatures up to 1200 °C. At this temperature, conventional braking materials are beyond their limits of thermal stability and wear resistance [83].

The presence of SiC can increase the coefficient of friction, the thermal shock resistance and the environmental stability [159]. However, the presence of SiC may increase wear rate due to its abrasive action and decrease the fatigue resistance depending on the pad material [160], [161]. Moreover, C/C-SiC brake discs paired with common pad materials may suffer from instability of the coefficient of friction during the braking [149] which is often noted as saddle-curve behaviour resulting in rising COF for low and high sliding speeds during a braking test (Fig. 2.9). The introduction of different ceramic phases could ensure broader adjustment of tribological properties. The carbon fibre plays a role of a lubricant to prevent occlusion during braking; the hybrid ceramics increase friction resistance. For example, ZrB_2 can rapidly form an oxidant layer during braking to prevent carbon fibre oxidation. Their effects result in more stable braking performants [162]. For these reasons, carbon fibre reinforced UHTC-ZrB_2 based material could be a new class of material for braking applications.

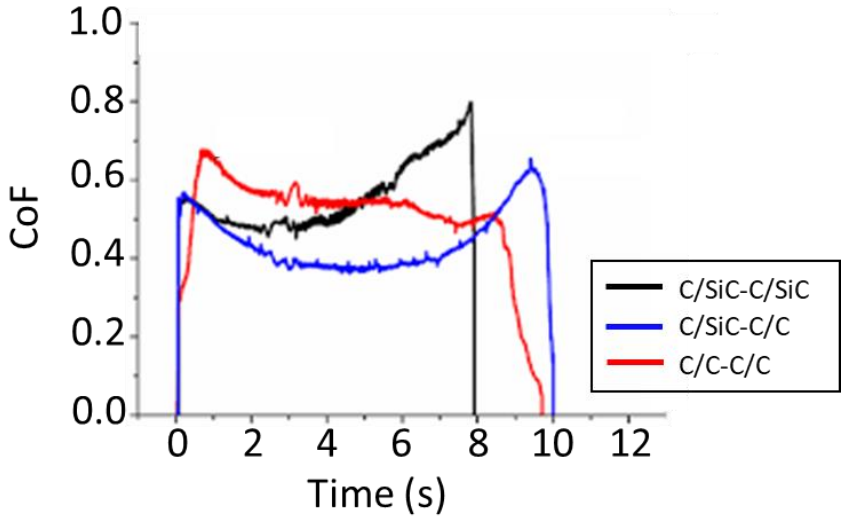

Fig. 2.9: Different behaviours of C/C and C/C-SiC brake disc with C/C and C/C-SiC pads [149].

2.4.2 UHTC based composites

ZrB_2 based ceramics are used in aerospace, automotive and nuclear industry in extreme environments thanks to their moderate density, high thermal conductivity, high temperature of melting, excellent creep resistance and high strength at high temperatures [73], [163], [164]. Moreover, the formation of B_2O_3 in high-speed sliding contacts and the formation of boric acid in humid environment reduce friction or wear [165]–[167]. Moreover, the presence of SiC improves the hardness, the flexural strength and the resistance against oxidation [168]–[172]. The generation of B_2O_3 provides self-healing of defects in severe conditions like ablation and high temperature erosion [75], [171], [173]. For these reasons, ZrB_2-SiC composites are investigated for different wear-resistant applications like mechanical seals, extrusion dies and cutting tool inserts in high-speed machining [174] .

In general, with ceramics, there are two types of wear: the adhesive and the abrasive (Fig. 2.10). The adhesive wear takes place when adhesion verifies across an interface between two ceramics surfaces or a ceramic surface and a metal. If a fracture occurs in the ceramic with the sliding or rubbing of one surface over the other (tangential motion), an adhesive wear has taken place. For this type of wear to happen, the fracture strength of one of the two materials in contact must be less than that of the interfacial junction. However, if the bonding at the junctions is less than that in the two materials, fracture will occur at the interface without wear. Moreover, micro welding may take place due to the heat generated by the friction. This results in detachment or material transfer from one surface to the other. Adhesive wear can improve the roughness and generate protrusions above the surface. Surface held apart by lubricating films, oxide film etc, reduce the adhesion mechanism. In some cases, the wear resistance is based on the transfer from the softer metal to the harder metal, forming a thin layer of softer metal on the harder metal. For example, when a silicon carbide surface is put in contact with a metal surface, the silicon carbide deforms elastically. However, high pressures are developed at the interface and the adhesive bonds generated at silicon carbides - metal interface are strong enough to fracture the metal bonds and transfer metal on the silicon carbide surface. The presence of defects such as vacancies, voids, impurities or microcracks in the superficial layers of the materials in contact will usually dictate where wear damages are generated. The distribution and extent of these defects, will determine the wear damage and the size of the wear particles generated [175].

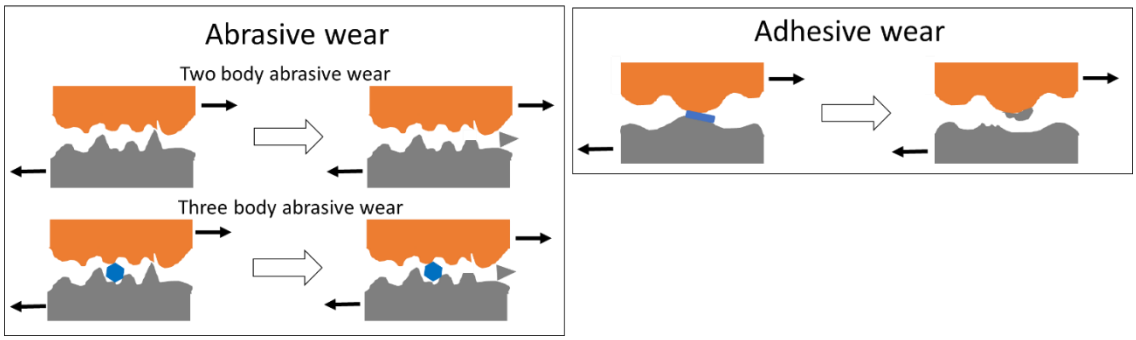

Fig. 2.10: Representation of abrasive wear on the left and adhesive wear on the right (in orange the hardest material, in grey the softer material)

Abrasive wear occurs when the material is lost due to the moving of protuberances that are put in contact. Most specifically, it occurs when a hard-rough surface slides across a softer surface and it is referred to as grinding wear. The harder material can be one of the rubbing surfaces of hard particles. Abrasion mainly involves microscale cutting and plowing processes. There are two possible abrasive wear mechanisms:

- Two-body abrasive wear: it occurs when the hard particles remove material from the opposite surface like plowing operation.

- Three-body abrasive wear: It occurs when the particles are free to roll and slide on the surface. The wear can be open or closed and it depends to the contact environments. When the surfaces are enough displaced to be independent of one another, an open contact environment is present [175].

There are many strategies for mitigating abrasive wear, but the general rule is that harder is better.

Due to their mechanical properties and hardness, ZrB_2 based composites wear was investigated in previous studies. In particular, friction and wear rates of SiC reinforced ZrB_2 in dry condition of sliding against different counter-bodies were studied [176]. The material removal mechanism was affected by the SiC amount in the composites and the counter-body. The average coefficient of friction for ZrB_2 based composites against different counter-body (SiC, Al_2O_3, ZrO_2) was found to range from 0.49 to 0.69 and with the SiC counter-body resulted quite stable (Fig. 2.11) [176].

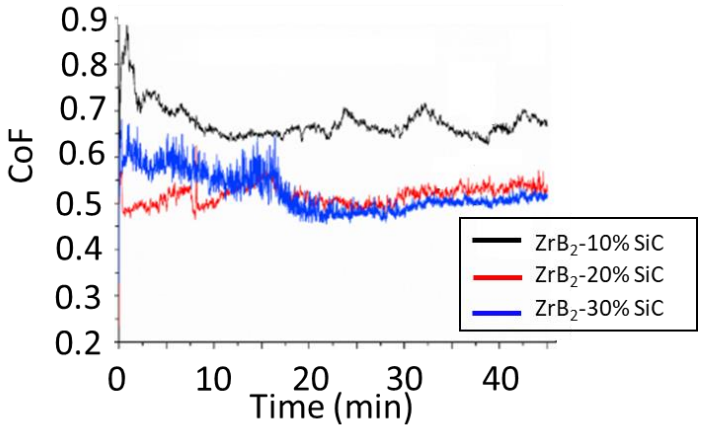

Fig. 2.11: A typical plot of coefficient of friction of ZrB_2-SiC vs sliding time against SiC counter-body.

Usually, the wear rates and the CoF are investigated via a wear tester (Fig. 2.12), where a load is applied on a stationary ball against the composites disc which rotates at a linear speed for a determinate time and produces a wear track on the disc. This machine is useful for the investigation of the material properties, but it does not reproduce a real braking mechanism. For this reason, in this work and industrial testing machine that reproduces the braking mechanism was used.

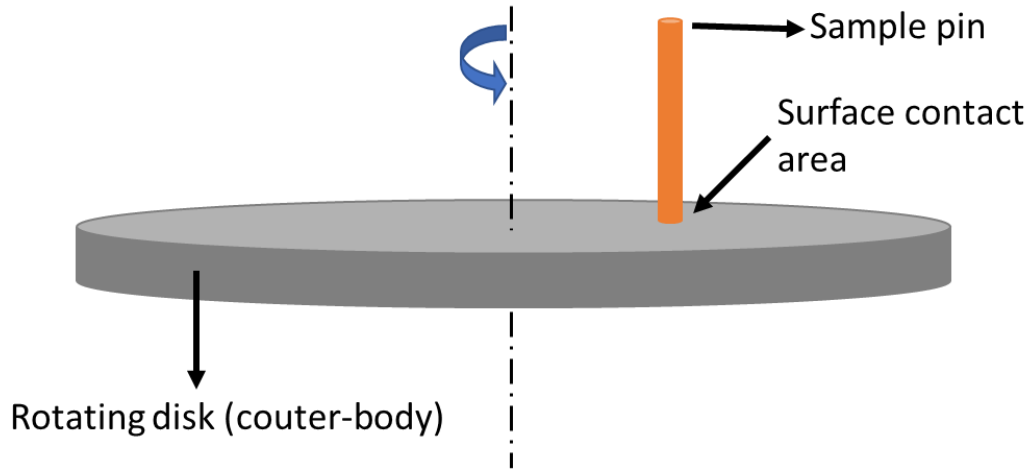

Fig. 2.12: schematic of pin-on disc wear machine

2.5 References

[1] D. R. U. W. D. Kingery, H. K. Bowen, *Introduction to Ceramics*, 2nd Editio. 1976.

[2] W. E. L. David W. Richerson, *Modern ceramic engineering*. 1992.

[3] W. G. Fahrenholtz, E. J. Wuchina, W. E. Lee, and Y. Zhou, *Ultra-High Temperature Ceramics: Materials for Extreme Environment Applications*, vol. 9781118700785. Wiley Blackwell, 2014.

[4] E. Wuchina, E. Opila, M. Opeka, W. Fahrenholtz, and I. Talmy, "UHTCs: Ultra-High Temperature Ceramic materials for extreme environment applications," *Electrochem. Soc. Interface*, vol. 16, no. 4, pp. 30–36, Dec. 2007, doi: 10.1149/2.F04074IF.

[5] W. G. Fahrenholtz and G. E. Hilmas, "Ultra-high temperature ceramics: Materials for extreme environments," *Scr. Mater.*, vol. 129, pp. 94–99, Mar. 2017, doi: 10.1016/J.SCRIPTAMAT.2016.10.018.

[6] M. J. Gasch, D. T. Ellerby, and S. M. Johnson, "Ultra High Temperature Ceramic Composites," *Handb. Ceram. Compos.*, pp. 197–224, Aug. 2005, doi: 10.1007/0-387-23986-3_9.

[7] M. M. Opeka, I. G. Talmy, and J. A. Zaykoski, "ULTRA-HIGH TEMPERATURE CERAMICS Oxidation-based materials selection for 2000 • C + hypersonic aerosurfaces: Theoretical considerations and historical experience."

[8] D. Ni *et al.*, "Advances in ultra-high temperature ceramics, composites, and coatings," *J. Adv. Ceram.*, vol. 11, no. 1, pp. 1–56, 2022, doi: 10.1007/s40145-021-0550-6.

[9] L. Kaufman and E. V Clougherty, "INVESTIGATION OF BORIDE COMPOUNDS FOR VERY HIGH-TEMPERATURE APPLICATIONS." 01-Oct-1963.

[10] M. M. Opeka, I. G. Talmy, E. J. Wuchina, J. A. Zaykoski, and S. J. Causey, "Mechanical, Thermal, and Oxidation Properties of Refractory Hafnium and zirconium Compounds," *J. Eur. Ceram. Soc.*, vol. 19, no. 13–14, pp. 2405–2414, 1999, doi: 10.1016/s0955-2219(99)00129-6.

[11] S. A. Tucker and H. R. Moody, "II.—The production of hitherto unknown metallic borides," *J. Chem. Soc. Trans.*, vol. 81, no. 0, pp. 14–17, Jan. 1902, doi: 10.1039/CT9028100014.

[12] P. Liu, P. Zhang, X. Pang, Q. Wang, and T. Liu, "A study on fabrication technique of ZrB2 target," *Procedia Eng*, vol. 27, pp. 1305–1312, 2012, doi: 10.1016/j.proeng.2011.12.586.

[13] M. M. Nasseri, "Comparison of HfB2 and ZrB2 behaviors for using in nuclear industry," *Ann. Nucl. Energy*, vol. 114, pp. 603–606, Apr. 2018, doi: 10.1016/J.ANUCENE.2017.12.060.

[14] S. C. Middleburgh, D. C. Parfitt, P. R. Blair, and R. W. Grimes, "Atomic Scale

Modeling of Point Defects in Zirconium Diboride," *J. Am. Ceram. Soc.*, vol. 94, no. 7, pp. 2225–2229, Jul. 2011, doi: 10.1111/J.1551-2916.2010.04360.X.

[15] F. W. Glaser and B. Post, "System Zirconium-Boron," *JOM 1953 59*, vol. 5, no. 9, pp. 1117–1118, Nov. 2017, doi: 10.1007/BF03397597.

[16] P. Rogl and P. E. Potter, "A critical review and thermodynamic calculation of the binary system: Zirconium-boron," *Calphad*, vol. 12, no. 2, pp. 191–204, Apr. 1988, doi: 10.1016/0364-5916(88)90021-1.

[17] F. S. Kaplan, T. L. Kalyada, N. S. Gaenko, A. A. Kortel', and K. V. Simonov, "Porous structure of the periclase plates of steel-teeming ladle slide gates," *Refractories*, vol. 23, no. 11–12, pp. 625–630, Nov. 1982, doi: 10.1007/BF01387484/METRICS.

[18] K. Vedula and J. 111991 D, "Ultra-High Temperature Ceramic-Ceramic Composites, Final Report on Project WRDC-TR-89-4089."

[19] H. C. Graham, A. P. Katz, and R. J. Kerans, "Ultrahigh temperature Assessment Sudy - Ceramic Matrix Compsites, Final Report WL-TR-91-4061. Composites," 1992.

[20] D. Rasky, J. Bull, and J. Bull, "Ultra-High Temperature Ceramics." 1994.

[21] S. Hampshire, "Engineering Properties of Nitrides," in *Schneider, S.J., Ed., ASTM Engineered Materials Handbook, Vol. 4 Ceramics and Glasses, ASM International, Almere, 812-820*, 1991.

[22] P. T. B. Shaffer, "Engineering Properties of Carbides," in *Engineered Materials Handbook, Vol.4, Ceramics and Glasses 804–811*, 1991.

[23] T. Endo *et al.*, "Engineering Properties of Borides," *Ceram. Glas. Eng. Mater. Handb.*, vol. 4, no. 8, pp. 787–803, Aug. 1991, doi: 10.2497/JJSPM.54.601.

[24] W. G. Fahrenholtz, G. E. Hilmas, I. G. Talmy, and J. A. Zaykoski, "Refractory diborides of zirconium and hafnium," *J. Am. Ceram. Soc.*, vol. 90, no. 5, pp. 1347–1364, May 2007, doi: 10.1111/j.1551-2916.2007.01583.x.

[25] C. R. Weinberger, G. B. Thompson, and C. R. Christopher Weinberger, "Review of phase stability in the group IVB and VB transition-metal carbides," *J. Am. Ceram. Soc.*, vol. 101, no. 10, pp. 4401–4424, Oct. 2018, doi: 10.1111/JACE.15768.

[26] K. E. Spear, "Chemical bonding in AlB2-type borides," *J. Less Common Met.*, vol. 47, no. C, pp. 195–201, Jun. 1976, doi: 10.1016/0022-5088(76)90096-5.

[27] J. K. Burdett, G. J. Miller, and E. Canadell, "Electronic Structure of Transition-Metal Borides with the A1B2 Structure," *J. Am. Chem. Soc.*, vol. 108, no. 21, pp. 6561–6568, 1986, doi: 10.1021/JA00281A020/ASSET/JA00281A020.FP.PNG_V03.

[28] S. Yu *et al.*, "First-principles study of Zr–N crystalline phases: phase stability, electronic and mechanical properties," *RSC Adv.*, vol. 7, no. 8, pp. 4697–4703, Jan. 2017, doi: 10.1039/C6RA27233A.

[29] K. H. Wu, Y. Jiang, S. Jiao, K. C. Chou, and G. H. Zhang, “Synthesis of high purity nano-sized transition-metal carbides,” *J. Mater. Res. Technol.*, vol. 9, no. 5, pp. 11778–11790, Sep. 2020, doi: 10.1016/J.JMRT.2020.08.053.

[30] S.-J. L. Kang, “Liquid phase sintering,” *Sinter. Adv. Mater.*, pp. 110–129, Jan. 2010, doi: 10.1533/9781845699949.1.110.

[31] L. Ratke and P. W. Voorhees, “Growth and Coarsening,” 2002, doi: 10.1007/978-3-662-04884-9.

[32] J. K. Sonber and A. K. Suri, “Synthesis and consolidation of zirconium diboride: review,” *https://doi.org/10.1179/1743676111Y.0000000008*, vol. 110, no. 6, pp. 321–334, Aug. 2013, doi: 10.1179/1743676111Y.0000000008.

[33] E. Y. Jung, J. H. Kim, S. H. Jung, and S. C. Choi, “Synthesis of ZrB2 powders by carbothermal and borothermal reduction,” *J. Alloys Compd.*, vol. Complete, no. 538, pp. 164–168, Oct. 2012, doi: 10.1016/J.JALLCOM.2012.05.076.

[34] A. L. Ortiz, V. Zamora, and F. Rodríguez-Rojas, “A study of the oxidation of ZrB2 powders during high-energy ball-milling in air,” *Ceram. Int.*, vol. 4, no. 38, pp. 2857–2863, May 2012, doi: 10.1016/J.CERAMINT.2011.11.058.

[35] A. L. Chamberlain, W. G. Fahrenholtz, and G. E. Hilmas, “Reactive hot pressing of zirconium diboride,” *J. Eur. Ceram. Soc.*, vol. 29, no. 16, pp. 3401–3408, Dec. 2009, doi: 10.1016/J.JEURCERAMSOC.2009.07.006.

[36] R. Heid, B. Renker, H. Schober, P. Adelmann, D. Ernst, and K. P. Bohnen, “Lattice dynamics and electron-phonon coupling in transition-metal diborides,” *Phys. Rev. B*, vol. 67, no. 18, p. 180510, May 2003, doi: 10.1103/PhysRevB.67.180510.

[37] D. Sciti, S. Guicciardi, A. Bellosi, and G. Pezzotti, “Properties of a Pressureless-Sintered ZrB2–MoSi2 Ceramic Composite,” *J. Am. Ceram. Soc.*, vol. 89, no. 7, pp. 2320–2322, Jul. 2006, doi: 10.1111/J.1551-2916.2006.00999.X.

[38] D. Sciti, F. Monteverde, S. Guicciardi, G. Pezzotti, and A. Bellosi, “Microstructure and mechanical properties of ZrB2-MoSi2 ceramic composites produced by different sintering techniques,” *Mater. Sci. Eng. A*, vol. 434, no. 1–2, pp. 303–309, Oct. 2006, doi: 10.1016/J.MSEA.2006.06.112.

[39] L. Silvestroni and D. Sciti, “Effects of MoSi2 additions on the properties of Hf–and Zr–B2 composites produced by pressureless sintering,” *Scr. Mater.*, vol. 2, no. 57, pp. 165–168, Jul. 2007, doi: 10.1016/J.SCRIPTAMAT.2007.02.040.

[40] L. Silvestroni and D. Sciti, “Densification of ZrB2-TaSi2 and HfB 2-TaSi2 ultra-high-temperature ceramic composites,” *J. Am. Ceram. Soc.*, vol. 94, no. 6, pp. 1920–1930, Jun. 2011, doi: 10.1111/J.1551-2916.2010.04317.X.

[41] L. Silvestroi, H. J. Kleebe, S. Lauterbach, M. Müllet, and D. Sciti, “Transmission electron microscopy on Zr- and Hf-borides with MoSi2 addition: Densification mechanisms,” *J. Mater. Res.*, vol. 25, no. 5, pp. 828–834, May 2010, doi: 10.1557/JMR.2010.0126.

[42] F. Monteverde and A. Bellosi, “Microstructure and Properties of an HfB2-SiC

Composite for Ultra High Temperature Applications," *Adv. Eng. Mater.*, vol. 6, no. 5, pp. 331–336, May 2004, doi: 10.1002/ADEM.200400016.

[43] F. Monteverde, Monteverde, and F., "Beneficial effects of an ultra-fine α-SiC incorporation on the sinterability and mechanical properties of ZrB2," *ApPhA*, vol. 82, no. 2, pp. 329–337, Feb. 2006, doi: 10.1007/S00339-005-3327-9.

[44] D. Sciti, L. Silvestroni, V. Medri, and S. Guicciardi, "Pressureless sintered in situ toughened ZrB2–SiC platelets ceramics," *J. Eur. Ceram. Soc.*, vol. 31, no. 12, pp. 2145–2153, 2011.

[45] B. Diletta Sciti, C. Melandri, A. Bellosi, D. Sciti, C. Melandri, and A. Bellosi, "Properties of ZrB2-Reinforced Ternary Composites," *Adv. Eng. Mater.*, vol. 6, no. 9, pp. 775–781, Sep. 2004, doi: 10.1002/ADEM.200400039.

[46] D. Sciti, S. Guicciardi, and L. Silvestroni, "Are short Hi-Nicalon SiC fibers a secondary or a toughening phase for ultra-high temperature ceramics?," *Mater. Des.*, vol. 55, pp. 821–829, 2014, doi: 10.1016/j.matdes.2013.10.019.

[47] J. K. Sonber, T. S. R. C. Murthy, C. Subramanian, R. C. Hubli, and A. K. Suri, "Processing Methods for Ultra High Temperature Ceramics," pp. 180–202, Jan. 1AD, doi: 10.4018/978-1-4666-4066-5.CH006.

[48] A. Balbo and D. Sciti, "Spark plasma sintering and hot pressing of ZrB2-MoSi2 ultra-high-temperature ceramics," *Mater. Sci. Eng. A*, vol. 475, no. 1–2, pp. 108–112, Feb. 2008, doi: 10.1016/J.MSEA.2007.01.164.

[49] D. Sciti, S. Guicciardi, and M. Nygren, "Spark plasma sintering and mechanical behaviour of ZrC-based composites," *Scr. Mater.*, vol. 6, no. 59, pp. 638–641, Sep. 2008, doi: 10.1016/J.SCRIPTAMAT.2008.05.026.

[50] D. Sciti, L. Silvestroni, and M. Nygren, "Spark plasma sintering of Zr- and Hf-borides with decreasing amounts of MoSi2 as sintering aid," *J. Eur. Ceram. Soc.*, vol. 28, no. 6, pp. 1287–1296, Jan. 2008, doi: 10.1016/J.JEURCERAMSOC.2007.09.043.

[51] D. Sciti, G. Bonnefont, G. Fantozzi, and L. Silvestroni, "Spark plasma sintering of HfB2 with low additions of silicides of molybdenum and tantalum," *J. Eur. Ceram. Soc.*, vol. 15, no. 30, pp. 3253–3258, 2010, doi: 10.1016/J.JEURCERAMSOC.2010.06.006.

[52] D. Sciti, A. Balbo, and A. Bellosi, "Oxidation behaviour of a pressureless sintered HfB2-MoSi2 composite," *J. Eur. Ceram. Soc.*, vol. 29, no. 9, pp. 1809–1815, Jun. 2009, doi: 10.1016/J.JEURCERAMSOC.2008.09.018.

[53] L. B. Pankratz, J. M. Stuve, and N. A. Gokcen, "Thermodynamic Data for Mineral Technology," 1984.

[54] R. G. Munro, "Material Properties of a Sintered α-SiC," *J. Phys. Chem. Ref. Data*, vol. 26, no. 5, pp. 1195–1203, 1997, doi: 10.1063/1.556000.

[55] J. Laszkiewicz-Łukasik, L. Jaworska, P. Putyra, P. Klimczyk, and G. Garzeł, "The influence of SPS heating rates on the synthesis reaction of tantalum diboride," *Boletín la Soc. Española Cerámica y Vidr.*, vol. 55, no. 4, pp. 159–

168, Jul. 2016, doi: 10.1016/J.BSECV.2016.03.001.

[56] J. Watts, G. Hilmas, and W. G. Fahrenholtz, “Mechanical Characterization of ZrB2–SiC Composites with Varying SiC Particle Sizes,” *J. Am. Ceram. Soc.*, vol. 94, no. 12, pp. 4410–4418, Dec. 2011, doi: 10.1111/J.1551-2916.2011.04885.X.

[57] A. L. Chamberlain, W. G. Fahrenholtz, G. E. Hilmas, and D. T. Ellerby, “High-strength zirconium diboride-based ceramics,” *J. Am. Ceram. Soc.*, vol. 87, no. 6, pp. 1170–1172, 2004, doi: 10.1111/j.1551-2916.2004.01170.x.

[58] E. W. Neuman, G. E. Hilmas, and W. G. Fahrenholtz, “Mechanical Behavior of Zirconium Diboride-Silicon Carbide-Boron Carbide Ceramics up to 2200 ^{0}C,” *J. Eur. Ceram. Soc.*, vol. 35, no. 2, p. 463, Feb. 2015, doi: 10.1016/j.jeurceramsoc.2014.09.021.

[59] A. Paul, J. Binner, and B. Vaidhyanathan, “UHTC Composites for Hypersonic Applications,” *Ultra-High Temp. Ceram. Mater. Extrem. Environ. Appl.*, vol. 9781118700785, pp. 144–166, Nov. 2014, doi: 10.1002/9781118700853.CH7.

[60] E. Zapata-Solvas, D. D. Jayaseelan, H. T. Lin, P. Brown, and W. E. Lee, “Mechanical properties of ZrB2- and HfB2-based ultra-high temperature ceramics fabricated by spark plasma sintering,” *J. Eur. Ceram. Soc.*, vol. 33, no. 7, pp. 1373–1386, Jul. 2013, doi: 10.1016/J.JEURCERAMSOC.2012.12.009.

[61] R. Zhang, X. Cheng, D. Fang, L. Ke, and Y. Wang, “Ultra-high-temperature tensile properties and fracture behavior of ZrB2-based ceramics in air above 1500 °C,” *Mater. Des.*, vol. 52, pp. 17–22, Dec. 2013, doi: 10.1016/J.MATDES.2013.05.045.

[62] E. W. Neuman, G. E. Hilmas, and W. G. Fahrenholtz, “Mechanical behavior of zirconium diboride–silicon carbide ceramics at elevated temperature in air,” *J. Eur. Ceram. Soc.*, vol. 15–16, no. 33, pp. 2889–2899, Dec. 2013, doi: 10.1016/J.JEURCERAMSOC.2013.05.003.

[63] H. E. Exner, “Physical and chemical nature of cemented carbides,” *http://dx.doi.org/10.1179/imtr.1979.24.1.149*, vol. 24, no. 1, pp. 149–170, Jan. 2013, doi: 10.1179/IMTR.1979.24.1.149.

[64] W. Lengauer, “Transition Metal Carbides, Nitrides, and Carbonitrides,” *Handb. Ceram. Hard Mater.*, pp. 202–252, Mar. 2008, doi: 10.1002/9783527618217.CH7.

[65] P. Sarin *et al.*, “In situ studies of oxidation of ZrB2 and ZrB2–SiC composites at high temperatures,” *J. Eur. Ceram. Soc.*, vol. 30, no. 11, pp. 2375–2386, Aug. 2010, doi: 10.1016/J.JEURCERAMSOC.2010.03.009.

[66] L. Silvestroni, G. Meriggi, and D. Sciti, “Oxidation behavior of ZrB2 composites doped with various transition metal silicides,” *Corros. Sci.*, vol. 83, pp. 281–291, 2014, doi: 10.1016/j.corsci.2014.02.026.

[67] P. Hu, X. H. Zhang, J. C. Han, X. G. Luo, and S. Y. Du, “Effect of Various Additives on the Oxidation Behavior of ZrB2-Based Ultra-High-Temperature Ceramics at 1800°C,” *J. Am. Ceram. Soc.*, vol. 93, no. 2, pp. 345–349, Feb. 2010, doi: 10.1111/J.1551-2916.2009.03420.X.

[68] K. S. Cissel and E. Opila, “Oxygen diffusion mechanisms during high-temperature oxidation of ZrB2-SiC,” *J. Am. Ceram. Soc.*, vol. 101, no. 4, pp. 1765–1779, Apr. 2018, doi: 10.1111/JACE.15298.

[69] D. Sciti, M. Brach, and A. Bellosi, “Oxidation behavior of a pressureless sintered ZrB2–MoSi2 ceramic composite,” *J. Mater. Res.*, vol. 20, no. 4, pp. 922–930, Apr. 2005, doi: 10.1557/JMR.2005.0111.

[70] L. Silvestroni, D. Sciti, and A. Bellosi, “Microstructure and Properties of Pressureless Sintered HfB2-Based Composites with Additions of ZrB2 or HfC,” *Adv. Eng. Mater.*, vol. 9, no. 10, pp. 915–920, Oct. 2007, doi: 10.1002/ADEM.200700170.

[71] L. Zhao, D. Jia, X. Duan, Z. Yang, and Y. Zhou, “Oxidation of ZrC–30 vol% SiC composite in air from low to ultrahigh temperature,” *J. Eur. Ceram. Soc.*, vol. 32, no. 4, pp. 947–954, Apr. 2012, doi: 10.1016/J.JEURCERAMSOC.2011.10.024.

[72] L. Silvestroni, A. Bellosi, D. Sciti, and S. Guicciardi, “Processing, mechanical properties and oxidation behavior of TaC and HfC composites containing 15 vol% TaSi 2 or MoSi 2,” *J. Mater. Res.*, Jan. 2009.

[73] A. L. Chamberlain, W. G. Fahrenholtz, G. E. Hilmas, and D. T. Ellerby, “Characterization of zirconium diboride for thermal protection systems,” in *Key Engineering Materials*, 2004, vol. 264–268, no. I, pp. 493–496, doi: 10.4028/www.scientific.net/kem.264-268.493.

[74] S. R. Levine, E. J. Opila, M. C. Halbig, J. D. Kiser, M. Singh, and J. A. Salem, “Evaluation of ultra-high temperature ceramics for aeropropulsion use,” *J. Eur. Ceram. Soc.*, vol. 22, no. 14–15, pp. 2757–2767, 2002, doi: 10.1016/S0955-2219(02)00140-1.

[75] X. Zhang, P. Hu, J. Han, and S. Meng, “Ablation behavior of ZrB2-SiC ultra high temperature ceramics under simulated atmospheric re-entry conditions,” *Compos. Sci. Technol.*, vol. 68, no. 7–8, pp. 1718–1726, Jun. 2008, doi: 10.1016/J.COMPSCITECH.2008.02.009.

[76] R. Savino, M. De Stefano Fumo, L. Silvestroni, and D. Sciti, “Arc-jet testing on HfB2 and HfC-based ultra-high temperature ceramic materials,” *J. Eur. Ceram. Soc.*, vol. 28, no. 9, pp. 1899–1907, Jan. 2008, doi: 10.1016/J.JEURCERAMSOC.2007.11.021.

[77] L. Pienti, D. Sciti, L. Silvestroni, A. Cecere, and R. Savino, “Ablation tests on HfC- and TaC-based ceramics for aeropropulsive applications,” *J. Eur. Ceram. Soc.*, vol. 35, no. 5, pp. 1401–1411, May 2015, doi: 10.1016/j.jeurceramsoc.2014.11.018.

[78] E. Ionescu *et al.*, “Phase separation of a hafnium alkoxide-modified polysilazane upon polymer-to-ceramic transformation—A case study,” *J. Eur. Ceram. Soc.*, vol. 32, no. 9, pp. 1873–1881, Jul. 2012, doi: 10.1016/J.JEURCERAMSOC.2011.09.003.

[79] I. Chant and K. L. Murty, “Structural materials issues for the next generation fission reactors,” *JOM*, vol. 62, no. 9, pp. 67–74, Sep. 2010, doi:

10.1007/S11837-010-0142-3/METRICS.

[80] B. Basu, G. B. Raju, and A. K. Suri, “Processing and properties of monolithic TiB2 based materials,” *http://dx.doi.org/10.1179/174328006X102529*, vol. 51, no. 6, pp. 352–374, Dec. 2013, doi: 10.1179/174328006X102529.

[81] Y. T. Hou *et al.*, “High performance tantalum carbide metal gate stacks for nMOSFET application,” *Tech. Dig. - Int. Electron Devices Meet. IEDM*, vol. 2005, pp. 31–34, 2005, doi: 10.1109/IEDM.2005.1609258.

[82] E. Wuchina *et al.*, “Designing for ultrahigh-temperature applications: The mechanical and thermal properties of HfB2, HfCx, HfNx and αHf(N),” *J. Mater. Sci.*, vol. 39, no. 19, pp. 5939–5949, Oct. 2004, doi: 10.1023/B:JMSC.0000041690.06117.34.

[83] W. Krenkel, *Ceramic Matrix Composites: Fiber Reinforced Ceramics and their Applications*. John Wiley and Sons, 2008.

[84] D. B. Marshall and B. N. Cox, “Integral Textile Ceramic Structures,” *https://doi.org/10.1146/annurev.matsci.38.060407.130214*, vol. 38, pp. 425–443, Jul. 2008, doi: 10.1146/ANNUREV.MATSCI.38.060407.130214.

[85] J. A. Dever, M. V. Nathal, and J. A. DiCarlo, “Research on High-Temperature Aerospace Materials at NASA Glenn Research Center,” *J. Aerosp. Eng.*, vol. 26, no. 2, pp. 500–514, Apr. 2013, doi: 10.1061/(ASCE)AS.1943-5525.0000321.

[86] R. R. Naslain, Naslain, and R. R., “Ceramic Matrix Composites: Matrices and Processing,” *emst*, pp. 1060–1066, 2001, doi: 10.1016/B0-08-043152-6/00196-0.

[87] H. Hald, “Operational limits for reusable space transportation systems due to physical boundaries of C/SiC materials,” *Aerosp. Sci. Technol.*, vol. 7, no. 7, pp. 551–559, Oct. 2003, doi: 10.1016/S1270-9638(03)00054-3.

[88] D. D. Jayaseelan, Y. Xin, L. Vandeperre, P. Brown, and W. E. Lee, “Development of multi-layered thermal protection system (TPS) for aerospace applications,” *Compos. Part B Eng.*, vol. 79, pp. 392–405, Sep. 2015, doi: 10.1016/J.COMPOSITESB.2015.04.017.

[89] S. Tang, J. Deng, S. Wang, and W. Liu, “Fabrication and characterization of an ultra-high-temperature carbon fiber-reinforced ZrB2-SiC matrix composite,” *J. Am. Ceram. Soc.*, vol. 90, no. 10, pp. 3320–3322, Oct. 2007, doi: 10.1111/J.1551-2916.2007.01876.X.

[90] H. J. Yu, X. G. Zhou, W. Zhang, H. X. Peng, C. R. Zhang, and Z. L. Huang, “Mechanical properties of 3D KD-I SiCf/SiC composites with engineered fibre-matrix interfaces,” *Compos. Sci. Technol.*, vol. 71, no. 5, pp. 699–704, Mar. 2011, doi: 10.1016/J.COMPSCITECH.2011.01.014.

[91] N. Padmavathi, P. Ghosal, N. Eswara Prasad, J. Subramanyam, and K. K. Ray, “Synthesis of carbon fibre-reinforced, silicon carbide composites by soft-solution approach,” *Sadhana - Acad. Proc. Eng. Sci.*, vol. 37, no. 4, pp. 493–502, Aug. 2012, doi: 10.1007/S12046-012-0093-1/FIGURES/7.

[92] B. Heidenreich, “C/SiC and C/C-SiC Composites,” *Ceram. Matrix Compos.*

Mater. Model. Technol., vol. 9781118231166, pp. 147–216, Nov. 2014, doi: 10.1002/9781118832998.CH6.

[93] K. H. Bang, G. Y. Chung, and H. H. Koo, "Preparation of C/C composites by the chemical vapor infiltration (CVI) of propane pyrolysis," *Korean J. Chem. Eng.*, vol. 28, no. 1, pp. 272–278, Jan. 2011, doi: 10.1007/S11814-010-0352-Y/METRICS.

[94] P. Delhaès, M. Trinquecoste, J.-F. Lines, A. Cosculluela, J.-M. Goyhénèche, and M. Couzi, "Chemical vapor infiltration of C/C composites: Fast densification processes and matrix characterizations," *Carbon N. Y.*, vol. 43, no. 4, pp. 681–691, 2005.

[95] G. L. Vignoles, "Chemical vapor deposition/ infiltration processes for ceramic composites," *Adv. Compos. Manuf. Process Des.*, pp. 147–176, Jul. 2015, doi: 10.1016/B978-1-78242-307-2.00008-7.

[96] C. A. Nannetti, A. Ortona, D. A. de Pinto, and B. Riccardi, "Manufacturing SiC-Fiber-Reinforced SiC Matrix Composites by Improved CVI/Slurry Infiltration/Polymer Impregnation and Pyrolysis," *J. Am. Ceram. Soc.*, vol. 87, no. 7, pp. 1205–1209, Jul. 2004, doi: 10.1111/J.1551-2916.2004.TB20093.X.

[97] Y. Tong, S. Bai, X. Liang, Q. H. Qin, and J. Zhai, "Reactive melt infiltration fabrication of C/C-SiC composite: Wetting and infiltration," *Ceram. Int.*, vol. 15, no. 42, pp. 17174–17178, Nov. 2016, doi: 10.1016/J.CERAMINT.2016.08.007.

[98] S. Chen, C. Zhang, Y. Zhang, and H. Hu, "Influence of pyrocarbon amount in C/C preform on the microstructure and properties of C/ZrC composites prepared via reactive melt infiltration," *Mater. Des.*, vol. 58, pp. 570–576, Jun. 2014, doi: 10.1016/J.MATDES.2013.12.071.

[99] S. Chen, C. Zhang, Y. Zhang, and H. Hu, "Preparation and properties of carbon fiber reinforced ZrC–ZrB2 based composites via reactive melt infiltration," *Compos. Part B Eng.*, vol. 60, pp. 222–226, Apr. 2014, doi: 10.1016/J.COMPOSITESB.2013.12.067.

[100] M. Kütemeyer, L. Schomer, T. Helmreich, S. Rosiwal, and D. Koch, "Fabrication of ultra high temperature ceramic matrix composites using a reactive melt infiltration process," *J. Eur. Ceram. Soc.*, vol. 36, no. 15, pp. 3647–3655, Nov. 2016, doi: 10.1016/j.jeurceramsoc.2016.04.039.

[101] C. Tian, D. Gao, Y. Zhang, C. Xu, Y. Song, and X. Shi, "Oxidation behaviour of zirconium diboride–silicon carbide ceramic composites under low oxygen partial pressure," *Corros. Sci.*, vol. 53, no. 11, pp. 3742–3746, Nov. 2011, doi: 10.1016/J.CORSCI.2011.07.020.

[102] H. Zhou, L. Gao, Z. Wang, and S. Dong, "ZrB2–SiC Oxidation Protective Coating on C/C Composites Prepared by Vapor Silicon Infiltration Process," *J. Am. Ceram. Soc.*, vol. 93, no. 4, pp. 915–919, Apr. 2010, doi: 10.1111/J.1551-2916.2009.03481.X.

[103] O. Haibo *et al.*, "Self-healing ZrB2–SiO2 oxidation resistance coating for SiC coated carbon/carbon composites," *Corros Sci*, vol. 110, pp. 265–272, Sep. 2016,

doi: 10.1016/j.corsci.2016.04.040.

[104] L. Liu, H. Li, W. Feng, X. Shi, K. Li, and L. Guo, “Ablation in different heat fluxes of C/C composites modified by ZrB2–ZrC and ZrB2–ZrC–SiC particles,” *Corros. Sci.*, vol. Complete, no. 74, pp. 159–167, Sep. 2013, doi: 10.1016/J.CORSCI.2013.04.038.

[105] Z. Hao *et al.*, “Microstructure and ablation properties of a gradient Cf/C-XSi2-SiC (X = Mo,Ti) composite fabricated by reactive melt infiltration,” *J. Eur. Ceram. Soc.*, vol. 36, no. 15, pp. 3775–3782, Nov. 2016, doi: 10.1016/J.JEURCERAMSOC.2016.04.006.

[106] L. S. Walker and E. L. Corral, “Self-Generating High-Temperature Oxidation-Resistant Glass-Ceramic Coatings for C-C Composites Using UHTCs,” *J. Am. Ceram. Soc.*, vol. 97, no. 9, pp. 3004–3011, Sep. 2014, doi: 10.1111/jace.13017.

[107] L. Zoli, V. Medri, C. Melandri, and D. Sciti, “Continuous SiC fibers-ZrB2 composites,” *J. Eur. Ceram. Soc.*, vol. 35, no. 16, pp. 4371–4376, Dec. 2015, doi: 10.1016/J.JEURCERAMSOC.2015.08.008.

[108] D. Sciti, L. Pienti, A. Natali Murri, E. Landi, V. Medri, and L. Zoli, “From random chopped to oriented continuous SiC fibers-ZrB2 composites,” *Mater. Des.*, vol. 63, pp. 464–470, Nov. 2014, doi: 10.1016/j.matdes.2014.06.037.

[109] D. Sciti, A. Natali Murri, V. Medri, and L. Zoli, “Continuous C fibre composites with a porous ZrB2 Matrix,” *Mater. Des.*, vol. 85, pp. 127–134, Nov. 2015, doi: 10.1016/j.matdes.2015.06.136.

[110] S. Guo, “Thermal and electrical properties of hot-pressed short pitch-based carbon fiber-reinforced ZrB2-SiC matrix composites,” *Ceram. Int.*, vol. 39, no. 5, pp. 5733–5740, Jul. 2013, doi: 10.1016/J.CERAMINT.2012.12.091.

[111] F. Yang, X. Zhang, J. Han, and S. Du, “Processing and mechanical properties of short carbon fibers toughened zirconium diboride-based ceramics,” 2008, doi: 10.1016/j.matdes.2008.03.011.

[112] S. Guo, K. Naito, and Y. Kagawa, “Mechanical and physical behaviors of short pitch-based carbon fiber-reinforced HfB2-SiC matrix composites,” *Ceram. Int.*, vol. 39, no. 2, pp. 1567–1574, Mar. 2013, doi: 10.1016/j.ceramint.2012.07.108.

[113] L. Silvestroni, D. Sciti, C. Melandri, and S. Guicciardi, “Tyranno SA3 fiber-ZrB2 composites. Part II: Mechanical properties,” *Mater. Des.*, vol. 65, pp. 1264–1273, Jan. 2015, doi: 10.1016/j.matdes.2014.08.075.

[114] L. Zoli, A. Vinci, L. Silvestroni, D. Sciti, M. Reece, and S. Grasso, “Rapid spark plasma sintering to produce dense UHTCs reinforced with undamaged carbon fibres,” *Mater. Des.*, vol. 130, pp. 1–7, Sep. 2017, doi: 10.1016/j.matdes.2017.05.029.

[115] W. Hong, K. Gui, P. Hu, X. Zhang, and S. Dong, “Preparation and characterization of high-performance ZrB2–SiC–Cf composites sintered at 1450 °C,” *J. Adv. Ceram.*, vol. 6, no. 2, pp. 110–119, Jun. 2017, doi: 10.1007/S40145-017-0223-7.

[116] L. Pienti, D. Sciti, L. Silvestroni, and S. Guicciardi, “Effect of milling on the mechanical properties of chopped SiC fiber-reinforced ZrB2,” *Materials (Basel).*, vol. 6, no. 5, pp. 1980–1993, 2013, doi: 10.3390/ma6051980.

[117] Z. Nasiri, M. Mashhadi, and A. Abdollahi, “Effect of short carbon fiber addition on pressureless densification and mechanical properties of ZrB2-SiC-Csf nanocomposite,” *Int. J. Refract. Met. Hard Mater.*, vol. 51, pp. 216–223, Jul. 2015, doi: 10.1016/j.ijrmhm.2015.04.005.

[118] J. Lin, X. Zhang, W. Han, and D. Sun, “Influence of milling time on the synthesis, microstructure and mechanical properties of ZrB2SiCZrO2f ceramic composites,” *Ceram. Int.*, vol. 39, no. 4, pp. 4213–4219, May 2013, doi: 10.1016/j.ceramint.2012.11.003.

[119] J. J. Sha *et al.*, “Improved microstructure and fracture properties of short carbon fiber-toughened ZrB2-based UHTC composites via colloidal process,” *Int. J. Refract. Met. Hard Mater.*, vol. 60, pp. 68–74, Nov. 2016, doi: 10.1016/j.ijrmhm.2016.07.010.

[120] W. S. Yang *et al.*, “Microstructure and mechanical properties of short carbon fibre/SiC multilayer composites prepared by tape casting,” *Compos. Sci. Technol.*, vol. 72, no. 6, pp. 675–680, Mar. 2012, doi: 10.1016/j.compscitech.2012.01.014.

[121] J. Lu *et al.*, “Fabrication and microstructure evolution of Csf/ZrB2-SiC composites via direct ink writing and reactive melt infiltration,” *J. Adv. Ceram.*, vol. 10, no. 6, pp. 1371–1380, 2021, doi: 10.1007/s40145-021-0512-z.

[122] J. W. Kemp *et al.*, “Direct ink writing of ZrB2-SiC chopped fiber ceramic composites,” *Addit. Manuf.*, vol. 44, Aug. 2021, doi: 10.1016/j.addma.2021.102049.

[123] Z. Zhang *et al.*, “Direct writing of continuous carbon fibers/epoxy thermoset composites with high-strength and low energy-consumption,” *Addit. Manuf.*, vol. 47, p. 102348, Nov. 2021, doi: 10.1016/J.ADDMA.2021.102348.

[124] J. Binner *et al.*, “Selection, processing, properties and applications of ultra-high temperature ceramic matrix composites, UHTCMCs – a review,” *IMRv*, vol. 65, no. 7, pp. 389–444, Oct. 2020, doi: 10.1080/09506608.2019.1652006.

[125] V. Rubio *et al.*, “Materials Characterisation and Mechanical Properties of Cf-UHTC Powder Composites.”

[126] A. Paul, S. Venugopal, J. G. P. Binner, B. Vaidhyanathan, A. C. J. Heaton, and P. M. Brown, “UHTC-carbon fibre composites: Preparation, oxyacetylene torch testing and characterisation,” *J. Eur. Ceram. Soc.*, vol. 33, no. 2, pp. 423–432, Feb. 2013, doi: 10.1016/j.jeurceramsoc.2012.08.018.

[127] F. Uhlmann, C. Wilhelmi, S. Schmidt-Wimmer, S. Beyer, C. Badini, and E. Padovano, “Preparation and characterization of ZrB2 and TaC containing Cf/SiC composites via Polymer-Infiltration-Pyrolysis process,” *J. Eur. Ceram. Soc.*, vol. 37, no. 5, pp. 1955–1960, May 2017, doi: 10.1016/j.jeurceramsoc.2016.12.048.

[128] P. Galizia, D. Sciti, and N. Jain, “Insight into microstructure and flexural strength

of ultra-high temperature ceramics enriched SICARBON^{TM} composite," *Mater. Des.*, vol. 208, Oct. 2021, doi: 10.1016/J.MATDES.2021.109888.

[129] B. W. Chen *et al.*, "Ablation behavior of Cf/ZrC-SiC-based composites fabricated by an improved reactive melt infiltration," *J. Eur. Ceram. Soc.*, vol. 39, no. 15, pp. 4617–4624, Dec. 2019, doi: 10.1016/J.JEURCERAMSOC.2019.07.007.

[130] A. Vinci, L. Zoli, P. Galizia, M. Kütemeyer, D. Koch, and D. Sciti, "Reactive melt infiltration of carbon fibre reinforced ZrB2/B composites with Zr2Cu," *Compos. Part A Appl. Sci. Manuf.*, vol. 137, p. 105973, Oct. 2020, doi: 10.1016/J.COMPOSITESA.2020.105973.

[131] L. Zoli *et al.*, "Ultra-high temperature ceramic matrix composites," *Encycl. Mater. Tech. Ceram. Glas.*, vol. 2–3, pp. 340–352, May 2021, doi: 10.1016/B978-0-12-818542-1.00023-0.

[132] D. Zhao, C. Zhang, H. Hu, and Y. Zhang, "Preparation and characterization of three-dimensional carbon fiber reinforced zirconium carbide composite by precursor infiltration and pyrolysis process," *Ceram. Int.*, vol. 37, no. 7, pp. 2089–2093, Sep. 2011, doi: 10.1016/J.CERAMINT.2011.02.024.

[133] J. Jiang, S. Wang, W. Li, Z. Chen, and Y. Zhu, "Preparation of 3D Cf/ZrC-SiC composites by joint processes of PIP and RMI," *Mater. Sci. Eng. A*, vol. 607, pp. 334–340, Jun. 2014, doi: 10.1016/J.MSEA.2014.03.071.

[134] Z. Wang *et al.*, "Fabrication and Properties of Cf/SiC–ZrC Composites," *J. Am. Ceram. Soc.*, vol. 91, no. 10, pp. 3434–3436, Oct. 2008, doi: 10.1111/J.1551-2916.2008.02632.X.

[135] D. W. Ni *et al.*, "Fabrication and properties of Cf/ZrC-SiC-based composites by an improved reactive melt infiltration," *J. Am. Ceram. Soc.*, vol. 101, no. 8, pp. 3253–3258, Aug. 2018, doi: 10.1111/JACE.15534.

[136] X. Chen *et al.*, "Microstructure and mechanical properties of three dimensional Cf/SiC-ZrC-ZrB2 composites prepared by reactive melt infiltration method," *J. Eur. Ceram. Soc.*, vol. 36, no. 16, pp. 3969–3976, Dec. 2016, doi: 10.1016/j.jeurceramsoc.2016.07.002.

[137] L. Zoli, A. Vinci, P. Galizia, C. Melandri, and Di. Sciti, "On the thermal shock resistance and mechanical properties of novel unidirectional UHTCMCs for extreme environments," *Sci. Rep.*, vol. 8, no. 1, Dec. 2018, doi: 10.1038/s41598-018-27328-x.

[138] D. Sciti, L. Zoli, L. Silvestroni, A. Cecere, G. D. Di Martino, and R. Savino, "Design, fabrication and high velocity oxy-fuel torch tests of a Cf-ZrB2- fiber nozzle to evaluate its potential in rocket motors," *Mater. Des.*, vol. 109, pp. 709–717, Nov. 2016, doi: 10.1016/J.MATDES.2016.07.090.

[139] L. Zoli and D. Sciti, "Efficacy of a ZrB2–SiC matrix in protecting C fibres from oxidation in novel UHTCMC materials," *Mater. Des.*, vol. 113, pp. 207–213, Jan. 2017, doi: 10.1016/j.matdes.2016.09.104.

[140] Q. Li, S. Dong, Z. Wang, and G. Shi, "Fabrication and properties of 3-D

Cf/ZrB2-ZrC-SiC composites via polymer infiltration and pyrolysis," *Ceram. Int.*, vol. 39, no. 5, pp. 5937–5941, Jul. 2013, doi: 10.1016/j.ceramint.2012.11.074.

[141] A. Vinci, L. Zoli, and D. Sciti, "Influence of SiC content on the oxidation of carbon fibre reinforced ZrB2/SiC composites at 1500 and 1650 °C in air," *J. Eur. Ceram. Soc.*, vol. 38, no. 11, pp. 3767–3776, Sep. 2018, doi: 10.1016/j.jeurceramsoc.2018.04.064.

[142] A. Vinci, L. Zoli, E. Landi, and D. Sciti, "Oxidation behaviour of a continuous carbon fibre reinforced ZrB2–SiC composite," *Corros. Sci.*, vol. 123, pp. 129–138, Jul. 2017, doi: 10.1016/j.corsci.2017.04.012.

[143] S. Mungiguerra *et al.*, "Ultra-high-temperature testing of sintered ZrB2-based ceramic composites in atmospheric re-entry environment," *Int. J. Heat Mass Transf.*, vol. 156, Aug. 2020, doi: 10.1016/j.ijheatmasstransfer.2020.119910.

[144] B. Baker *et al.*, "Ablation behaviour of carbon fibre ultra-high temperature composites at oblique angles of attack," *Mater. Des.*, vol. 212, p. 110199, Dec. 2021, doi: 10.1016/J.MATDES.2021.110199.

[145] P. Galizia *et al.*, "Retained strength of UHTCMCs after oxidation at 2278 K," *Compos. Part A Appl. Sci. Manuf.*, vol. 149, p. 106523, Oct. 2021, doi: 10.1016/J.COMPOSITESA.2021.106523.

[146] A. Vinci, L. Zoli, P. Galizia, and D. Sciti, "Influence of Y2O3 addition on the mechanical and oxidation behaviour of carbon fibre reinforced ZrB2/SiC composites," *J. Eur. Ceram. Soc.*, vol. 40, no. 15, pp. 5067–5075, Dec. 2020, doi: 10.1016/j.jeurceramsoc.2020.06.043.

[147] A. Vinci, T. Reimer, L. Zoli, and D. Sciti, "Influence of pressure on the oxidation resistance of carbon fiber reinforced ZrB2/SiC composites at 2000 and 2200 °C," *Corros. Sci.*, vol. 184, May 2021, doi: 10.1016/j.corsci.2021.109377.

[148] S. Mungiguerra, G. D. Di Martino, R. Savino, L. Zoli, L. Silvestroni, and D. Sciti, "Characterization of novel ceramic composites for rocket nozzles in high-temperature harsh environments," *Int. J. Heat Mass Transf.*, vol. 163, p. 120492, Dec. 2020, doi: 10.1016/J.IJHEATMASSTRANSFER.2020.120492.

[149] P. Kumar and V. K. Srivastava, "Tribological behaviour of C/C–SiC composites—A review," *J. Adv. Ceram.*, vol. 5, no. 1, pp. 1–12, 2016, doi: 10.1007/s40145-015-0171-z.

[150] S. K. Rhee, M. G. Jacko, and P. H. S. Tsang, "The role of friction film in friction wear and noise of automotive brakes," *Wear*, vol. 146, no. 1, pp. 89–97, May 1991, doi: 10.1016/0043-1648(91)90226-k.

[151] Ralph Renz, *Entwicklung eines Werkstoff- und Bauweisenkonzepts für keramische Verbundbremsscheiben (Band 14)*. 2018.

[152] G. (Gary) Savage, "Carbon-carbon composites," p. 389, 1993.

[153] G.Savage, *Savage 1993 - Carbon-carbon composites.pdf*. Chapman & Hall, 1993.

[154] P. Kumar and V. K. Srivastava, “A Review on Wear and Friction Performance of Carbon–Carbon Composites at High Temperature,” *Int. J. Appl. Ceram. Technol.*, vol. 13, no. 4, pp. 702–710, 2016, doi: 10.1111/ijac.12538.

[155] B. H. R. R. W Krenkel, “C/C–SiC composites for advanced friction systems,” *Adv Eng Mater*, vol. 4, pp. 427–436, 2002, doi: 10.1002/1527-2648(20020717)4:7<427::aid-adem427>3.0.co.

[156] H. A. El-Hija, W. Krenkel, and S. Hugel, “Development of C/C-SiC brake pads for high-performance elevators,” *Int. J. Appl. Ceram. Technol.*, vol. 2, no. 2, pp. 105–113, 2005, doi: 10.1111/J.1744-7402.2005.02012.X.

[157] W. Krenkel, B. Heidenreich, and R. Renz, “C/C-SiC composites for advanced friction systems,” *Adv. Eng. Mater.*, vol. 4, no. 7, pp. 427–436, 2002, doi: 10.1002/1527-2648(20020717)4:7<427::AID-ADEM427>3.0.CO;2-C.

[158] R. Renz and W. Krenkel, “C/C-SiC Composites For High Performance Emergency Brake Systems,” 2000.

[159] W. Krenkel and F. Berndt, “C/C–SiC composites for space applications and advanced friction systems,” *Mat Sci Eng A*, vol. 412, no. 1–2, pp. 177–181, Dec. 2005, doi: 10.1016/j.msea.2005.08.204.

[160] S. Fouquet, M. Rollin, R. Pailler, and X. Bourrat, “Tribological behaviour of composites made of carbon fibres and ceramic matrix in the Si–C system,” *Wear*, vol. 264, no. 9–10, pp. 850–856, Apr. 2008, doi: 10.1016/j.wear.2006.12.081.

[161] P. Fournier, P. Reynaud, F. Platon, and J. Absi, “Tribological behaviour of carbon-fibre-reinforced SiC matrix composites,” *Proc. IMechE Part J J Eng. Tribol.*, vol. 214, no. 3, pp. 291–306, 2000, doi: 10.1243/1350650001543188.

[162] Y. Qian, W. Zhang, M. Ge, and X. Wei, “Frictional response of a novel C/C-ZrB2-ZrC-SiC composite under simulated braking,” *J. Adv. Ceram.*, vol. 2, no. 2, pp. 157–161, 2013, doi: 10.1007/s40145-013-0055-z.

[163] A. L. Chamberlain, W. G. Fahrenholtz, and G. E. Hilmas, “High-Strength Zirconium Diboride-Based Ceramics,” vol. 1172, pp. 1170–1172, 2004.

[164] M. Mallik, K. K. Ray, and R. Mitra, “Effect of Si3N4 Addition on Compressive Creep Behavior of Hot-Pressed ZrB2–SiC Composites,” *J. Am. Ceram. Soc.*, vol. 97, no. 9, pp. 2957–2964, Sep. 2014, doi: 10.1111/JACE.13022.

[165] C. Huang, B. Zhang, H. Lan, L. Du, and W. Zhang, “Friction properties of high temperature boride coating under dry air and water vapor ambiences,” *Ceram. Int.*, vol. 40, no. 8 PART A, pp. 12403–12411, 2014, doi: 10.1016/J.CERAMINT.2014.04.091.

[166] S. Chakraborty, A. R. Mallick, D. Debnath, and P. K. Das, “Densification, mechanical and tribological properties of ZrB2 by SPS: Effect of pulsed current,” *Int. J. Refract. Met. Hard Mater.*, vol. 48, pp. 150–156, 2015, doi: 10.1016/J.IJRMHM.2014.09.004.

[167] I. A. Podchernyaeva, O. N. Grigor’ev, V. I. Subbotin, A. D. Kostenko, L. P. Isaeva, and E. A. Artemenko, “Wear-resistant layered electrospark coatings

based on ZrB 2," *Powder Metall. Met. Ceram.*, vol. 43, no. 7–8, pp. 391–395, 2004, doi: 10.1023/B:PMMC.0000048133.84178.97/METRICS.

[168] J. Zou, G. J. Zhang, H. Zhang, Z. R. Huang, J. Vleugels, and O. Van Der Biest, "Improving high temperature properties of hot pressed ZrB2–20 vol% SiC ceramic using high purity powders," *Ceram. Int.*, vol. 39, no. 1, pp. 871–876, Jan. 2013, doi: 10.1016/J.CERAMINT.2012.06.018.

[169] A. Rezaie, W. G. Fahrenholtz, and G. E. Hilmas, "Effect of hot pressing time and temperature on the microstructure and mechanical properties of ZrB2–SiC," *J. Mater. Sci.*, vol. 42, no. 8, pp. 2735–2744, Apr. 2007, doi: 10.1007/S10853-006-1274-2.

[170] F. Monteverde, R. Savino, and M. De Stefano Fumo, "Dynamic oxidation of ultra-high temperature ZrB2-SiC under high enthalpy supersonic flows," *Corros. Sci.*, vol. 53, no. 3, pp. 922–929, Mar. 2011, doi: 10.1016/J.CORSCI.2010.11.018.

[171] S. Kumar Sharma, Yashpal, A. W. Selokar, B. V. M. Kumar, and T. Venkateswaran, "High temperature erosion behavior of spark plasma sintered ZrB2-SiC composites," *Ceram. Int.*, vol. 12, no. 43, pp. 8982–8988, Aug. 2017, doi: 10.1016/J.CERAMINT.2017.04.039.

[172] M. Mallik *et al.*, "Abrasive wear performance of zirconium diboride based ceramic composite," *Int. J. Refract. Met. Hard Mater.*, vol. 79, no. December 2018, pp. 224–232, 2019, doi: 10.1016/j.ijrmhm.2018.12.008.

[173] Z. Wu, Z. Wang, G. Shi, and J. Sheng, "Effect of surface oxidation on thermal shock resistance of the ZrB2-SiC-ZrC ceramic," *Compos. Sci. Technol.*, vol. 71, no. 12, pp. 1501–1506, Aug. 2011, doi: 10.1016/J.COMPSCITECH.2011.06.008.

[174] J. He, Y. Cao, Z. Li, and Y. Wang, "Study of tribological properties of polymer derived ZrB2-SiC ceramics," *Ceram. Int.*, vol. 44, no. 13, pp. 15627–15630, 2018, doi: 10.1016/j.ceramint.2018.05.231.

[175] D. H. Buckley and K. Miyoshi, "Friction and wear of ceramics," *Wear*, vol. 100, no. 1–3, pp. 333–353, 1984, doi: 10.1016/0043-1648(84)90020-6.

[176] Y. Gupta and B. V. Manoj Kumar, "ZrB2–SiC composites for sliding wear contacts: Influence of SiC content and counterbody," *Ceram. Int.*, vol. 48, no. 10, pp. 14560–14567, May 2022, doi: 10.1016/J.CERAMINT.2022.01.349.

3. Experimental

3.1 Experimental techniques employed in this work

Microstructural characterization

The microstructure of a material is the union of the compositional, morphological and crystallographic characteristics of its phases. The characterization of the microstructure is important to understand the chemical, thermal, electrical and mechanical properties of a material. In this work, the main techniques used are X-Ray Diffraction (XRD), Digital Optical Microscopy, Scanning Electron Microscopy (SEM) and Energy Dispersive X-Ray Spectroscopy (EDS).

3.1.1 X-ray diffraction analysis

The X-ray diffraction (XRD) is a non-destructive analytical technique used in material science for characterizing the atomic and molecular structure of a material. It is used especially for the identification of crystalline phases of a material, but it can also provide information on structural parameters such as preferential crystal orientations, crystallite size, crystallinity, lattice defect and strain [1]]. The diffraction of the X-ray is a subset of the general X-ray scattering phenomena. XRD - which is generally used to mean wide-angle X-Ray diffraction (WAXD)- falls under several methods. Other elastic scattering-based X-ray techniques include small angle X-ray scattering (SAXS). SAXS measures structural correlations of the scale of several nanometres or large and X-ray reflectivity that measures the thickness, roughness and density of thin films. X-ray diffraction principle can be applied on a single crystal (Single Crystal X-ray Diffraction, SC-XRD) to obtain information about the internal lattice such as electronic density, bond angles, bond length and unit cell dimensions [2]. However, obtaining a single crystal is usually difficult. For this reason, this technique is less widespread.

The XRD analysis is based on the elastic scattering of X-rays due to structure with a long-range order. X-ray are high-energy electromagnetic radiation with wavelength ranging from 10 nm to 1 pm, Fig. 3.1. Usually, the wavelength choice in an XRD analysis is 1 Å, because it is in the order of lattice structure.

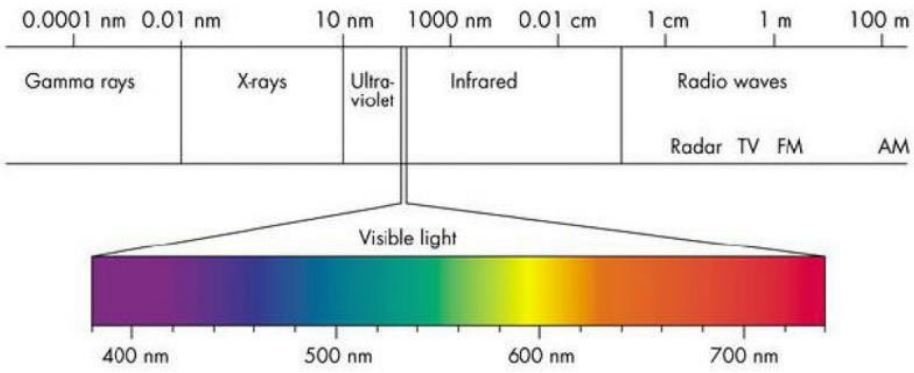

Fig. 3.1: Range of frequencies of electromagnetic radiations. X-ray fall in the range 0.01 – 10 nm.

During an XRD analysis, a sample is irradiated with incident X-rays that hit a crystal lattice and diffract from the lattice points. At certain angles of incidence, the diffracted parallel waves interfere constructively, destructively or giving a partial reinforcement. The constructive interference can create a detectable peak in intensity. This phenomenon (Fig. 3.2) was identified by W.H. Bragg and reported in the following equation [1]:

$$n\lambda = 2dsin\theta$$

Where λ is the wavelength of the X-rays used, *d* is the spacing between a particular set of planes, θ is the angle of incidence at which a diffraction peak is measured and *n* is an integer (1,2,3…*n*) that represents the "harmonic order" of the diffraction. At *n* =1, for example, there is the first harmonic. This means that the path of X-rays diffracted through the crystal is exactly 1 λ. So, during an analysis - as the λ is known and θ are measured- the Bragg's equation allows to obtain the distance between the lattice planes, which are different for each crystalline cell. With the comparison between the obtained results and a known diffractogram (JCPDS standard), it is possible to identify the phases present in the sample [3].

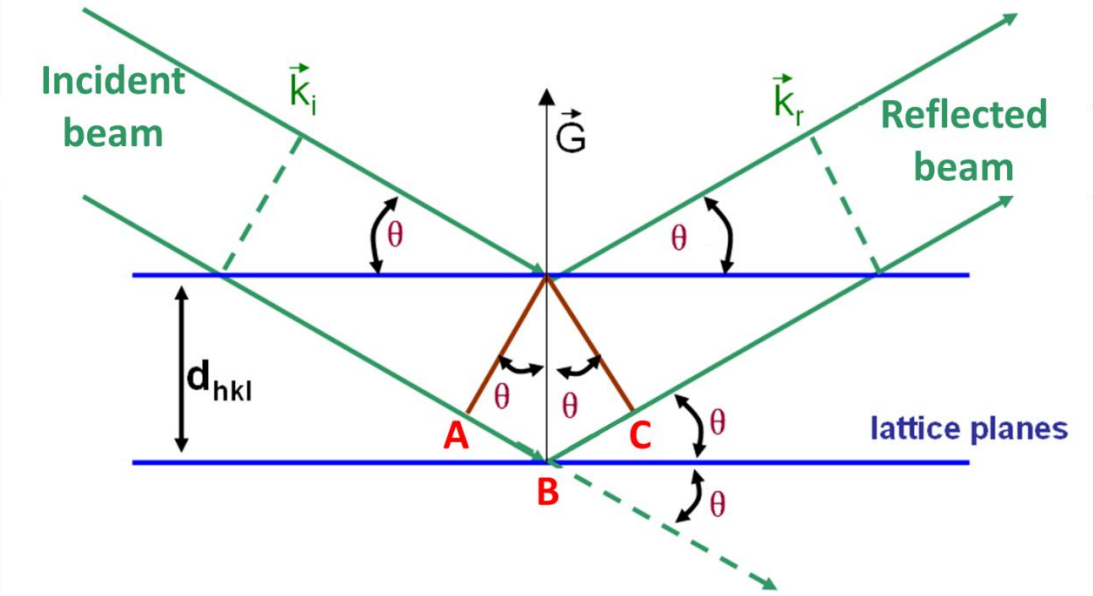

Fig. 3.2: Representation of the Bragg's law: X-ray diffraction in a crystal lattice.

The most used geometry for the XRD diffractometers is the Bragg-Brentano, reported in Fig. 3.3. In this geometry, the incident and diffracted beams move on a circle which is centred on the sample. The main part constituting the instrument are an X-ray tube composed by a cathode of tungsten filament that emit electron when heated, a sample holder, and a detector where the interaction between X-rays and a gas generates ions which are collected as a current. In the XRD instrument, two different goniometer configurations can be used: a θ – θ configuration (where the sample is fixed, and the X-ray tube and detector rotate around it) and a θ – 2θ configuration (where the sample is tilted by a θ angle and the position of X-ray tubes fixed [4].

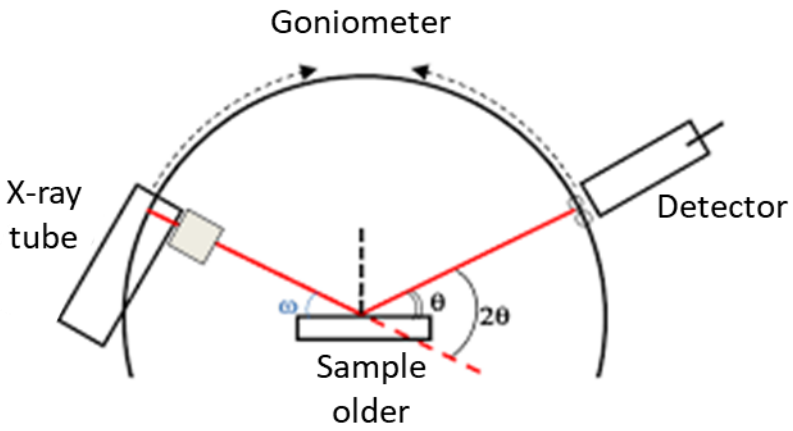

Fig. 3.3: Schematic representation of an X-ray diffractometer with a Bragg-Brentano geometry

In the present work, X-ray diffraction analysis was conducted using an instrument with a Bragg-Brentano θ-θ geometry (D8 Advance, Bruker, Germany) equipped with a LYNXEYE detector and a Cu K_α radiation as X-ray source (λ=1.54178 Å). The spectra were collected from 10° to 80° with a step of 0.02 and a step time of 0.5 s. The analyses were carried out on the solid samples (not powders) before and after oxidation tests in order to observe the presence of different phases.

3.1.2 Digital microscope

A digital microscope is a variation of a traditional optical microscope that uses optics and digital camera to obtain an image that is shown on a computer monitor. One of the main differences between the optical and the digital microscopy is the magnification. In an optical microscopy, the magnification is determined by multiplying the eyepiece magnification times the objective magnification. For the digital microscopes, the magnification is independent of the size of the monitor used. The difference in magnification between the two microscopes is around 40 % positively for the digital microscope. Moreover, the digital microscope provides better quality images thanks to the anti-halation that reduces the glare, HDR that provides better colour and contrast, and lighting regulation that provide more texture. In addition, some digital microscope can measure samples in 2D measuring the distance between the pixel and in some cases 3D

measure is possible using a step motor to take images from the lowest focal plane in the field of view to the highest focal plane [5,6].

In this thesis, a digital microscope, RH-2000, Hirox Europe, France (Fig. 3.4) was used for the fracture surface analysis and for the surface analysis of green samples.

Fig. 3.4: Digital microscope Hirox RH-2000.

3.1.3 Scanning electron microscopy

Scanning electron microscopy (SEM) is an imaging technique that allows to observe samples with a very high magnification (> 100k). For this technique, a scanning electron microscope (SEM) is used. It is a microscope where a focused beam of electrons is used to scan the surface of a sample to obtain images with a high-resolution.

The main parts constituting a typical SEM (Fig. 3.5) are:

- Electron source (gun): is usually constituted by a thermionic emission (TE) gun and its task is to generate the electrons beam. The thermal electrons are emitted from a filament (cathode) made of a thin tungsten wire (around 0.1 mm) by heating the filament at high temperature (near 2800 K). For the cathode tungsten is usually used because it possesses the highest melting point and lowest vapour pressure of all metals. The finest point of the beam is called crossover and regarded as an electron source with a diameter of 15 – 20 μm for the TE gun. The thermionic emission gun is the most used in general, but other

materials (such as LaB_6 or CeB_6 single crystal) can be used even though they require high vacuum due to their high activity. Other electron gun is the field emission electron gun (FE gun) or the Schottky-emission gun (SE gun). In the field-emission electron gun the field emission effect is used. This phenomenon takes place when a high electric field is applied to a metal surface (usually tungsten wire), called emitter. To generate a field emission, the emitter must be very clean, so an ultra-high vacuum is required ($\approx 10^{-8}$ Pa). The electron beam emitted from the emitter possesses a diameter of 5 – 10 nm, so the FE produces a much smaller electron source than the TE gun, resulting in a high-resolution SEM. The Schottky-emission Gun uses the Schottky-emission effect that takes place when a high electric field is applied to a heated metal surface covered by ZrO/ZrO_2. An advantage of the SE gun is the high stability of the electron beam thanks to emitter that avoids the gas absorption. Compared to the FE gun, the energy spread of the electron beam is somewhat large, but the SE gun produces large probe currents. The electrons generated from the gun are gathered as an electron beam by applying a positive voltage to the anode (constituted by a metal plate) that forces the electrons to flow through it. Moreover, when an electrode (Wehnelt electrode) is put between the cathode and anode and a negative voltage is applied on it, it is possible to adjust the current of the electron beam.

-Electromagnetic lenses: the two-stage lens positioned below the electron gun allows to adjust the diameter of the electron beam and obtain a small electron probe. The scanning coils lens deflect the beam in the x and y directions to scan the sample [7,8].

-Analysis chamber: it is under vacuum and it is the location where the interaction between the samples and the electron beam takes place. The sample is put on a specimen stage that allows to have horizontal movement (X, Y axis), vertical movement (Z axis), tilting and rotation. The movement on the X and Y axis are used for the selection of a field view, the movement on the Z axis allows to change the image resolution.

-Detectors: are used to collect the several signals resulting from the interaction between the sample and the electron.

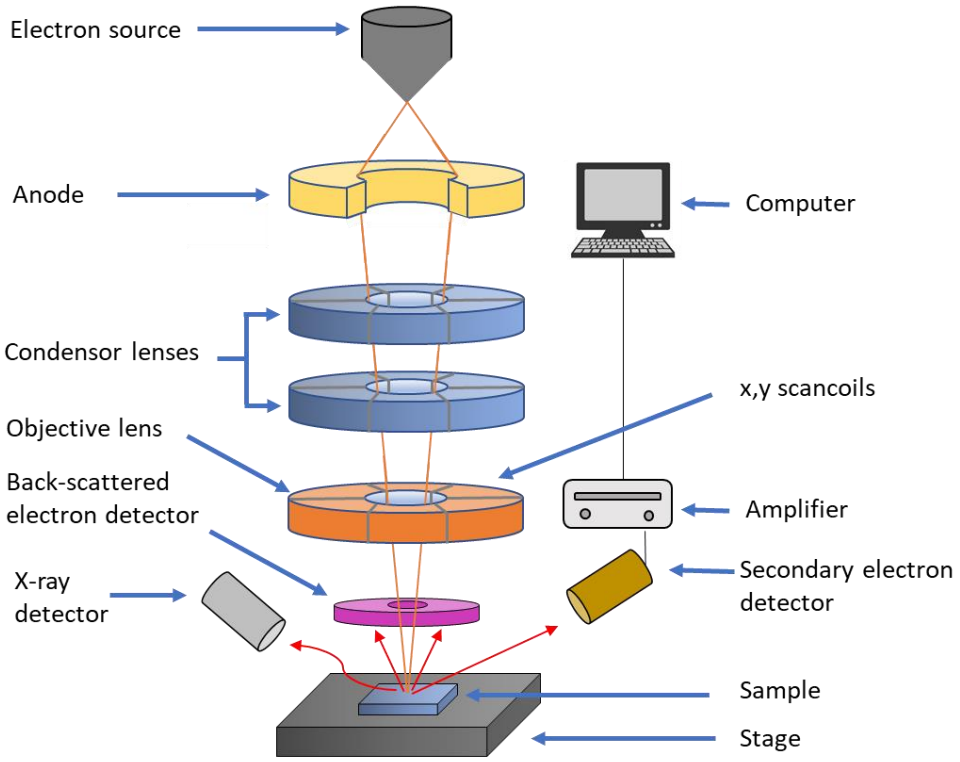

Fig. 3.5: Schematic representation of a scanning electron microscope (SEM)

When electrons collide with the sample, they are scattered with a teardrop-shaped volume (Fig. 3.6) and gradually lose their energy until absorption in the sample. The scattering of the electrons inside the sample depends on the electron energy, the atomic numbers of the elements, and the density of the constituent atoms. The interaction volume may extend from 100 nm to 5 μm. The higher the energy is, the larger the scanning range is. So, if the atomic number and density are large, the scanning range is smaller [9].

The signals derived from electron-sample interaction are analysed. Between them, the most used are: secondary electrons, backscattered electrons (BSEs) and X-rays.

-Secondary electrons are generated as a result of inelastic interactions of the beam with the valance electrons of the constituted atoms in the sample. The energy of secondary electrons is very small (<50 eV) so those generated at a deep region are quickly absorbed by the sample. Only those generated at the top surface of the specimen are emitted outside of the material. For these reasons, the secondary electrons are very sensitive to the surface.

-Backscattered electrons (BSEs) are derived from the interaction between the electrons beam and the atomic nuclei in the sample. They possess higher energy than secondary electrons (> 50 eV), so they contain information of relatively deep regions. The BSEs are

sensitive to the composition of the specimen. In fact, heavy elements (high atomic number) present a larger yield than light element resulting in a brighter area in the final image.

- X-rays are high-energy photons derived from the excitation of deep electrons and they are used especially for the elemental microanalysis.

The SEM possesses many advantages as for example the fact that it allows to acquire high resolution images at high magnification (> 100k), as well as to obtain continuous enlargements with the same objective. However, SEM instrument usually requires conductive solid sample stable in vacuum (10^{-5}-10^{-6}). For these reasons, in case of an insulating sample, the surface has to be made electrically conductive by graphite glue/tape or by conductive coating.

In this work a FE-SEM (field emission gun scanning electron microscope) was used, with a W/ZrO_2 emission source with a Schottky effect (Zeiss Sigma, Carl Zeiss Microscopy Gmbh, Germany) and equipped with a detector for secondary electrons (SE2), low energy (SE1) and backscattered electros (BSE). Samples for the microscopy analysis were prepared starting with the polishing of the surface with a semi-automatic polishing machine (Tegramin-25, Struers, Italy), then they were washed in an ultrasonic bath with ethanol or acetone and cleaned in a plasma cleaner (Colibrì Plasma RF 50 KHz, Gambetti, Italy) at 40 W for 5 min in nitrogen atmosphere. Non-conductive samples, (e.g. oxidized materials), were coated with a layer of carbon with a turbo-pumped spatter coater (Q150 ES, Quorum Technologies Ltd, UK). To analyse the images and to obtain information on the surface morphologies (e.g. mean grain size), a commercial software package was used (Image-Pro Plus analyser 7.0, Media Cybernetics, U.S.A).

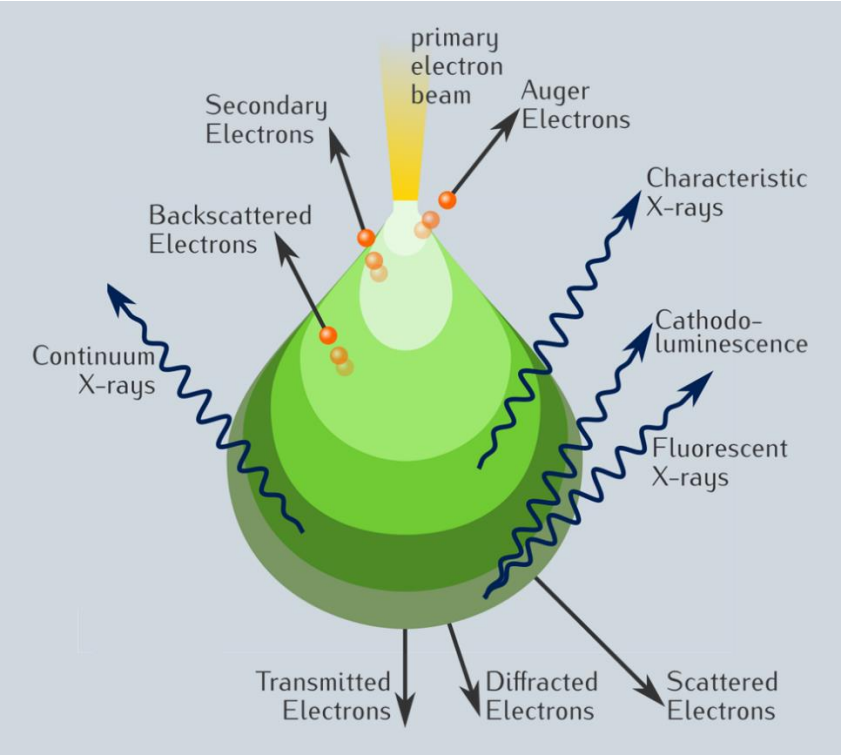

Fig. 3.6: Electron volume interaction with matter and different generated signals

3.1.4 Energy- dispersive X-ray spectroscopy

Energy-dispersive X-ray spectroscopy (known as EDS, EDX or EDXA) is a technique that enables to analyse the elemental composition of a sample [9]. The principle at the base of the EDS is the capacity of high energy electromagnetic radiation (X-rays) to eject "core" electrons from an atom. This effect is known as Moseley's law and states that there is a direct correlation between the frequency of light released and the atomic number of the atom. When the electrons are removed from the "core", they leave behind a hole that a higher energy electron can fill in, releasing energy as it relaxes. This energy is usually released as X-ray fluorescence and its value is equal to the difference between the higher-energy shell (where there is the electron that drops off) and the lower-energy shell (where the vacancy is). The energy released during the relaxation is unique and different for each element. So, bombarding a sample with X-rays can be used to identify what elements are present and in which proportion. In Fig. 3.7 an example of how EDS works is reported. The different energy levels are called with the letters K, L and M that refer to the *n* value of the electron in the shell (i.e., K electrons are $n = 1$ electrons) and the size of the transition are indicated with α and β. The relaxation from M to L or L to K is described as Lα or Kα, while going from M to K is a Kβ transition. This method is known as Siegbahn notation [9].

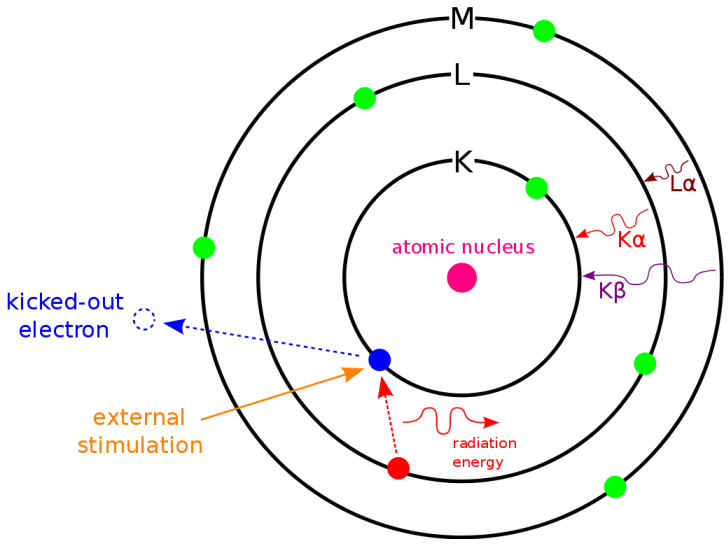

Fig. 3.7: schematic representation of the mechanism at the base of the EDS technique.

The EDS system is constituted by three different parts: an emitter, a collector and an analyser. These parts are usually integrated with an electron microscopy instrument like the scanning electron microscopy (SEM) or transmission electron microscopy (TEM). This system allows to obtain information about how many X-rays are released and their energy (in comparison to the energy of the initial X-rays used to hit the sample). The data collected by EDS are presented as a graph with KeV on the x-axis and an intensity peak on the y-axis. The EDS analysis is a very useful technique but presents some problems. It is not a particularly sensitive analysis, if the amount of elements in the samples is too low it is difficult to obtain a correct proportion of the element. Moreover, the EDS generally does not work for elements with a low atomic number. For example, H and He have only n =1 shell, so there are not core electrons that can be removed and allow the formation of X-rays.

The EDS is primarily a qualitative tool. However, it is possible to carry out quantitative analysis after calibration with a metal standard, usually a cobalt target. The accuracy of the analysis depends on the nature of the sample and the energy of the electron beam. For the heavy metal samples, high energy is required to emit X-rays that can negatively affect the accuracy on lighter elements due to the higher depth of penetration of the beam [10].

In this thesis, a qualitative and a semiquantitative analysis were conducted with an EDS (Oxford Energy X-act, Oxford Instruments, UK, interfaced by INCA software) coupled with scanning electron microscopy (FE-SEM, Carl Zeiss Sigma NTS Gmbh

Öberkochen, Germany). The analyses were conducted with a voltage between 5 to 10 KeV due to the different elements present in the samples (i.e. B, C, Si, Zr, …). To optimize the semiquantitative measurements, a calibration with cobalt was made.

Mechanical testing

3.1.5 Flexural strength

The flexural strength is defined as the maximum stress that can be applied to the material before it failure [11]. For a bulk ceramic, the flexural strength depends on different factors such as size, shape grain size, density, pores and flaws distribution. In fact, residual porosity, large grains can decrease the mechanical properties. More in detail, the pores decrease the area where the load is applied and can act as defects where the stress is concentrated and leads to a catastrophic failure [12]. The flexural strength is obtained through a bending test of samples with a cylindrical or rectangular cross-section with a three- or four-point fixture [13,14]. In the fibre-reinforced ceramic composites the determination of the bending strength is more difficult than in a bulk ceramic due to the interaction between matrix and fibres. For these materials, porosity is usually higher than the corresponding bulk material and achieving full density often results in a damaged fibre [15]. Moreover, the value of strength is highly influenced by the fibre orientation due to the intrinsic anisotropy. For example, in samples reinforced with unidirectional fibres where the load is applied perpendicular to the fibre orientation, the load is fully transferred to the fibre that act as a reinforcement and allows to obtain the maximum strength value. However, when the load is parallel to the fibre, the fibre acts as defects and the bar suffers a brittle fracture [16]. These materials can also incur failure by interlaminar shear stress due to their layered structure, therefore attention has to be paid during three-point and four-point bending tests in order to minimize shear stresses, such as using high span/thickness ratios to promote failure by tensile stresses. In the case of short fibre reinforced composites, this issue is less emphasized due to the more isotropic structure of the material.

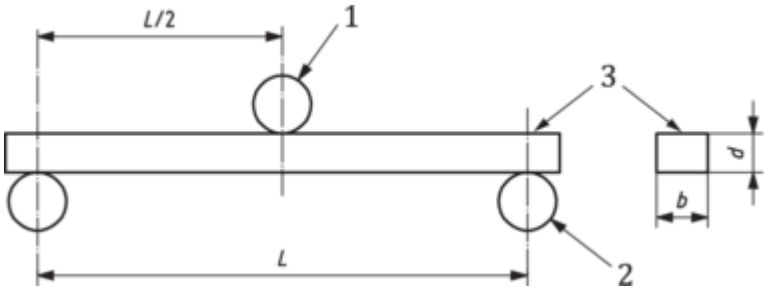

$$\sigma = \frac{3P_{Kg}9.81a}{2bd^2}$$

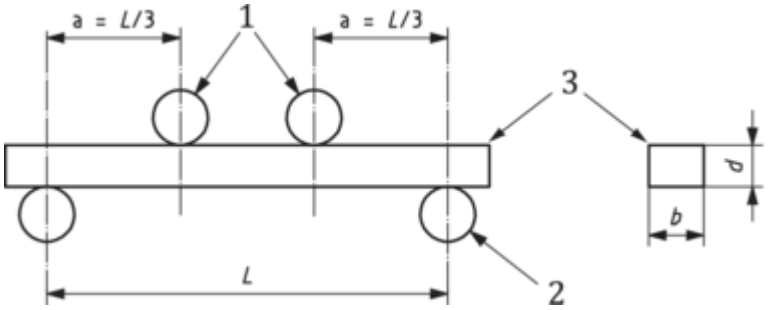

$$\sigma = \frac{3P_N a}{bd^2}$$

$$\sigma = \frac{3P_{Kg}9.81a}{bd^2}$$

Fig. 3.8: Four-point geometry reported in ISO 14704:2016 and relative formula for the flexural strength calculation. Where, P_N is the force in newton, P_{Kg} is the force in Kg and b and d are the width and thickness respectively.

Fig. 3.9: Illustration of Z050, Zwick-Roell (left) and a semi-articulated test fixture for the four-point bending strength test (right).

In the present work, composite materials reinforced with short carbon fibre were studied in order to investigate the mechanical behaviour. For these reasons, three-point

bending strength tests were carried out on long bars, with a dimension of 45 mm x 4 mm x 3 mm (length, width, thickness, respectively) with a semi-articulated test fixture. Four-point bending strength tests were carried out on short bar of 25 mm x 2.5 mm x 2 mm (length, width and thickness, respectively) using a semi-articulated test fixture with a lower span of 20mm and upper span of 10 mm using a screw-driver testing machine (Z050, Zwick-Roell, Germany), Fig. 3.9. During the tests, the guideline of standard ISO 14704:2016 was followed Fig. 3.8. Every test was conducted at room temperature with a cross head speed of 1 mm/min. At least three bars were tested for each material at each condition. Due to the random distribution of the short carbon fibre inside the samples tested in this thesis, the influence of the fibre orientation in the horizontal plane is almost negligible. However, its influence is still present when passing from a horizontal orientation to a vertical orientation. For all these reasons, samples with same matrix but different fibre amount of carbon fibre or different length (i.e. ZrB_2 based matrix reinforced with 20-35-50 % of carbon fibres with a length of 3-5 mm) were tested with a four-point bending strength. Also, samples with same composition (i.e. ZrB_2 based matrix reinforced with 35 % of carbon fibres with a length of 5 mm) were tested with a three-point bending strength changing the orientation of the layer constituting the samples. Finally, samples with a semi vertical short carbon fibre orientation were tested with a four-point bending strength. The different carbon fibre orientation tested are schematized in Fig. 3.10.

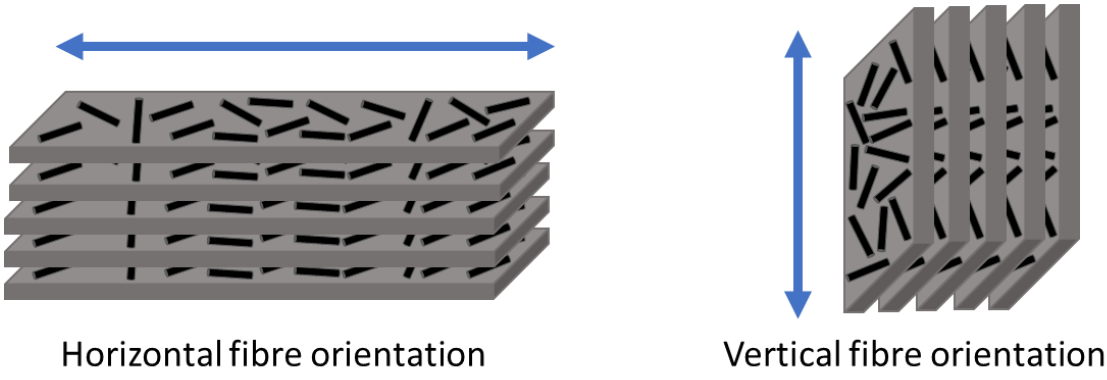

Fig. 3.10: Schematic illustration of the different fibre orientation subjected to bending strength tests.

3.1.6 Fracture toughness (hardness)

Fracture toughness is commonly used to describe the ability of a material containing a crack to resist crack propagation the [17]. It is represented with K_{Ic}, which

is the plane strain fracture toughness, i.e. the critical value of stress intensity factor K in mode I loading measured under plane strain conditions that leads to brittle fracture [18,19]. The value of K_{Ic} depends on the nature of the material. It is high for ductile materials and low for brittle materials, such as ceramics. To determine this parameter several methods are known, such as Vickers hardness indentations [20–22]. In this method, an indenter penetrates the sample surface inducing the generation of cracks from the corner of the indentation. The length of the cracks produced can be correlated to the resistance of the material to the fracture toughness. However, this method is not valid in the case of reinforced composites because the cracks can be arrested by the presence of fibres. The preferred methods for the evaluation of fracture toughness in composites materials are techniques based on the introduction of a notch where all the stresses are concentrated, and the samples are tested in bending [23]. In Fig. 3.11 are illustrated the different notch geometries.

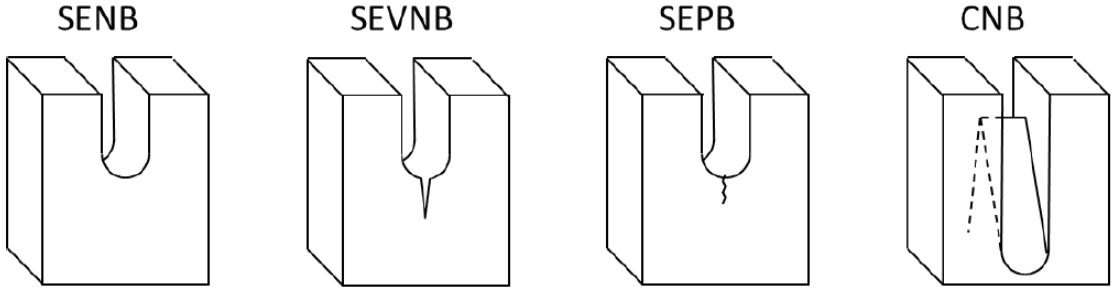

Fig. 3.11: Schematic representation of the different notch geometries.

The single edge notched beam (SENB) is a test where a flat notch is introduced. However, the introduction of a notch with a radius below 25 μm is difficult and the data tends to be scattered [24]. The single edge V-notched (SEVNB), is similar to SENB, and allows to introduce more critical defect. However, the introduction of a straight notch is a limiting factor. The single edge pre-cracked beam (SEPB), is also similar to SENB. In this test, the critical defect is introduced by pre-cracking the beam at low loads. This method allows to obtain accurate results, but in case of fibre reinforced materials it is difficult to initiate the crack. The chevron notched beam (CNB), is a method where a triangle-shaped notch is introduced. The application of the load initiates a crack that starts on the top of the triangle and propagates from there. The advantage of this method is the lack of issue due to the curvature radius at the crack tip. With the CNB, the fracture toughness is calculated

from the maxim load (P_{max}) calculated in a four-point bending test trough the equation of Munz [23]. Following are reported the CNB model and relative formulas, Fig. 3.12.

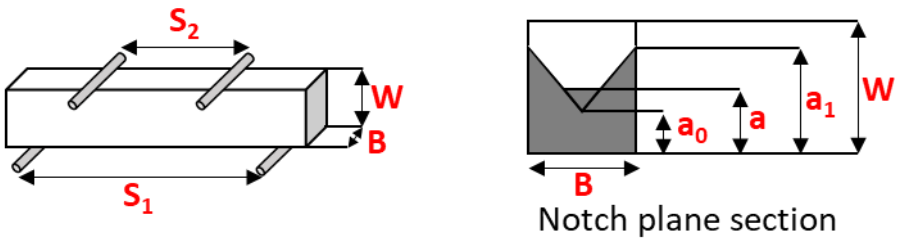

$$\alpha_0 = \frac{a_0}{W}$$

$$\alpha_1 = \frac{a_1}{W}$$

$$y^* = (3.08 + 5\alpha_0 + 8.33\alpha_0^2)\frac{(S_1 - S_2)}{W}(1 + 0.007\sqrt{\frac{S_1 S_2}{W^2}})(\frac{\alpha_1 - \alpha_0}{1 - \alpha_0})$$

$$K_{IC} = \frac{P_{max}}{B\sqrt{W}}y^*$$

Fig. 3.12: Chevron notch model for the CNB and relative formulas for the determination of K_{IC}.

In this thesis, the fracture toughness (K_{IC}) was calculated with the chevron-notched beams (CNB) by four-point banding test. The tests followed the indication reported in the EN14425-3:2010. The tests were conducted on bars with a dimension of 25.00 mm × 2.0 mm × 2.5 mm (length, width, thickness) with a notch tip of 0.12 mm and 0.80 mm, chevron-notch tip depth and average side length respectively. The testing setup was constituted by a screw-drive frame (Z050, Zwick-Roell, Germany) with a cross head speed of 0.05 mm/min and a four-point fixture with a lower span of 20 mm and upper span of 10 mm.

3.1.7 Tensile testing

The tensile testing is a test in which a sample is subjected to a controlled tension until failure. With this test, it is possible to measure the ultimate tensile strength, the breaking strength, the maximum elongation and reduction area. Moreover, it is possible to determine different properties of the materials such as the Young's modulus and the Poisson's ratio. The most commonly used test is the uniaxial tensile testing, but for some

materials the biaxial testing could be made. The main difference between these two tests is how the load is applied on the material.

In the present work, the uniaxial tensile tests were carried out at room temperature on “dogbones” specimens with dimensions reported in Fig. 3.13 following the guideline of standard EN 658-1:1999 norm. Every test was conducted using a couple of grips (Fig. 3.13) incorporated with a screw-driver testing machine (Z050, Zwick-Roell, Germany) with a cross head speed of 1 mm/min. At least three bars were tested for each material [1]. The force measurement is used to calculate the engineering stress, σ, using the following equation:

$$\sigma = \frac{F_n}{A}$$

where F is the tensile force and A is the nominal cross-section of the specimen.

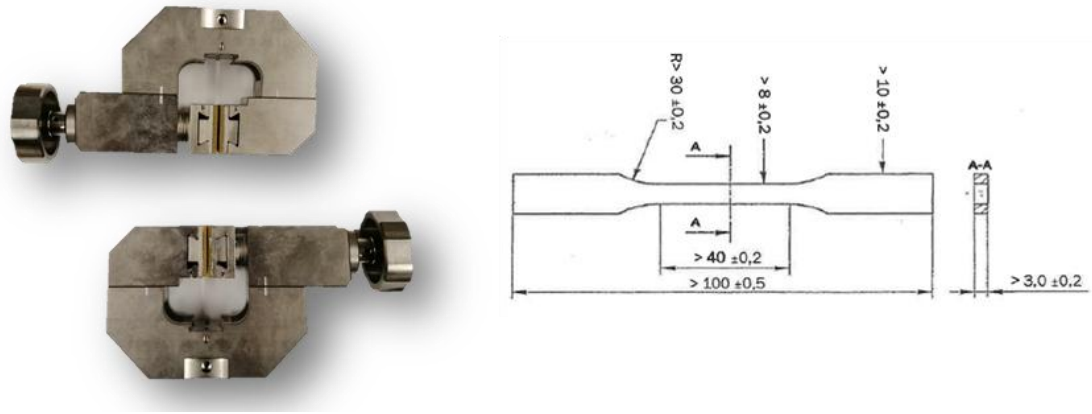

Fig. 3.13: Illustration of the clamps (left) and the geometry of the specimen (right) used for the tests.

3.1.8 Critical fibre length

The interaction of fibre and matrix is a crucial parameter for composites performance in terms of strength, especially in short fibre reinforced composites. The ability to transfer the stress, in the case of short fibres, is defined by the critical length. If the critical length is exceeded, fibre breakage will occur, and no further improvement is possible in the material [25]. The critical fibre length is usually calculated by using the following equation [26]:

$$l_c = \frac{\sigma_f D_f}{2\tau_c}$$

where σ_f is the tensile strength of fibre, D_f is fibre diameter and τ_c is the fibre-matrix bond strength. However, this method would have required a detailed study to measure and calculate all the individual parameters. Previous studies [27] discovered an easier and more direct method to determine the critical fibre length through the image analysis. In accordance with this method, first the average of all pulled- out fibres is determined (It may vary between 0 and half of the critical length). Then, the average is multiplied by 4 to obtain the critical fibre length. In this thesis, to determine the critical length this method based on the image analysis was used.

3.2 Materials processing

The fabrication of carbon fibre reinforced UHTC composites requires several steps to obtain the final material. The processes for the production of bulk ceramics are well known but the presence of the fibre reinforcement is an obstacle to the consolidation of the ceramic powders. In fact, previous studies showed that the presence of fibres hindered the powder sintering, resulting in high porosity in the final product [28,29].

This Ph.D. research was focused on the development of a novel water-based processing route for the fabrication of UHTC reinforced with short carbon fibre and the possible application of this material. The experimental procedures of some steps (i.e., powder treatment, slurry preparation and sintering) are the result of previous studies conducted at the ISTEC CNR [28,30–34].

3.2.1 Materials

Commercial products were used as raw materials for the fabrication of the samples.

Ceramic powders:

- ZrB_2 (Grade B, H.C. Starck, Germany; specific surface area 1.0 m2/g, particle size range 0.5–6 μm, impurities (wt%): 0.25 C, 2 O, 0.25 N, 0.1 Fe, 0.2 Hf);
- α-SiC (Grade UF-25, H.C. Starck, Germany, specific surface area 23–26 m^2/g, D_{50} 0.45 μm, impurities (wt%): 2.5 O);
- Y_2O_3 (Grade C, H.C Starck, Germany, specific surface area 10−16m^2/g, D_{50} 0.90 μm, impurities (wt.%): 0.005 Al, 0.003 Ca, 0.005 Fe);
- $MoSi_2$ (Aldrich, Milwaukee, particle size range 0.5–6 μm, oxygen content 1 wt.%);

- TiB_2 (H.C. Starck, Grade F, D_{90} 4.0–7.0 μm, D_{50} 2.5–3.5 μm, < 4.5 μm, impurities (wt. %): 0.4 C, 2.5 O, 0.5 N, 0.1 Fe);
- B_4C (H.C. Starck Grade HS-A, D_{90} 2.0–4.0 μm, D_{50} 0.6–1.2 μm, B:C ratio 3.7, impurities (wt. %): 0.7 N, 1.7 O, 0.05 Fe, 0.15 Si, 0.05 Al)

Fibres:

- Granoc Yarn XN80-6K fibers; tensile modulus of 780 GPa and tensile strength 3.4 GPa, 10 μm diameter Supplier: Angeloni

The carbon fibres are defined as fibres with a carbon content above 92 wt%. Nowadays, most of the amount of carbon fibres are made by carbonizing precursors and can be divided in three different types based on the precursor used: PAN-based, pitch-based and rayon-based [35]. Between these, the PAN- and pitch-based are the most diffused. The Pan-based carbon fibres present a balanced performance (high strength and low - intermediate modulus) and lower production costs [36,37]. The pitch-based fibres possess an ultra-high modulus and high thermal/electrical conductivity [38]. Thanks to their high temperature properties and refractoriness to thermal treatments, in this work, pitch-based carbon fibres were used.

Thickener:

- Alginic acid sodium salt (high viscosity, Thermo Fisher, Germany)

Sodium alginate ($NaC_6H_7O_6$) is a linear polysaccharide present in the cell wall component of marine brown algae and contains approximately 30-60 % of alginic acid. The conversion of alginic acid to sodium alginate allows its solubility in water. An important characteristic of alginates is its liquid-gel behaviour in aqueous solutions. In fact, monovalent ions (e.g. sodium in sodium alginate) can be exchanged for divalent ions (e.g. calcium). The reaction proceeds immediately, changing from a low viscosity solution to a gel structure. The gel is a copolymer composed by two kinds of monomer units (Fig. 3.14) [39].

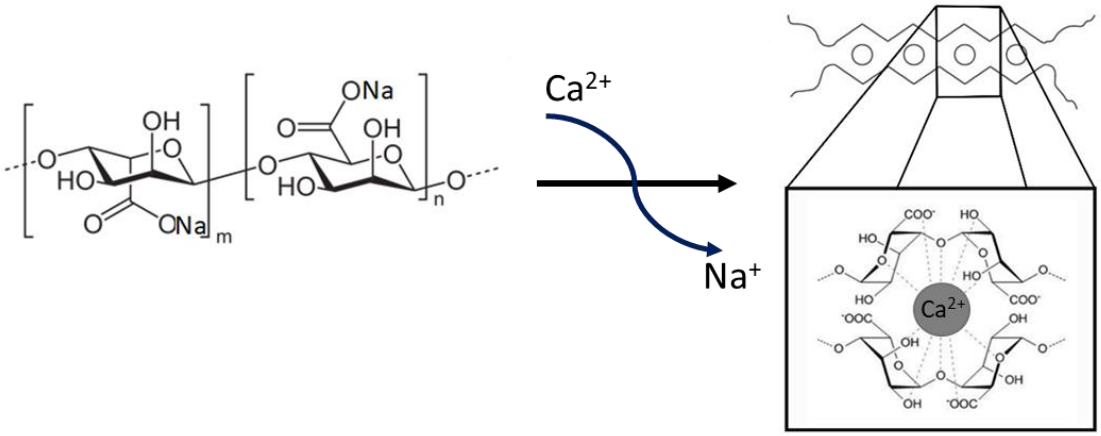

Fig. 3.14: schematic representation of sodium alginate (1,4-β-d-mannuronic (M) and α-l-guluronic (G) acids) and the reaction of gelification with calcium ions.

3.2.2 Powder ball milling

The preparation of the powder mixtures and their homogenization is the first step. In this work, the ball milling technique was used. It is based on the capability of hard materials (e.g. SiC or Si_3N_4) to grind softer powders, reducing the particle size and homogenizing the mixture. In this case, ball milling was mostly used to break powder aggregates and homogenise the powder mixture, while the potential contamination of the powders with the grinding media is negligible. The presence of a solvent (e.g. ethanol in this work) helps the powder mixing and to minimize the particles oxidation and heat production. On the basis of the required composition, the powder mixtures were prepared by wet ball milling of the starting powder with Si_3N_4 grinding media in absolute ethanol for 24 h at ≈60 rpm. The presence of water must be avoided as much as possible in order to minimize the powder surface oxidation [40]. The ratio between powder, solvent and grinding media is 1: 1: 1 by weight. After the ball milling, the powders were dried with a rotary evaporator and then sieved (250 μm mesh) in order to break the powder agglomerates.

3.2.3 Slurry casting

The dry powders were dispersed in deionized water in order to obtain an aqueous slurry. To homogenize the powders with the solvent and avoid precipitation, poly-acrylates dispersant and a mixing of 3h in a HDPE bottle at ≈60 rpm were used in accordance with previous studies [30]. The prepared slurries were mixed with the short carbon fibres of desired length (i.e. 3 mm or 5 mm length in this thesis and different amount based on the desired volume in the final sample) and the thickener with the use

of a planetary mixer (Thinky mixer ARE-500CE, Thinky, USA) for 3 min at 900 rpm and 1 min and 1200 rpm for the defoaming. After mixing, the obtained product was transferred in a plaster mould where it was dried at 80 °C for ≈30 min to remove water. The green layers (not consolidated) with a final thickness of ≈ 100 μm were cut in the desired dimensions and overlapped to obtain the thickness of the final samples. In Fig. 3.15 the process for the slurry casting is shown.

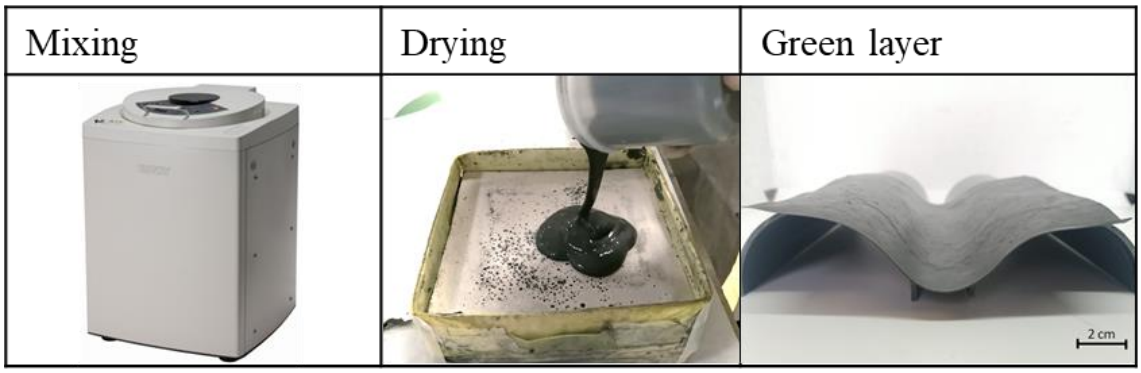

Fig. 3.15: Different steps for the slurry casting: 1st – mixing of the materials; 2nd drying in the gypsum mould; 3rd final green layer.

3.2.4 Debinding

In order to avoid potential contamination of the hot-pressing machine, a debonding is required to eliminate the organic residues inside the samples before the sintering. The debonding was conducted in air or argon. To decrease the environmental impact of these materials - in this thesis - a debonding in air was used. The temperature for the debonding must be under 400-500 °C in order to avoid the carbon fibre oxidation [41] The thermogravimetric analysis (Netzsch STA-449C) conducted on the green in air, Fig. 3.16, shows that at ≈ 300 °C there is a considerable weight loss which can be attributed to the loss of organic material. For these reasons, the debonding was conducted in an oven in air. The green was heated from RT to 300 °C at rate of 120 °C/h, and dwell time of 30 min, and finally cooling down at RT.

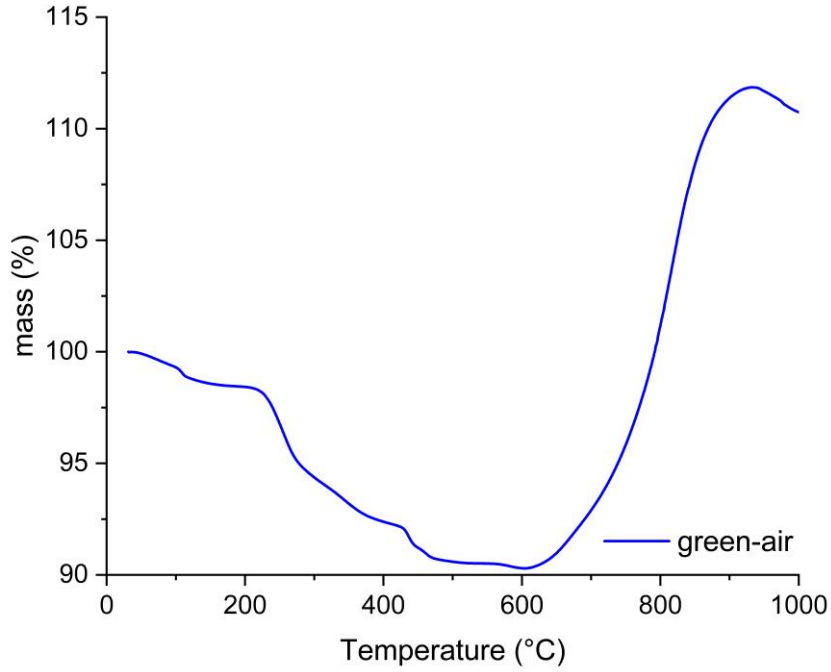

Fig. 3.16: Thermogravimetric analysis of the green sample in air, flow rate 30 mL/min, heating 30 °C/min.

3.2.5 Hot Pressing

To consolidate the UHTCMC materials, hot pressing was carried out in high vacuum (≈ 10^{-5} bar). The susceptor is made of graphite and is heated by induction heating. The treated material is placed in the graphite die and a uniaxial pressure is applied via the action of two pistons made of graphite that are separated by the steel piston with an alumina block to avoid direct contact with the hot elements and minimize the potential of arc formation. In Fig. 3.17, the vacuum chamber for hot pressing (MP 20(II), SIATEM, Ing. Allaria Alto Vuoto, Italy) is shown.

In this thesis, for every material an initial low pressure at 900 °C was applied and then it was increased to 40MPa at the final temperature, 1900 °C. In order to avoid the formation of bubbles in the final composites, the heating ramp was not too fast. This is important in particular for the samples containing ZrB_2 since the B_2O_3 impurities can be released [42]. At 1900 °C, the pressure was maintained for 10-15 min. At the end, the pressure was removed, and the samples were cooled down at room temperature.

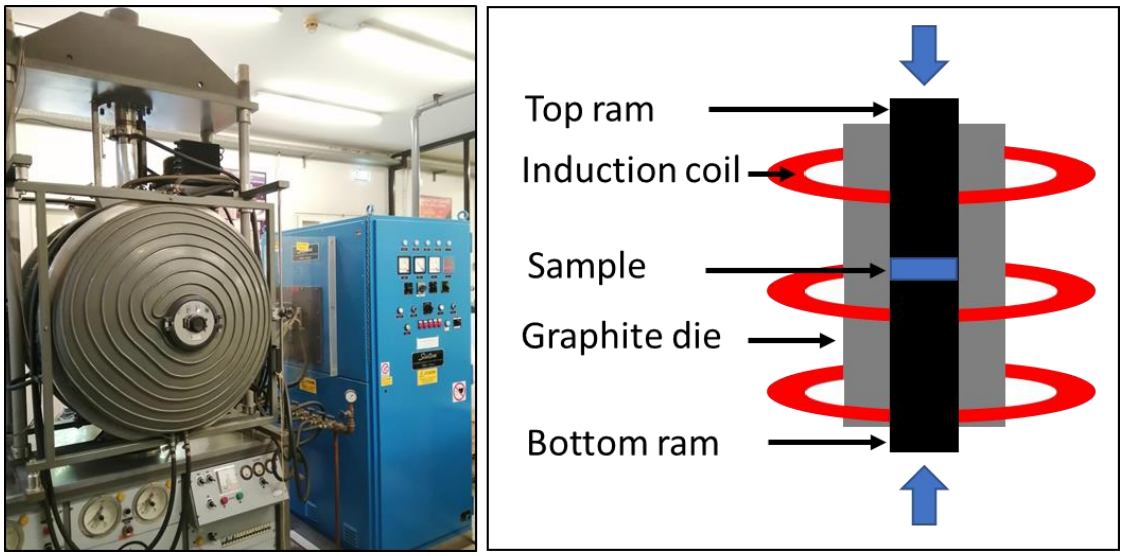

Fig. 3.17: Image of vacuum oven for hot pressing (MP 20(II), SIATEM, Ing. Allaria Alto Vuoto, Italy) (left), and schematic representation of internal structure (right)

3.3 Oxidation resistance

3.3.1 Air furnace oxidation testing

To evaluate the resistance in extreme environments of composites with a different composition (e.g. different matrix or fibre amount), harsher tests were conducted in a bottom-up loading furnace (Fig. 3.18).

Fig. 3.18: Bottom loading furnace (Nannetti S.r.l. Italy)

This type of furnace is equipped with a vertically moving elevator plate where the sample is placed. The vertically moving elevator allows a simple sample loading inside the high-temperature chamber. Moreover, the heating elements inside the walls ensures to obtain uniform heating. Thanks to these characteristics, it is possible to test the oxidation resistance of the materials which are directly exposed at the target temperature (e.g. 1650 °C). In fact, the furnace can be heated to the test temperature and only when it is reached the samples are introduced in the chamber. By this way, the quick exposition at high temperature was tested by-passing potential oxidation phenomena that could occur at lower temperature. In the present work, samples with an approximate dimension of 5 × 10 × 3 mm (width × length × thickness) were tested. The samples were cleaned with acetone in an ultrasonic bath and dried under IR lamp. Tests were performed in a bottom loading furnace (FC18-0311281, Nannetti S.R.L, Italy) at 1650 °C in air for 1 minute. When the target temperature was reached, the samples were introduced in the furnace using a porous zirconia sample holder. After reaching the thermal equilibrium (≈ 2min), the isothermal stage began (1 min). At the end of the oxidation test, the samples were quickly removed and let to cool down naturally in air. The samples were weighed right before (w_{in}) and after (w_{fin}) the oxidation test. Mass variation was normalized over the initial surface area (S) with the following equation: $\frac{\Delta m}{S} = \frac{w_{fin} - w_{in}}{S}$.

3.4 Tribological characterization

3.4.1 Coefficient of friction

Nowadays, the last theory believed that the 90% of the total friction comes from interatomic adhesion between two surfaces [43]. The coefficient of friction (COF) is a measure of the amount of friction existing between two surfaces. It indicates the resistance to motion at the interface of two surfaces. The COF is a dimensionless number which is defined as the ratio between the friction force ($F_{friction}$) and the normal force (F_{normal}) [[44]] and depends on the nature of the materials and the surface roughness (Fig. 3.19).

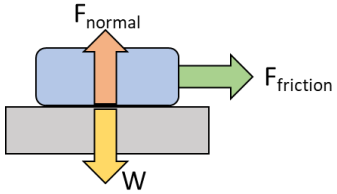

$$COF = \frac{F_{friction}}{F_{normal}}$$

Fig. 3.19: Schematic representation of COF and related formula

In this work, the COF during the braking tests was collected. Its values were automatically calculated by the instrument with the use of the value of friction force and normal force. The normal forces (F_{normal}) were given by the calliper pressures. The friction force was collected by a sensor pit at the base of the sample that measures the braking torque.

3.4.2 Braking tests

The tribological tests were conducted with a self-designed inertia dynamometer (CMC institute, University of Bayreuth, Germany), schematically illustrated in Fig. 3.20. During a test the flywheel with a mass of 800 Kg is accelerated by a 45 kW motor in 20 s to 1030 rpm and then turned off. Immediately after, the pneumatic brake calliper is engaged with a surface pressure of 1 or 3 MPa to a complete stop. Then, the next cycle is started immediately. The braking energy for every cycle is around 5,43 MJ with different sliding speed due to the different friction radius of the disc tested.

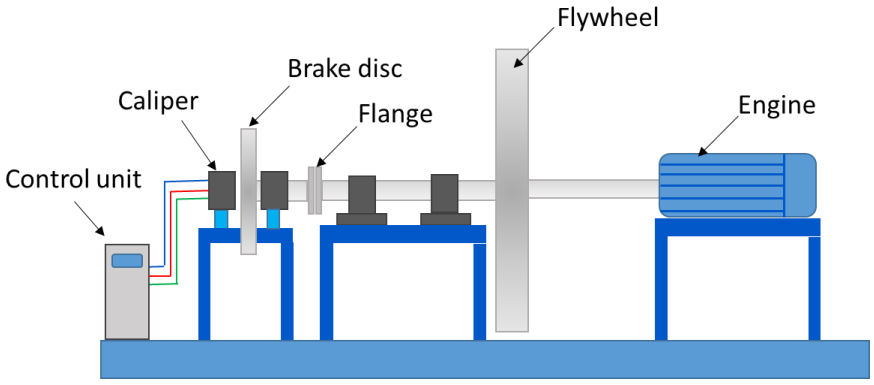

Fig. 3.20: Schematic representation of the self-designed inertia dynamometer

For each test, two braking pads (30 x 30 x 10 mm^3) were tested against commercial and self-made discs as counterparts. Two different kinds of pad materials were tested:

- ZrB_2-10%SiC-5%Y_2O_3 ceramics reinforced with 40 vol % pitch-based carbon fibre fabric arranged in 0°/90° orientation

- ZrB_2-10%SiC-5%Y_2O_3 ceramics reinforced with 35 vol % randomly orientated chopped pitch-based carbon fibre with length of 5 mm

Three different discs were used as a counterpart for the tests:

- Commercial, C/C brake disc

- Commercial, internally ventilated C/C-SiC brake disc with SiC-rich friction layer (SGL, Germany), friction radius of 184 mm; diameter 400 mm

- Self-made, solid steel brake disc, constituted by S235 Steel, friction radius of 173 mm; diameter 380 mm; thickness 40 mm

Each braking test consists of 10 braking cycles to a complete stop. Before every test, 5 pre-braking cycles were made, and the system was cooled down at temperature ≤ 30°C.To calculate the volume and mass wear rates, weight and thickness of braking pads were measured at four points before and after a braking test. The temperatures during the tests were continuously recorded with thermocouples put on the backside of both the pads and on the sliding surface of the disc. As previously indicated, the COF is calculated by continually measuring clamp pressure and braking torque with 100 Hz. The different braking conditions are summarized in Table. 3.1.

Table 3.1: Summary of the braking conditions.

Disc material	**C/C-SiC**	**Steel**	**C/C**
Pad material	ZrB_2 +40% short Cf ZrB_2 +40% long Cf	ZrB_2 +40% short Cf ZrB_2 +40% long Cf	ZrB_2 +40% short Cf ZrB_2 +40% long Cf
Clamp pressure (MPa)	1 + 3	1 + 3	1 + 3
Sliding speed (m/s)	20	18.7	13.5
Friction radius (mm)	184	173	125
Rpm flywheel	1030	1030	1030
Rotation energy (MJ)	≈ 5.4	≈ 5.4	≈ 5.4

3.5 References

[1] B.D Cullity, Elements of X-RAY DIFFRACTION, 1994.

[2] A. Putnis, An Introduction to Mineral Sciences, (1992). https://doi.org/10.1017/CBO9781139170383.

[3] T.N. Blanton, T.C. Huang, H. Toraya, C.R. Hubbard, S.B. Robie, D. Louër, H.E. Göbel, G. Will, R. Gilles, T. Raftery, JCPDS—International Centre for Diffraction Data round robin study of silver behenate. A possible low-angle X-ray diffraction calibration standard, Powder Diffr. 10 (1995) 91–95. https://doi.org/10.1017/S0885715600014421.

[4] E.J. Mittemeijer, U. Welzel, Modern Diffraction Methods., (2013) 556.

[5] X. Chen, B. Zheng, H. Liu, Optical and digital microscopic imaging techniques and applications in pathology, Anal. Cell. Pathol. (Amst). 34 (2011) 5–18. https://doi.org/10.3233/ACP-2011-0006.

[6] B.R. Masters, Confocal Microscopy and Multiphoton Excitation Microscopy, Confocal Microsc. Multiphot. Excit. Microsc. Genes. Live Cell Imaging. (2006) 607–621.

[7] P. Kruit, Introduction to Charged Particle Optics, n.d.

[8] L. Reimer, Scanning Electron Microscopy, 45 (1998). https://doi.org/10.1007/978-3-540-38967-5.

[9] J.I. Goldstein, D.E. Newbury, J.R. Michael, N.W.M. Ritchie, J.H.J. Scott, D.C. Joy, Scanning electron microscopy and x-ray microanalysis, Scanning Electron Microsc. X-Ray Microanal. (2017) 1–550. https://doi.org/10.1007/978-1-4939-6676-9/COVER.

[10] J. Konopka, T.F. Scientific, Options for Quantitative Analysis of Light Elements by SEM/EDS, (n.d.).

[11] W.D. Callister, D.G. Rethwisch, Scienza ed ingegneria dei materiali, (2019). https://www.edisesuniversita.it/area_tecnica/callister-scienza-e-ingegneria-dei-materiali-2019.html (accessed December 22, 2022).

[12] M. Barsoum, Fundamentals of ceramics, (1997) 568.

[13] M. Vable, K.R. Vable, S. Gautam Vable, Mechanics of Materials Second Edition, (2010). http://www.me.mtu.edu/~mavable/MoM2nd.htmhttp://www.me.mtu.edu/~mavable/MoM2nd.htm (accessed December 22, 2022).

[14] R.W. Davidge, Mechanical behaviour of ceramics, (1979) 165.

[15] L. Zoli, A. Vinci, L. Silvestroni, D. Sciti, M. Reece, S. Grasso, Rapid spark plasma sintering to produce dense UHTCs reinforced with undamaged carbon fibres, Mater. Des. 130 (2017) 1–7. https://doi.org/10.1016/j.matdes.2017.05.029.

[16] F.C. Campbell, Structural Composite Materials, (2010). www.asminternational.org (accessed December 22, 2022).

[17] D.R. Askeland, P. Fulay, W.J. Wright, C. Mapelli, Scienza e tecnologie dei materiali, (2017) 747. https://www.goodbook.it/scheda-libro/donald-r-askeland-pradeep-p-fulay-wendelin-j-wright/scienza-e-tecnologia-dei-materiali-9788825174151-1131526.html (accessed December 22, 2022).

[18] S. Suresh, Fatigue of Materials, Fatigue Mater. (1998). https://doi.org/10.1017/CBO9780511806575.

[19] G.A. Gogotsi, Fracture toughness of ceramics and ceramic

composites, Ceram. Int. 29 (2003) 777–784. https://doi.org/10.1016/S0272-8842(02)00230-4.

[20] G.D. Quinn, R.C. Bradt, On the Vickers Indentation Fracture Toughness Test, J. Am. Ceram. Soc. 90 (2007) 673–680. https://doi.org/10.1111/J.1551-2916.2006.01482.X.

[21] A.G. EVANS, E.A. CHARLES, Fracture Toughness Determinations by Indentation, J. Am. Ceram. Soc. 59 (1976) 371–372. https://doi.org/10.1111/J.1151-2916.1976.TB10991.X.

[22] E. Rocha-Rangel, E. Rocha-Rangel, Fracture Toughness Determinations by Means of Indentation Fracture, Nanocomposites with Unique Prop. Appl. Med. Ind. (2011). https://doi.org/10.5772/18127.

[23] D.G. Munz, J.L. Shannon, R.T. Bubsey, Fracture toughness calculation from maximum load in four point bend tests of chevron notch specimens, Int. J. Fract. 16 (1980) 137–141. https://doi.org/10.1007/BF00013393.

[24] N. CLAUSSEN, Fracture Toughness of Al2O3 with an Unstabilized ZrO2Dispersed Phase, J. Am. Ceram. Soc. 59 (1976) 49–51. https://doi.org/10.1111/J.1151-2916.1976.TB09386.X.

[25] D. Heim, M. Hartmann, J. Neumayer, C. Klotz, Ö. Ahmet-Tsaous, S. Zaremba, K. Drechsler, Novel method for determination of critical fiber length in short fiber carbon/carbon composites by double lap joint, Compos. Part B Eng. 54 (2013) 365–370. https://doi.org/10.1016/j.compositesb.2013.05.026.

[26] D.P. Ura, K. Berniak, U. Stachewicz, Critical length reinforcement in core-shell electrospun fibers using composite strategies, Compos. Sci.

Technol. 211 (2021) 108867. https://doi.org/10.1016/j.compscitech.2021.108867.

[27] S.Y. Fu, B. Lauke, Y.H. Zhang, Y.W. Mai, On the post-mortem fracture surface morphology of short fiber reinforced thermoplastics, Compos. Part A Appl. Sci. Manuf. 36 (2005) 987–994. https://doi.org/10.1016/j.compositesa.2004.11.005.

[28] D. Sciti, A. Natali Murri, V. Medri, L. Zoli, Continuous C fibre composites with a porous ZrB2 Matrix, Mater. Des. 85 (2015) 127–134. https://doi.org/10.1016/j.matdes.2015.06.136.

[29] L. Zoli, V. Medri, C. Melandri, D. Sciti, Continuous SiC fibers-ZrB2 composites, J. Eur. Ceram. Soc. 35 (2015) 4371–4376. https://doi.org/10.1016/J.JEURCERAMSOC.2015.08.008.

[30] D. Sciti, L. Pienti, A. Natali Murri, E. Landi, V. Medri, L. Zoli, From random chopped to oriented continuous SiC fibers-ZrB2 composites, Mater. Des. 63 (2014) 464–470. https://doi.org/10.1016/j.matdes.2014.06.037.

[31] L. Zoli, D. Sciti, Efficacy of a ZrB2–SiC matrix in protecting C fibres from oxidation in novel UHTCMC materials, Mater. Des. 113 (2017) 207–213. https://doi.org/10.1016/j.matdes.2016.09.104.

[32] A. Vinci, L. Zoli, D. Sciti, C. Melandri, S. Guicciardi, Understanding the mechanical properties of novel UHTCMCs through random forest and regression tree analysis, Mater. Des. 145 (2018) 97–107. https://doi.org/10.1016/j.matdes.2018.02.061.

[33] A. Vinci, L. Zoli, D. Sciti, Influence of SiC content on the oxidation of carbon fibre reinforced ZrB2/SiC composites at 1500 and 1650 °C in air, J. Eur. Ceram. Soc. 38 (2018) 3767–3776.

https://doi.org/10.1016/j.jeurceramsoc.2018.04.064.

[34] V. Medri, C. Capiani, D. Gardini, Slip Casting of ZrB2–SiC Composite Aqueous Suspensions, Adv. Eng. Mater. 12 (2010) 210–215. https://doi.org/10.1002/ADEM.200900275.

[35] E.D. Weil, Carbon fibers, 2nd edition by J. B. Donnet and R. C. Bansal, Marcel Dekker, New York (1990), ISBN 470 pp., price $150.00, Polym. Adv. Technol. 3 (1992) 47–47. https://doi.org/10.1002/PAT.1992.220030109.

[36] Y. Matsuhisa, A.R. Bunsell, Tensile failure of carbon fibers, Handb. Tensile Prop. Text. Tech. Fibres. (2009) 574–602. https://doi.org/10.1533/9781845696801.2.575.

[37] B.A. Newcomb, Processing, structure, and properties of carbon fibers, Compos. Part A Appl. Sci. Manuf. 91 (2016) 262–282. https://doi.org/10.1016/J.COMPOSITESA.2016.10.018.

[38] M.G. Huson, High-performance pitch-based carbon fibers, Struct. Prop. High-Performance Fibers. (2017) 31–78. https://doi.org/10.1016/B978-0-08-100550-7.00003-6.

[39] L.A. Loureiro dos Santos, Natural Polymeric Biomaterials: Processing and Properties, Ref. Modul. Mater. Sci. Mater. Eng. (2017). https://doi.org/10.1016/B978-0-12-803581-8.02253-0.

[40] J. Yin, H. Zhang, Y. Yan, Z. Huang, X. Liu, Y. Yang, D. Jiang, Hydrolysis behavior of zirconium diboride during attrition milling, Mater. Chem. Phys. 133 (2012) 8–15. https://doi.org/10.1016/J.MATCHEMPHYS.2011.11.004.

[41] A. Vinci, L. Silvestroni, N. Gilli, L. Zoli, D. Sciti, Advancements in carbon fibre reinforced ultra-refractory ceramic composites: Effect of

rare earth oxides addition, Compos. Part A Appl. Sci. Manuf. 156 (2022) 106858. https://doi.org/10.1016/J.COMPOSITESA.2022.106858.

[42] W.G. Fahrenholtz, G.E. Hilmas, I.G. Talmy, J.A. Zaykoski, Refractory diborides of zirconium and hafnium, J. Am. Ceram. Soc. 90 (2007) 1347–1364. https://doi.org/10.1111/j.1551-2916.2007.01583.x.

[43] C. Rubenstein, A General Theory of the Surface Friction of Solids, Proc. Phys. Soc. Sect. B. 69 (1956) 921–933. https://doi.org/10.1088/0370-1301/69/9/306.

[44] H. Zhang, Surface Characterization Techniques for Polyurethane Biomaterials, Elsevier Ltd, 2016. https://doi.org/10.1016/B978-0-08-100614-6.00002-0.

4. Manufacturing of layered, UHTCMCs using pliable, short fibre-reinforced ceramic sheets

4.1 Introduction

To improve the fracture properties of UHTCs, short or long carbon fibres can be added as reinforcement [1–5]. For this application, PAN-based carbon fibres or pitch-based carbon fibres can be used. PAN-based carbon fibres are good candidates because of their lower price, availability on the market and higher versatility in the manufacturing and shaping processes [6,7]. Pitch-based carbon fibres are attractive for their superior thermal conductivity, chemical stability and high elastic modulus [8]. Furthermore, pitch-based carbon fibres without coating in UHTC matrices proved to be able to bring forth intra-fibre pull-out during fracture [9]. Nowadays, short pitch-based fibre-reinforced ZrB_2 composites are gaining more interest in industries, especially owing to their convenient manufacturing process/low fabrication costs [10]. Moreover, short fibres are easy to adapt to conventional and new manufacturing techniques [11].

As mentioned before, there are several ways to introduce short fibres into a ceramic matrix based on the slurry techniques. Some of the most used are ball milling, colloidal process, and tape casting. However, each of them possesses pros and cons. For example, the ball milling process allows incorporation of high volumetric amount of fibres, but it causes fibres surface damage and reduction of the fibre length to few hundred micro-meters [12]. Moreover, fibres with a rough surface react strongly with matrix phase during sintering, increasing fibre-matrix interfacial bonding [3] which reduces fibre pull-out [4,5]. The colloidal process, instead, avoids the fibre damage but requires the use of organic solvents (e.g. ethanol) [13]. The tape casting process presents the same problems, in fact, a mixture of organic solvents (e.g. ethanol and butanol) and non-green surfactant are used. In addition, tape casting allows to add only a low amount of fibres, 10-15% vol. [14].

In this chapter, a new water-based free to organic solvent-process was designed to homogenously disperse short pitch-based carbon fibres in a ceramic matrix, maintaining their original dimension and minimizing fibre damage. This new route was conceived to prepare single sheets in the order of 100 µm thick with a tuneable fibre

content, between 0 and ≈ 100 % vol, and tuneable thickness. Green layers were overlapped and densified by hot pressing.

The microstructure and properties of individual samples with 20%-35%-50% fibre volumetric content and 3 mm or 5 mm long pitch-based carbon fibres, were analysed to understand the effect of fibre length and concentration. Moreover, the samples obtained via the new process were compared with composites processed by conventional ball milling processes.

4.2 New manufacturing route for short carbon fibre reinforced-UHTC composites

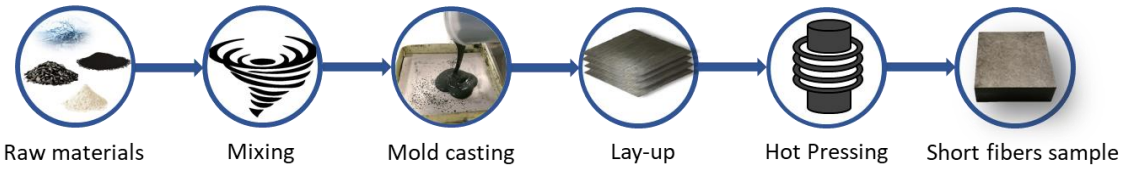

Fig. 4.1: Flow chart for the entire process: the starting materials are mixed and then cast into a mould to obtain fibre/powder sheets, and then hot pressing to produce the sintered pellet.

Samples with a different amount of short carbon fibre and different fibre length were fabricated via a new slurry casting-based process. The process flow chart was illustrated in Fig. 4.1. UHTC powder mixtures with compositions ZrB_2 – 90 vol. % SiC – 10 vol. % were prepared by wet ball milling and dried with a rotary evaporator. In the first step, raw materials, including UHTC powder mixture, chopped carbon fibres, water and sodium alginate dissolved in water, were gently mixed for a few minutes with a planetary centrifugal mixer (Thinky mixer are-500CE) exploiting the natural thickener as medium. Then, the resulting product was transferred into a mould where it was left to dry. The mould was made of gypsum in order to speed up the drying process and avoid possible material stratification. After that, the obtained stacked green layers underwent debonding in air at mild temperature (300 °C) for few hours in order to remove the biodegradable dispersant but avoid fibres damage. Lastly, a hot pressing cycle was carried out at 1900 °C and 30 MPa, similarly to previous studies [15–17] to obtain a good final densification. Samples with different contents and length of carbon fibres were made. (Table. 4.1).

The two mains points of this new method were the usage of sodium alginate as fibres dispersant and the use of the planetary centrifugal mixer that avoids damage to the fibres as it happens for the ball milling process [12]. More in detail, the planetary centrifugal mixer is a device that allows to mix materials without using blades and to simultaneously deaerate the resulting mixture. To obtain these effects three factors were used (Fig. 4.2). Firstly, a revolution effect that helps to move the material away from the centre thanks to the centrifugal force. Secondly, rotation of the container that causes flow of the material (rotation and shearing). Lastly, the tilting of 45 ° that allows to achieve a three-dimensional flow.

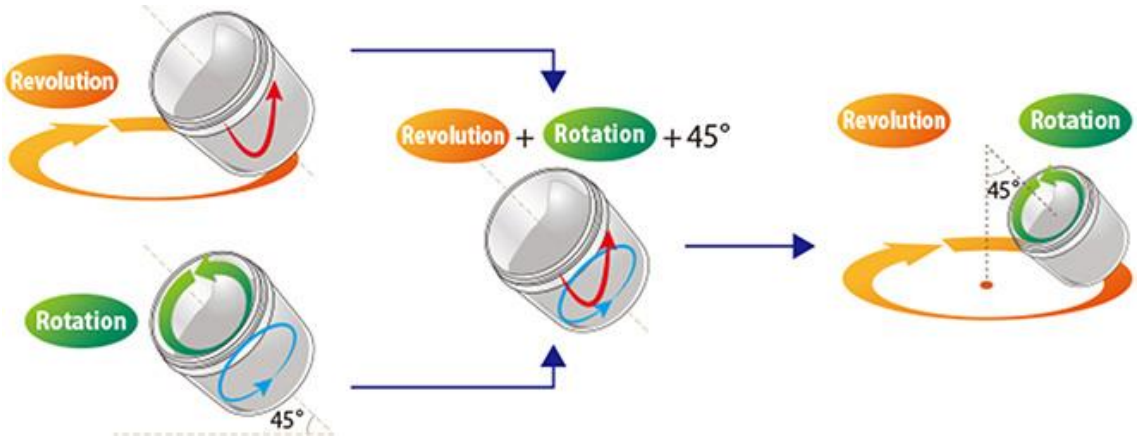

Fig. 4.2: Schematic representation of the mixing mechanism [18]

Moreover, the flow speed and direction changes suddenly between the container and the liquid surface, generating complicated flow and strong shearing forces. These shearing forces allow to obtain droplets and smaller particles, increasing their dispersibility. At the same time, the same effect is visible on air bubbles that are also finely dispersed. In this way it is possible to uniformly mix even high-viscosity materials (as were our composition with a high amount of fibres) in a short time (some minutes) without using agitator blades that could damage the carbon fibres. Moreover, the thinky mixer (are-500CE) possess a “deaeration mode” that can remove bubbles of several hundred microns. Deaeration takes place by changing the balance between revolution speed and rotation speed because the “centrifugal force due to revolution” forces light bubbles to the liquid surface and applying a slow rotation bubbles that have risen to the liquid surface are destroyed by shearing forces [18].

In this chapter samples with the same matrix were investigated. However, one of the most important advantages of this method was the possibility to use every kind of different matrix composition only changing the amount of sodium alginate in order to obtain a good fibre homogenization.

Table. 4.1: Contents and length of carbon fibres in the samples, theorical density, experimental density and relative density.

Sample	Fibres (% vol)	Fibres length (mm)	ρ_{exp} (g/cm^3)	ρ_{teo} (g/cm^3)	ρ_{rel} (%)
Z3-20	20	3	4.4	5.0	88
Z3-35	35	3	4.1	4.4	91
Z3-50	50	3	3.8	3.9	96
Z5-35	35	5	4.1	4.4	95

4.3 Morphologies and microstructure

4.3.1 Characteristics of the fibre sheet

The microstructure was analysed on polished and fractured surfaces with a field emission scanning electron microscopy (FE-SEM, Carl Zeiss Sigma NTS Gmbh Öberkochen, Germany). SEM analysis of the mixed powder/fibres ("green" sample) confirmed that the fibres were not visibly damaged during the mixing process with a planetary centrifugal mixer and maintained their original length. More in detail, in Fig. 4.3, the difference between the fibres after the milling process (Fig. 4.3-a) and after the new process described in this chapter (Fig. 4.3-b) is visible. The fibres subjected to ball milling showed a non-round cross section with a damaged surface and a high roughness. These characteristics decrease the mechanical properties of the fibre and increase the chemical reactivity between the matrix and the fibre surface, thus leading to a strong interface between them. A completely different situation was presented for the fibre subjected to the new process. In this case, the fibres maintained their round shape and a non-damaged surface with a low roughness.

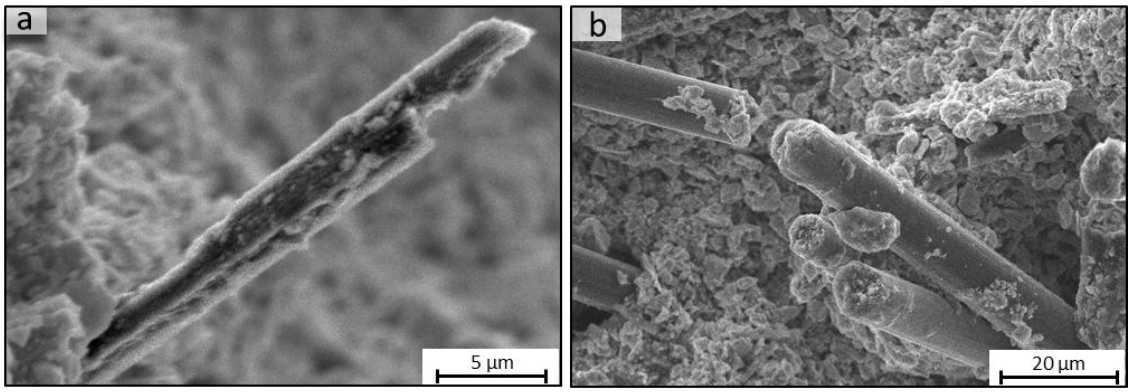

Fig. 4.3: Carbon fibre morphologies: (a) green body obtained with ball milling process; (b) green body obtained with the new process here described.

The slurry obtained after the mixing step was homogeneous and easily transferable in the mould. This allowed to obtain sheets without defects, such as bubbles or non-homogeneous parts (Fig. 4.4-a,b) also thanks to the mixing system as previously explained. An important characteristic of these sheets was their flexibility, which allowed to bend and fold the sheets at an angle of 180° with a radius of curvature of 5 mm, thanks to which it was possible to prepare near net shaped samples, as for example a wavy shape, see Fig. 4.4-c. Another important property is their low thickness, measuring around 150-200 µm in the green state, tuneable up to few millimetres that allowed to minimize the defect in the final samples.

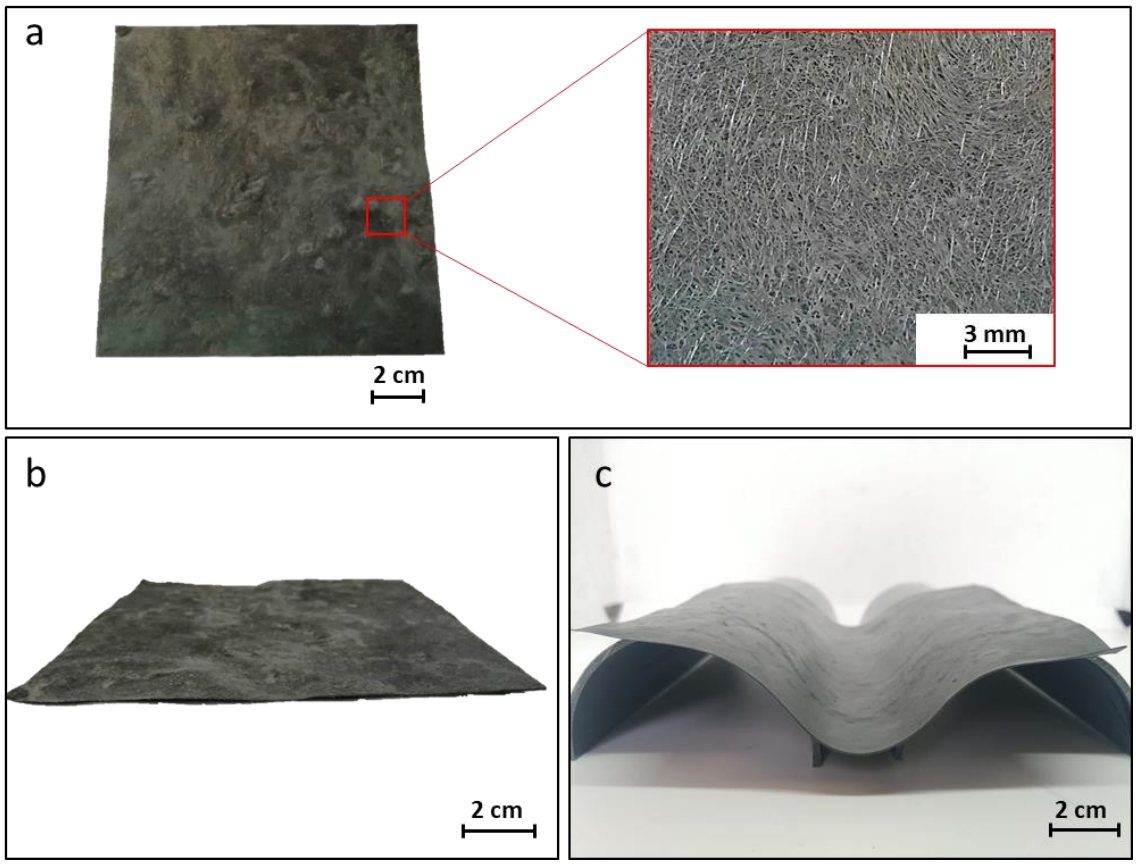

Fig. 4.4: Green sheet morphologies: (a) top view; (b) side view; (c) flexibility.

4.3.2 Tensile properties of individual sheets in the "green" state

The room temperature tensile stress values of the green sheets obtained through the new process explained in Chapter 4 are summarized in Table 4.2 and represented in Fig. 4.6. More in detail, four different types of green samples were investigated and for each of them at least three samples were tested:

a) Dog-bone specimens composed of a single layer of short carbon fibres and sodium alginate (Cf-green)

b) Dog-bone specimens composed of a single layer of ZrB_2 based slurry reinforced with 40 vol. % of short carbon fibre (Monolayer).

c) Dog-bones specimens composed of two overlapped layers of ZrB_2 based slurry reinforced with 40 vol. % of short carbon fibre (Doublelayer).

d) Dog-bones specimens composed of two overlapped layers of ZrB_2 based slurry reinforced with 40 vol. % of short carbon fibre press together through a cold isostatic press (Doublelayer CIP).

The images of the dog-bones specimens and they are reported in Fig. 4.5.

Fig. 4.5: images of the dog-bones Cf-Green and Monolayer (left) and a dog-bones during the test (right).

Table. 4.2: Tensile values of the green samples

Label	Sample features	σ (MPa)
A	Cf-Green	3.2 ± 0.8
B	ZrB2 – SiC + Cf, Monolayer	2.4 ± 0.1
C	ZrB2 – SiC + Cf, Doublelayer	2.2 ± 0.4
D	ZrB2 – SiC + Cf, Doublelayer CIP	1.5 ± 0.2

The green sample made just with carbon fibres and sodium alginate (A) presented the highest value of tensile strength ≈ 3.2MPa. This result could be attributed to the high amount of carbon fibres (100 vol. %) that intertwine with each other and the glue effect of the sodium alginate. Sample B, with fibre and slurry, showed a value of ≈ 2.4MPa. This decrease was probably due to the lower amount of fibre incorporated in B sheets. It is interesting to note that the value obtained for sample C, ≈ 2.3 MPa, was similar to the sample composed of only one green sheet (B). This indicated that no interaction between the green sheets was present during the overlapping and the mechanical properties did not

improve. A lower value was observed for sample D, ≈ 1.5 MPa, that was cold isostatically pressed. This indicates that a pressure applied on the sample to improve the interaction between the layers negatively affected the tensile properties probably because the fibres were damaged reducing their reinforcement effect.

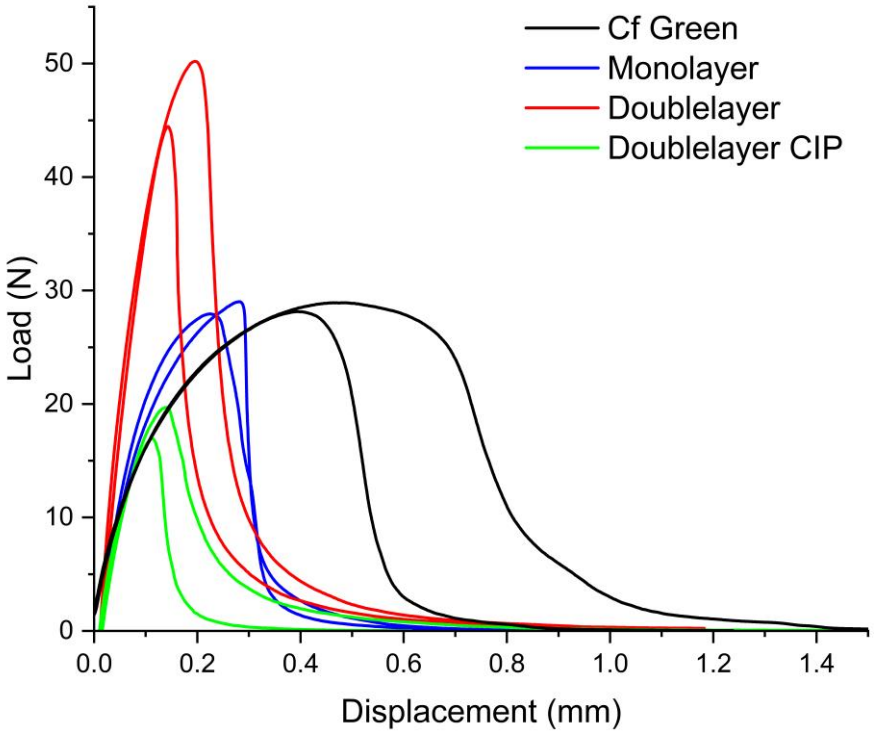

Fig. 4.6: Load displacement curves for the tensile tests of different green samples.

The values obtained for the different samples resulted interesting and indicated a good physical stability for the green sheets. This feature is important for manipulating the sheets and shaping them into complex shapes that require bending or folding.

4.3.3 Morphologies and microstructure of sintered samples

Fig. 4.7 is an illustration of the microstructure of the samples after hot-pressing at 1950 °C under a pressure of 30 MPa. The composites exhibited an anisotropic microstructure. Most of the fibres were aligned in the XY plane, perpendicular to the pressing direction, Z-axis. Since the fibres in each layer were in the order of the mm, and the layer was just 200 micron, the fibres were rather aligned in the XY plane, a feature that was further enhanced by the application of pressure during sintering [12,19]. The

original layers were no longer distinguishable in the final product, thanks to the good adhesion and low thickness of the layers.

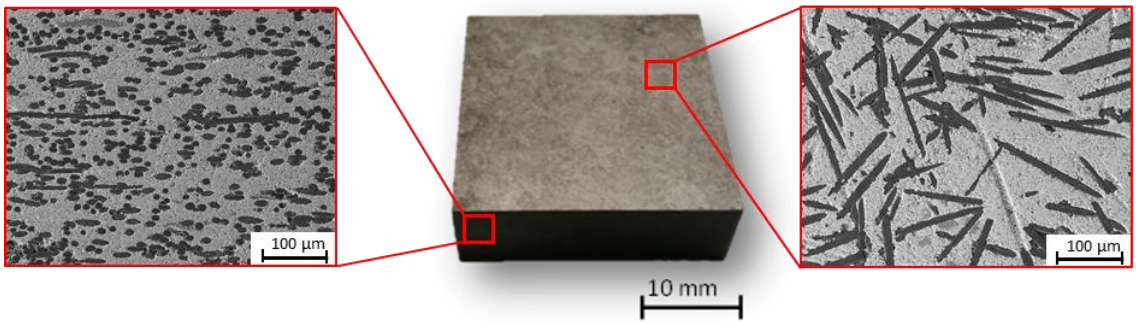

Fig. 4.7: Macro and micro images for Z5-35.

Despite the better alignment compared to the ball milling technique, the mechanical pressure application caused some fibre breakage and reduced the effective length from 3 mm to 1.5 mm (as visible in the Fig 4.8), still much longer compared to milled fibre process, 250-400 µm [10]. These measurements were carried out on the longest fibres observed on the surface in order to qualitatively assess the minimum degree of fibre damage that was around 50%. It can be hypothesized that the average degree of fibre damage is much higher than this figure, but nonetheless lower than specimens reinforced with ball milled fibres. This difference in the final fibre length due to the different process would affect the final mechanical properties. Indeed, previous studies [20] demonstrated that a double increase in the fibre length significantly improved the final properties of the sample.

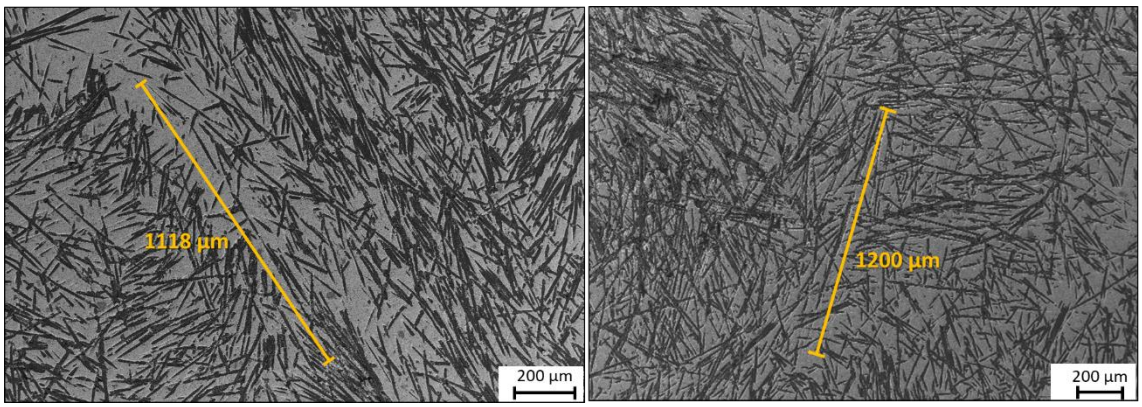

Fig. 4.8: Top view of the fibre length in the sample Z3-50

The investigation of the matrix composition, Fig. 4.9, allowed to obtain information on the sintering mechanism. The ZrB_2 grain dimensions suggested dissolution and re-precipitation mechanisms as indicated in previous studies [22]. Y_2O_3 formed liquid phases with the oxide impurities present on the boride and carbide particles. This resulted in the strengthening of grain boundaries [21]. Minor additional Y-B-C-O phases with lamellar structure were observed, in agreement with previous results [22]. They were likely originated from the reduction of the impurities, Y_2O_3 and B_2O_3 with the carbon of the fibres [23,24],[25], (Fig. 4.7).

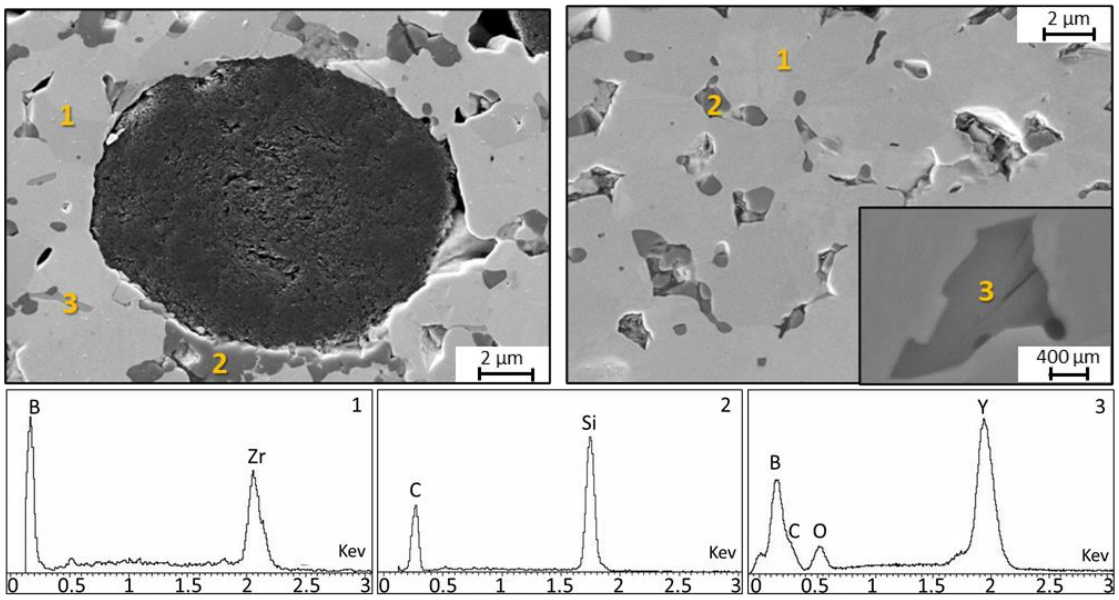

Fig. 4.9: High magnification SEM images of UHTC matrix showing the Y-B-C-O phases with EDS spectra collected at 5 KeV. The light and dark grey phases are ZrB_2 (1) and SiC (2) respectively, the white particles are ZrC. Occasionally, Y-B-C-O phases (3) were observed near SiC particles.

As mentioned before, among the many advantages of the new method developed in this work, were a homogeneous fibres distribution and absence of debris, Fig. 4.10. This indicates that the process limits fibres damage and improves their dispersion. Moreover, from the fibre regions, no evidence of a strong chemical reaction between fibre and matrix was found. Indeed, the fibres maintained their original shape (Fig. 4.10-b-d-f-h). In contrast, the ball milling process caused abrasion of the fibre external surface, thus promoting the reactivity between the fibre and the matrix and reducing the final properties of the material [3,26]. In Fig. 4.10-b-d-f-h the different matrices are visible. In all the

samples SiC particles showed no sign of coarsening, retaining their original particle size < 0.45 μm, and only occasionally were found as aggregates. At the same time, ZrB_2 particles had a mean grain size around 2-4 μm. Samples Z3-20 and Z3-35 presented visible holes on the surface and these defects decreased the density of the samples down to around 88 – 91%. On the contrary, samples Z3-50 and Z5-35 were nearly fully dense, density of 96 -95% respectively. This difference in porosity between the samples was attributed to the variance of experimental conditions like the debonding temperature that may have damaged the fibres in a different way.

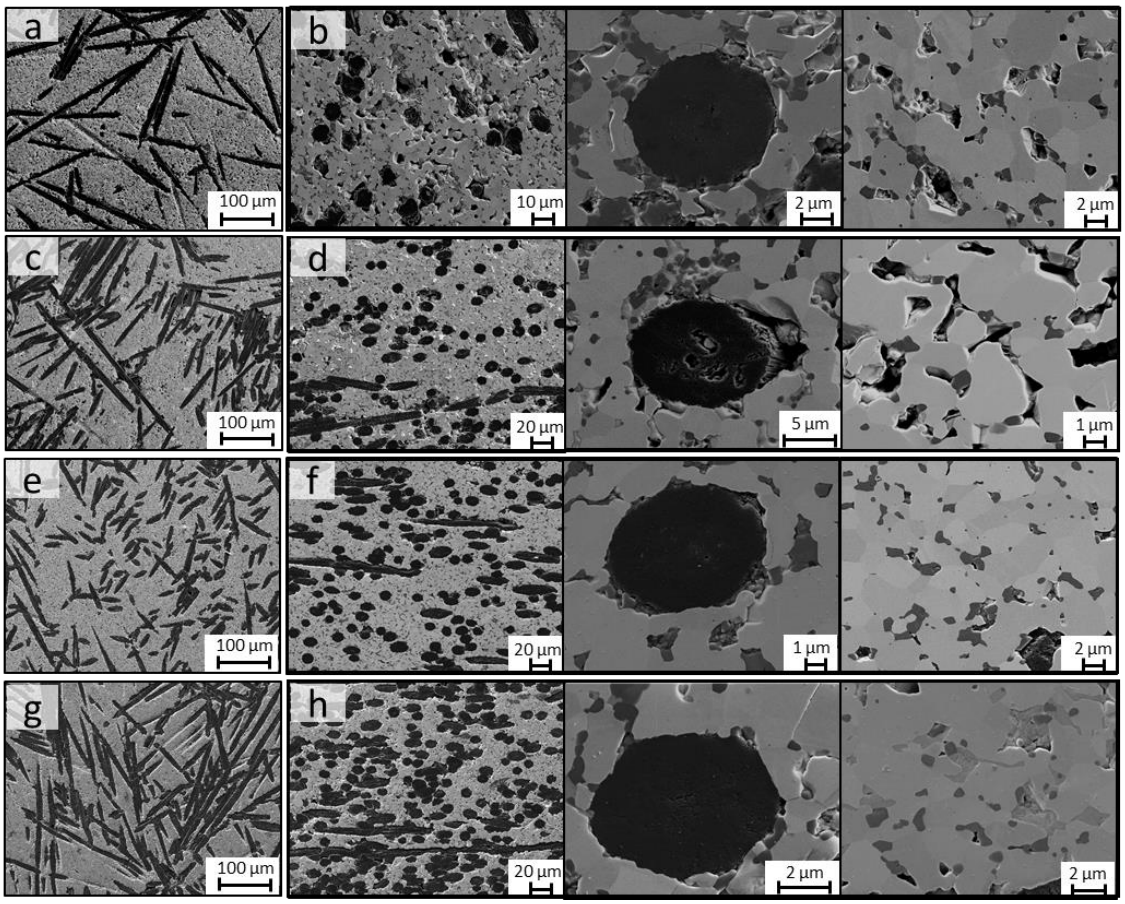

Fig. 4.10: Surface morphologies. Sample Z3-20: (a) X-Y plane; (b) X-Z plane; Sample Z3-35: (c) X-Y plane; (d) X-Z plane; Sample Z3-50: (e) X-Y plane; (f) X-Z plane; Sample Z5-35 (g) X-Y plane; (h) X-Z plane.

4.4 Mechanical properties

In Table. 4.3 room temperature strength and fracture toughness of the fabricated samples were reported. As reported in literature the bending strength of fibre-reinforced

UHTC composites was found to be lower than the corresponding bulk ceramics [3]. However, for fibre contents above a certain threshold (> 50 vol. %), a relative increase of the flexural strength was registered, but this value was still lower than the bulk ceramic. This suggests that there is still a minimum fibre amount necessary to improve the mechanical properties, especially the fracture toughness, even though the original strength of the bulk ceramic cannot be recovered. Similar results were also reported in the works of Yang et al. [27] and Sha et al. [28], which showed a decrease of flexural strength of about 11% and 21%, respectively, by adding 20 vol% of short carbon fibre.

Samples with a lower amount of fibres, Z3-20, Z3-35 (20-35%) had a value of strength of 117 MPa and 111 MPa, respectively, and an elastic deformation typical of ceramic samples. With 50% of fibres, the strength was 141 MPa and the load/displacement was divided in two parts. The first part had a constant slope (linear elastic behaviour), while the second part showed a decrease of stiffness. Correspondingly, the strength at the proportional limit (determined by the best fit of the linear portion of the load/displacement curves with $R^2 > 0.995$) was 94.5 MPa and the ultimate strength was 141 MPa.

Moreover, the load/displacement curve of sample Z3-50 showed the highest displacement. No difference in bending strength was observed among samples with the same amount of fibres but different length, suggesting that a slight difference in the fibre length does not affect this property. To achieve high strength in a composite material, a fundamental parameter is the load transfer between matrix and reinforcement (fibres in our case). In order to have an efficient load transfer, the Young's modulus of the fibre needed to be higher than that of the matrix [29]. Low modulus carbon fibres are not ideal to reinforce UHTC matrices with moduli of 500 GPa due to the inefficient load transfer, while in our case, the use of high modulus carbon fibres (E = 780 GPa) allowed a more efficient load transfer since the difference in moduli is > 50%. An interesting comparison can be made between the samples described above and the samples obtained via ball milling in precedent works. The samples were constituted by the same matrix and a similar amount of carbon fibres, 46 vol% (labelled Milled-46, Table. 4.2) [30]. In this case, due to the highly damaged fibres and strong interaction between fibre and matrix, the flexural strength was lower for the sample obtained via ball milling compared with

the samples presented in this chapter reinforced with the same amount of carbon fibres, ≈ 100 MPa and ≈ 140 MPa, respectively.

Table. 4.3: Mechanical properties of the samples and a reference material with milled fibres, labelled Milled-46

Sample	ρ (g/cm^3)	Porosity (vol%)	σ (MPa)	K_{Ic} ($MPa \cdot m^{0,5}$)	y_{WOF} (J/m^2)	Pull-out (µm)	HV1 (GPa)
Z3-20	4.4	12	117 ± 31	3.0 ± 0.5	108 ± 6	57.40	≈3.6 ± 0.2
Z3-35	4.1	9	111 ± 12	3.0 ± 0.2	121 ± 7	52.23	≈3.4 ± 0.1
Z3-50	3.8	4	141 ± 14	4.0 ± 0.1	253 ± 30	56.40	≈3.8 ± 0.3
Z5-35	4.1	5	107 ± 13	3.6 ± 0.2	183 ± 38	58.22	≈5.4 ± 1.7
Milled-46 [30]	3.4	15	103 ± 3	2.4	160-180	-	-

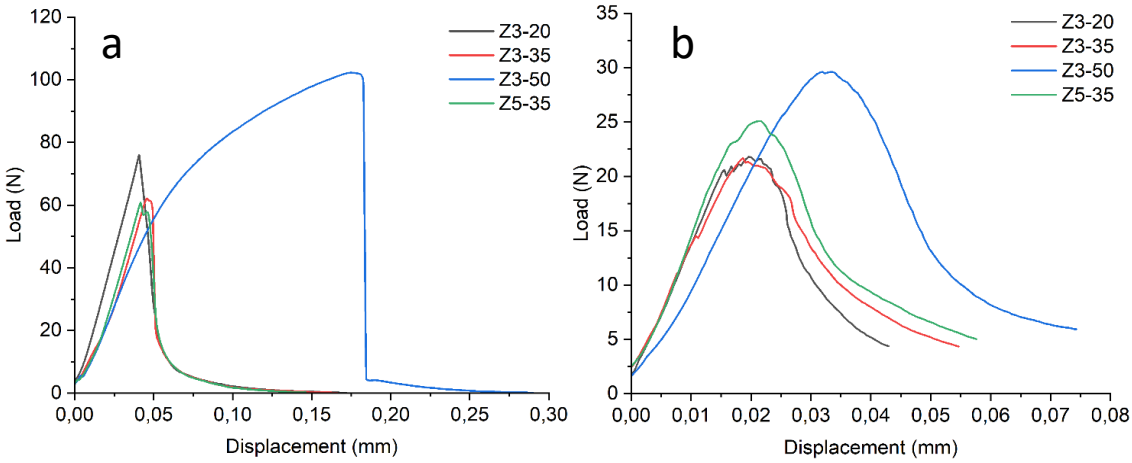

Fig. 4.11: (a) Load displacement curves for the 4-point flexural strength of samples; (b) Load displacement curves for fracture toughness of samples (CNB).

The test made on the samples showed values of fracture toughness that ranged from 3 to 4 $MPa \cdot m^{0.5}$. The load-displacement curves (Fig. 4.11-b) showed an increase in K_{Ic} for the samples with an amount of fibre ≥50 vol. % compared with the samples reinforced with

< 35 vol. %. This indicated that an increase in the fibre volumetric content introduced effective obstacles to the crack propagation. As a consequence, the composite was toughened. Moreover, in the load-displacement curves recorded during the fracture toughness test it was evident how all samples were characterized by similar mechanical behaviours indicated by the similar trends. During the crack propagation, the fibres were pulled out from the matrix, which contributed to increasing the energy required for the crack to propagate [31]. In detail, in the fibre bridging phenomenon, the fibres of adjacent plies acted as bridges in the crack and prevented it from propagating. As a consequence, this could have reduced the stress intensity at the crack tip and applied a tensile force on the opposite fracture faces which halted the crack opening.

To better evaluate the mechanical properties, the work of fracture was calculated starting from the fracture toughness results by using the following equation:

$$\gamma_{WOF} = \frac{W}{2A}$$

Where W is the integral area of the load/displacement curve and A is the notch-less cross section of the samples. The values of work of fractures are reported in Table. 4.2, and showed an increase in the properties for the samples with 5 mm long carbon fibre compared to the samples with 3 mm long carbon fibre, indicating that the carbon fibre length in the mechanical properties could affect work of fracture value. The fracture toughness (CNB tests) and work of fracture can be used both for the characterization of toughness. However, there are some differences between them. Fracture toughness represents the critical stress intensity at peak load, while work of fracture measures the average fracture energy relative to the whole propagating process of a crack [28,32]. So, an increase in fibre length consumed more fracture energy, as indicated by the high work of fracture for the samples with carbon fibre of 5 mm compared to samples with fibre of 3 mm. This is in accordance with what we expected. In fact, a lengthy path is required with a longer fibre, so it becomes more difficult for the crack to go around the fibre itself. By this way, the resistance to crack propagation was improved. This effect was clearly visible when comparing Z3-50 with milled-46. In fact, the ball milling process decreased the length of the fibre, from 3 mm to 250-400 μm, and this reduced drastically the work of fracture from 253 to ≈ 180 J/m^2.

To investigate the composites hardness, indentations tests were collected both on the samples surface and core with similar results. The values obtained were in range of 3.6-5.4 GPa. The lowest values were found for the samples Z3-20 and Z3-35 due to their matrix porosity (Table. 4.3). Instead, for the sample Z3-50, the low value of hardness came from the contribution of carbon fibres that possess a lower hardness compared to the matrix composition. However, the indentations tests collected provided only an approximation on the hardness of the composites because the elasticity of carbon fibres avoided to obtain an indentation with defined contours, making the measurement difficult and not fully accurate.

4.5 Fracture surface

Fig. 4.12 shows the morphologies of the fracture surface of samples Z3-20, Z3-35 and Z3-50 after bending strength tests. For all the samples, the fractured fibres can be seen clearly. Moreover, in all the specimens, a well visible fibre pull-out was observed. In general, the strong interfacial bonding in ceramic matrix composites would result in a brittle fracture. In these samples, very low interaction between fibres and matrix was observed Fig. 4.12-b-d-f, indeed the fibres maintained their round shapes which resulted in extensive pull-out. It was possible to suppose that when the crack propagated, fibres detached from the matrix and acted as bridges. This happened when the strength of the fibre/matrix interface was lower than the applied stress, resulting in the premature detachment of the fibre from the matrix [33].

The interaction of the fibre–matrix bond strength affected the mechanical properties. Indeed, its value influenced the critical fibre length which is an important parameter for short carbon fibre composites [34]. The critical fibre length is typically calculated in literature by using the following equation [35]:

$$l_c = \frac{\sigma_f D_f}{2\tau_c}$$

Where σ_f is the tensile strength of fibre, $D_f$is fibre diameter and τ_c is the fibre–matrix bond strength. However, this method requires an in-depth study and the measurement of many experimental parameters. Previous studies [36] developed an easier and more direct method to determine the critical fibre length. According to this method, the average of all pulled-out fibres is determined first (which may vary between 0 and half of the critical

length) and then the average is multiplied by 4 to obtain the critical fibre length. On the basis of image analysis and with the above-mentioned method, the critical length for our samples measured around 230 μm for every sample (Table. 4.2). In principle, the fibre length in the sample would be enough to improve the mechanical properties; however, due to the random fibre distribution, only a small fraction of the fibres was effective as a reinforcement. In a previously published work it was shown that in a material reinforced with randomly orientated chopped fibre, the strength measured along the fibre orientation was 50% higher [37]. No visible differences in the pull-out were found between the samples with a different amount of fibre, 20-35-50% vol. They presented the same pull-out length, fibre dimension and shape, Fig. 4.12. Moreover, the same behaviour was visible in the samples Z3-35 and Z5-35, where the fibre length is 3 and 5 mm respectively, suggesting that the length of the fibre did not affect the pull-out. However, the difference in length between the fibres in our tests was low. For this reason, new tests with longer fibres (i.e. 10-15 mm) should be carried out.

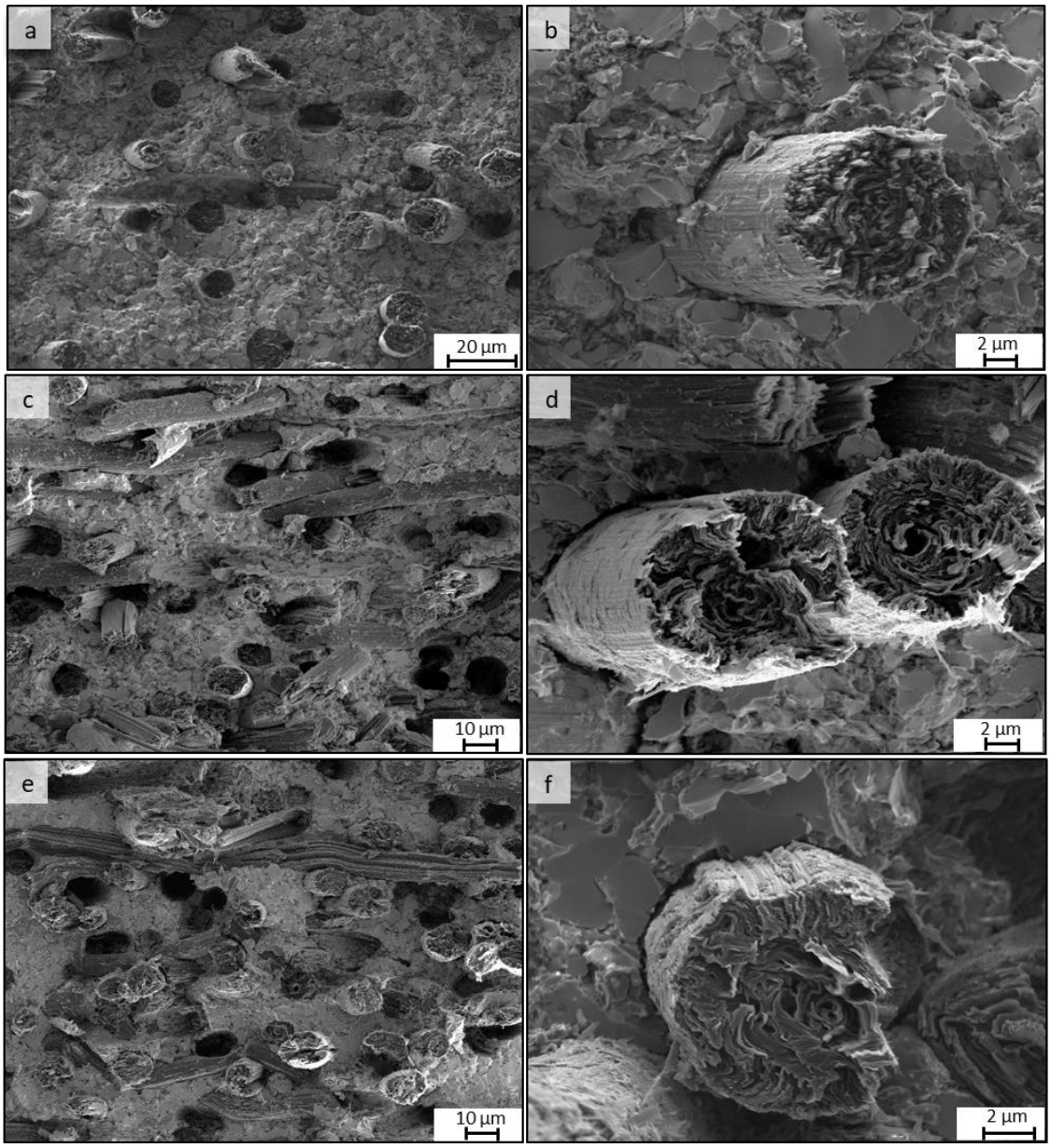

Fig. 4.12: (a-b) Fracture surface after bending test of samples with 20% vol Cf-3 mm; (c-d) Fracture surface after bending test of samples with 35% vol Cf-3 mm; (e-f) Fracture surface after bending test of samples with 50% vol Cf-3 mm.

4.6 Conclusions

Short carbon fibre reinforced ZrB_2 /SiC composites with varying fibre contents were produced with a novel free of organic solvent- process. These samples were obtained by stacking short fibre reinforced sheets with different fibre content. This new process can avoid fibre agglomeration and fibre damage, typical of the ball milling process, thanks to the mixing method used. The low thickness of the sheets, combined with sintering by hot pressing, allowed to minimize the structural defects in the final material. Moreover,

the distribution of fibres in the matrix was homogeneous both with the addition of low or high volumes of fibres. This characteristic was made possible thanks to the sodium alginate used as dispersant that with its high viscosity kept the fibres in suspension, avoiding agglomeration. The presence of a leftover carbon film, originated from the debonding process, prevented fibre damage during the sintering step. In fact, this film acted as sacrificial material and reacted with the matrix instead of the fibres. Increasing the amount of carbon fibres past a certain threshold (50 vol%) led to a significant improvement of the mechanical properties, especially the fracture toughness. However, the flexural strength remained lower than the bulk material for all the fibres reinforced samples. Finally, increasing the fibres length did not show any enhancement in the flexural strength but some improvement was observed in the work of fracture.

One of the main advantages of the new process was the possibility to extend it to other types of ceramic matrices or fibres. Moreover, the flexibility of the sheets opens the possibility of producing samples with complex shapes.

4.7 References

[1] Z. Balak, M. Zakeri, M. Rahimipour, E. Salahi, Taguchi design and hardness optimization of ZrB2-based composites reinforced with chopped carbon fiber and different additives and prepared by SPS, J. Alloys Compd. 639 (2015) 617–625. https://doi.org/10.1016/j.jallcom.2015.03.131.

[2] F. Yang, X. Zhang, J. Han, S. Du, Characterization of hot-pressed short carbon fiber reinforced ZrB2-SiC ultra-high temperature ceramic composites, J. Alloys Compd. 472 (2009) 395–399. https://doi.org/10.1016/j.jallcom.2008.04.092.

[3] Z. Nasiri, M. Mashhadi, A. Abdollahi, Effect of short carbon fiber addition on pressureless densification and mechanical properties of ZrB2-SiC-Csf nanocomposite, Int. J. Refract. Met. Hard Mater. 51 (2015) 216–223. https://doi.org/10.1016/j.ijrmhm.2015.04.005.

[4] D. Sciti, S. Guicciardi, L. Silvestroni, Are short Hi-Nicalon SiC fibers a secondary or a toughening phase for ultra-high temperature ceramics?, Mater. Des. 55 (2014) 821–829. https://doi.org/10.1016/j.matdes.2013.10.019.

[5] J. Lin, X. Zhang, W. Han, D. Sun, Influence of milling time on the synthesis, microstructure and mechanical properties of ZrB2SiCZrO2f ceramic composites, Ceram. Int. 39 (2013) 4213–4219. https://doi.org/10.1016/j.ceramint.2012.11.003.

[6] D. Zhang, P. Hu, S. Dong, Q. Qu, X. Zhang, Effect of pyrolytic carbon coating on the microstructure and fracture behavior of the Cf/ZrB2-SiC composite, Ceram. Int. 44 (2018) 19612–19618. https://doi.org/10.1016/j.ceramint.2018.07.210.

[7] C. Fellah, J. Braun, C. Sauder, F. Sirotti, M.H. Berger, Influence of the carbon interface on the mechanical behavior of SiC/SiC composites, Compos. Part A Appl. Sci. Manuf. 133 (2020). https://doi.org/10.1016/j.compositesa.2020.105867.

[8] Y. Huang, R.J. Young, Effect of fibre microstructure upon the modulus of PAN- and pitch-based carbon fibres, Carbon N. Y. 33 (1995) 97–107. https://doi.org/10.1016/0008-6223(94)00109-D.

[9] P. Galizia, S. Failla, L. Zoli, D. Sciti, Tough salami-inspired Cf/ZrB2 UHTCMCs produced by electrophoretic deposition, J. Eur. Ceram. Soc. 38 (2018) 403–409. https://doi.org/10.1016/j.jeurceramsoc.2017.09.047.

[10] F. De Bianchi, S.A. Ponnusami, L. Silvestroni, A.M. Grande, Thermo-elastic properties in short fibre reinforced ultra-high temperature ceramic matrix composites: Characterisation and numerical assessment, Mater. Today Commun. 29 (2021) 102754. https://doi.org/10.1016/j.mtcomm.2021.102754.

[11] X. He, Y. Zhou, D. Jia, Y. Guo, Effect of sintering additives on microstructures and mechanical properties of short-carbon-fiber-reinforced SiC composites prepared by precursor pyrolysis–hot pressing, Ceram. Int. 32 (2006) 929–934. https://doi.org/10.1016/J.CERAMINT.2005.07.007.

[12] L. Pienti, D. Sciti, L. Silvestroni, S. Guicciardi, Effect of milling on the

mechanical properties of chopped SiC fiber-reinforced ZrB2, Materials (Basel). 6 (2013) 1980–1993. https://doi.org/10.3390/ma6051980.

[13] J.J. Sha, J. Li, S.H. Wang, Z.F. Zhang, Y.F. Zu, S. Flauder, W. Krenkel, Improved microstructure and fracture properties of short carbon fiber-toughened ZrB2-based UHTC composites via colloidal process, Int. J. Refract. Met. Hard Mater. 60 (2016) 68–74. https://doi.org/10.1016/j.ijrmhm.2016.07.010.

[14] W.S. Yang, S. Biamino, E. Padovano, L. Fuso, M. Pavese, S. Marchisio, D. Vasquez, C. Vega Bolivar, P. Fino, C. Badini, Microstructure and mechanical properties of short carbon fibre/SiC multilayer composites prepared by tape casting, Compos. Sci. Technol. 72 (2012) 675–680. https://doi.org/10.1016/j.compscitech.2012.01.014.

[15] D. Sciti, A. Natali Murri, V. Medri, L. Zoli, Continuous C fibre composites with a porous ZrB2 Matrix, Mater. Des. 85 (2015) 127–134. https://doi.org/10.1016/j.matdes.2015.06.136.

[16] D. Sciti, P. Galizia, T. Reimer, A. Schoberth, C.F. Gutiérrez-Gonzalez, L. Silvestroni, A. Vinci, L. Zoli, Properties of large scale ultra-high temperature ceramic matrix composites made by filament winding and spark plasma sintering, Compos. Part B Eng. 216 (2021) 108839. https://doi.org/10.1016/j.compositesb.2021.108839.

[17] D. Sciti, L. Zoli, T. Reimer, A. Vinci, P. Galizia, A systematic approach for horizontal and vertical scale up of sintered Ultra-High Temperature Ceramic Matrix Composites for aerospace – Advances and perspectives, Compos. Part B Eng. 234 (2022) 109709. https://doi.org/10.1016/J.COMPOSITESB.2022.109709.

[18] Principal of “Planetary Centrifugal System” | The global standard for mixing, defoaming, dispersing, and pulverizing THINKY CORPORATION, (n.d.). https://www.thinkymixer.com/en-gl/planetary-centrifugal-system/ (accessed November 21, 2022).

[19] H. Tang, X. Zeng, X. Xiong, L. Li, Jizhao Zou, Mechanical and tribological properties of short-fiber-reinforced SiC composites, Tribol. Int. 42 (2009) 823–827. https://doi.org/10.1016/j.triboint.2008.10.017.

[20] C. Capela, S.E. Oliveira, J. Pestana, J.A.M. Ferreira, Effect of fiber length on the mechanical properties of high dosage carbon reinforced, Procedia Struct. Integr. 5 (2017) 539–546. https://doi.org/10.1016/J.PROSTR.2017.07.159.

[21] X. Zhang, X. Li, J. Han, W. Han, C. Hong, Effects of Y2O3 on microstructure and mechanical properties of ZrB2-SiC ceramics, J. Alloys Compd. 465 (2008) 506–511. https://doi.org/10.1016/j.jallcom.2007.10.137.

[22] A. Vinci, L. Zoli, L. Silvestroni, N. Gilli, D. Sciti, Synthesis, microstructure and mechanical properties of lamellar YB2C2 – based ultra-high temperature ceramic composites, J. Eur. Ceram. Soc. 43 (2023) 831–841. https://doi.org/10.1016/J.JEURCERAMSOC.2022.10.072.

[23] G. Zhao, J. Chen, Y. Li, M. Li, YB2C2: A machinable layered ternary ceramic

with excellent damage tolerance, Scr. Mater. 124 (2016) 86–89. https://doi.org/10.1016/j.scriptamat.2016.06.041.

[24] Y. Zhou, H. Xiang, X. Wang, W. Sun, F.Z. Dai, Z. Feng, Electronic structure and mechanical properties of layered compound YB2C2: A promising precursor for making two dimensional (2D) B2C2 nets, J. Mater. Sci. Technol. 33 (2017) 1044–1054. https://doi.org/10.1016/j.jmst.2016.09.028.

[25] A. Vinci, L. Zoli, P. Galizia, D. Sciti, Influence of Y2O3 addition on the mechanical and oxidation behaviour of carbon fibre reinforced ZrB2/SiC composites, J. Eur. Ceram. Soc. 40 (2020) 5067–5075. https://doi.org/10.1016/j.jeurceramsoc.2020.06.043.

[26] D. Sciti, L. Silvestroni, G. Saccone, D. Alfano, Effect of different sintering aids on thermo-mechanical properties and oxidation of SiC fibers - Reinforced ZrB2 composites, Mater. Chem. Phys. 137 (2013) 834–842. https://doi.org/10.1016/j.matchemphys.2012.09.071.

[27] F. Yang, X. Zhang, J. Han, S. Du, Mechanical properties of short carbon fiber reinforced ZrB2-SiC ceramic matrix composites, Mater. Lett. 62 (2008) 2925–2927. https://doi.org/10.1016/j.matlet.2008.01.076.

[28] J.J. Sha, J. Li, S.H. Wang, Y.C. Wang, Z.F. Zhang, J.X. Dai, Toughening effect of short carbon fibers in the ZrB2-ZrSi2 ceramic composites, Mater. Des. 75 (2015) 160–165. https://doi.org/10.1016/j.matdes.2015.03.006.

[29] L. Silvestroni, D. Sciti, G.E. Hilmas, W.G. Fahrenholtz, J. Watts, Effect of a weak fiber interface coating in ZrB2 reinforced with long SiC fibers, Mater. Des. 88 (2015) 610–618. https://doi.org/10.1016/j.matdes.2015.08.105.

[30] D. Sciti, L. Zoli, L. Silvestroni, A. Cecere, G.D. Di Martino, R. Savino, Design, fabrication and high velocity oxy-fuel torch tests of a Cf-ZrB2- fiber nozzle to evaluate its potential in rocket motors, Mater. Des. 109 (2016) 709–717. https://doi.org/10.1016/j.matdes.2016.07.090.

[31] R. Khan, Fiber bridging in composite laminates: A literature review, Compos. Struct. 229 (2019). https://doi.org/10.1016/j.compstruct.2019.111418.

[32] J.J. Sha, J. Li, Z.Z. Lv, S.H. Wang, Z.F. Zhang, Y.F. Zu, S. Flauder, W. Krenkel, ZrB2-based composites toughened by as-received and heat-treated short carbon fibers, J. Eur. Ceram. Soc. 37 (2017) 549–558. https://doi.org/10.1016/j.jeurceramsoc.2016.09.012.

[33] J.W. Hutchinson, H.M. Jensen, Models of fiber debonding and pullout in brittle composites with friction, Mech. Mater. 9 (1990) 139–163. https://doi.org/10.1016/0167-6636(90)90037-G.

[34] D. Heim, M. Hartmann, J. Neumayer, C. Klotz, Ö. Ahmet-Tsaous, S. Zaremba, K. Drechsler, Novel method for determination of critical fiber length in short fiber carbon/carbon composites by double lap joint, Compos. Part B Eng. 54 (2013) 365–370. https://doi.org/10.1016/j.compositesb.2013.05.026.

[35] D.P. Ura, K. Berniak, U. Stachewicz, Critical length reinforcement in core-shell electrospun fibers using composite strategies, Compos. Sci. Technol. 211 (2021)

108867. https://doi.org/10.1016/j.compscitech.2021.108867.

[36] S.Y. Fu, B. Lauke, Y.H. Zhang, Y.W. Mai, On the post-mortem fracture surface morphology of short fiber reinforced thermoplastics, Compos. Part A Appl. Sci. Manuf. 36 (2005) 987–994. https://doi.org/10.1016/j.compositesa.2004.11.005.

[37] J.M. Hausherr, M. Eitel, W. Krenkel, Determination of material properties for short fibre reinforced C/C-SiC, MATEC Web Conf. 29 (2015). https://doi.org/10.1051/matecconf/20152900005.

5 Graded structures

5.1 Introduction

As previously mentioned in chapter 4, the new process developed allows to produce thin sheets of short carbon fibre reinforced UHTC with different characteristics such as the amount of fibre or the matrix composition. Thanks to these features, the overlapping of sheets with different compositions allows to obtain samples with hybrid structures that broaden the possible fields of application of UHTCMCs. For example, a coating of UHTC on a carbon fibre reinforced composite could improve the high-temperature performance of the material [1]. In fact, the high temperature resistance of UHTC bulk materials can protect the fibre reinforced layer below. The main problem in the preparation of hybrid materials is the CTE mismatch between the coating and the substrate due to the different matrix material or different amount of fibre used as reinforcement.

In this chapter, the realization of graded materials with the same matrix but different amount of pitch-based short carbon fibre reinforcement was investigated. In particular, a structure made of three different layers was considered. The first layer was composed only by bulk materials without any kind of reinforcement. The second layer was constituted by the same matrix material with a 20 vol. % of short pitch-based carbon fibre reinforcement and the last layer with a 50 vol. % of fibres. The focus of this study is to analyse the interfaces between the different layers and investigate the oxidation resistance of the graded materials.

The composition and fibres distribution of the materials investigated in this chapter is reported in Table. 5.1.

Table. 5.1: list of the samples tested and relative compositions.

Name	*Matrix composition*	*1st layer*	*2nd layer*	*3rd layer*
ZSY105	ZrB_2- 85 vol% SiC- 10 vol% Y_2O_3- 5 vol%	0 vol%-Cf	20 vol%-Cf	50 vol%-Cf
ZMo15	ZrB_2- 85 vol% $MoSi_2$- 15 vol%	0 vol%-Cf	20 vol%-Cf	50 vol%-Cf
SY65	SiC- 95 vol% Y_2O_3- 5 vol%	0 vol%-Cf	20 vol%-Cf	50 vol%-Cf

The amount of fibre reinforcement for each layer (0 - 20- 50 vol. %, respectively) has been chosen in order to retain damage tolerance across the specimen, while also maintaining the compatibility between each layer. The CTE of the materials used are the following, ≈ $6.7 \cdot 10^{-6}$/°C for ZrB_2, ≈ $4.0 \cdot 10^{-6}$/°C for SiC and $2.0 \cdot 10^{-6}$/°C for the pitch-based carbon fibres [2,3]. The samples were made by hot pressing of the "green" obtained overlapping 10 sheets for every composition at a temperature of 1900°C and a pressure of 30 MPa. Due the different amounts of fibres inside the layers and the different density of the matrices, the thickness of each layer was not the same but the ratio between the layer was similar in each sample.

5.2 Morphologies

The first study made on the three different samples was the investigation of the morphologies via SEM analysis. This analysis was made on the cross section of the samples to observe the interaction between the different layers. Before the analysis, the samples were polished and - in the case of the sample SY5 - the surface was coated with a thin layer of carbon with the use of a sputter coater to increase the conductivity.

5.2.1 ZSY105 structure

Graded sample ZSY105 had a matrix containing 85 vol.% - ZrB_2, 10 vol.% - SiC and 5 vol. % Y_2O_3, Table. 5.1, as for the samples investigated in chapter 4. The three different layers contained respectively 0 – 20 – 50 vol. % of short carbon fibres as reinforcement with a thickness of ≈ 820-1420-2050 μm, respectively. From SEM

micrographs of the polished cross section (Fig 5.1), the three zones with 0 – 20 – 50% fibres can be easily identified with a very sharp definition. Within each composition, the individual sheets cannot be distinguished because they were welded during the sintering steps, with no fibres aggregation or voids, forming a defect-free thick layer.

Worthy to note, the outer bulk material was completely free of cracks even in proximity of the interface with the fibre reinforced layer. Previous attempts of combining a bulk ceramic with a fibre reinforced composites typically led to the development of cracks in the ceramic matrix due to the CTE mismatch [4] In this case, no such defect was observed. Moreover, no defects were visible in the areas of interactions between the different layers (indicated by the yellow lines in Fig. 5.1) with SEM analysis. This demonstrated the possibility to produce a material with a graded structure without the issues related to the different layers CTE.

As the samples described in chapter 4, EDS spectra collected confirmed the presence of ZrB_2 light grey phase, SiC black phase, ZrC with particles and Y-B-C-O dark grey phases as reported in Fig. 4.7.

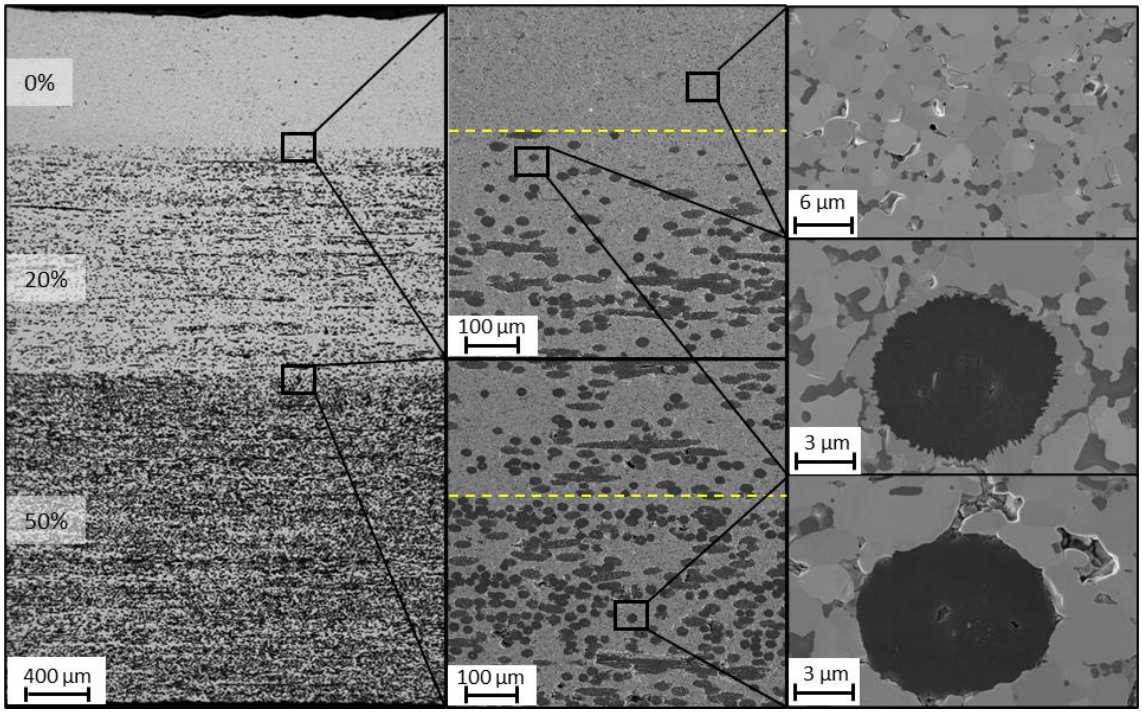

Fig. 5.1: Morphologies of graded ZSY105 structure composed of three areas: 0 %, 20 %, 50 % Cf.

Generally, the fibres did not present signs of degradation or reaction with the matrix and maintained their round shape in all the samples except for the first ≈ 100 μm of the layer reinforced with 20 vol. % of carbon fibres in the area directly in contact with the bulk layer. In this zone, the fibres were degraded radially by the ceramic matrix. More in detail, (Fig. 5.1 on the right) the fibre exterior was degraded but did not present cracks. EDS analysis conducted on this area showed the presence of Y-B-C phases (Fig. 5.2). The reaction that occurred was probably the following:

$$Y_2O_{3(s)} + 2B_2O_{3(s)} + 13C \rightarrow 2YB_2C_{2(s)} + 9CO_{(g)} \quad (5.1)$$

The B_2O_3 reported in the reaction were impurities present in the commercial ZrB_2 powder. The above reaction was particularly visible only on the fibres at the interface between the bulk layer and the layer with 20 vol.% carbon fibre. This is probably due to the migration of Y_2O_3 during sintering from the bulk area to the fibres. The migration took place in every part of the material because Y_2O_3, mixed with B_2O_3 and SiO_2, acted as a liquid phase during the sintering as observed in Chapter 4. However, while in the centre of the layer with the 20 and 50 vol. % of reinforcement, the reaction with the fibre was negligible due to the lower amount of oxide reactants, Fig. 5.2-a, in the contact area between the bulk layer and the 20% fibre layer all the liquid phase from the bulk reacted with the fibres at the interface Fig. 5.2-b.

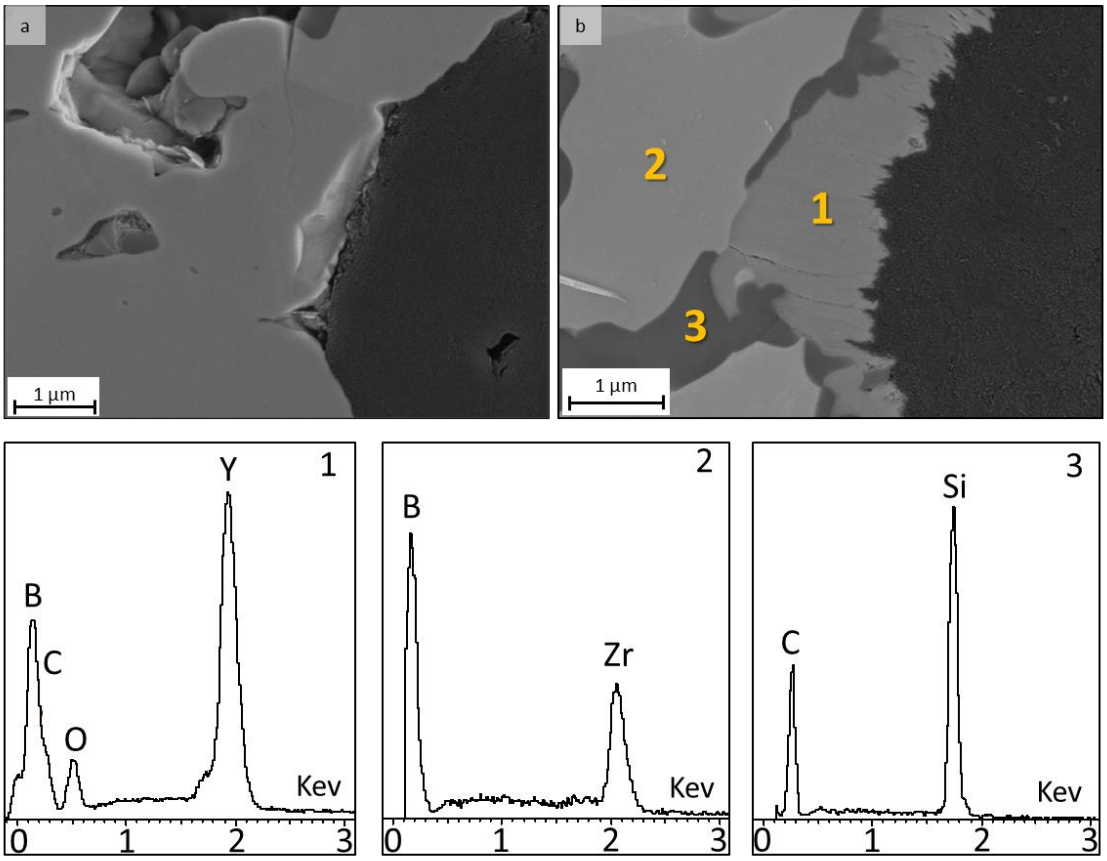

Fig. 5.2: High magnification SEM images of ZSY105 sample showing the EDS spectra collected at 5 KeV. The light and dark grey phases are ZrB_2 (2) and SiC (3) respectively. Occasionally, Y-B-C-O phases (1) were observed near SiC particles

5.2.2 ZMo15 structure

Graded sample ZMo15 had a matrix containing 85 vol % - ZrB_2 and 15 vol.% - $MoSi_2$, Table. 5.1. In this case, $MoSi_2$ acted like a sintering aid (similar to the previously used SiC and Y_2O_3), reducing the sintering temperatures and generating a transient liquid phase that improved the final density. As for sample ZSY105 reported previously, the composite was made by three different layers containing respectively 0 - 20 - 50 vol. % of short pitch-based carbon fibres. The thickness of each layer was respectively of ≈ 1450-2050-2100 µm. Even in this case, it was possible to observe the linear and clear separation between the different zones as observed for the sample ZSY105 for the same motivation exposed before. Moreover, no macro cracks or macro defects were visible across the sample. Only inside the bulk layer (0 vol. % of fibres reinforcement) some "scratches" arising from polishing were observed. The most critical regions were the interaction areas between the different layers (indicated by the yellow lines in Fig. 5.3). Even for this

material, no defects were visible in these areas. This demonstrated the possibility of obtaining carbon fibre reinforced graded structures with ZrB2 - MoSi2 as matrix without problems due to CTE mismatch.

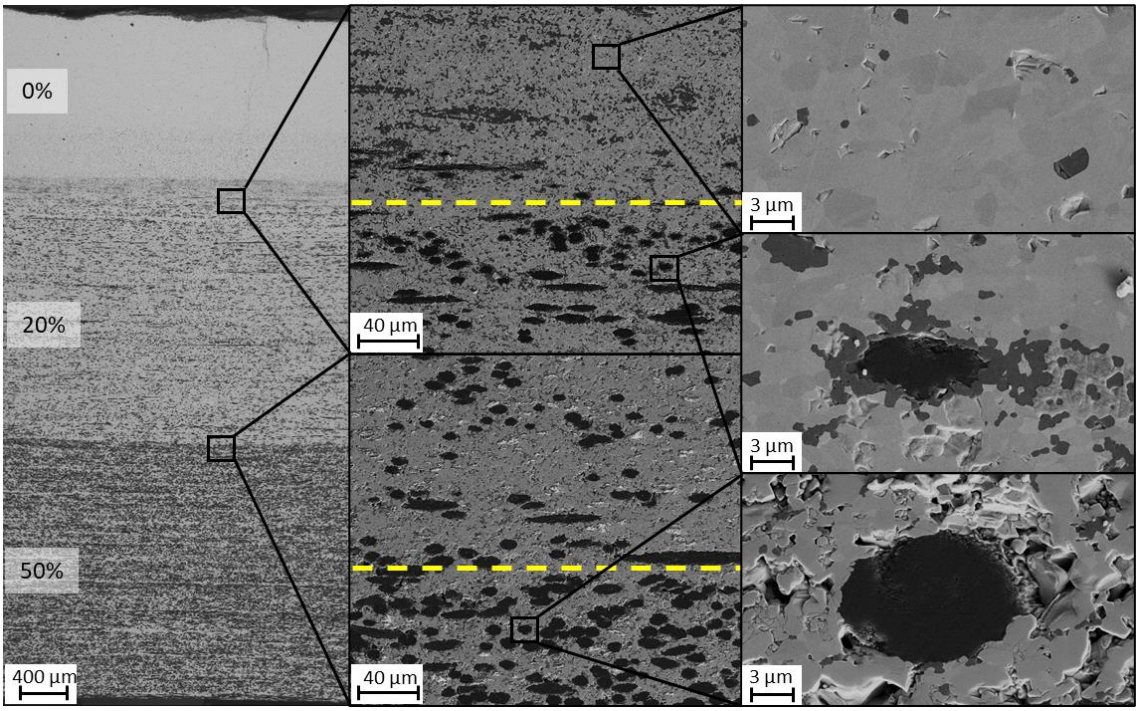

Fig. 5.3: Morphologies of graded ZMo15 structure composed of three areas: 0 %, 20 %, 50 % Cf.

The surface of the bulk layer (Fig 5.3) was fully dense and homogeneous, without voids or defects. The EDS collected on the ZrB_2 - $MoSi_2$ matrix (Fig. 5.4) showed the presence of a Mo-B phase, light grey, likely MoB, a ZrB_2 phase in darker grey and a SiC phase in black. The formation of MoB was observed in earlier studies of similar bulk systems and was probably due to the reaction of $MoSi_2$ with oxygen impurities during the sintering phase [5]:

$$2MoSi_2 + \frac{5}{2}O_2 + B_2O_3 \rightarrow 2MoB + 4\ SiO_2 \qquad (5.2)$$

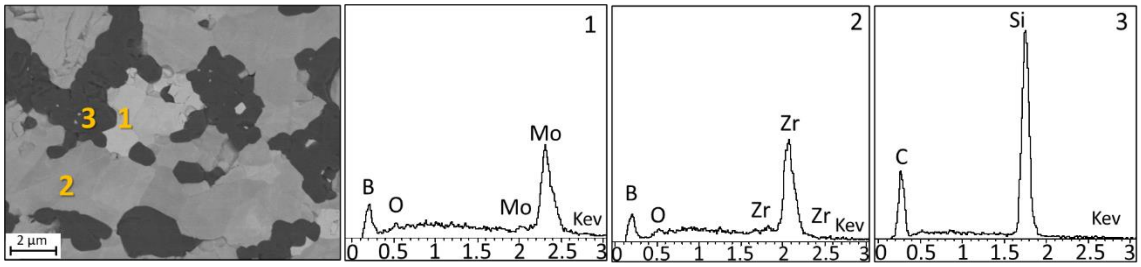

Fig. 5.4: High magnification SEM image of ZrB_2-$MoSi_2$ matrix and EDS spectra collected at 5 KeV. The light grey and black phase are MoB (1) and SiC (3), the darker grey is ZrB_2 phases (2).

As observed for sample ZSY105, even in this case the fibres did not present signs of high degradation due to the reaction with the matrix. They maintained their original shape approximately in all the samples except for a ≈ 50 µm thick area at the beginning of the second layer (20 vol.% fibre layer). In this region, the second layer was in contact with the bulk layer and the fibres reacted with the matrix, resulting in strong degradation. However, the reaction between the fibres and the matrix did not lead to the formation of visible critical defects. The different fibre shapes and the relative degree of reaction at the fibre/matrix interface are shown in Fig. 5.5. The EDS analysis conducted on the reacted area (Fig. 5.5) showed the presence of a high amount of SiC around the fibre, which was attributed to the reduction of MoSi2 and ZrB2 with the fibre according to the following reaction:

$$ZrB_{2(s)} + 2MoSi_{2(s)} + 5C_{(s)} \rightarrow ZrC_{(s)} + 2MoB_{(s)} + 4SiC_{(s)} \quad (5.3)$$

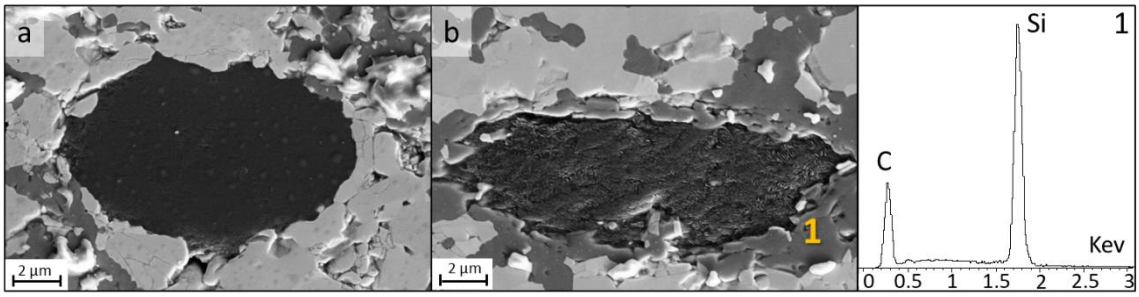

Fig. 5.5: Different fibre shapes and the relative degree of reaction for (a) all the sample, (b) area at the beginning of the second layer and SiC EDS (1)

As mentioned before this phenomenon was particularly visible at the interface between the bulk layer and the second layer likely due to the migration of the $MoSi_2$ liquid phase during the sintering from the bulk area towards the fibres. From Fig. 5.6 it was possible

to observe the progressive increase of a dark phase from the top to bottom. This phase was constituted by SiC -probably resulted from the reaction of the matrix with the carbon of the fibres.

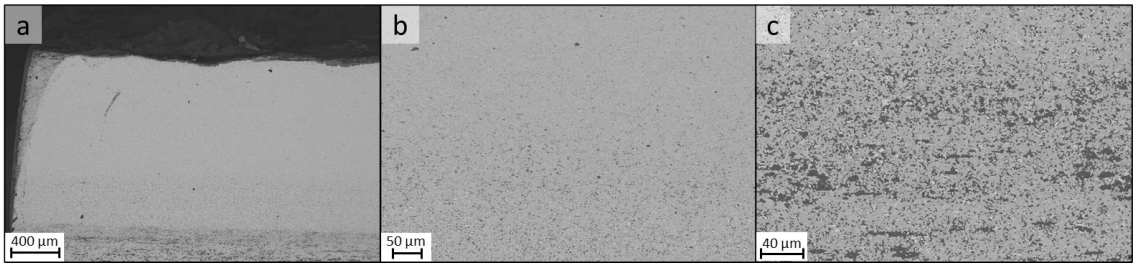

Fig. 5.6: Images of the increase of a dark phase from the top to bottom of the sample ZMo15 due to the $MoSi_2$ migration.

5.2.3 SY5 structure

Graded sample SY5 (Table. 5.1) had a matrix containing 65 vol. % - SiC and 5 vol. % - Y_2O_3. The Y_2O_3 acted like a sintering aid reducing the sintering temperatures and generating a liquid phase which reduced the porosity. For this matrix, two different kinds of SiC were used. This composition was chosen after several tests to avoid the formation of cracks on the matrix due to residual stresses deriving from sintering. In fact, the presence of powder with large grains size improved the rheology leading to a reduction of the mechanical stress. As for the two previous sample, the composite was made by three different layers containing respectively 0 – 20 – 50 vol. % of short pitch-based carbon fibres as reinforcement. The thickness of each layer was respectively of ≈ 2500-3900-4100 µm. From the SEM micrographs on the cross section, it was possible to observe the linear and clear separation between the different layers as seen in the previous samples for the same reasons mentioned before. The layers contained some residual porosity, but no cracks were visible in all the sample surface. More specifically, in the interaction areas between the layers (indicated by the yellow lines in Fig. 5.7) – which constitute the most critical parts of the sample - no macro defects were observed. This demonstrated the possibility to obtain carbon fibres reinforced graded structures with SiC-Y_2O_3 as matrix without issues due to the CTE mismatch. The only critical flaw identified was a series of voids propagating within one of the 50 vol% fibre layers. This likely originated from the local agglomeration of fibres that led to a very weak interface and the pull-out of the fibre bundles (Fig 5.7).

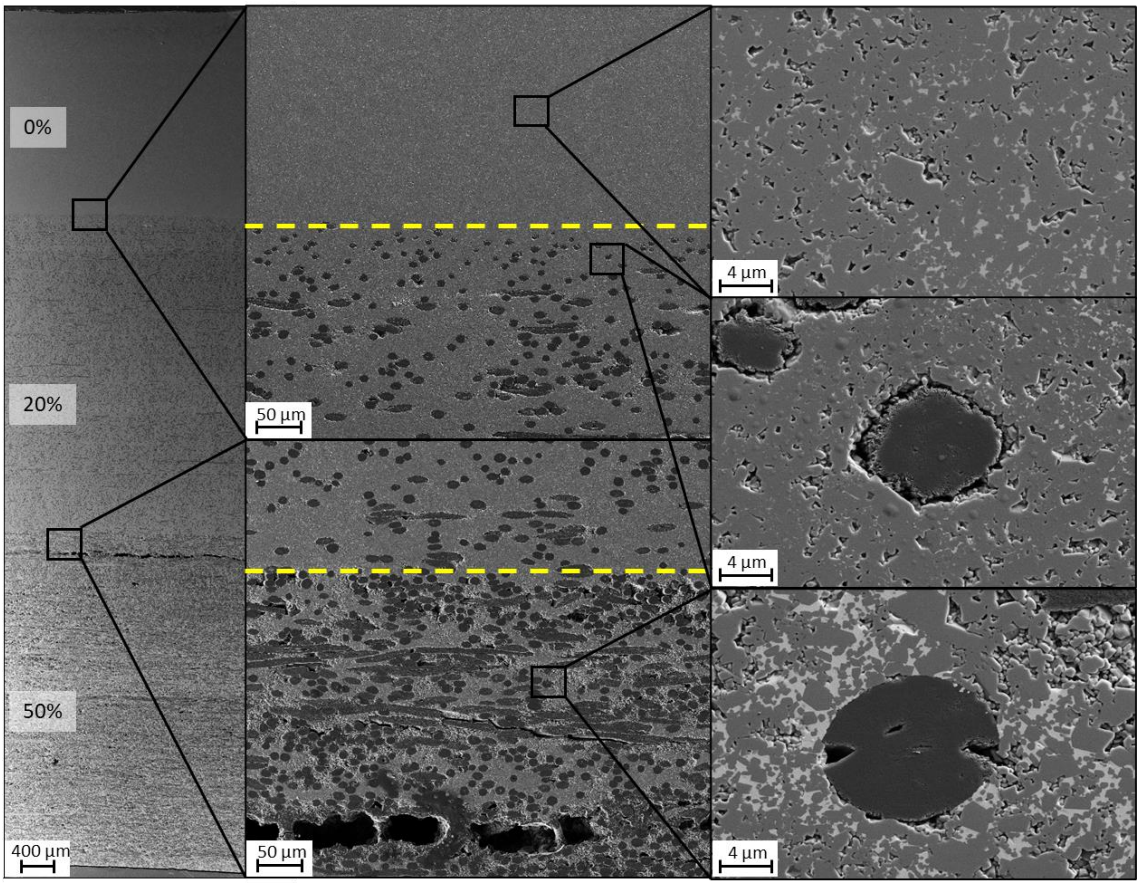

Fig. 5.7: Morphologies of graded SY5 structure composed of three areas: 0 %, 20 %, 50 % Cf.

The microstructure on the surface was homogeneous and crack free (Fig. 5.8), but presented some porosity due to incomplete sintering. The EDS collected on this area showed the presence of a SiC phase, dark grey and Y_2O_3, light grey.

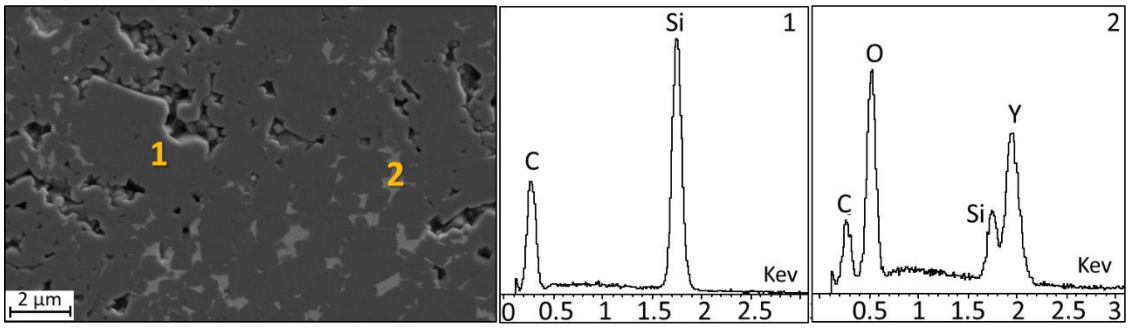

Fig. 5.8: High magnification SEM image of SiC-Y_2O_3 matrix and EDS spectra collected at 5 KeV. The dark grey phases are SiC (1), the light grey phases are Y_2O_3 (2).

As observed for the samples ZSY105 and ZMo15 before, even in this case the fibres did not present significant signs of degradation and maintained their original shape

approximately in all the samples, except for an area of ≈ 50 μm between the bulk layer and the second layer (20 vol% layer). In this region, the fibre was visibly eroded and was surrounded by voids (Fig. 5.9), but no cracks were observed in the matrix. In this case, the EDS analysis showed only the presence of SiC. Probably the SiC and the Y_2O_2 reacted with the C of the fibres generating $SiC_{(s)}$ and $CO_{(g)}$ that left some voids after the reaction.

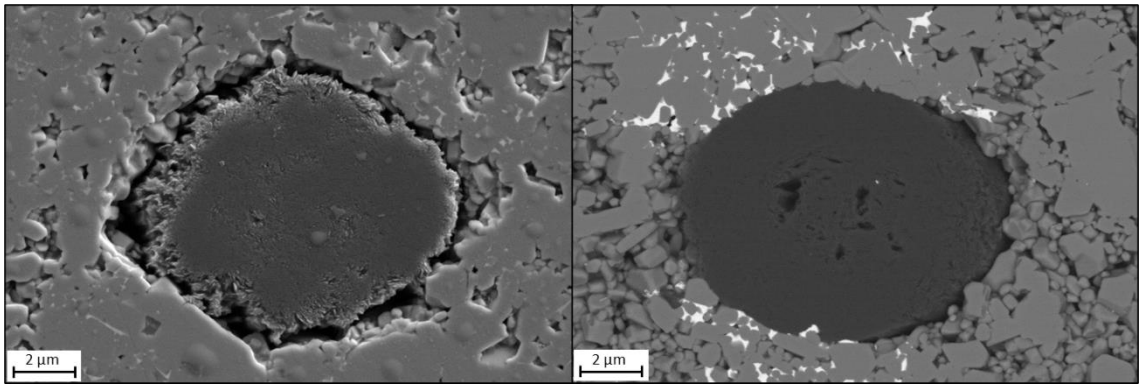

Fig. 5.9: Different fibre shapes and the relative degree of reaction for (right) area at the beginning of the second layer (left) all the sample,

Like the two previous cases, the fibres degradation was mostly visible at the interface between the bulk layer and the second layer. This was probably due to the higher presence of Y_2O_3 that migrated during the sintering from the bulk area towards the fibres. In this region a high concentration of white phase was detected at the interface between the layers as demonstration of the Y_2O_3 migration (Fig. 5.10).

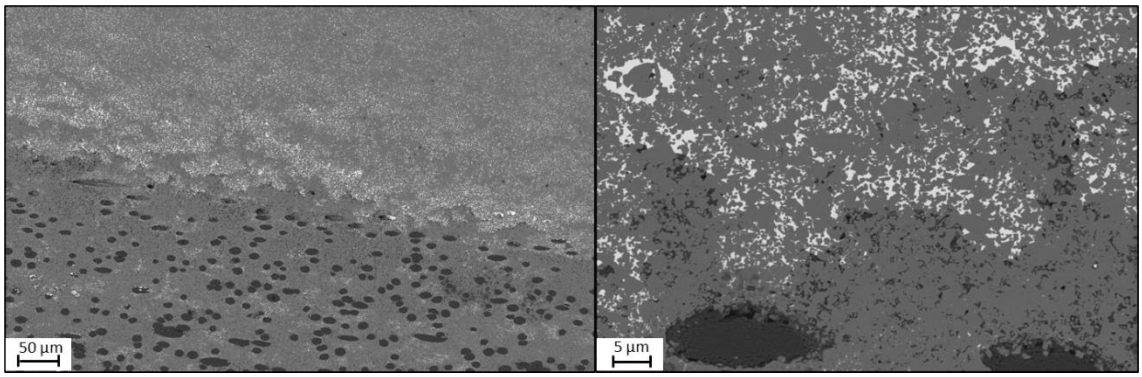

Fig. 5.10: Images of the Y_2O_3 phases (white) at the interface between the bulk layer and the 20 % reinforced layer.

5.3 Oxidation resistance

As reported in the previous chapters, the C/C composites can only retain the properties in an inertial atmosphere or vacuum due to the reaction with oxygen or other oxidizers at temperatures above 500 °C which will result in the consumption of C/C composites [6]. To overcome this problem, a coating with a UHTC layer or the use of UHTC as matrix has been considered. The graded structures presented in this chapter investigated the possible methods to improve the oxidation resistance. In fact, samples ZSY105 and ZMo15 presented a UHTC protective layer and a short carbon fibre reinforced UHTC matrix. Sample SY5 did not possess a borosilicate protective system for oxidation at temperatures >1600°C, due to lack of B2O3-bearing species and was used as comparison. More in detail, the effect of the secondary phases, SiC or $MoSi_2$, was investigated. In fact, as mentioned in chapter 2.1.7, ZrB_2 at temperature around 1100 °C lose its protective B_2O_3 and becomes susceptible to oxygen attack. To overcome this problem, silicides or SiC were added in order to obtain SiO_2 glasses that protect the material from the oxidation up to 1600 - 1700 °C. Among them, $MoSi_2$ is very interesting due to the high melting point and stability at 1800 °C in oxidizing atmosphere. Its oxidation resistance derives from the formation of a SiO_2 film at 600 °C that protect the material up to 1700 °C. However, due to the CTE mismatch with carbon, $MoSi_2$ was not directly used as protective coating but, as in this case, was incorporated into a different material [6].

One important problem regarding the oxidation test is the comparison between the material investigated and those reported in literature. In fact, the comparison among mass variations after oxidation tests is not reliable due to testing conditions (e.g. time and temperature exposure, oxidizing environment, specimen dimensions). In literature, oxidation tests are usually carried out under static air using a muffle furnace or thermo-gravimetric analysis (TGA).

In this study, a bottom loading furnace was used due to the advantage of introducing the specimens for 60 seconds when the target temperature (e.g. 1650 °C) was reached, avoiding further oxidation during heating ramp. Nevertheless, during the introduction of the specimens in the furnace, cold air enters the oxidation chamber, causing harsher conditions than a TGA. In fact, the exposure to air at 1500 °C for 1 min in the bottom

loading furnace induced the same oxidation degree of the equivalent TGA test carried out at 1550 °C for 2.5 h [7].

Table. 5.2: Values of density, sample temperature, exposure time at 1650 °C and the mass variation per area unit for the different samples.

	ZSY105	**ZMo15**	**SY5**
ρ (g/cm^2)	4.30	4.85	2.71
T_{min} (°C)	1572	1565	1580
t_{return} (s)	100	125	138
t_{1650} (s)	60	60	60
Δm (%)	-1.34	-0.14	-3.46
Δm/S (mg/cm^2)	-4.51	-0.56	-7.05

The values of density, sample temperature, exposure time at 1650 °C and the mass variation per area unit are reported in Table. 5.2. Sample ZMo15 presented the highest oxidation resistance with the lowest mass loss, – 0.56 mg/cm^2. Sample ZSY105 presented a mass loss of – 4.51 mg/cm^2, in accordance with previous studies made on long carbon fibre reinforced ZrB_2-SiC materials [7]. Finally, sample SY5 presented the highest mass loss. – 7.05 mg/cm^2 due to the oxidation behaviour.

5.3.1 Microstructures

Following the oxidation tests at 1650°C, the surface and the polished cross section of the graded specimen was investigated by SEM. Only the cross section relative to the outer layer (0 vol. % Cf) is of relevance for the desired application, as the inner layers with a higher fibre content would normally not be exposed to air. For comparison reasons, the oxidation of the inner layers was also investigated in this thesis to show how the fibre content would affect the oxidation resistance of the composite.

- ZSY105 oxidized structure

The oxidation behaviour of pitch-based carbon fibre reinforced ZrB_2-SiC-Y_2O_3 material was previously investigated [8], and the four main reactions that take place are:

$$- C_{(s)} + \frac{1}{2}O_{2(g)} \rightarrow CO_{(g)} \quad (5.4)$$

$$- C_{(s)} + O_{2(g)} \rightarrow CO_{2(g)} \quad (5.5)$$

$$-ZrB_{2(s)} + 5O_{2(g)} \rightarrow ZrO_{2(s)} + B_2O_{3(l,g)} \quad (5.6)$$

$$-SiC_{(s)} + \frac{3}{2}O_{2(g)} \rightarrow SiO_{2(l)} + CO_{(g)} \quad (5.7)$$

From SEM analysis carried out on sample ZSY105 after the oxidation (Fig. 5.11), no newly-formed cracks were observed between the layers. This indicated that during heating at 1650 °C the difference in CTE between the layers - due to the presence of a different vol. % of carbon fibres - did not significantly affect the structural integrity. The surface was covered by some porosity and bubbles. More specifically, the bulk layer (reinforced with 0 vol. % of carbon fibres) did not present holes or macro defects on its surface." Four leaves clover" - like structures composed by ZrO_2, white phase, and SiO_2, dark grey phase, were observed, with the presence of hemispherical structures composed by a very fine layer of ZrO_2. The formation of these "bubbles" could be attributed to the evolution of some gas like CO due to the reaction

$$Y_2O_{3(s)} + 2B_2O_{3(s)} + 13C \rightarrow 2YB_2C_{2(s)} + 9CO_{(g)} \quad (5.8)$$

or to the growth of the ZrO_2 phase.

The oxidation on the layers below was also investigated to compare its performance with the bulk layer, even though these layers are not normally exposed to air. The second layer, reinforced with 20 vol. % of carbon fibres, did not present bubbles like the previous layer but showed a high number of holes. These defects were generated by oxidation of the fibres that were removed as CO or CO_2 due to the reaction with oxygen. In this area, it was possible to observe that the matrix presented a higher amount of SiO_2 on the surface, visible as a dark grey phase. The third layer, reinforced with 50 vol. % of carbon fibres, showed a lot of defects on the surface due to the carbon fibre oxidation. However, in this area the resulting matrix was constituted predominantly by ZrO_2 as evidenced by the distribution of the white phase, showing how higher fibre contents lead to lower oxidation resistance.

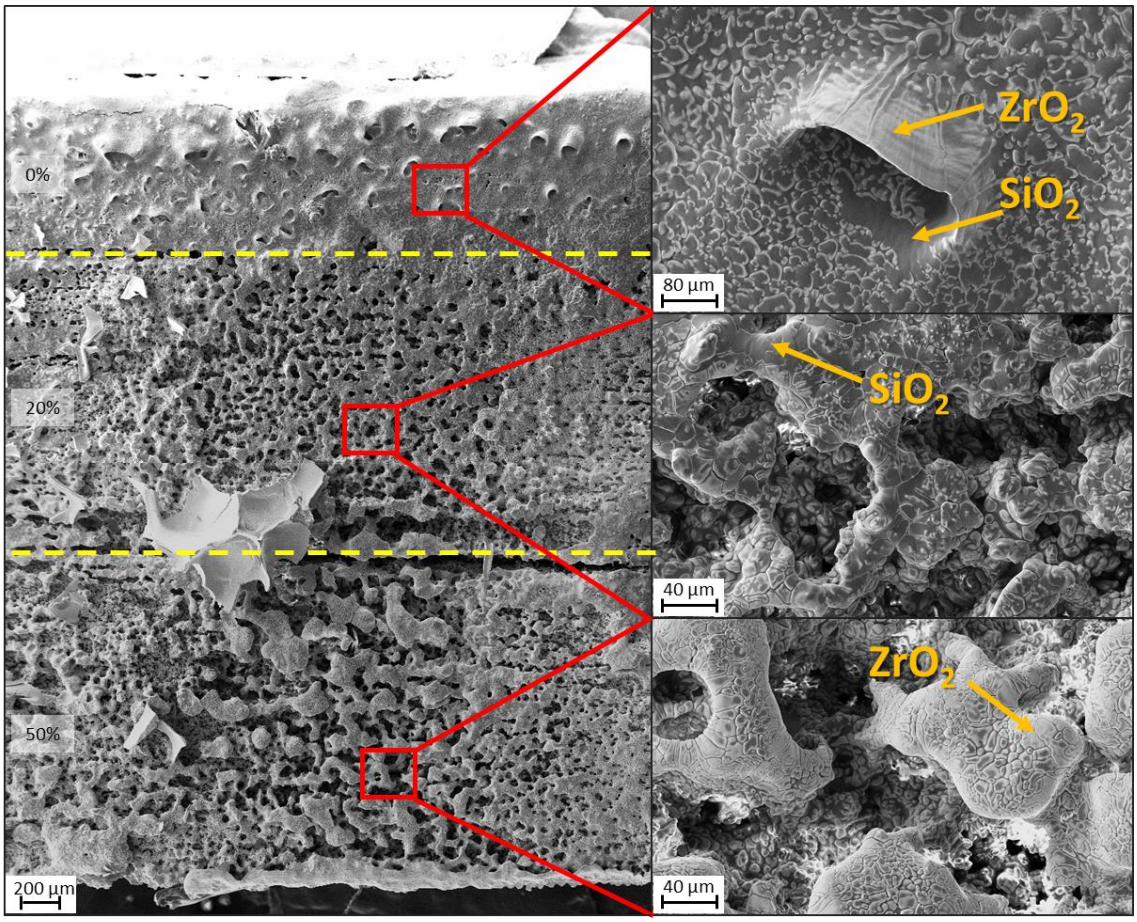

Fig. 5.11: Morphologies of graded ZSY105 structure composed of three areas: 0 %, 20 %, 50 % Cf, after oxidation at 1650 °C in air.

The EDS collected on the polished cross section of the oxidized material (Fig. 5.12) showed the presence of a SiO_2 phase, dark grey/black, a ZrO_2 phase light grey and a YBCO phase grey. The presence of C in all the spectra was due to the carbon layer deposited on the sample as observed with SEM.

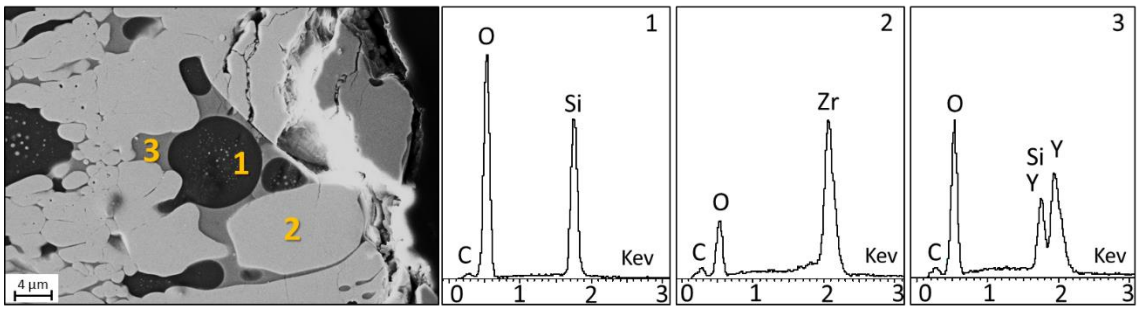

Fig. 5.12: High magnification SEM of ZrB_2-SiC-Y_2O_3 matrix and EDS spectra collected at 5 KeV. The dark grey phases were SiO_2 (1), the light grey phases were ZrO_2 (2) and the grey phases were Y-O (YBCO) (3).

The oxidation behaviour of the different layers was affected by the carbon fibre volume content as shown in Fig. 5.13. Starting from the bulk layer, a modified area with a thickness of ≈ 86 μm was visible. As reported in previous studies [9,10] for the matrix of ZrB_2-SiC-Y_2O_3 only one oxidized region was visible, consisting of ZrO_2 grains held together by a glassy phase of SiO_2 and Y-O. This glassy phase was more abundant near the surface where the oxidation was stronger. In this region, columnar ZrO_2 grains were observed, some grains of SiO_2 that were bigger than the SiC grains observed in the matrix before the oxidation and a little amount of YBCO grains. The presence of Y_2O_3 inhibited the formation of the classic two-regions structure observed in the ZrB_2-SiC matrix composites [7]. The two-regions structure was constituted by an outer silica layer and an intermediate scale of columnar ZrO_2 + SiO_2.

The layer reinforced with a 20 vol. % of carbon fibres presented a modified area of around 130 μm and the same structure and composition of the matrix reported before. However, in this case the external edge was damaged by carbon fibre vaporization, formation of holes, their partial filling with silica coming from SiC oxidation and ZrO2 grain growth. Finally, in the layer reinforced with a 50 vol. % of carbon fibres the above mentioned phenomena led to a greater degradation, with formation of large pores and deformation and the oxidised layers increased to 190 μm.

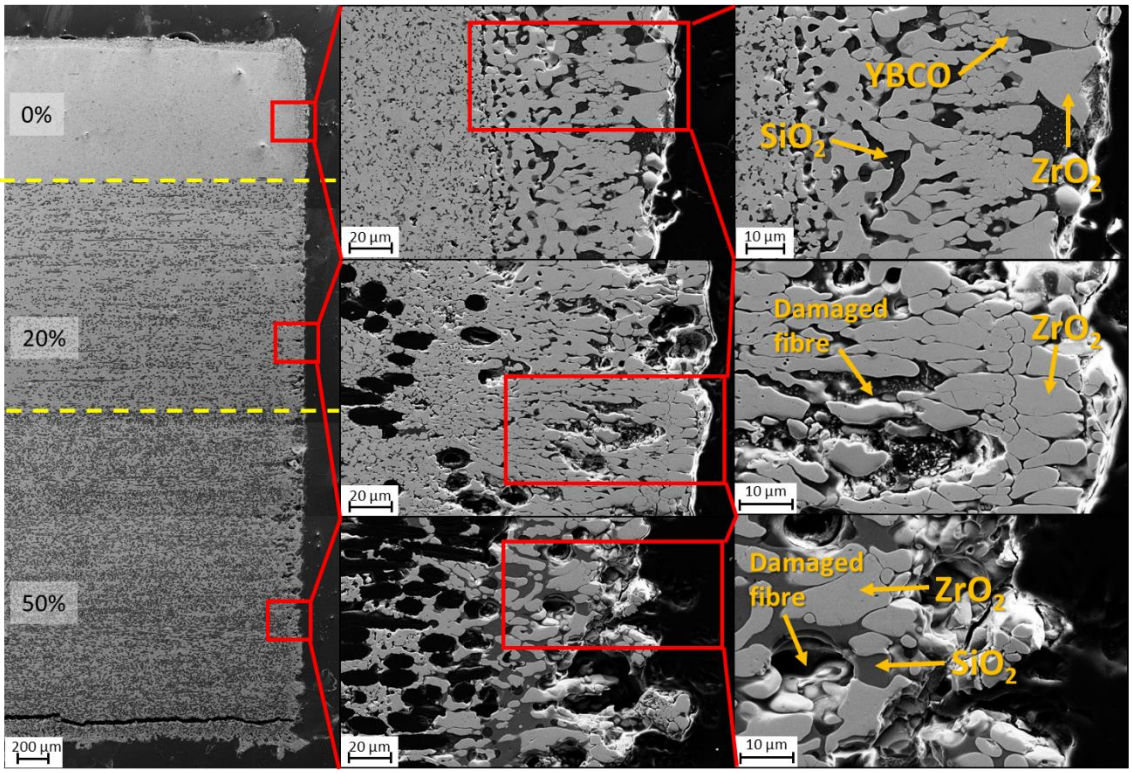

Fig. 5.13: Morphologies of polished graded ZSY105 structure tested at 1650 °C in air.

To investigate more in detail the oxidation thickness in each layer, EDS mapping was carried out (Fig 5.14). From top to bottom it is possible to see the increasing thickness of the oxidized area for each layer, from 70 to 120 to 190 µm for the 0, 20, and 50 vol. % fibre layers respectively, as evidenced by the oxygen signal (in red). Moreover, the distribution of the oxygen was approximately in correspondence of the composition variation.

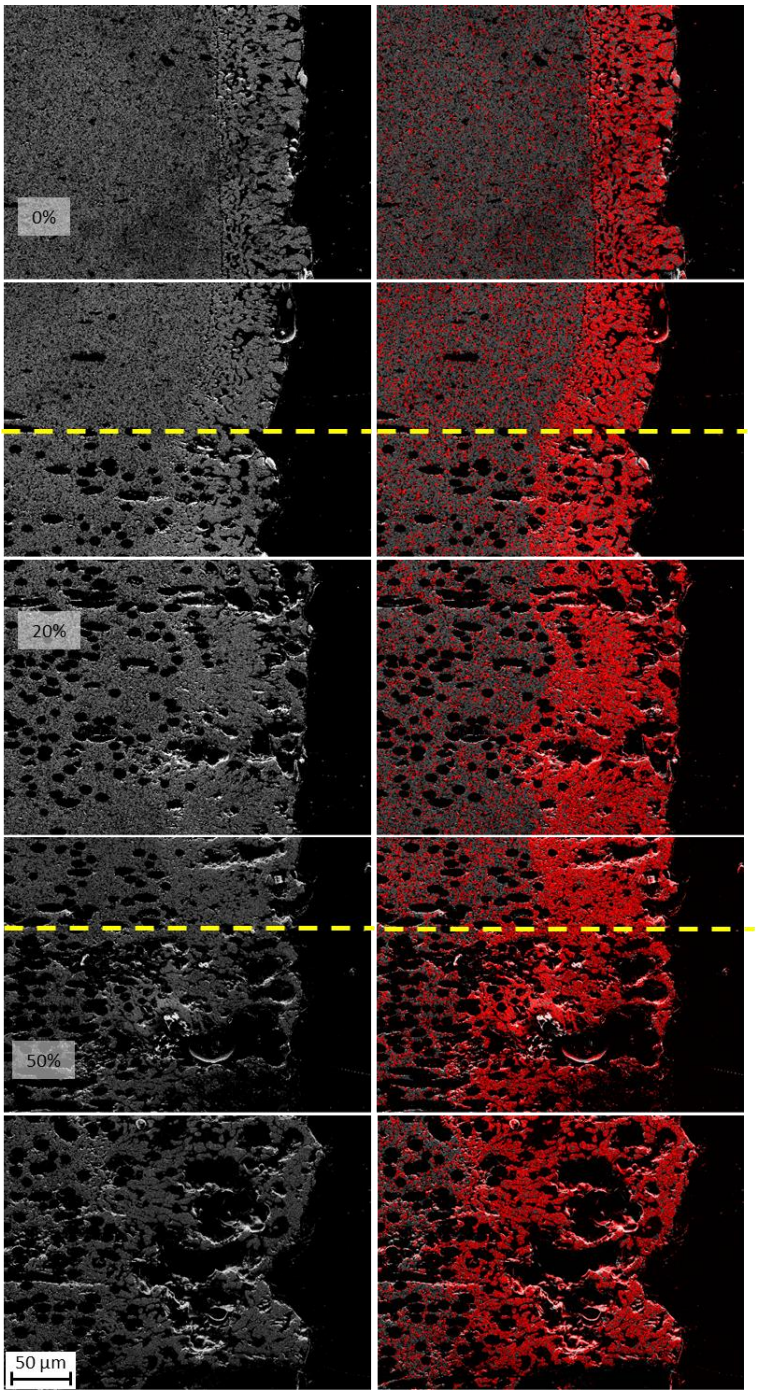

Fig. 5.14: Mapping images of the polished oxidized ZSY105 structure with the presence of oxygen reported in red.

From these studies, it is evident how a graded structure is beneficial to the improvement of the oxidation resistance. Even though the fibre-reinforced layers provide better structural integrity, their oxidation performance is inversely proportional to the fibre content.

- ZMo15 oxidized structure

The lateral surface of the sample ZMo15 after oxidation test is reported in Fig. 5.15. Even in this sample - like the ZSY105 - no cracks were visible at the interface between the different layers after the oxidation. This indicated that the CTE mismatch between the layers due to the different amount of carbon fibres did not affect the structural integrity. In this case, the surface of the entire sample was covered by a continuous dark grey layer that did not allow to identify micro or macro defects. This layer was constituted by SiO_2 formed during the oxidation of $MoSi_2$ according to the following reaction:

$$ZrB_{2(s)} + 2MoSi_{2(s)} + 5O_{2(g)} \rightarrow ZrO_{2(s)} + 4SiO_{2(s)} + 2MoB_{(s)} \quad (5.9)$$

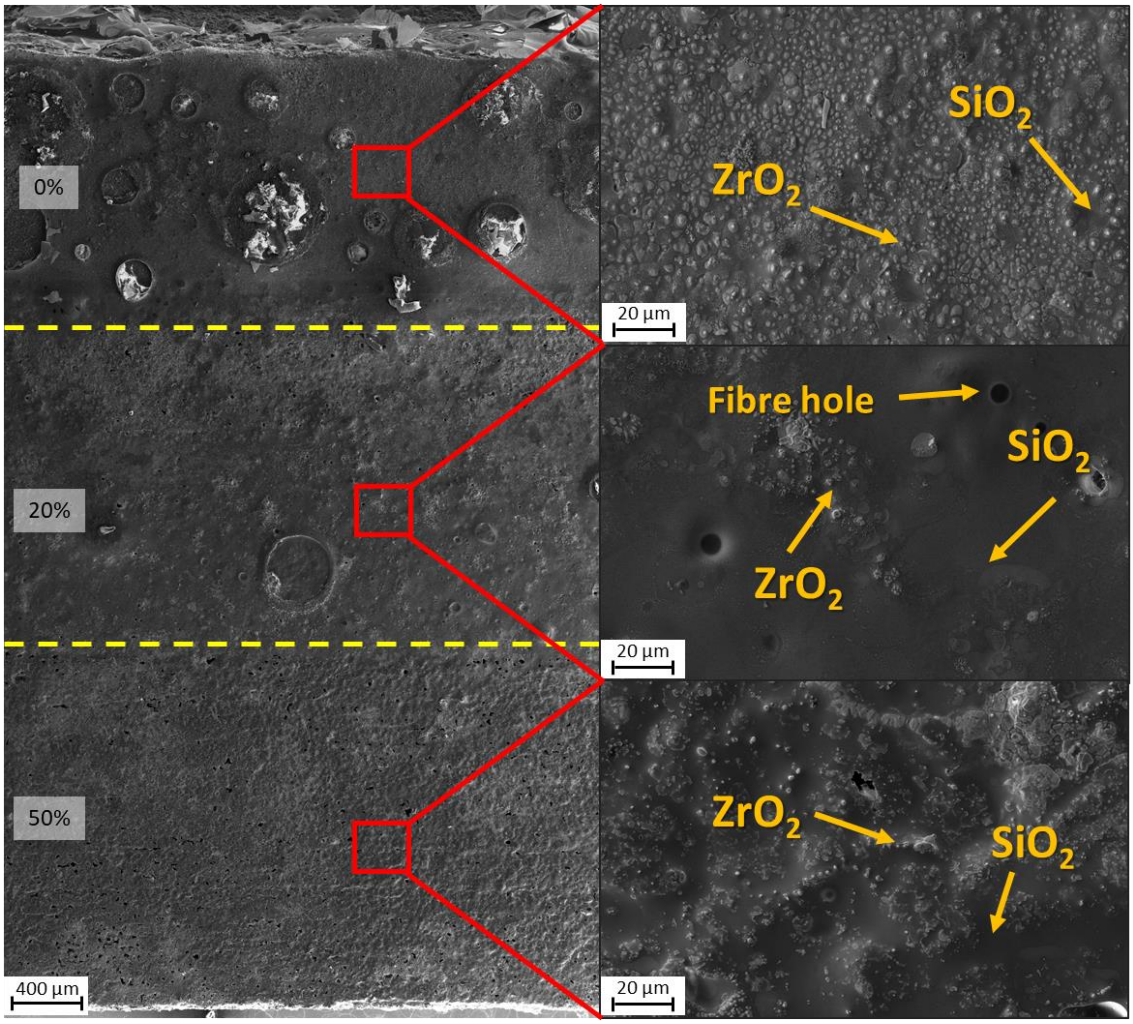

Fig. 5.15: Morphologies of graded ZMo15 structure after oxidation at 1650 °C in air.

More in detail, the bulk layer showed macro bubbles on the surface and was constituted by ZrO_2 grains covered by a SiO_2 film. The second layer, reinforced with 20 vol. % of pitch-based carbon fibre, did not present bubbles like the previous layer. In this area, the matrix was composed by a well visible film of SiO_2, dark grey, that covered evenly all

the surface, with some grains of ZrO_2. On the SiO_2 film, some porosity was observed, probably due to the holes generated by the fibre oxidation that the oxide film could not fill. Finally, the third layer - reinforced with 50 vol. % of short carbon fibres - showed the SiO_2 film with ZrO_2 grains on it. It can be hypothesized that the SiO_2 film covered the holes left from the oxidized carbon fibre. In this way, the underling fibres were protected from the oxygen diffusion during the oxidation, thus reducing the sample damage. A two-regions structure constituted by an outer silica layer that acted like a barrier for the oxygen and an internal ZrO_2 + SiO_2 layer was observed, like for the ZrB_2-SiC matrix composites [7].

The EDS analysis on the oxidized matrix is reported in Fig. 5.16. The EDS showed three different phases: a SiO_2 phase, black (Fig. 5.16-1), a ZrO_2 phase white (Fig. 5.16-2) and a grey phase attributed to MoO_3 (Fig. 5.16-3). The presence of C in all the spectra was due to the carbon layer deposited on the sample to observe it with SEM.

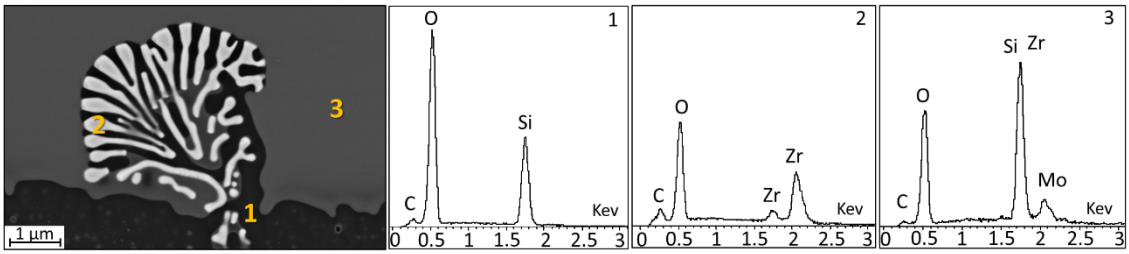

Fig. 5.16: High magnification SEM of ZrB_2-$MoSi_2$ matrix after oxidation and EDS spectra collected at 5 KeV. The black phases were SiO_2 (1), the white phases were ZrO_2 (2) and the grey phases were MoO_3 (3).

High magnification SEM images of the sample surface after oxidation at 1650 °C are reported in Fig. 5.17. The most interesting thing to observe was the presence of a different ZrO_2 structures immersed in a MoO_3 or SiO_2 "sea". Three different conformations were observed: "shell" like structures of ZrO_2 surrounded by MoO_3 (Fig. 5.17-a), an irregular agglomeration of ZrO_2 immersed in a SiO_2 phase (Fig. 5.17-b) and a coral like structure of ZrO_2 immersed in a SiO_2 and MoO_3 phases (Fig. 5.17-c).

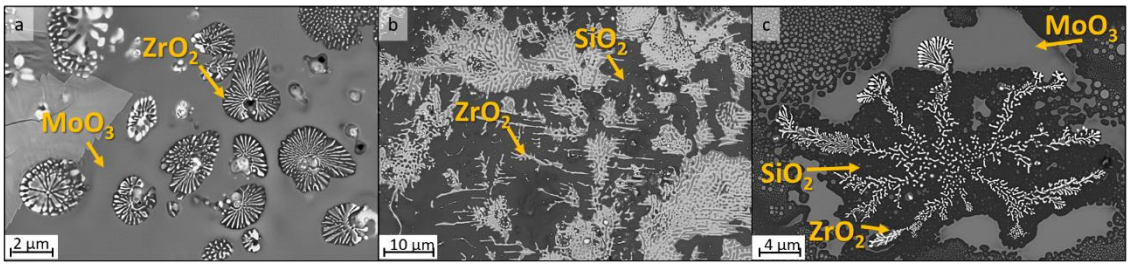

Fig. 5.17: SEM images of different ZrO_2 structures on the ZMo15 sample surface after oxidation at 1650 °C in air.

The polished cross section of sample ZMo15 is reported in Fig. 5.18. With this image, it was possible to observe more in detail the absence of cracks in the interaction areas between the layers even after the oxidation test. Moreover, the different degree of oxidation due to the difference in carbon fibre volume in the three different layers was visible. For the bulk layer, a modified area with a thickness of ≈ 85 µm was visible. The matrix presented a two regions structure after the oxidation: an external SiO_2 film that reduced the oxygen diffusivity and an internal ZrO_2 structure. Even in this case, the ZrO_2 grains presented a well-defined columnar structure held together by a glassy phase of SiO_2 like the ZSY105 sample.

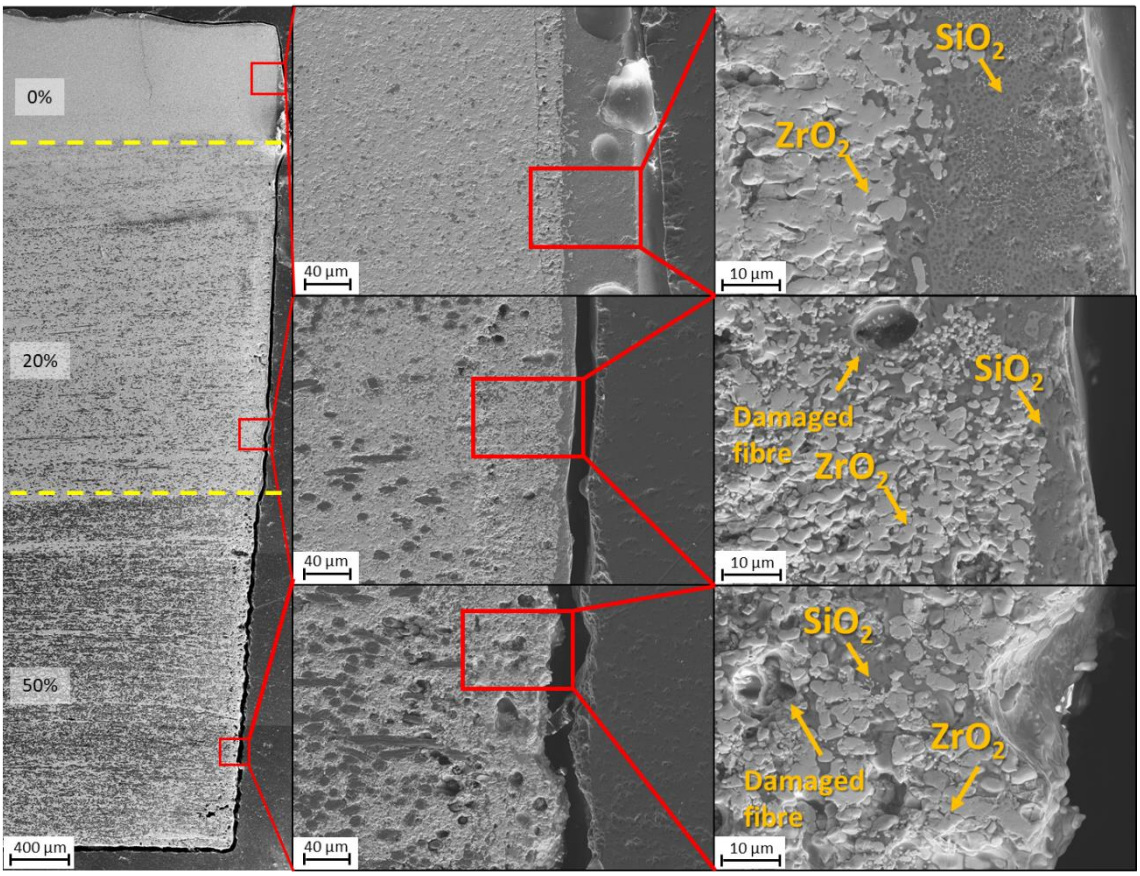

Fig. 5.18: Morphologies of polished graded ZMo15 structure tested at 1650 °C in air.

The second layer, reinforced with 20 col. % of short carbon fibres, showed a modified area with a thickness of around ≈ 75 µm and the same composition and structure observed for the previous layer. In this sample, the external edge presented some damage due to fibre oxidation. The fibres showed a lower degree of oxidation than the oxidized ZSY105 sample, probably due to the better protection provided by the SiO_2 film. The last layer, reinforced with 50 vol. % of carbon fibres showed a behaviour similar to that observed for the previous layer, in an area with a thickness of ≈ 75 µm. However, in this case the protective film of SiO_2 was very thin, resulting in a higher carbon fibres oxidation and corrugation of the external profile.

The matrix composition of the polished bulk layer after oxidation, with the relative EDS spectra, is reported in Fig. 5.19. The EDS analysis showed a ZrO_2 phase, light grey (Fig. 5.19-1), derived from the ZrB_2 oxidation, a MoO_3 phase, white (Fig. 5.19-2), derived from the $MoSi_2$ oxidation and a SiO_2 phase, dark grey (Fig. 5.19-3), derived from the $MoSi_2$ oxidation:

$$2MoSi_{2(s)} + 7\ O_{2(g)} \rightarrow 2MoO_{3(g,l)} + 4SiO_{2(s)} \qquad (5.10)$$

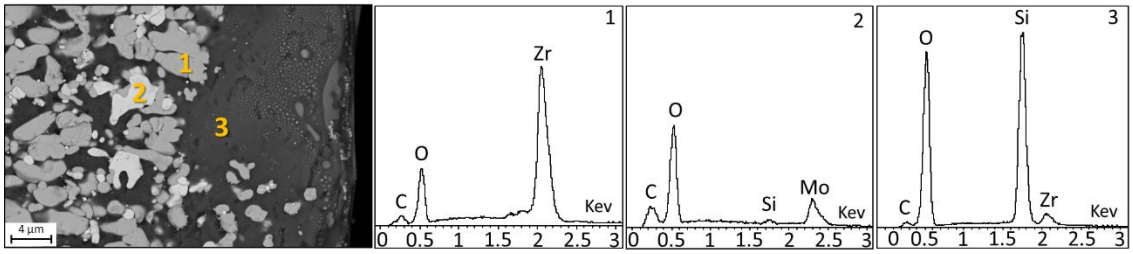

Fig. 5.19: High magnification SEM of ZrB_2-$MoSi_2$ polished matrix after oxidation and EDS spectra collected at 5 KeV. The light grey phases were ZrO_2 (1), the white phases were MoO_3 (2) and the dark grey/black phases were SiO_2 (3).

To understand more in detail the oxidation mechanism, an EDS mapping analysis was carried out to measure the oxide thickness in each layer, evidenced by the oxygen signal in red (Fig 5.20). The oxide layer measured ≈ 50-100-85 µm for the 0 – 20 – 50 vol. % fibre respectively. The distribution of oxygen was approximately in correspondence of the matrix morphologies change and that the changes in the oxygen penetration were in correspondence of the interfaces between the different layers.

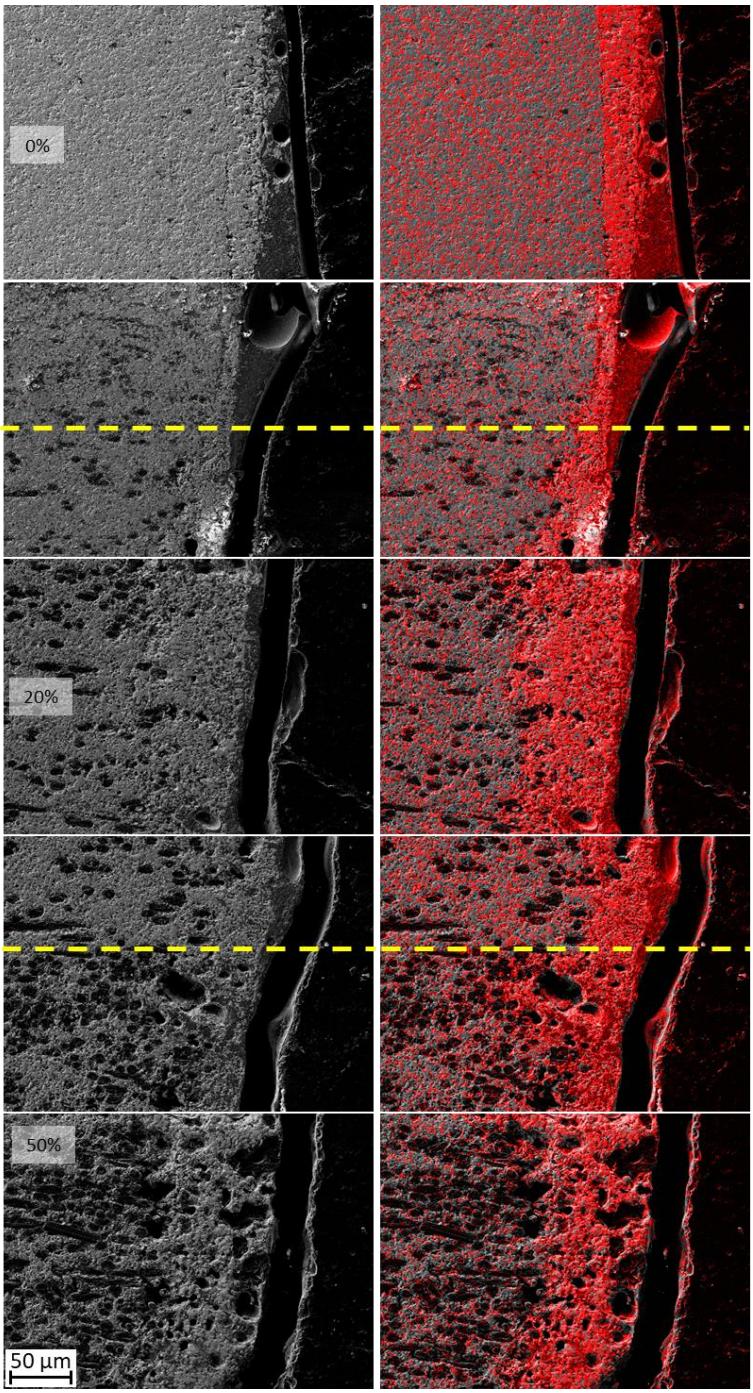

Fig. 5.20: Mapping images of the polished oxidized ZMo15 structure with the presence of oxygen marked in red.

- SY5 oxidized structure

The cross section of sample SY5 after oxidation at 1650 °C is reported in Fig. 5.21. No newly formed cracks were visible after oxidation at the interface between the different layers, suggesting that the CTE mismatch between the layers did not affect the

structural integrity. The surface was covered by a dark grey film that was constituted by SiO_2 deriving from the oxidation of SiC according to the following reaction:

$$SiC_{(s)} + \frac{3}{2}O_{2(g)} \rightarrow SiO_{2(s)} + CO(g) \quad (5.11)$$

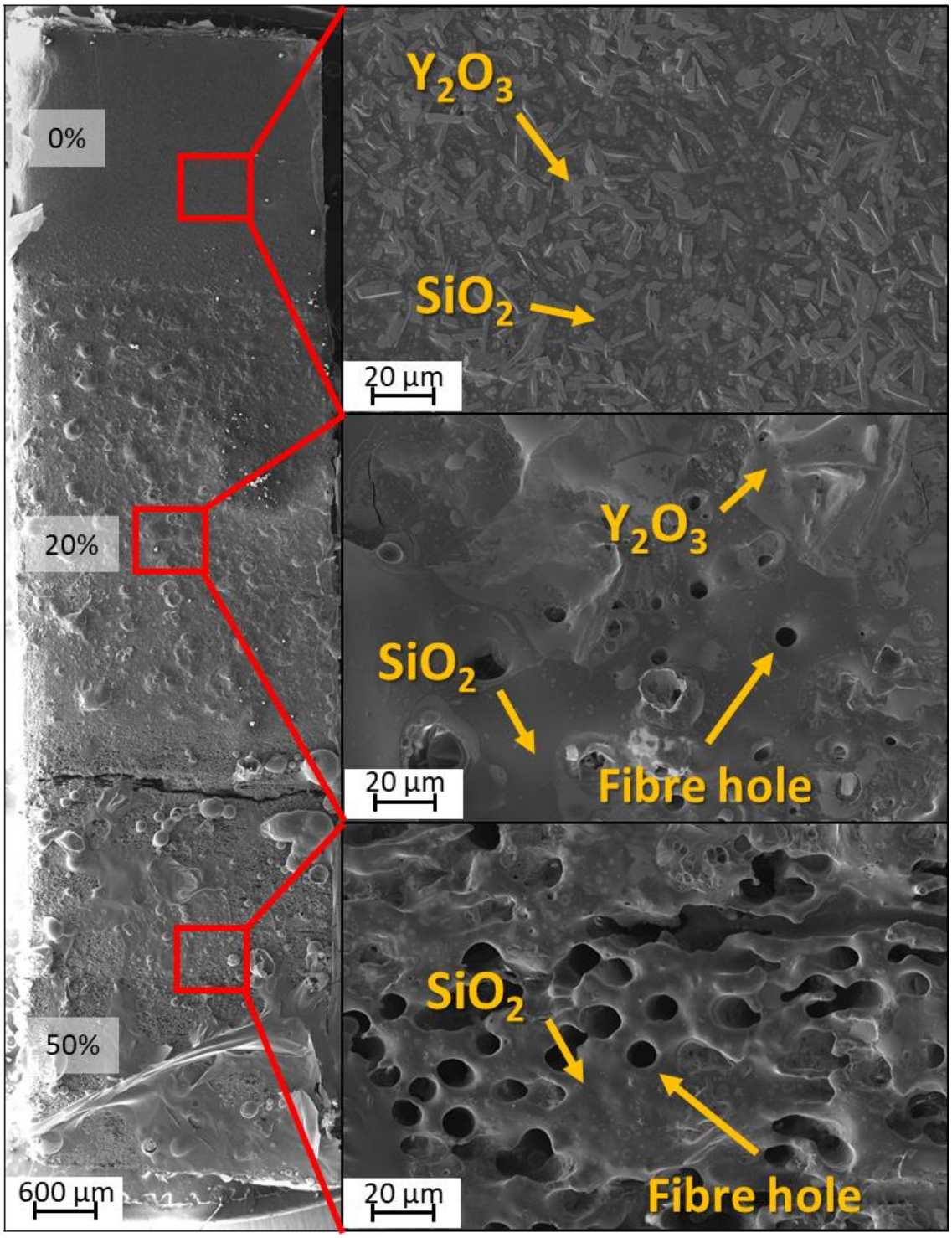

Fig. 5.21: Morphologies of graded SY5 structure after oxidation at 1650 °C in air.

In the bulk layer, a homogeneous SiO_2 dark grey film covered the entire sample. Within this film, lamellar Y_2O_3 phases were observed. This surface did not present any visible defect or presence of bubbles. Probably, the oxidation reaction took place only on the surface with a production of a small quantity of oxide species that minimized the formation of defects. In the second layer, reinforced with 20 vol. % of fibres, the SiO_2 film was still visible but without the lamellar Y_2O_3 grains. Moreover, some porosity was observed likely due to the fibre oxidation that left voids after the degradation that the SiO_2 film did not cover. This behaviour was more evident in the third layer - reinforced with 50 vol. % of fibres - where the SiO_2 film covered the entire area but left a higher number of visible holes due to the fibre oxidation, suggesting that the SiO_2 film generated during the SiC oxidation was not enough to effectively protect the fibres from oxidation.

From the EDS spectra collected on the surface oxide layer, it was possible to observe the same composition but different distribution. In the bulk layer (Fig. 5.22-a) light grey Y_2O_3 grains were immersed in a dark grey SiO_2 phase (Fig. 5.22-a1-2). In the fibres reinforced layers (Fig. 5.22-b1-2) the Y_2O_3 was not present as elongated grains, likely due to the porosity derived from carbon oxidation that hindered the grain growth. The presence of C in all the spectra was due to the carbon layer deposited on the sample.

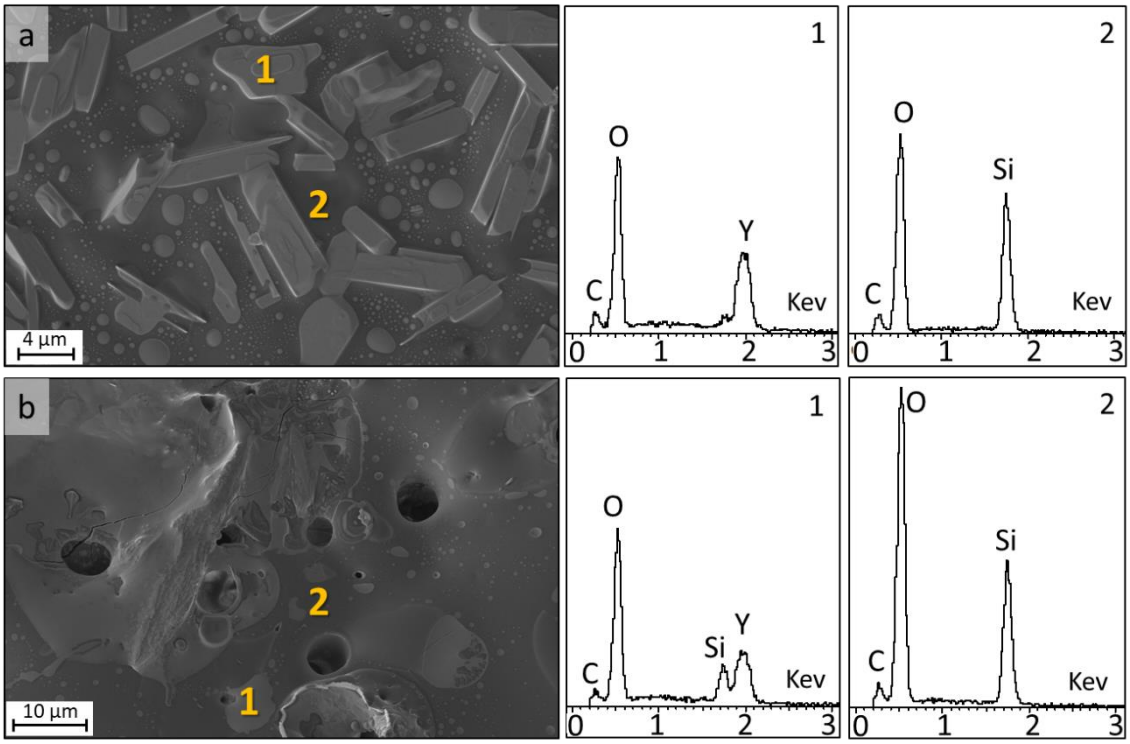

Fig. 5.22: High magnification SEM of SiC-Y_2O_3 matrix oxidation and EDS spectra collected at 5 KeV of bulk layer (a) and 20 vol % reinforced layer (b). In the bulk layer a light grey phase, Y_2O_3 (1), and a dark grey phase, SiO_2 (2) were observed. In the reinforced layer a light grey phase, Y_2O_3 (1), and a dark grey phase, SiO_2 (2) were observed.

The polished cross section of sample SY5 is shown in Fig. 5.23. The polished surface allowed to confirm the absence of cracks in the interface areas between the layers even after the oxidation test. Moreover, it was possible to observe the different oxidation behaviour for the different layers. For the top layer, the bulk one, a modified matrix after the exposition at 1650 °C was not clearly visible. In fact, the SiC matrix was mostly unaffected, without any grain growth or the formation of lamellar structures. However, a SiO_2 film was still present and observed with subsequent analyses. The second layer, reinforced with 20 vol. % of fibres, showed a film of SiO_2 on the external surface with a thickness of ≈ 220 µm but an unchanged SiC internal matrix.

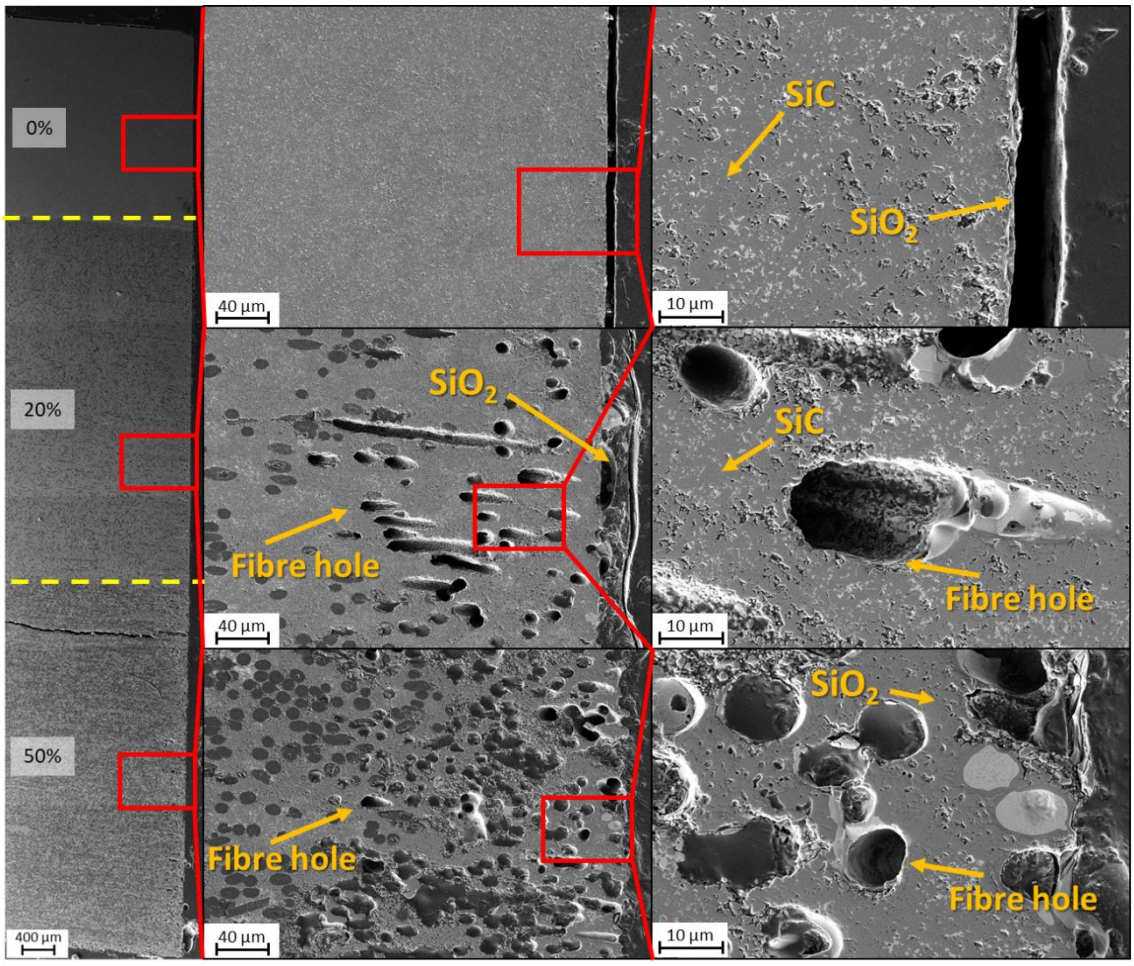

Fig. 5.23: Morphologies of polished SY5 structure tested at 1650 °C in air.

However, a lot of holes left by the carbon fibres oxidation were visible in the internal area. In this case, the holes have perfectly maintained their round shape, because the SiC grains were unaffected by oxidation. This is different from the previous cases where oxidation of ZrB_2 grains and ZrO_2 grain growth led to significant change/deformation. Holes left by the carbon fibres became preferential path for oxygen and this led to an augmented oxygen penetration. The third layer, reinforced with 50 vol. % of fibres, showed the same behaviour observed for the previous layer. However, in this case the effect of the fibres oxidation was stronger and more visible and it extended on an area with a thickness of ≈ 210 µm. Moreover, the external edge resulted severely damaged because of the material loss due to the formation of cracks between the holes left from the oxidized fibres. All these phenomena increased the porosity that could decrease the mechanical properties.

From the EDS spectra collected on the polished bulk layer after the test at 1650 °C, three different phases were identified: two different grey phases that were respectively SiC (Fig. 5.24-3) and SiO_2 (Fig. 5.24-1) and a light grey phase composed by Y_2O_3 (Fig. 5.24-2).

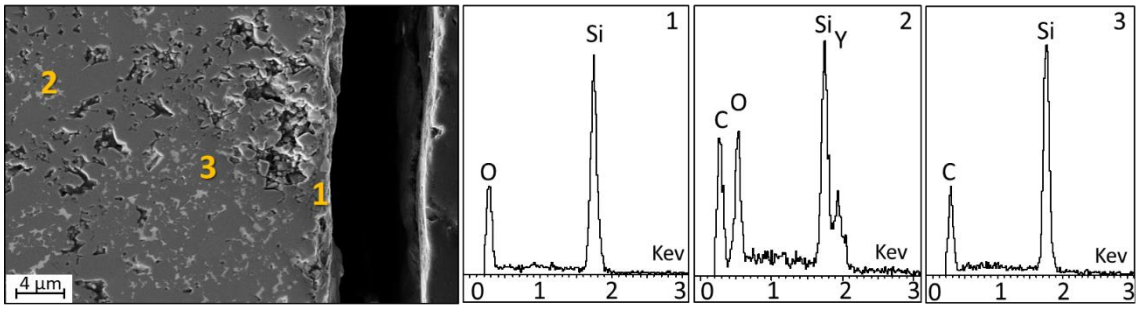

Fig. 5.24: High magnification SEM of SiC-Y_2O_3 polished matrix after oxidation and EDS spectra collected at 5 KeV. The grey phases were SiO_2 (1) and SiC (3), the light grey phases were Y_2O_3 (2)

Through a mapping analysis of oxygen distribution in the layer (marked in red) the different oxide thickness values were ≈ 2-140-230 µm for the 0 – 20 – 50 vol. % fibre layers, respectively. For the bulk layer, only a very thin oxide film was visible at high magnification. This was in accordance with the behaviour observed in Fig. 5.25 where the matrix was unchanged. For the second layer, reinforced with 20 vol. % of fibres, oxygen was found even below the silica layer, down to the area containing the degraded fibres. This suggests that the kinetics of formation of the SiO_2 protective film were slower and the outer fibres could not be protected from the oxidation. The third layer, reinforced with 50 vol. % of fibres, presented a very high oxygen diffusion that completely covered the area where the fibres were damaged and demonstrated the low efficiency of SiC alone as protective matrix for the carbon fibres oxidation.

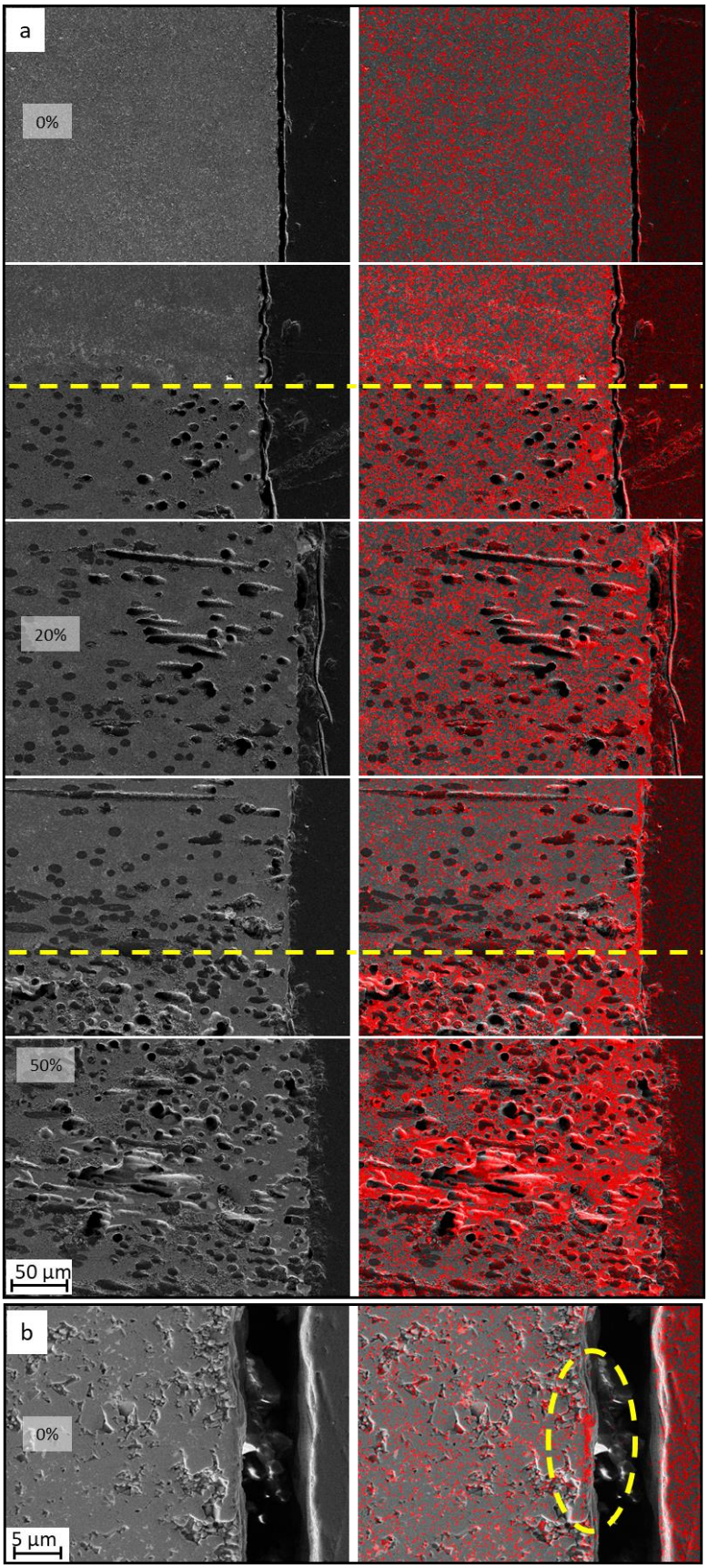

Fig. 5.25: (a) Mapping images of the polished oxidized SY5 structure with the presence of oxygen reported in red. (b) Magnification of the bulk section.

5.4 Conclusions

The possibility to produce short carbon fibre reinforced-UHTC materials with a gradient composition was investigated. Three composites with different matrix composition were investigated: ZrB_2-SiC-Y_2O_3, ZrB_2-$MoSi_2$ and SiC-Y_2O_3. Each sample was composed by three different layers reinforced respectively with 0 – 20 – 50 % of carbon fibres in order to minimize cracks formation derived from CTE mismatch between the layers. The samples analysed did not present cracks or defects in the interface area between the different layers, demonstrating the feasibility of the process and the versatility of the sheets produced by the new slurry casting method. However, a migration of the liquid phases was observed in all samples, from the bulk layer to the fibres reinforced layer. These phenomena did not produce defects in the contact point between the layers but led to an increase of the chemical reactions between the fibres and the matrix in an area of ≈ 50-100 μm of thickness. These reactions slightly damaged the surface of the fibres and led to a stronger interface between the fibres and the matrix but did not affect the final integrity of the composites.

The three-layered structure allowed to simultaneously investigate three different oxidation behaviours in each sample. The oxidation tests performed at 1650 °C demonstrated the good interaction between the different layers constituting the composites materials. In fact, no cracks were observed due to the different CTE mismatch. However, the oxidation behaviour was different for each sample due to the different matrix composition.

Sample ZSY105, composed by a ZrB_2-SiC-Y_2O_3 matrix showed the formation of a ZrO_2-SiO_2-B_2O_3 film that homogeneously covered the sample. This film was richer of SiO_2 in the first layer and richer in ZrO_2 in the third layer. The ZrO_2 grains were in the form of columnar structures. The formation of this oxidized film acted as a barrier against oxygen diffusion, reducing the oxidation effects. Moreover, the growth of columnar ZrO_2 grains partially filled the holes deriving from fibre degradation.

Sample ZMo15, composed by a ZrB_2-$MoSi_2$ matrix, showed the formation of a SiO_2 film that homogeneously covered the sample and, in the layers reinforced with fibres, filled the holes left from the oxidized fibres improving the oxidation resistance. The high oxidation resistance of these samples was due to the two regions structure. An external

SiO_2 film that completely filled the holes left by the fibres and reduced the oxygen diffusivity and an internal ZrO_2 columnar structure that helped to close the newly formed defects.

Sample SY5, composed by a SiC-Y_2O_3 matrix, showed the same behaviour as the previous two samples on the surface, with the formation of a SiO_2 film covering the sample. In the bulk layer Y_2O_3 elongated grains were present in the glassy film and the resulting oxide was very thin (2 um), while the internal matrix did not show any signs of oxidation. However, the presence of the SiO_2 film was not enough to protect the outer carbon fibres that, in the fibre-reinforced layers, were oxidized in an area of ≈ 200 μm. This led to an increase in porosity and an increase in potential critical failure. The low efficiency of the protective film was also demonstrated from the presence of visible holes on the surface after the oxidation that have not been filled by the SiO_2 phases as observed for the previous samples.

In conclusion, sample ZMo15 showed the best oxidation performance with the lowest mass loss ≈ - 0,5 mg/cm^2 thanks to the rapid formation of a SiO_2 protective film that reduced the oxygen diffusion and thanks to the ZrO_2 grains growth that closed the holes left by the fibre oxidation, reducing the pathways for oxygen diffusion. Sample ZSY105 showed a good oxidation resistance with a mass loss of ≈ - 5 mg/cm^2 thanks to the formation of B_2O_3 layer and the ZrO_2 columnar grains growth that reduced the porosity. Finally, the sample SY5 showed a low oxidation resistance with a mass loss of ≈ - 7 mg/cm^2 due to the inefficient formation of SiO_2 protective film at 1650°C and the impossibility to close the holes left by the fibre oxidation. However, the high mass loss is also due to the low mass increasing due to the oxygen absorption that resulted higher for the ZrB_2 based ceramic (formation of ZrO_2 and B_2O_3).

5.5 References

[1] W.G. Fahrenholtz, E.J. Wuchina, W.E. Lee, Y. Zhou, Ultra-High Temperature Ceramics: Materials for Extreme Environment Applications, Wiley Blackwell, 2014. https://doi.org/10.1002/9781118700853.

[2] P. Galizia, L. Zoli, D. Sciti, Impact of residual stress on thermal damage accumulation, and Young's modulus of fiber-reinforced ultra-high temperature ceramics, Mater. Des. 160 (2018) 803–809. https://doi.org/10.1016/j.matdes.2018.10.019.

[3] W. Lengauer, Transition Metal Carbides, Nitrides, and Carbonitrides, Handb. Ceram. Hard Mater. (2008) 202–252. https://doi.org/10.1002/9783527618217.CH7.

[4] F. Servadei, L. Zoli, P. Galizia, A. Vinci, D. Sciti, Development of UHTCMCs via water based ZrB2 powder slurry infiltration and polymer infiltration and pyrolysis, J. Eur. Ceram. Soc. 40 (2020) 5076–5084. https://doi.org/10.1016/j.jeurceramsoc.2020.05.054.

[5] D. Sciti, S. Guicciardi, A. Bellosi, G. Pezzotti, Properties of a Pressureless-Sintered ZrB2–MoSi2 Ceramic Composite, J. Am. Ceram. Soc. 89 (2006) 2320–2322. https://doi.org/10.1111/J.1551-2916.2006.00999.X.

[6] Z. He, H. Li, X. Shi, Q. Fu, H. Wu, Microstructure and oxidation resistance of SiC-MoSi2 multi-phase coating for SiC coated C/C composites, Prog. Nat. Sci. Mater. Int. 24 (2014) 247–252. https://doi.org/10.1016/J.PNSC.2014.05.005.

[7] A. Vinci, L. Zoli, D. Sciti, Influence of SiC content on the oxidation of carbon fibre reinforced ZrB2/SiC composites at 1500 and 1650 °C in air, J. Eur. Ceram. Soc. 38 (2018) 3767–3776. https://doi.org/10.1016/j.jeurceramsoc.2018.04.064.

[8] A. Vinci, L. Zoli, P. Galizia, D. Sciti, Influence of Y2O3 addition on the mechanical and oxidation behaviour of carbon fibre reinforced ZrB2/SiC composites, J. Eur. Ceram. Soc. 40 (2020) 5067–5075. https://doi.org/10.1016/j.jeurceramsoc.2020.06.043.

[9] A. Vinci, L. Zoli, P. Galizia, D. Sciti, Influence of Y2O3 addition on the mechanical and oxidation behaviour of carbon fibre reinforced ZrB2/SiC composites, J. Eur. Ceram. Soc. 40 (2020) 5067–5075. https://doi.org/10.1016/j.jeurceramsoc.2020.06.043.

[10] A. Vinci, L. Zoli, E. Landi, D. Sciti, Oxidation behaviour of a continuous carbon fibre reinforced ZrB2–SiC composite, Corros. Sci. 123 (2017) 129–138. https://doi.org/10.1016/j.corsci.2017.04.012.

6 Complex shapes properties

6.1 Introduction

As previously explained (Chapter 2.3.6), UHTCMCs are usually densified by hot pressing or spark plasma sintering [1,2]. However, these techniques allow to obtain only simple shapes that require machining with diamond abrasives or dedicated cutting tools. One approach to obtain complex shapes include flash sintering [3]. Nowadays, this method allows to obtain complex shapes but it does not allow to obtain UHTCMCs samples, which are more commonly densified by repeated cycles of pressure-less sintering [4]. For these reasons, for the fibro-reinforced UHTC materials the most used densification methods to obtain complex shapes are the Hot- Pressing or the Pressure-less sintering.

In this chapter, different processing alternatives were investigated, exploiting the versatility and flexibility of the sheets. Moreover, Hot Pressing with special moulds and pressure-less sintering methods were used to consolidate samples with complex shapes. In detail, four different process variants were investigated:

1) A zig- zag fibre microstructure, obtained applying the hot pressing not parallel but perpendicular to the pile-up direction. The possibility to dispose sheets along different orientations (e.g. vertically instead of horizontally) allowed to reproduce a kind of different fibre disposal that influenced the mechanical properties [5] (sample Z3-40-Z)
2) Squared shaped tile with a ZrB_2-rich matrix in the centre and SiC-rich in the edges, to reproduce a prototype where the hottest part is the inner throat (sample Z3-40-Q).
3) A flat washer with double matrix compositions, SiC-rich in the centre and ZrB2-rich matrix in the border, piling up the layers as the zig-zag sample and consolidating them by hot pressing with a special mould (Z3-40-C).
4) Conical shape sample, in which green sheets were wrapped around a cone as to obtain a hollow conical shape, similar to a nosecone. Conical shapes were consolidated by pressure-less sintering [6].

6.2 Characterization of the samples

Similar to previous described samples, after densification, the density was measured through the Archimede's method. Samples were cut and polished and cross sections were analysed by optical or SEM analysis in order to observe the fibres/layers orientation and distribution. In order to investigate the characteristics of the different sample configurations, the mechanical properties were investigated. Most specifically, the flexural strength was calculated for the sample Z3-40-Z and Z3-40-Q and not for the sample Z3-40-C due to its dimension and shape that were not suitable for the production of bars with the characteristics required for the tests.

6.2.1 Zig-zag sheets orientation

In chapter 4, a new process to fabricate UHTC short carbon fibre reinforced materials sintered by Hot-Pressing was presented. During this process, the green layers were overlapped and the pressure was applied perpendicularly to the sheets. In this paragraph, samples with a vertical layer orientation sintered by Hot-Pressing (Fig. 6.1) were investigated.

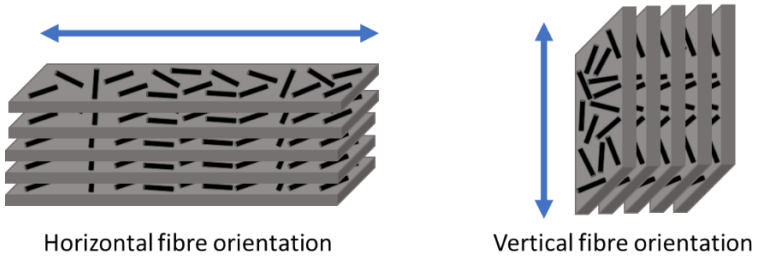

Fig. 6.1: Different sheets orientation, horizontal sheets orientation (left) and vertical sheets orientation (right).

To compare the effects of the layer's orientation, the same composition used for the samples in chapter 4 was used. Ceramic matrices composed by ZrB_2-85 vol. %, SiC- 10 vol. %, Y_2O_3-5 vol. % reinforced with short pitch-based carbon fibres with a length of 3 mm were used (as reported in Table. 6.1) Even for this sample, the sintering was conducted by HP at a temperature of 1900 °C with a pressure of 30 MPa.

Table. 6.1: Sample composition, theorical density, experimental density and relative density.

Sample label	Composition	Carbon fibres (% vol)	Fibres length (mm)	ρ_{exp} (g/cm^3)	ρ_{teo} (g/cm^3)	ρ_{rel} (%)
Z3-40-Z	ZrB_2- 85 vol% SiC- 10 vol% Y_2O_3- 5 vol%	40	3	3.9	4.3	93

The sample obtained showed a final density of 3.9 g/cm^3, with a ρ_{rel} of 93 %, indicating a good level of densification. After sintering, the top view (x-y axis) and the side view (x-z axis) were investigated by optical microscope (Fig. 6.2). On the top of the sample, it was possible to observe a vertical line structure due to the layers orientation that were not well pressed from the side, thus resulting in less homogenization between them (Fig. 6.2-a). On the side view, it was possible to observe a non-homogeneous fibre distribution with a visible layer folding in the middle (Fig. 6.2.-b). This phenomenon was caused by the empty space between the sheets that resulted in the sheets bending. In fact, the "green" height was ≈ 30.0 mm before the HP and ≈ 5 mm after the sintering, so a high amount of empty space was present and filled during the sintering.

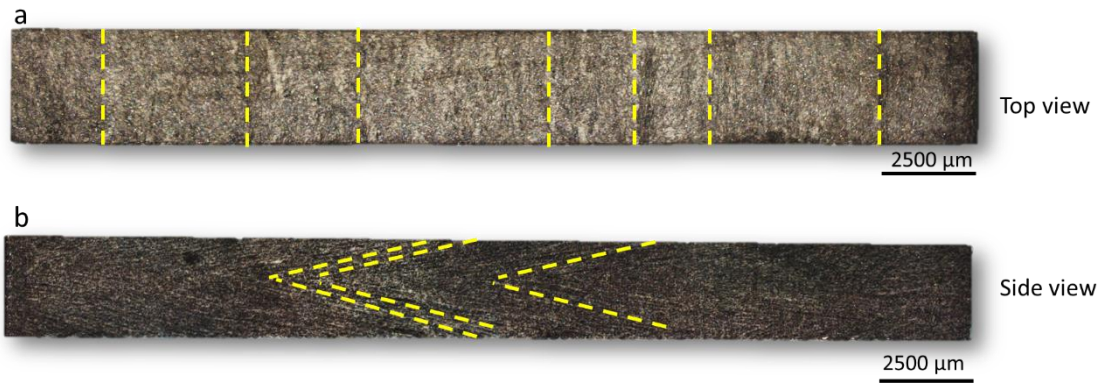

Fig. 6.2: Optical image of the Z3-40-Z sample, (a) top view, (b) side view.In yellow the sheets trend.

In SEM images we, it was observed the zig-zag fibre disposal caused by the sheets bending during sintering (Fig. 6.3-a,b). This bending caused fibre agglomerations generating some defects in the samples, as visible in (Fig. 6.3-c). Even for this sample - as noted for the samples in chapter 4 - the matrix was homogeneous, and the carbon fibres maintained their shape (Fig. 6.3-d).

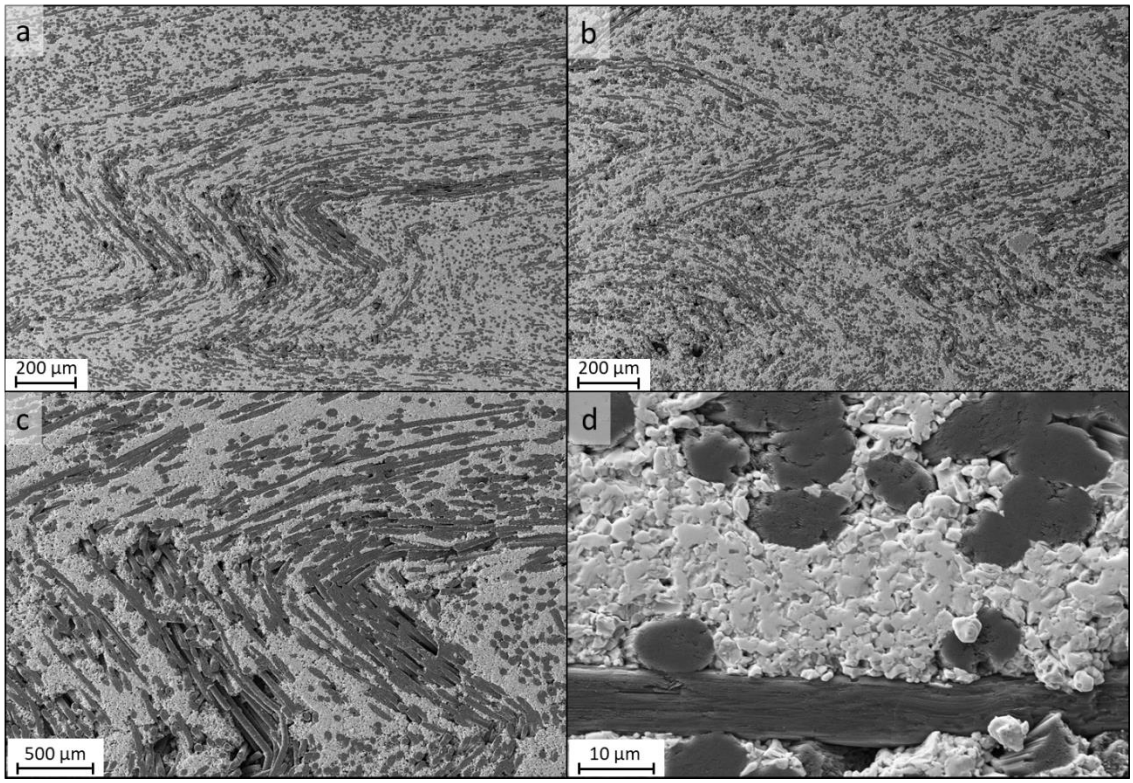

Fig. 6.3: Cross section surface morphologies of sample Z3-40-Z observed at SEM with different magnification

- Zig-Zag mechanical properties

In Table. 6.2 the flexural strength in MPa at room temperature of the Z3-40-Z sample via ISO 14704:2016 were reported. As mentioned in Chapter 4, the bending strength of the fibre-reinforced UHTC composites was lower than the corresponding bulk ceramics [7]. The sample possessed an average value of strength of 130 MPa and an elastic deformation typical of ceramic samples. An interesting comparison can be made between the sample described above and the sample with horizontals sheets orientation obtained in Chapter 4 which possesses the same matrix composition and only a little difference in the fibre amount. Sample Z3-40-Z possessed a little higher value of flexural strength - 120 MPa compared with 111 MPa - despite the presence of fibre agglomeration observed in the

sheets bending area, suggesting that a different fibre distribution could improve the mechanical properties.

Table. 6.2: Flexural strength of the sample Z3-40-Z in MPa and the average value for the sample Z3-35 analysed in Chapter 4.

Sample	σ (MPa)
1	143.0
2	141.9
3	106.7
4	126.9
Average	130 ± 17
Z3-35 (Chapter 4)	111 ± 12

The load displacement curves (Fig. 6.4-a) showed a typical elastic deformation, as observed in Chapter 4 for the samples with an amount of fibre lower than 50 vol. %, followed by a pseudo-plastic behaviour, likely due to the fibre bridging phenomenon [8]. Moreover, this effect could reduce the stress intensity at the crack tip. The comparison between the load displacement curves of the samples Z3-40-Z and Z3-35 (Fig. 6.4-b) showed the higher value in flexural strength for the samples with the vertical sheets' orientation. In addition, it was possible to notice a difference in the curves slope with low load (< 20 N) where the sample Z3-40-Z exhibited a lower slope. Even though quantifying this change in a four-point bending setup is difficult, some comparisons can be made among these specimens; the same behaviour was observed by comparing the sample with 35 vol. % of carbon fibre reinforcement with samples reinforced with 50 vol. % of carbon fibres in Chapter 4, suggesting that this difference in slope could be attributed to the difference of fibre content or in a possible transition from a plastic to an elastic-plastic behaviour due to the different sheets' orientation.

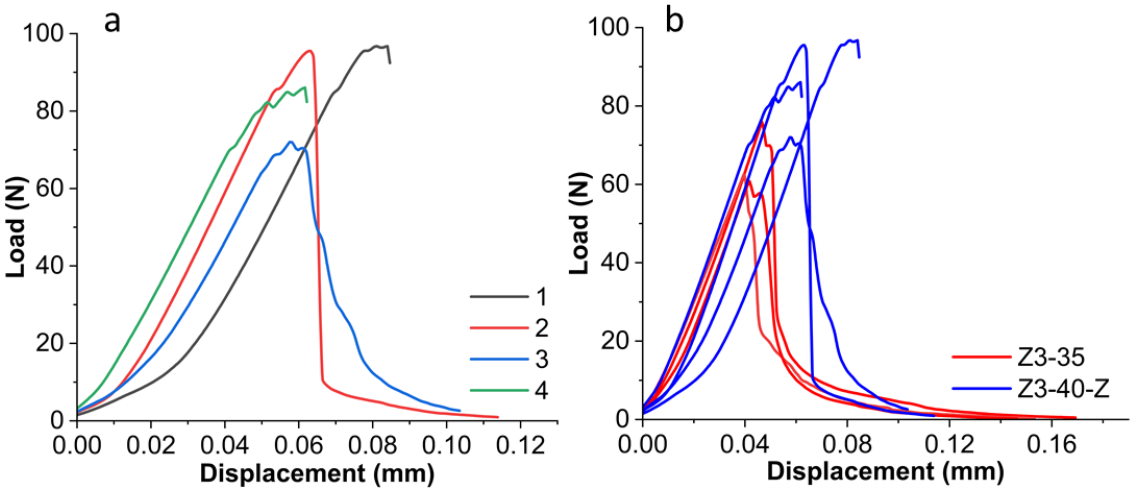

Fig. 6.4: (a) Load displacement curves for the 4-point fracture toughness strength of sample Z3-40-Z; (b) Comparison of the load displacement curves for the 4-point fracture toughness strength of the sample Z3-40-Z and Z3-35.

6.2.2 Double composition square

This tile was designed to have an inner part with ZrB_2 rich matrix and a lighter external part, with a SiC rich matrix (Table. 6.3). This configuration resembles that of a nozzle, where the throat is the part that has to resist to higher temperatures. The sample was fabricated producing 50 x 50 mm^2 sheets with a matrix of ZrB_2-35 vol. %, SiC- 60 vol. %, Y_2O_3-5 vol. % reinforced with 40 vol. % of short pitch-based carbon fibres with a length of 3 mm (ZSY605) and 50 x 50 mm^2 sheets with composed by ZrB_2-85 vol. %, SiC- 10 vol. %, Y_2O_3-5 vol. % reinforced with 40 vol. % of short pitch-based carbon fibres with a length of 3 mm (ZSY105).

All layers were punched with a 30 x 30 mm^2 punch. ZrB_2-rich squares with dimensions 30 x 30 mm^2 were then inserted into 50 x 50 mm^2 SiC-rich squares with the squared hole in the centre. The sample was sintered by Hot-pressing at a temperature of 1900 °C with a pressure of 30 MPa.

Table. 6.3: Sample composition, theorical density, experimental density and relative density.

Sample label	Outer composition (ZSY605)	Inner composition (ZSY105)	Cf (% vol)	Cf length (mm)	ρ_{exp} (g/cm^3)	ρ_{teo} (g/cm^3)	ρ_{rel} (%)
Z3-40-Q	ZrB_2-35vol% SiC-60vol% Y_2O_3-5vol%	ZrB_2-85vol% SiC-10vol% Y_2O_3-5vol%	40	3	3.3	3.8	87

The obtained sample had a final density of 3.3 g/cm^3, with a ρ_{rel} of 87 %. This suggests that some defects or voids remained after sintering, most probably at the interface between the two compositions. Looking at the samples (Fig. 6.5), it was possible to notice a clear detachment at the interface between the inner and the outer square which the sintering pressure did not close.

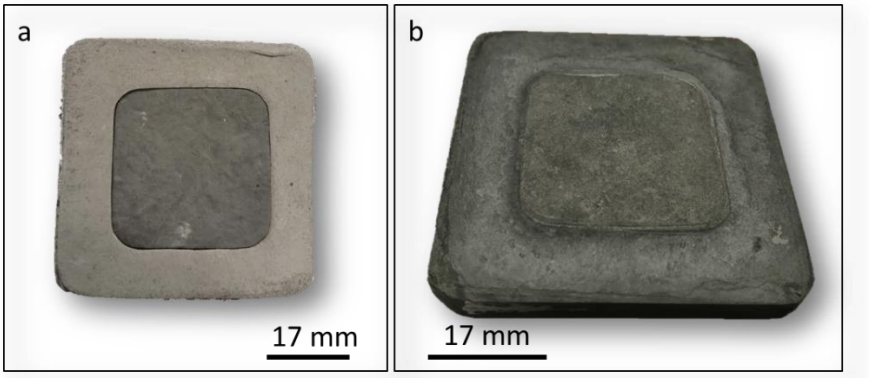

Fig. 6.5: Images of (a) "Green" and (b) sintered Z3-40-Q sample composed by an inner square 30 x 30 mm of ZrB_2-85 vol. %, SiC- 10 vol. %, Y_2O_3-5 vol. % reinforced with 40 vol. % of short pitch-based carbon fibres with a length of 3 mm and an outer square 50 x 50 mm of ZrB_2-35 vol. %, SiC- 60 vol. %, Y_2O_3-5 vol. % reinforced with 40 vol. % of short pitch-based carbon fibres with a length of 3 mm.

The outer part, composed of the SiC-rich composition, showed a matrix without visible micro or macro defects with a ZrB_2 grains, light grey, immersed in a SiC matrix, dark grey (Fig. 6.6-b). Moreover, the unjagged round shape of the carbon fibre (Fig. 6.6-a), indicates that almost no reaction occurred between fibres and matrix during sintering. [8]. Also, the inner square – with the ZrB2-rich composition - showed (Fig. 6.6-d) a good

matrix density without macro defects with SiC grains, dark grey, immersed in a ZrB_2 matrix, light grey. Even in this part of the sample, the carbon fibres maintained their round shape (Fig. 6.6-c). The low interaction between the fibre and the matrix observed in both the compositions, confirmed the versatility and the affordability of the new slurry casting process presented in Chapter 4.

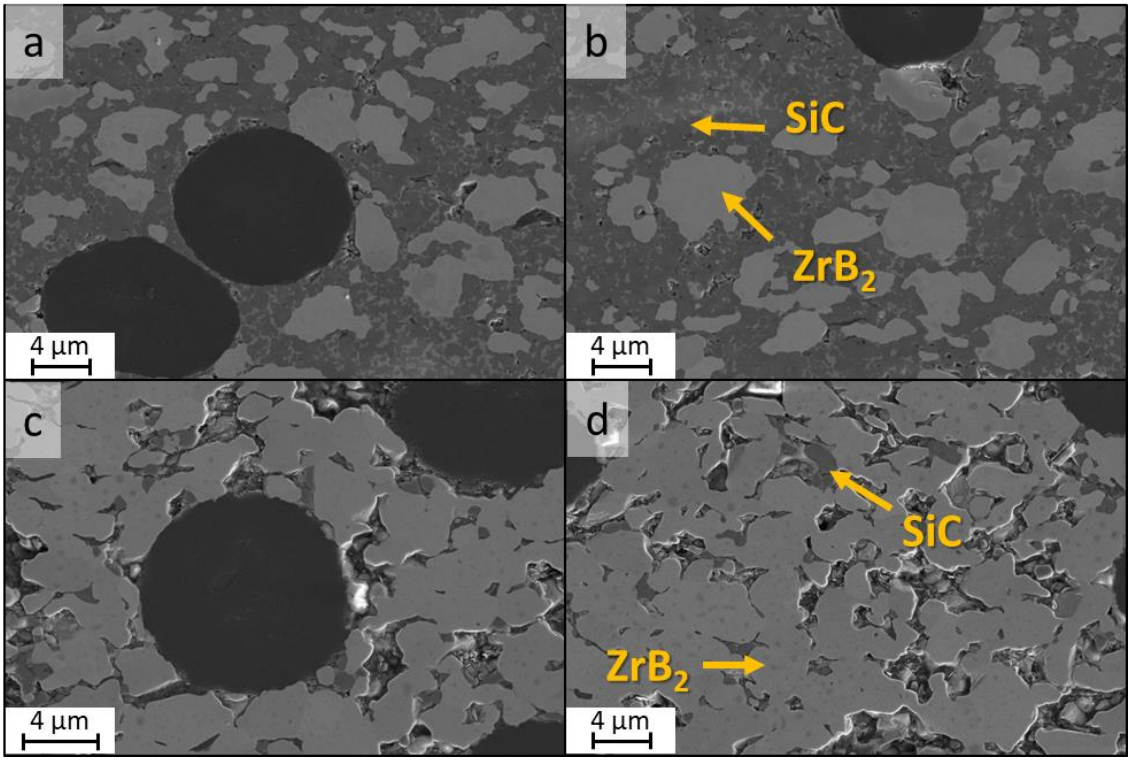

Fig. 6.6: Cross section surface morphologies of the sample Z3-40-Q. (a,b) ZSY605 area, (c,d) ZSY105 area.

With SEM analysis, the border area between the two compositions were investigated (Fig. 6.7). The interface was not straight but showed a jagged profile. Indeed, the juxtaposition of the sheets was not perfect but there were overlaps or gaps, which created defects. Very likely, during sintering the applied pressure deformed the sheets and their expansion caused a collision between the sheets with different composition, thus generating ripples or dips which led to the fibre agglomeration and defects formation. Noteworthy, despite these defects, no cracks were formed.

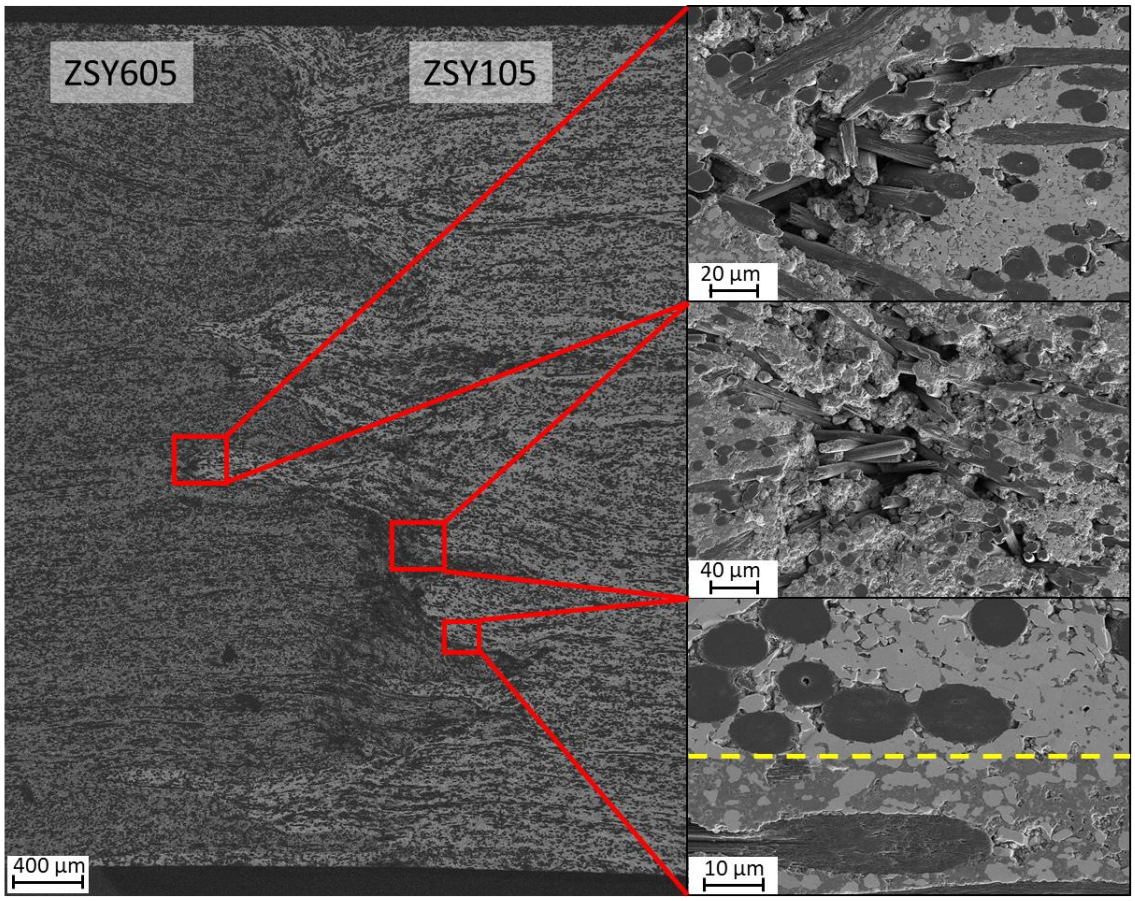

Fig. 6.7: Cross section surface morphologies of sample Z3-40-Q at the interaction between the ZSY605 and ZSY105 areas.

- Double-square mechanical properties

To evaluate the mechanical properties of the sample Z3-40-Q, three different areas were tested via ISO 14704:2016 standard. In fact, due to its structure, three different areas could be identified. Bars were machined from external square with ZrB_2-rich composition, from the inner square, rich in SiC and at the interface, as depicted in Fig. 6.8.

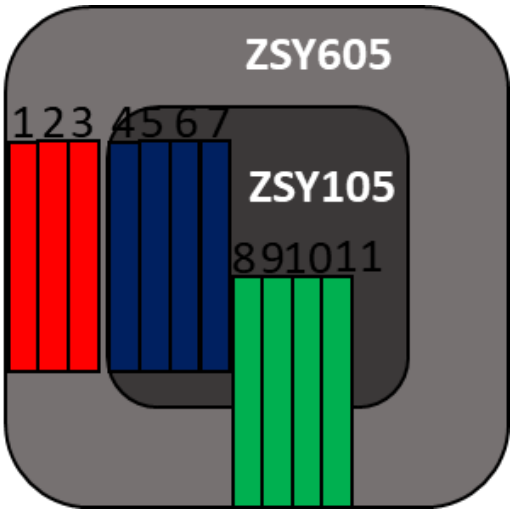

Fig. 6.8: Schematic representation of the sample Z3-40-Q with the bar's distribution. Red bars for the ZSY605 area, Blue for the ZSY105 area and Green for the interface area.

The values of flexural strength at room temperature of the sample Z3-40-Q were reported in Table. 6.4. The samples obtained by the areas called ZSY605 and ZSY105 showed a similar average value of ≈ 85 MPa and ≈ 98 MPa, respectively. The specimens obtained at the interface were characterized by a significantly lower strength, ≈ 45 MPa, suggesting an accumulation of defects at the interface.

Table. 6.4: Flexural strength of the sample Z3-40-Q in MPa with the value divided in three different parts, ZSY605, ZSY105 and Interface.

Sample	σ (MPa)
1	62.2
2	100.1
3	91.2
ZSY605	85 ± 20
4	114.6
5	90.7
6	85.2
7	101.2
ZSY105	98 ± 13
8	34.6
9	41.2
10	79.1
11	25.3
Interface	45 ± 24

The load displacement curves are reported in Fig. 6.9 and are divided for the three different areas. The load displacement curves for the ZSY605 area (Fig. 6.9-a) showed a typical elastic deformation behaviour with a decrease of the slope near the top of the curve, which was attributed to fibre pull-out; this behaviour was more marked for the ZSY105 area (Fig. 6.9-b). In one of the cases (bar 4), the trend observed was similar to that observed for the samples Z3-50 as seen in Chapter 4, where the curve was divided in two parts. The first part with a constant slope represented the linear elastic behaviour and the second part showed the pseudo plastic behaviour. The load displacement curves for the interface area (Fig. 6.9-c) presented low values and a predominantly elastic behaviour more typical of brittle ceramics.

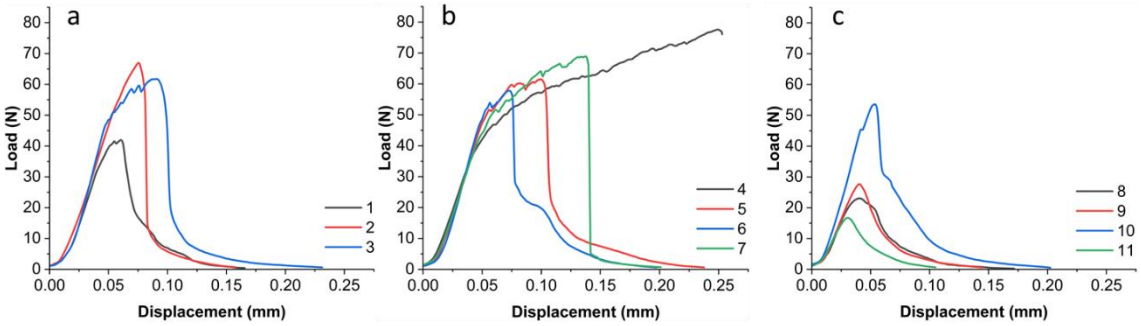

Fig. 6.9: Load displacement curves for the 4-point flexural strength of sample Z3-40-Q (a) ZSY605 area (b) ZSY105 area (c) Interface area.

The morphologies of the fracture surface of the Interface bars after bending tests were investigated (Fig. 6.10). In the images, the fibres can be seen clearly, indicating a good pull-out behaviour. In general, the strong interfacial interaction in ceramic matrix composites would result in a brittle fracture. In this case, the interaction between fibres and matrix did not lead to fibre degradation and the fibres maintained their shape as observed in with SEM analyses. In principle, these characteristics should favour a more damage tolerant behaviour [9]. However, in this case the value of flexural strength was considerably lower, ≈ 45 MPa. This happened probably because of the defects observed in the SEM images (Fig. 6.7) that have weakened the matrix and generated a preferential crack route.

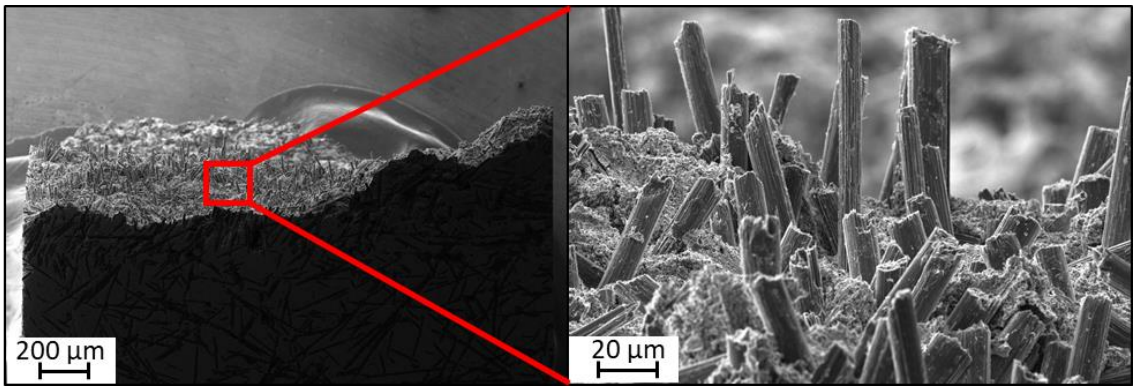

Fig. 6.10: fracture surface after bending test of the bar obtained from the Interface area of sample Z3-40-Q

6.2.3 Washer shape

In the previous paragraphs (6.2.1 and 6.2.2), the possibility to produce a sample with sheets in vertical orientation or with different composition but not a vertical

interaction between the different materials was investigated, showing interesting results. For these reasons, the production of a cylinder constituted by two different compositions and with the vertical oriented sheets was investigated. The sample was composed by a cylinder with outer diameter of $Ø_{out}$= 60 mm, and inner diameter of $Ø_{in}$= 30 mm. The outer matrix consisted of ZrB_2-35 vol. %, SiC- 60 vol. %, Y_2O_3-5 vol. % reinforced with 40 vol. % of short pitch-based carbon fibres with a length of 3 mm in the inner part (ZSY605) and the inner matrix consisted of ZrB_2-85 vol. %, SiC- 10 vol. %, Y_2O_3-5 vol. % reinforced with 40 vol. % of short pitch-based carbon fibres with a length of 3 mm in the outer part (ZSY105) (Table. 6.5). To produce this structure, the different sheets were overlapped in vertical direction around a central piston and subsequently debonded and sintered by HP at 1900 °C with a pressure of 20 MPa.

Table. 6.5: Sample composition, theorical density, experimental density and relative density.

Sample label	**Inner composition (ZSY605)**	**Outer composition (ZSY105)**	**Cf (% vol)**	**Cf length (mm)**	**ρ_{exp} (g/cm^3)**	**ρ_{teo} (g/cm^3)**	**ρ_{rel} (%)**
Z3-40-C	ZrB_2-35vol% SiC-60vol% Y_2O_3-5vol%	ZrB_2-85vol% SiC-10vol% Y_2O_3-5vol%	40	3	3.9	4.3	91

The obtained sample (Fig. 6.11) had a final density of 3.9 g/cm^3, with a ρ_{rel} of 91 % which indicated a quite good densification during the sintering. In fact, there were no visible macro defects or macro cracks on all the surfaces (Fig. 6.12). In particular, the interface between the two-composition was homogeneous.

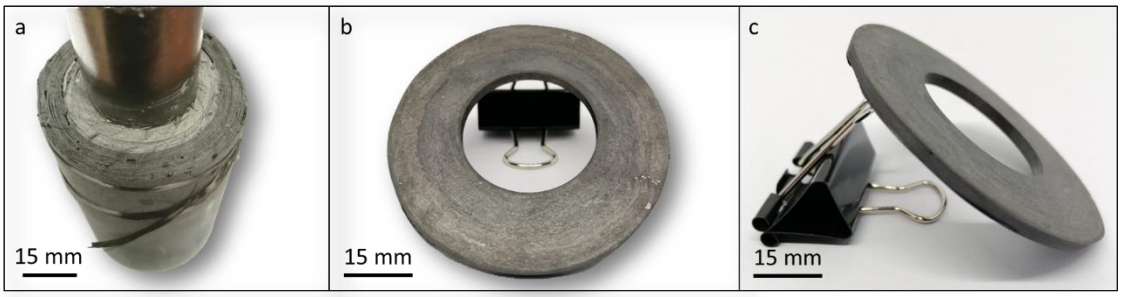

Fig. 6.11: Images of the (a) "green" and (b), (c) sintered Z3-40-C sample composed by ZrB_2-85 vol. %, SiC- 10 vol. %, Y_2O_3-5 vol. % reinforced with 40 vol. % of short pitch-based carbon fibres with a length of 3 mm in the inner part and ZrB_2-35 vol. %, SiC- 60 vol. %, Y_2O_3-5 vol. % reinforced with 40 vol. % of short pitch-based carbon fibres with a length of 3 mm in the outer part.

From SEM images it was immediately possible to notice a structure like the one observed for the sample Z3-40-Z in paragraph 6.2.1, which was created by multiple sheets bending. The sheets which made up the sample were folded, especially in the middle and - as assumed before - this happened because the empty space between the sheets was filled during sheets bending. In this case the "green" height was ≈ 31.90 mm before the HP and ≈ 3.05 mm after the sintering.

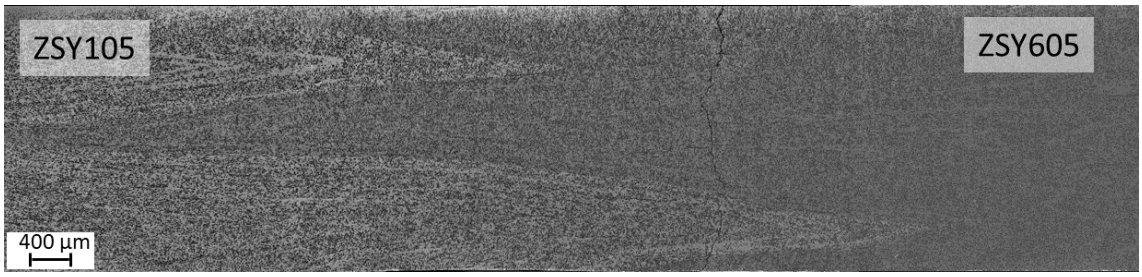

Fig. 6.12: SEM image of the side view/cross section of the sample Z3-40-C.

The external part consisted of a matrix of ZrB_2-85 vol. %, SiC- 10 vol. %, Y_2O_3-5 vol. % reinforced with carbon fibre (Fig. 6.13-b) without visible defects at the micron scale, with SiC grains, dark grey immersed in the ZrB_2 grain, light grey. In this area, the carbon fibres kept their round shape even after the sintering (Fig. 6.13-a), indicating the low interaction between fibre and matrix and probably improving the pull-out effect and the mechanical properties, especially the resistance to cracks propagation [8]. Also, the inner part, consisting of a matrix of ZrB_2-35 vol. %, SiC- 60 vol. %, Y_2O_3-5 vol. % reinforced with carbon fibre (Fig. 6.13-d), showed a good matrix surface without micro or macro defects

composed by ZrB_2 grains, light grey, immersed in SiC, dark grey. Even in this area, the carbon fibres maintained their shape (Fig. 6.13-c), indicating the absence of reaction between the fibre and the matrix. No fibre agglomeration or macro defects were present at the interface between the two compositions (Fig. 6.13-e). Moreover, by increasing the magnification (Fig. 6.13-f), it was possible to observe that the interaction between the two different matrices was homogeneous and without defects, in spite of the CTE mismatch.

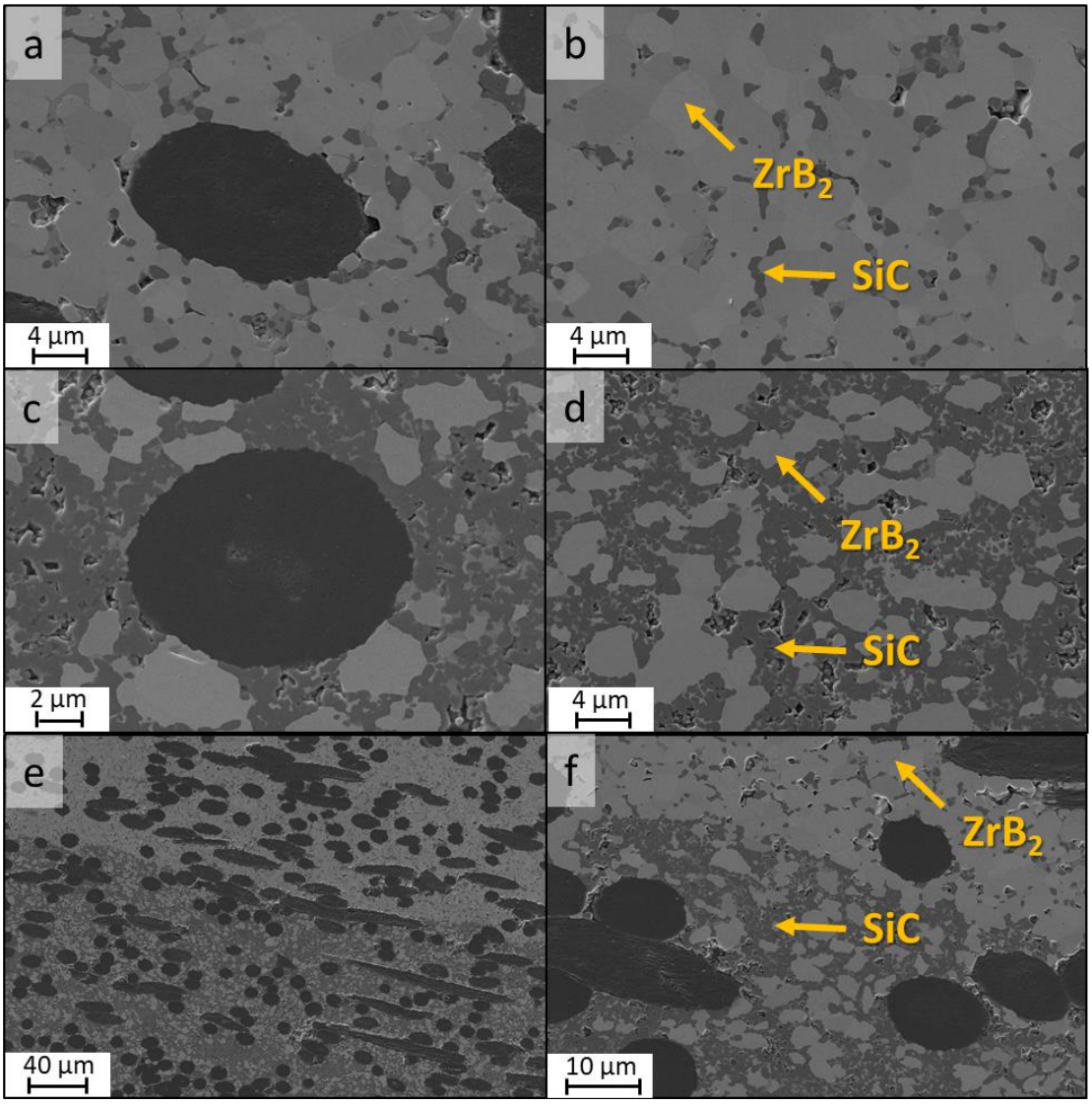

Fig. 6.13: Cross section surface morphologies of sample Z3-40-C. (a,b) external area composed by ZrB_2-85 vol. %, SiC- 10 vol. %, Y_2O_3-5 vol. % reinforced with carbon fibre, (c,d), internal area composed by ZrB_2-35 vol. %, SiC- 60 vol. %, Y_2O_3-5 vol. % reinforced with carbon fibre (e,f).

6.2.4 Pressure-less cone

Some interesting shapes for the aerospace field are the cones due to their similarity with the spacecrafts nosecones. For this reason, the UHTCMCs are the ideal material for this application [10]. The flexibility of the "green" UHTCMCs sheets observed in Chapter 4 is a fundamental parameter for the fabrication of samples with complex shapes. In fact, this property allows to use a mould to give the samples a shape. The steps for the fabrication of a cone starting from the UHTCMCs sheets are reported in Fig. 6.14. The sheets were composed by a matrix of ZrB_2-85 vol. %, SiC- 10 vol. %, Y_2O_3-5 vol. % reinforced with 40 vol. % of short pitch-based carbon fibres with a length of 3 mm and obtained with the slurry casting process explained in Chapter. 4. Five green sheets were wrapped around a rigid cone and were vacuum bagged in order to obtain a good adherence between the UHTCMC material and the mould. Subsequently, the "green" sample could be pressed with a cold isostatic press (CIP) at 2000 bar to obtain a joint between the different sheets and consolidate the shape. The obtained sample – owning its shape to the mould - was then subjected to debonding at 300 °C in air in order to remove the organic dispersant. Finally, the sample was sintered in a pressure-less oven at a temperature of 1900 °C under argon atmosphere.

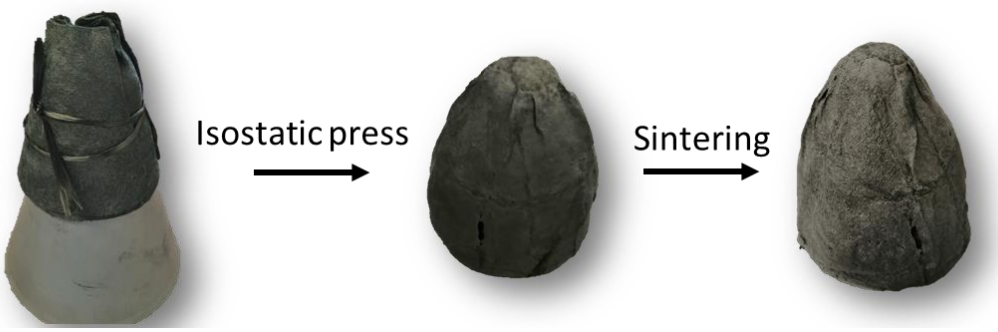

Fig. 6.14: Steps for the fabrication of a cone by pressure-less sintering. From left to right are shown the green layers around the mould, the green after the pressing with CIP and the sample after sintering at 1900 °C.

As visible in Fig. 6.15, the sample obtained presented an internal smooth surface thanks to the mould surface. However, the external surface resulted covered by ripples. In fact, the UHTCMCs sheets acted like paper sheets and during the pressing the sheets folded in the external direction. Despite this problem, the different layers composing the samples resulted well attached to each other.

Fig. 6.15: Sintered images of the obtained cone

6.2.5 Hybrid process (SI + LSI)

The production of a near-net shape UHTCMCs for aerospace application is an important area of investigation to reduce machining costs and enable a faster processing of complex structures. In literature, the production of UHTCMC materials via 3D printing is reported in a few papers with interesting results. However, this method allows to introduce a low amount of fibre reinforcement (< 10 vol. %) [11–13].

The process described in Chapter 4, allowed to introduce a high amount of carbon fibre in a ceramic slurry. The slurry obtained presented a good fibre dispersion without agglomeration. Moreover, it maintained its “liquid” state with the possibility to pour it in a mould with a complex shape. However, the use of a large size mould (more than one sheet) generated green samples with a high porosity (>50-60%).

The Polymer Infiltration and Pyrolysis (PIP) is a method for the fabrication of CMCs or UHTCMCs comprising an infiltration of a low viscosity polymer into the reinforcing ceramic structure (e.g.: fabric) followed by pyrolysis, e.g., heating of the polymer precursor in absence of oxygen to decompose and convert it into a ceramic [14]. The low viscosity of the polymer allows it to penetrate in all the samples and reduce the final porosity.

In the following paragraph a sample produced by slurry casting with a large size dimension was subjected to a PIP process in order to reduce its internal porosity.

As polymer precursor, the polycarbosilane (SMP 10) was used. After the pyrolysis, this polymer leaves a SiC matrix. To investigate the possibility to introduce a polymer precursor inside a green obtained via slurry casting, a sample with a pyramidal shape e.g., similar to a wedge, was infiltrated and subjected to four cycles of PIP (Table. 6.6). In each cycle, a high amount of polymer was introduced inside the green resulting in a sample mass improvement. This proved that the PIP could reduce the porosity in the sample.

Table. 6.6: Cycle of PIP with the amount of polymer introduced in the sample, mass loss after the pyrolysis at 1050 °C and the green mass before and after the cycle.

PIP cycle	Green mass (g)	Polymer used (g)	Mass loss after pyrolysis (%)	Green mass after Pyrolisis (g)
1	16.1	7.6	8.9	21.6
2	21.6	11.1	16.2	28.1
3	28.1	6.9	5.8	33.0
4	33.0	6.6	8.3	36.3

The final sample presented an external surface without visible defects and wich manteined the green shape (Fig. 6.16). The initial porosity was decreased from 50-60% to 30-40%. Although the matrerial is still under microstructural analysis for a proper determination of microstructural features and residual porosity,, the results obtained suggest that this method is very interesting for future development of complex shapes with large sizes.

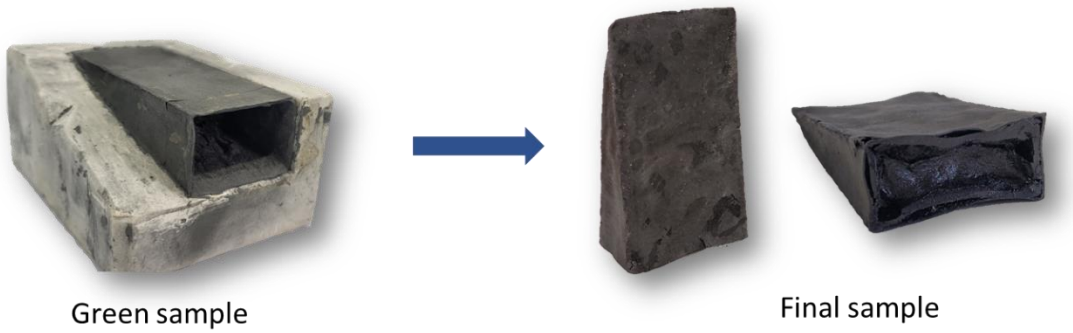

Fig. 6.16: Images of the green sample and of the sample after four cycles of PIP.

6.4 Conclusions

Different methods for the production of complex structures were investigated. More in detail, the possibilities to use different layers overlapping orientation, to produce "complex" shapes with the Hot pressing as sintering method and the production of UHTCMC cones by pressure-less sintering were studied. The production of samples by hot pressing with the use of a vertical UHTCMCs layer orientation showed that the layer resulted to be bending like a paper sheet due to the empty space between them. This bending phenomenon generated some fibres agglomeration and some defects in the matrix. However, the final sample resulted stable and without macro defects thus demonstrating the possibilities to change the layer orientation. The use of HP as sintering mechanism to obtain samples with more complex shapes was investigated through the sample Z3-40-Q and Z3-40-C. The production of a square sample with 2 different matrix compositions (sample Z3-40-Q) showed that the different composition areas possess a good densification but the interface between them was characterized by fibre agglomeration and macro defects that weakened the entire structure even though the interaction between the two different matrices was good. The production by hot pressing of a cylinder sample with a double matrix composition with a vertical layer orientation, sample Z3-40-C, showed a good interaction between the different layers and the sheets bending typical of the vertical orientation observed for the sample Z3-40 Z. Moreover, no significant fibre agglomeration that could weaken the sample were present. This opened up to the possibility to make a cylinder sample with an appropriate mould by hot pressing thanks to the vertical layer orientation. The investigation of samples with a nozzle like shape obtained by pressure-less sintering showed the possibility to obtain a

good final sample thanks to the flexibility of the UHTCMCs sheets obtained by the slurry casting process with short fibres. The main step in this process was the pressing through cold isostatic press, which allows to model the UTCMC material around a mould. The main disadvantage of this process was the presence on the external surface of macro defects.

Among the materials obtained, the mechanical properties of the samples Z3-40-Z and Z3-40-Q were tested through four-point bending strength. The sample Z3-40-Z - with its vertical layer orientation - presented a higher flexural resistance (130 MPa) than the sample obtained with a horizontal layer orientation (110 MPa) in spite of the presence of fibre agglomeration and voids in the matrix. This indicated that a different layer orientation can influence the final mechanical properties. For the samples Z3-40-Q, three different areas were investigated due to their different composition. The internal and external areas, ZSY105 and ZSY605 respectively, showed the typical fibre-reinforced ceramic behaviour with the ZSY105 samples that presented an interesting pseudo plastic-behaviour. The Interface area showed a very low value of flexural strength (45 MPa), due to the defects present between the two squares constituting the sample.

6.5 References

[1] W.G. Fahrenholtz, G.E. Hilmas, I.G. Talmy, J.A. Zaykoski, Refractory diborides of zirconium and hafnium, J. Am. Ceram. Soc. 90 (2007) 1347–1364. https://doi.org/10.1111/J.1551-2916.2007.01583.X.

[2] A. Snyder, D. Quach, J.R. Groza, T. Fisher, S. Hodson, L.A. Stanciu, Spark Plasma Sintering of ZrB2–SiC–ZrC ultra-high temperature ceramics at 1800 °C, Mater. Sci. Eng. A. 528 (2011) 6079–6082. https://doi.org/10.1016/J.MSEA.2011.04.026.

[3] C. Manière, G. Lee, E.A. Olevsky, Flash sintering of complex shapes, Appl. Mater. Today. 26 (2022) 101293. https://doi.org/10.1016/J.APMT.2021.101293.

[4] C. Manière, L. Durand, A. Weibel, C. Estournès, Spark-plasma-sintering and finite element method: From the identification of the sintering parameters of a submicronic α-alumina powder to the development of complex shapes, Acta Mater. 102 (2016) 169–175. https://doi.org/10.1016/J.ACTAMAT.2015.09.003.

[5] J.M. Hausherr, M. Eitel, W. Krenkel, Determination of material properties for short fibre reinforced C/C-SiC, MATEC Web Conf. 29 (2015). https://doi.org/10.1051/matecconf/20152900005.

[6] W.G. Fahrenholtz, E.J. Wuchina, W.E. Lee, Y. Zhou, Ultra-High Temperature Ceramics: Materials for Extreme Environment Applications, Wiley Blackwell, 2014. https://doi.org/10.1002/9781118700853.

[7] Z. Nasiri, M. Mashhadi, A. Abdollahi, Effect of short carbon fiber addition on pressureless densification and mechanical properties of ZrB2-SiC-Csf nanocomposite, Int. J. Refract. Met. Hard Mater. 51 (2015) 216–223. https://doi.org/10.1016/j.ijrmhm.2015.04.005.

[8] R. Khan, Fiber bridging in composite laminates: A literature review, Compos. Struct. 229 (2019). https://doi.org/10.1016/j.compstruct.2019.111418.

[9] J.W. Hutchinson, H.M. Jensen, Models of fiber debonding and pullout in brittle composites with friction, Mech. Mater. 9 (1990) 139–163. https://doi.org/10.1016/0167-6636(90)90037-G.

[10] D. Sciti, L. Zoli, T. Reimer, A. Vinci, P. Galizia, A systematic approach for horizontal and vertical scale up of sintered Ultra-High Temperature Ceramic Matrix Composites for aerospace – Advances and perspectives, Compos. Part B Eng. 234 (2022) 109709. https://doi.org/10.1016/J.COMPOSITESB.2022.109709.

[11] J. Lu, D. Ni, C. Liao, H. Zhou, Y. Jiang, B. Chen, X. Zou, F. Cai, Y. Ding, S. Dong, Fabrication and microstructure evolution of Csf/ZrB2-SiC composites via direct ink writing and reactive melt infiltration, J. Adv. Ceram. 10 (2021) 1371–1380. https://doi.org/10.1007/s40145-021-0512-z.

[12] J.W. Kemp, A.A. Diaz, E.C. Malek, B.P. Croom, Z.D. Apostolov, S.R. Kalidindi, B.G. Compton, L.M. Rueschhoff, Direct ink writing of ZrB2-SiC chopped fiber ceramic composites, Addit. Manuf. 44 (2021). https://doi.org/10.1016/j.addma.2021.102049.

[13] Z. Zhang, R. Liu, W. Li, Y. Liu, H. Luo, L. Zeng, J. Qiu, S. Wang, Direct writing of continuous carbon fibers/epoxy thermoset composites with high-strength and low energy-consumption, Addit. Manuf. 47 (2021) 102348. https://doi.org/10.1016/J.ADDMA.2021.102348.

[14] F. Servadei, L. Zoli, P. Galizia, A. Vinci, D. Sciti, Development of UHTCMCs via water based ZrB2 powder slurry infiltration and polymer infiltration and pyrolysis, J. Eur. Ceram. Soc. 40 (2020) 5076–5084. https://doi.org/10.1016/j.jeurceramsoc.2020.05.054.

7 Braking properties

7.1 Introduction

One possible field of application for the UHTCMCs is the use as friction material. In fact, UHTCs were also considered for tribological applications in several works [13–17]. Brake materials for the use in vehicles, require high and stable coefficient of friction (COF), low wear rate, low life cycle cost, low weight, good noise, vibration and harshness properties (NVH) and a high degree of freedom in the structural design [18,19]. Brakes are commonly used in a pad on disc configuration. The most common disc materials include steel, carbon-carbon (C/C) and carbon fibre reinforced carbon-silicon carbide (C/C-SiC). Steel brakes are used prevalently for standard automotive; they are cheap, possess a relatively high and stable coefficient of friction and present low wear rate [20]. However, they are not indicated for high-performance applications, where operating temperatures are high (≈ 400 °C [21]). C/Cs discs are used especially in aircrafts and racing vehicles e.g., formula 1 and formula E. They possess a low density (<2 g/cm^3) and are capable to absorb huge amounts of energy in a short time [22]. However, C/C materials start to oxidize at 600 °C and present low COF in wet or cold conditions due to the lubrication ability of graphite [22,23]. C/C-SiC are used in high performance cars [24]. They exhibit high wear resistance, quite high oxidation resistance and a high COF in different weather conditions at the expense of weight and limited operating temperature [23]. They are usually paired with organic or metallic pads with some research being carried out on ceramic pads for full-ceramic brake systems [25,26] but with C/C-SiC pads present high thermal conductivity issues. The introduction of different ceramic phases could ensure broader adjustment of tribological properties. For example, the presence of SiC increase the coefficient of friction, the thermal shock resistance and the environmental stability [27] but at the same time increase wear rate due to its abrasive action and decrease the fatigue resistance [28,29]. The carbon fibres play the role of a lubricant to prevent occlusions during braking; the hybrid ceramics increase friction resistance, for example ZrB_2 can rapidly form an oxide layer during braking to prevent carbon fibre oxidation. Their effects result in more stable braking performants [30]. For these reasons carbon fibre reinforced -ZrB_2-based materials could be a new class of materials for braking applications.

In this chapter the tribological behaviour of two different carbon fibre reinforced, UHTC-ZrB_2 based materials was investigated on C/C-SiC, Steel and C/C discs. The COF, wear and temperatures were recorded at different braking pressures of 1 and 3 MPa. Beside the composites produced with the short fibres, a set of samples fabricated with continuous fibre preforms was also produced and tested for comparison purposes. SEM, EDX and XRD analysis have been carried out in order to determine the friction layer formation and explain corresponding tribological results.

7.2 Braking samples

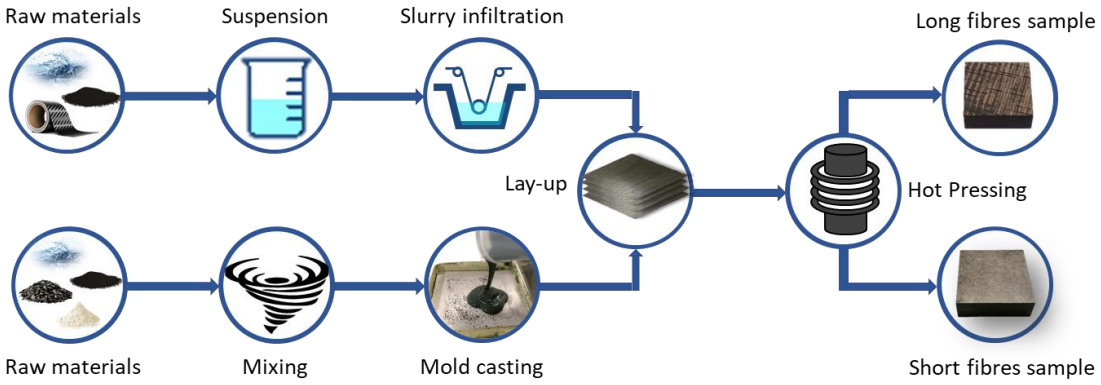

Fig. 7.1: Flow chart of the processes used to obtain the samples with long fibres (top) and chopped fibres (bottom) reinforcement

All UHTCMC sample materials investigated were composed of a matrix of ZrB_2-85 vol. %, α-SiC- 10 vol. % and a little amount of Y_2O_3-5 vol. %. As a reinforcement, pitch-based based high modulus (HM) carbon fibres were used with the same volume percentage.

Two types of pad materials were studied:

1) ZrB_2-10%SiC-5%Y_2O_3 ceramics reinforced with ≈ 40 vol % pitch-based carbon fibre fabric arranged in 0°/90° directions (ZL).
2) ZrB_2-10%SiC-5%Y_2O_3 ceramics reinforced with ≈ 35 vol % randomly orientated chopped pitch-based carbon fibre with length of 5 mm (ZS).

The samples were produced by slurry based techniques followed by hot-pressing sintering (Fig. 7.1):

1) The continuous fibre reinforced composites were fabricated via slurry infiltration of the fibre bundles; the unidirectional fibre layers were piled up in a 0°/90°

configuration to get a XY-plane fibre orientation. The samples were hot pressed at 1900 °C using a pressure of 35 MPa, in accordance with previous studies [31].

2) The short fibre reinforced samples were prepared via slurry casting of chopped fibres. According to the process described in Chapter 4. The layers with random XY-plane fibre orientation were piled up and hot pressed at 1900 °C using a pressure of 35 MPa, as reported for the process in chapter 4.

The samples compositions are summarized in Table. 7.1. To obtain the final sample dimensions, the material was cut, and the surface was ground (ZL with Ra= 2.858 ± 2.027; Rt= 19.04 ± 14.22 and ZS with Ra= 0.609 ± 0.166; Rt= 3.55 ± 1.00) to obtain 10 mm thick pads with a surface area of 900 mm^2 (30 mm x 30 mm) (Fig. 7.2).

Table. 7.1: Matrix composition in the samples, contents and length of carbon fibres and their orientation.

Sample (unit)	**ZrB_2 (vol %)**	**SiC (vol %)**	**Fibre amount (vol %)**	**Fibre length (mm)**	**Fibre distribution**
ZL	85	15	40 ± 5	fabric	0°/90°
ZS	85	15	35 ± 5	5	random

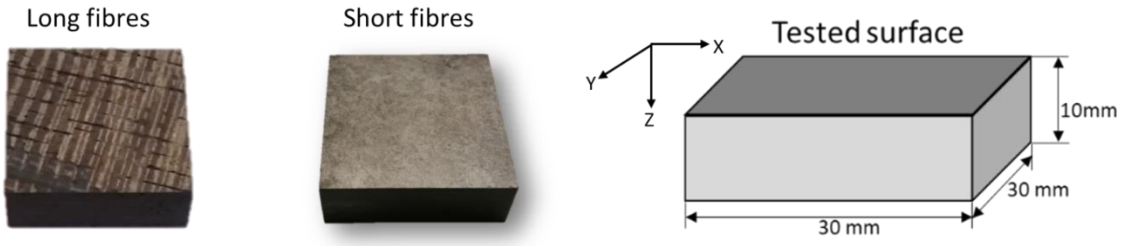

Fig. 7.2: Macro and schematic images of the samples before testing.

In Table. 7.2 bulk densities, open porosities and the mechanical properties, flexural strength and fracture toughness, are reported.

Table 7.2: Summary of the mechanical properties of ZL and ZS samples.

Sample	Density (g/cm^3)	Residual porosity (%)	Bending strength σ (MPa)	K_{IC} ($MPa \cdot m^{0,5}$)	Fibre volume content (%)
ZL	3,6	9,5	218 ± 30	6,1 ± 0,3	40
ZS	4,1	6	107 ± 13	3,57 ± 0,2	35

Sample ZL (long fibres) presented better mechanical (bending strength and fracture toughness) properties than the sample ZS (short fibres). This can be explained by the better reinforcement provided by the carbon fibre fabric compared to short carbon fibres. Moreover, for the sample ZL, the fabric orientation of 0°/90° further improves the resistance to mechanical load [31]. Due to low difference in the amount of carbon fibre of ≈ 5 vol.%, the samples ZL is characterized by a lower density compared with the ZS samples. An important difference between the samples was the porosity. The samples ZL showed higher porosities probably due to the difficulties in the fabric infiltration relative to the weaving geometry. This problem did not occur with the short fibre samples which possess more freedom and can give a better packing. For this reason, the sample ZS had a lower porosity.

7.3 Tribological tests

Tribological tests were conducted on a self-designed inertia dynamometer. The flywheel is accelerated to 1030 rpm and then switched off. Then the pneumatic brake calliper is engaged with a surface pressure of 1 or 3 MPa to a complete stop. The next cycle is then started immediately.

With each test, two braking pads (30x30x10 mm^3) are tested against commercial and self-made (machined) discs as counterparts:

- Commercial, internally ventilated C/C-SiC brake disc with SiC-rich friction layer (SGL, Germany), friction radius of 184 mm; diameter 400 mm.
- Self-made, solid steel brake disc, constituted by S235 Steel, friction radius of 173 mm; diameter 380 mm.

- Self-made, C/C brake disc, friction radius of 125 mm; diameter 300 mm.

Each braking test consists of 10 braking cycles to a complete stop preceded by 5 pre-braking cycles. Weight and thickness of braking pads were measured to calculate volume and mass wear rates. Temperatures are recorded continuously on the backside of both pads and on the sliding disc surfaces by thermocouples. COF is calculated by continually measuring clamp pressure and braking torque. In Table. 7.3 are summarized the conditions during braking.

Table 7.3: Summary of braking conditions during the tests.

Disc material	**C/C-SiC**	**Steel**	**C/C**
Pad material	ZL + ZS	ZL + ZS	ZL + ZS
cycles per test	10	10	10
Clamp pressure (MPa)	1 + 3	1 + 3	1 + 3
Sliding speed (m/s)	20	18.7	13.5
Friction radius (mm)	184	173	125
Rpm	1030	1030	1030
Energy per cycle (MJ)	≈ 5.4	≈ 5.4	≈ 5.4

During the tribological tests, temperature and coefficient of friction (COF) were collected as function of the braking time. For every braking, the COF trend obtained was calculated as an average COF value for that single braking and reported as a point in the final cumulative test plot. In the same way, for every braking, the temperature trend obtained was calculated as an average value and reported as a point in the final cumulative test plot.

7.3.1 ZL and ZS vs C/C-SiC disc

- ZL pads

The tribological results for the ZL sample (continuous fibres) tested on the C/C-SiC-disc with a pressure of 1 MPa, showed a high friction coefficient of 0.81, Fig. 7.3. The COF (average values for one braking cycle) started at 0.76 and increased slightly with the number of braking cycles to 0.83 for the 10^{th} cycle. The higher temperatures measured at the disc surfaces ranged from 220 °C to 340 °C. The measured temperature was likely lower than the real one due to the distance between pads and thermoelements as well as the not ideal heat transfer to the sliding thermocouples. Single braking cycles showed a very stable COF throughout the braking process and only marginal change with temperature and sliding speed.

With pressure increase to 3 MPa, the friction coefficient lowered to 0.56 (Fig. 7.4) like C/C-SiC discs tested in similar conditions [25,32]. In fact, COF was reduced for higher pressures because small surface defects did no longer impact the friction behaviour. The change in friction coefficient was highest with 0.6 at the second cycle and lowered to 0.52 for the last cycles. Temperatures were higher than the test with 1 MPa of pressure and ranged from 250 °C to about 450 °C for the 10^{th} cycle. This increase in temperature was expected for a higher energy conversion rate. The single braking curves demonstrated a quite stable behaviour with little dependence on temperature in cold conditions (first-second-third braking) in the form of rising COF for low sliding speeds but stabilizing with temperature increase.

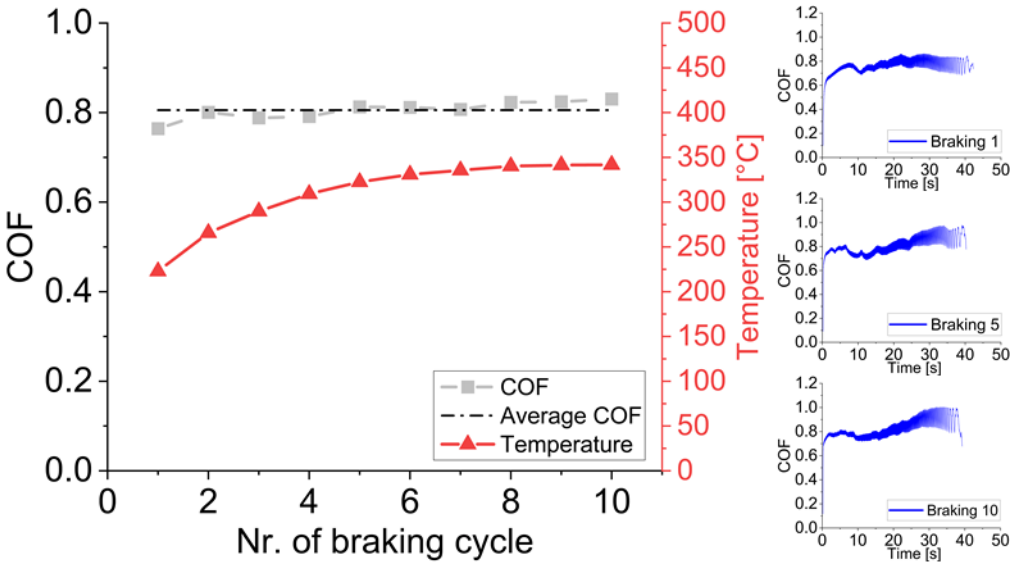

Fig. 7.3: Average friction coefficient of ZL material with the C/C-SiC disc and corresponding disc-temperatures and 1st, 5th and 10th braking curve at 1 MPa.

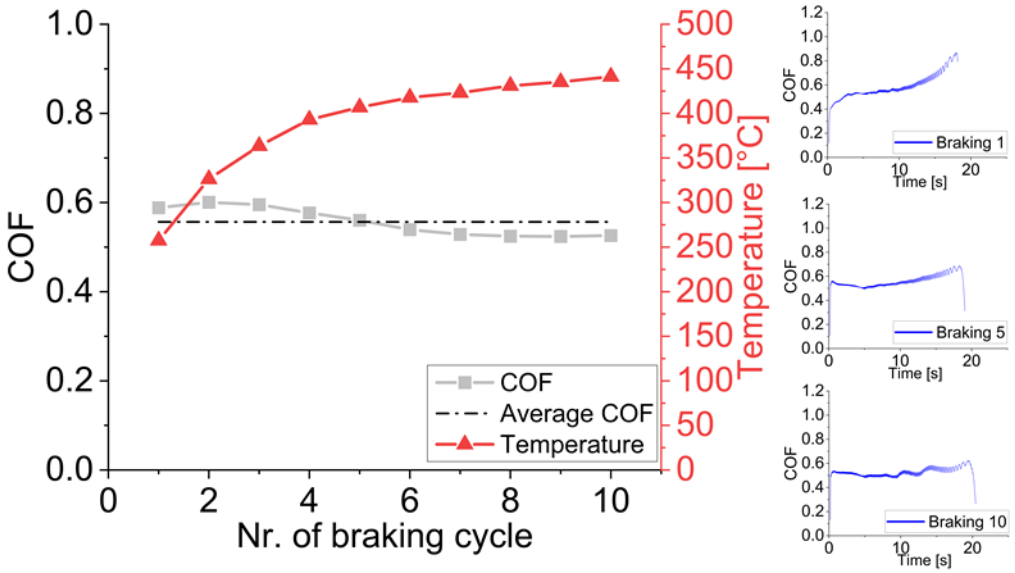

Fig. 7.4: Average friction coefficient of ZL material with the C/C-SiC disc and corresponding disc-temperatures and 1st, 5th and 10th braking curve at 3 MPa.

- ZS pads

Sample ZS (short fibres) was tested only with a pressure of 1 MPa due to severe pad damage during the 3 MPa cycles, as visible in Fig. 7.21. The average COF observed was 0.67 and therefore lower than ZL at 1 MPa (Fig. 7.5). Only the first cycle presented higher COF with 0.715 which lowered then to 0.67. Temperatures were lower than those observed for the sample ZL, as expected from the lower COF, and rose from 200 °C to

300 °C for the 10th cycle. The single friction curves showed a behaviour similar to the ZL samples. In fact, they showed a stable COF and had little dependence on temperature and sliding speed. A small rise of COF was observed for ZL and ZS samples for low sliding speeds under all conditions.

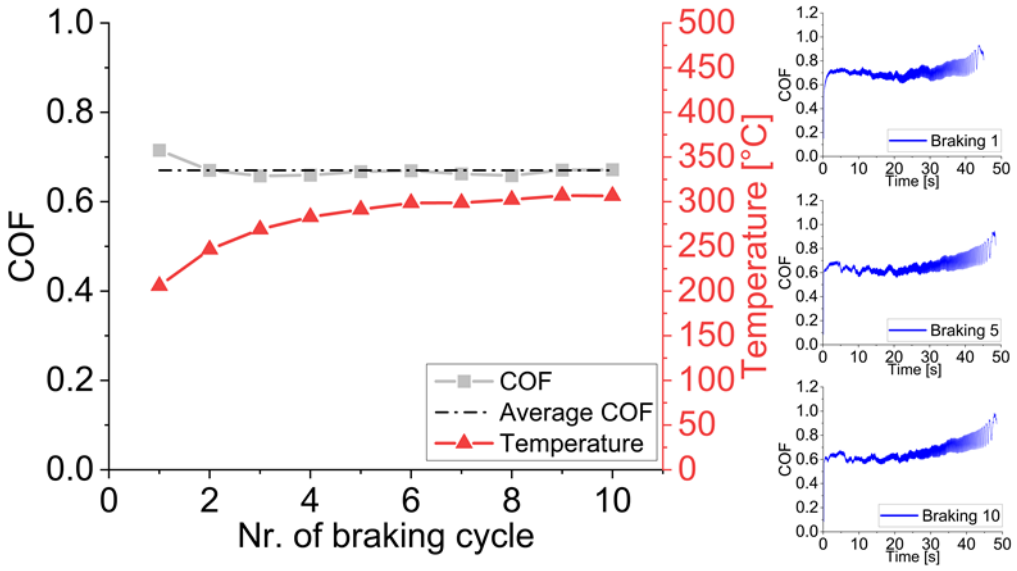

Fig. 7.5: Average friction coefficient of ZS material with the C/C-SiC disc and corresponding disc-temperatures and 1st, 5th and 10th braking curve at 1 MPa.

7.3.2 ZL and ZS vs Steel disc

- ZL pads

The tests conducted on the ZL pads with a steel disc at a pressure of 1 MPa (Fig. 7.6) showed a very high friction coefficient, starting from 0.94 and decreasing to 0.8 for the 10th braking with an average value of 0.86 thus being less stable than paired with the C/C-SiC disc (Fig. 7.3). Opposite to the tests on C/C-SiC discs mentioned earlier, the COF became very low for low sliding speeds in all. The temperature observed was up to 430 °C due to the high COF and solid steel disc used that was not ventilated as was for the C/C-SiC disc.

Tests with a pressure of 3 MPa (Fig. 7.7**)** presented an average COF of 0.4, ranging from 0.5 for the first braking to 0.33 for the 10th braking, much lower compared with the test at 1 MPa because COF decreased at higher pressures, like the previous case. This drop-in friction coefficient could explain the temperatures behaviour, exceeding 440 °C for the last braking. Moreover, this temperature increase was due to the higher energy conversion

rate. As for the 1 MPa tests, the COF dropped low for low sliding speeds after the 3rd braking test.

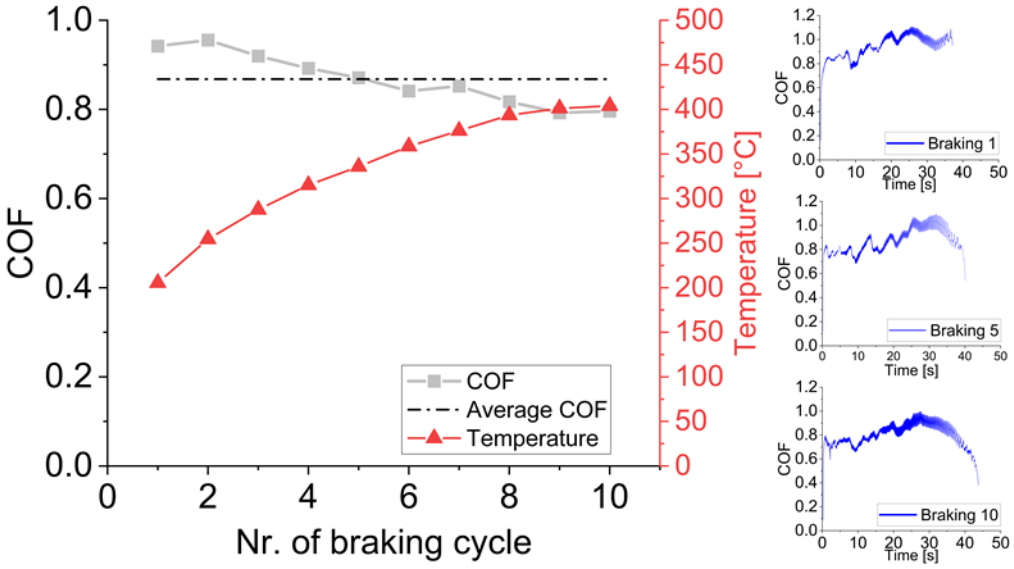

Fig. 7.6: Average friction coefficient of ZL material with the Steel disc and corresponding disc-temperatures and 1st, 5th and 10th braking curve at 1 MPa.

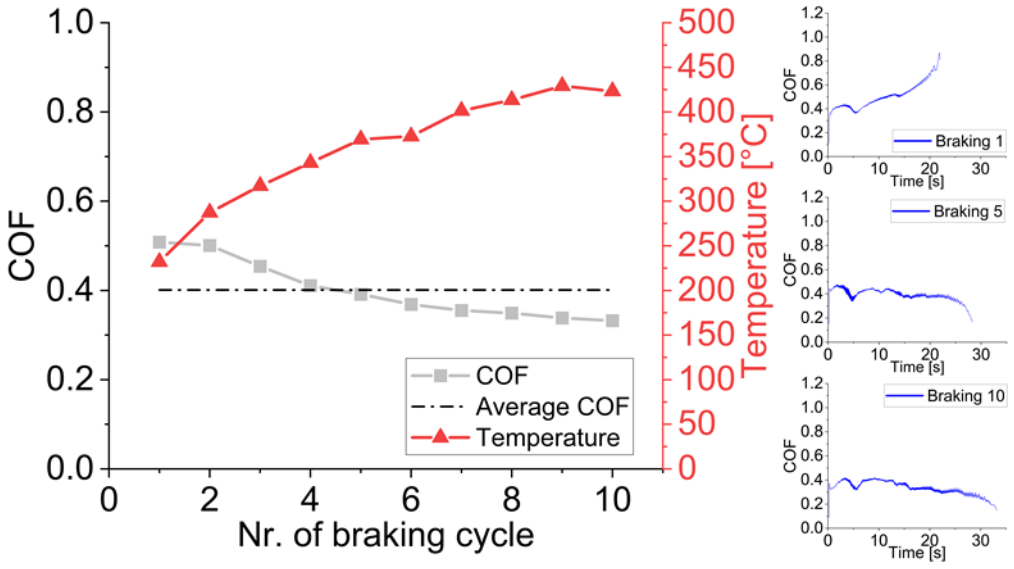

Fig. 7.7: Average friction coefficient of ZL material with the Steel disc and corresponding disc-temperatures and 1st, 5th and 10th braking curve at 3 MPa.

- ZS pads

ZS sample tested with a steel disc (Fig. 7.8) at 1 MPa showed a low average coefficient of friction of 0.56. The COF ranged from 0.60 to 0.55 from first to last braking test, resulting in a stable average. The single braking tests showed a temperature

independent COF behaviour with an increasing in COF value for lower sliding speeds. This was in contrast with the ZL samples (Fig. 7.6) where, for low sliding speeds, the COF dropped down after the 3rd braking test. This behaviour could be the effect of metal-on-metal adhesion between abraded steel from the disc on the pads surface and the disc themselves. The temperatures collected was maximum of 360 °C, lower that the ZL sample due to the lower COF and therefore longer period for heat dissipation.

With 3 MPa tests (Fig. 7.9), the average friction coefficient was significantly lower, 0.43, and also with a quite stable trend with a variation of 0.05 within the braking cycle. This demonstrated the independence of pressure and temperature for the short fibre material, opposite to the ZL pads.

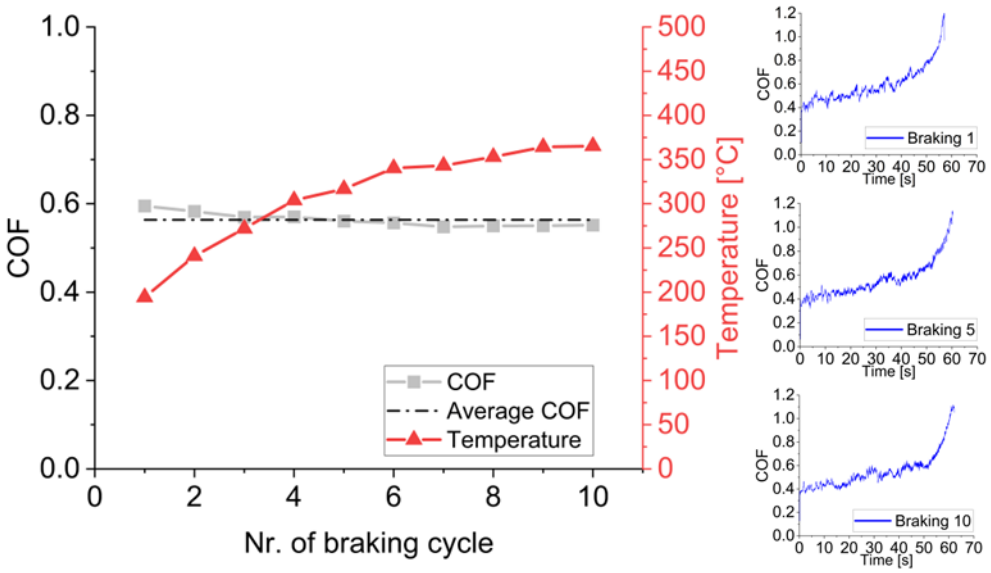

Fig. 7.8: Average friction coefficient of ZS material with the Steel disc and corresponding disc-temperatures and 1st, 5th and 10th braking curve at 1 MPa.

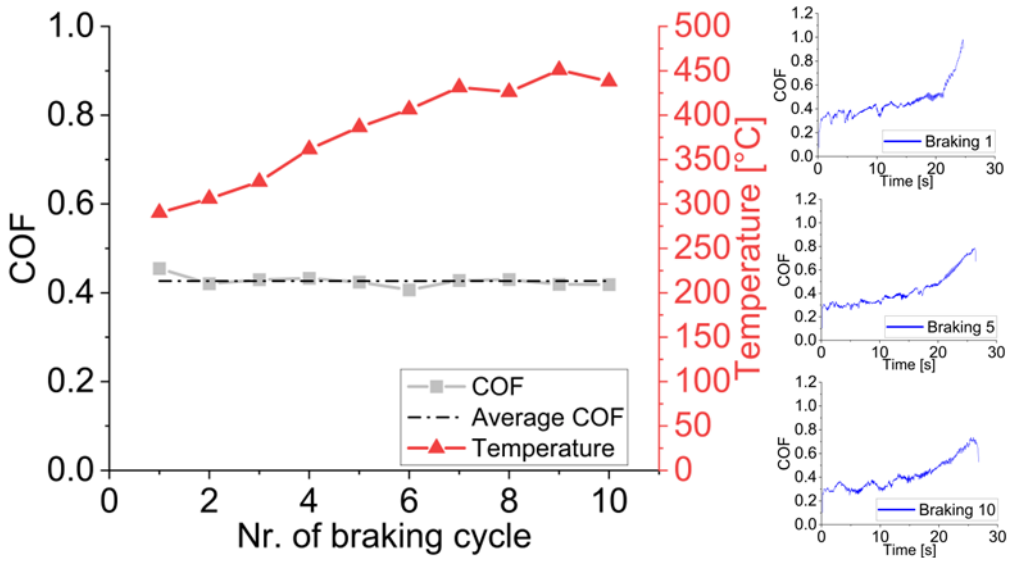

Fig. 7.9: Average friction coefficient of ZS material with the Steel disc and corresponding disc-temperatures and 1st, 5th and 10th braking curve at 3 MPa.

7.3.3 ZL and ZS pads vs C/C disc

- ZL pads

The results obtained during the tests of ZL pads *w*ith C/C disc at 1 MPa showed a relative low coefficient of friction, starting from 0.45, increasing to 0.71 and finally arriving at 0.62 for the 10th braking (Fig. 7.10). Like the behaviour observed for the ZL samples tested with Steel disc, even in this case, the COF dropped low for low sliding speeds after the 3rd braking test. The temperature observed was the higher than the previous disc test, up to ≈ 500 °C due to the not ventilated disc and its low thermal conductivity.

With 3 MPa test (Fig. 7.11), the behaviour of the ZL sample was like the one observed with 1 MPa of pressure. In fact, the COF resulting very low starting from 0.52, increase to 0.72 and finally decreasing at 0.27 for the 5th braking and remaining constant for the remaining brake. In this case the drop of COF was clary visible after the second braking. Probably this was correlated to the temperature reacted. In fact, at temperature around ≈ 450 °C the carbon starts to oxidize creating a different interaction surface between disc and pads, resulting in a different COF. Even for this disc the final COF was lower than the test with 1 MPa because, as mentioned before, for the C/C-SiC disc and Steel disc, the COF is reduced for higher pressures because small surface defects played a lesser role in the overall COF calculation. Even in this case the temperature increasing, ≈ 580 °C,

compared with the test at 1MPa, ≈ 520 °C was due to the higher energy conversion rate. In the single braking tests a temperature dependent COF behaviour was more visible, with a decrease in COF value for lower sliding speeds up to a constant value

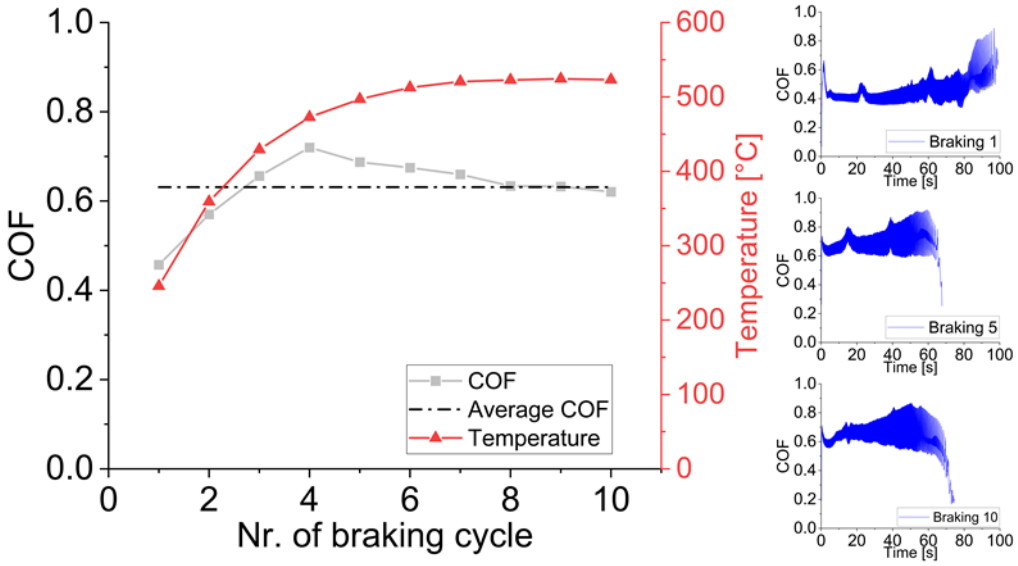

Fig. 7.10: Average friction coefficient of ZL material with the C/C disc and corresponding disc-temperatures and 1st, 5th and 10th braking curve at 1 MPa.

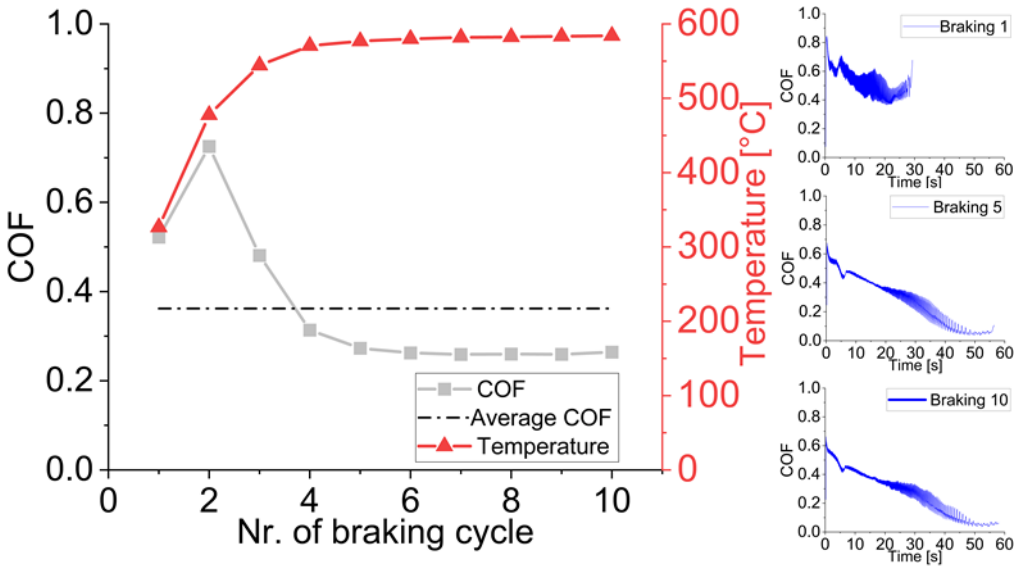

Fig. 7.11: Average friction coefficient of ZL material with the C/C disc and corresponding disc-temperatures and 1st, 5th and 10th braking curve at 3 MPa.

- ZS pads

ZS sample tested with a C/C disc (Fig. 7.12) at 1 MPa showed a quite stable average coefficient of friction of ≈ 0.5, compared with the trend of the sample ZL. The

single braking tests showed a temperature independent COF behaviour with a decrease in COF value for lower sliding speeds after the 3rd braking test. This was in accordance with the ZL samples (Fig. 7.10) The temperatures collected was maximum of 470 °C, lower that the ZL sample due to the lower COF.

With 3 MPa test (Fig. 7.13), similar to ZL samples (Fig. 7.11) the COF passed from 0.34, increasing to 0.47 and finally decreased to 0.29 during the 5th braking, remaining constant. Even for this material, the final COF was lower than the test with 1 MPa. Moreover, as observed for the ZL tested with 3 MPa on C/C disc, at temperature around ≈ 500 °C the COF value dropped because carbon started to oxidize, creating a different interaction surface between disc and pads. Comparing with the test with 1 MPa the temperature increased up to ≈ 560 °C, due to the higher energy conversion rate. As for ZL sample in the single braking tests, COF decreased for lower sliding speeds up to a constant value.

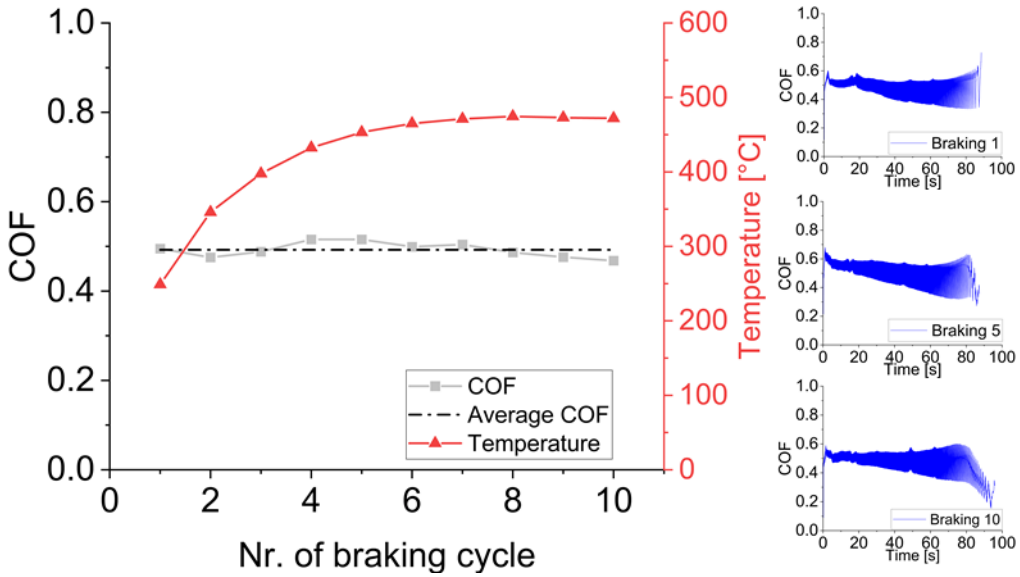

Fig. 7.12: Average friction coefficient of ZS material with the C/C disc and corresponding disc-temperatures and 1st, 5th and 10th braking curve at 1 MPa.

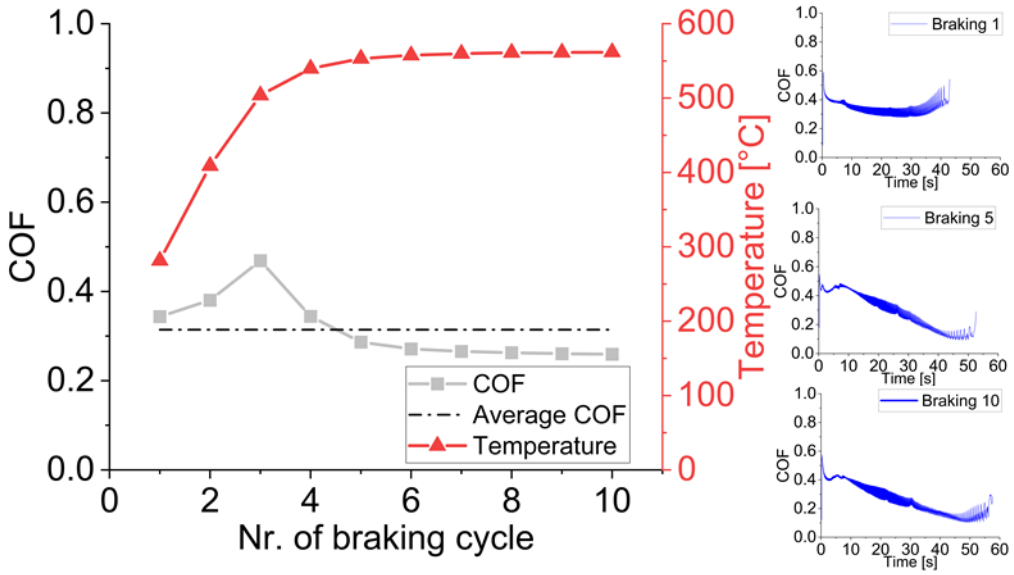

Fig. 7.13: Average friction coefficient of ZS material with the C/C disc and corresponding disc-temperatures and 1st, 5th and 10th braking curve at 3 MPa.

7.4 Wear

Wear was determined by weighing pads before and after the friction tests. In Fig. 7.15 are summarizes the weight changes of the pads.

7.4.1 ZL and ZS pads vs C/C-SiC-disc

Wear tests of pad against C/C-SiC-disc revealed that higher pressures led to significantly higher wear rates for ZL material due to the fact that more energy was converted to wear energy at the same time (Fig. 7.15). In fact, the braking time decreased from about 40 s with a pressure of 1 MPa to about 20 s with a pressure of 3 MPa. Due to the C/C-SiC disc not significantly taking part in the wear process, the loss of material in the pads was higher, e.g. ≈ 317 mg/MJ with 1 MPa and ≈ 450 mg/MJ with 3 MPa. For ZS material, mass wear was even higher, ≈ 692 mg/MJ, due to pad failure during the test with 1 MPa test. This can be seen as small cracks forming in and transversal to the frictional surface (XY-plane) after the 1 MPa test in Fig. 7.14 as well as in the XY-plane leading to material loss throughout the sample.

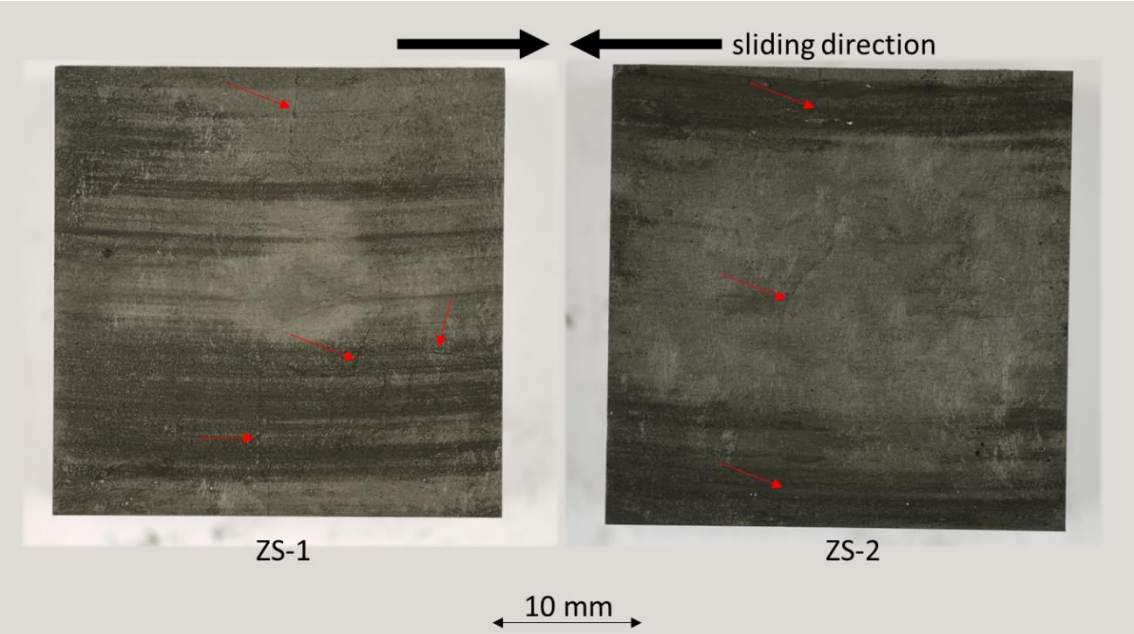

Fig. 7.14: Visible cracks in the ZS material (left and right pads) after testing on the C/C-SiC-Disc with 1 MPa. The sliding direction is from the outside inwards.

7.4.2 ZL and ZS pads vs Steel disc

For the braking cycles with the steel disc, pad wear was significantly reduced, with the disc contributing to the friction film as seen as grooves in the steel disc (Fig. 7.18) and indicating transferred steel material. Also, no signs of failure of the ZS material can be observed which correlates to no visible damage. This might be due to the softer nature of the steel disc with catching material being abraded from the disc. This is not possible for the C/C-SiC disc, which leads to strong local mechanical forces inside the pads which exceed the ZS samples limits. ZS material showed less wear for 1 and 3 MPa tests (≈ 172 mg/MJ and ≈ 246 mg/MJ respectively) than ZL long fibre pads (≈ 202 mg/MJ and ≈ 280 mg/MJ respectively). Even in this case it was observed that higher pressures led to significantly higher wear rates (Fig. 7.15).

7.4.3 ZL and ZS vs C/C disc

Regarding the pads wear against the C/C disc tests, as observed for the previous discs, a higher-pressure led to significantly higher wear rates (Fig. 7.15). In this case a very low pads wear was observed for both ZL and ZS samples, namely ≈ 70 mg/MJ (1MPa) and ≈ 173 mg/MJ (3 MPa) for ZL, ≈ 65 mg/MJ (1 MPa) and ≈ 84 mg/MJ (3 MPa) for ZS. This might be due to lubricant action of C/C debris that reduced the pads wear

significantly. Moreover, even for this disc, no signs of failure of the materials was observed.

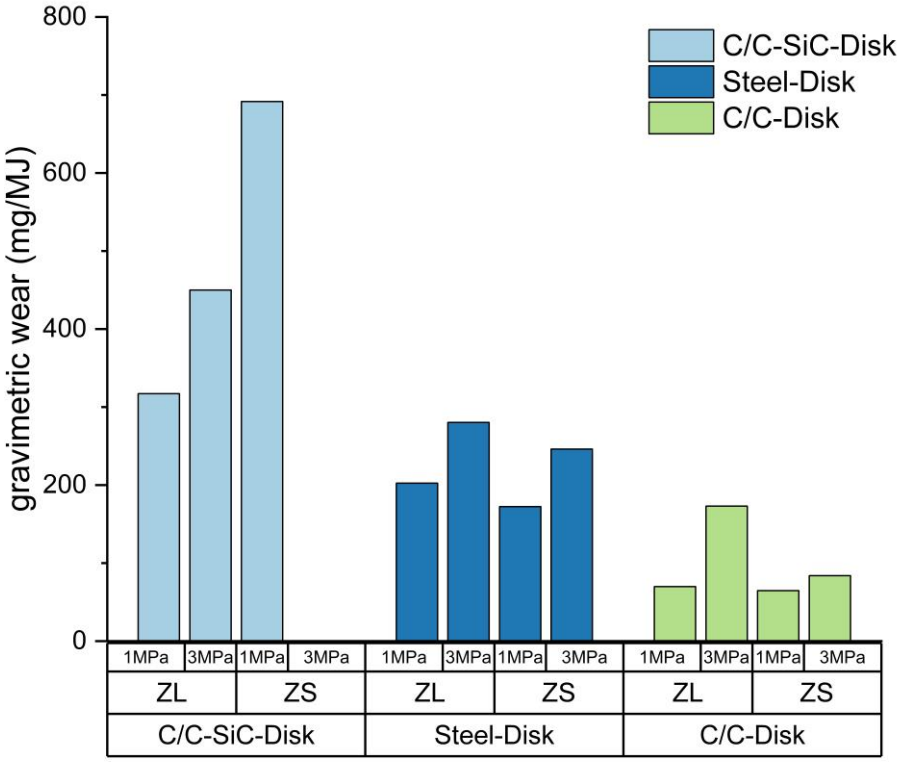

Fig. 7.15: Gravimetric wear of the ZL and ZS pads tested with C/C-SiC, steel and C/C discs.

7.5 Microstructural analysis

The microstructure was analysed before and after the friction tests. Before the tests, the microstructures were analysed on the polished surface by FESEM.

After the friction tests, pad worn surfaces were analysed without further treatment on the XY-surface to investigate the friction layer.

7.5.1 Microstructure of as sintered materials, ZL and ZS

In Fig. 7.16 the microstructures of the samples ZL and ZS before the tribological tests are shown. In the XY surface of the sample ZL, Fig. 7.16-a, the unidirectional fibre

orientation was clearly visible. Moreover, in Fig. 7.16-b, the XZ surface of the sample ZL shows the 0°/90° alternating carbon fibre layers and the presence of the typical excess of matrix in between the fibre layers due to the structure of the sample. The XY surface of the sample ZS is shown in Fig. 7.16-c with the homogeneous and random fibre distribution in the matrix were visible. A homogeneous fibre distribution was also visible in the XZ surface of the sample ZS (Fig. 7.16-d) where an excess of matrix in between layers was not observed.

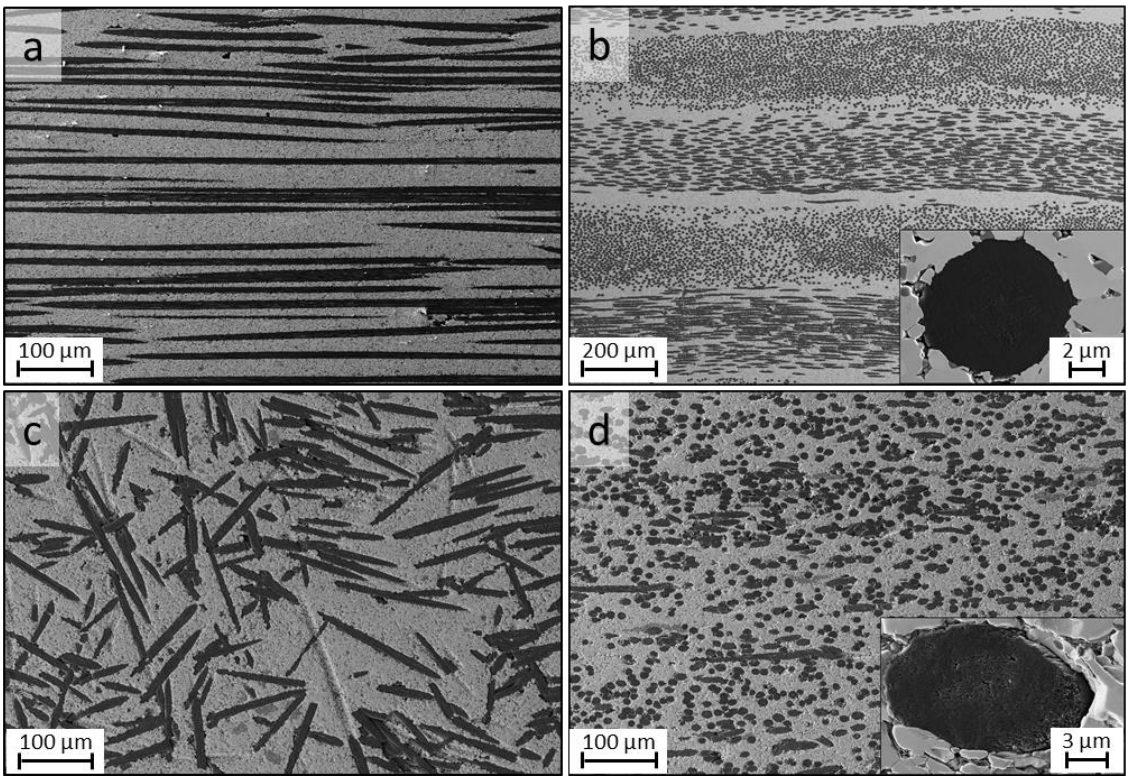

Fig. 7.16: Surface morphologies before the tests. ZL sample: (a) XY plane; (b) XZ plane. ZS sample: (c) XY plane; (d) XZ plane.

7.5.2 Features of worn discs

After the tribological tests, the pads and discs were analysed. In Fig. 7.17 the macro-photographs of the C/C-SiC disc friction surface after the tribological tests with 1 MPa and the ZL sample are reported. The discs used for the testing of ZS samples has a similar appearance (not shown). Neither evident damage, such as missing material, nor grooves could be detected. However, a lot of pad material was transferred to the disc and was visible as a black film. This was in accordance with the wear data collected during the tribological tests that showed high pad wear rates for all tests against the C/C-SiC disc.

Fig. 7.17: C/C-SiC-Disc after braking with ZL sample at 1 MPa. Brake pad material is visible on the surface (black film).

A different situation was visible on the surface of the steel disc after the tribological tests with sample ZL at 1 MPa (Fig. 7.18). In this case the disc presented a lot of scratches and grooves on the surface due to the abrasive action of the pads. The material removed from the disc was transferred to the pad surface and helped the formation of the friction layer. In contrast, no significant amount of pad material was transferred to the disc surface, in agreement with the low measured wear of the pads observed during the tests. The same was observed for the ZS samples and the 3 MPa tests. The light blue tempering colour on the disc surface indicated a temperature during the test of above 320 °C inside the friction radius [33].

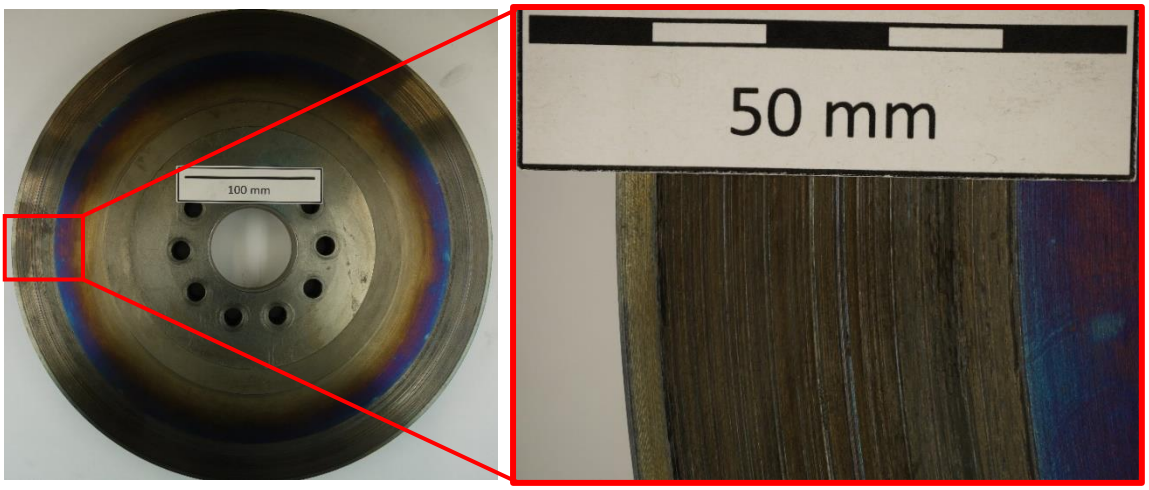

Fig. 7.18: Steel-Disc after braking with ZL material at 1 MPa. Visible groves are present.

The same behaviour observed for the steel disc was visible for the C/C disc after the tribological tests with sample ZL at 1 MPa (Fig. 7.19). In fact, in this case the disc did not present scratches or grooves on the surface but showed a completely abraded area due to the abrasive action of the pads. The material removed from the disc was probably transferred to the pad surface where acted as lubricant polishing the pads surface without damage. Moreover, no pad material was transferred to the disc surface. The same behaviour was observed for the ZS samples and the 3 MPa tests.

Fig. 7.19: C/C-Disc after braking test with ZL material at 1 MPa.

7.5.3 ZL pads morphology vs C/C-SiC

The so-called third body is the friction layer formed between the disc (first body) and the pad material (second body) and has the important function to stabilize the COF and reduce the wear. The abraded material is not removed but “reused” and ground to smaller particles thus acting as a sink for energy and therefore wear.

The surface images of the ZL samples after the tests with the C/C-SiC disc are reported in Fig. 7.20. For both samples, tested with a pressure of 1 MPa (Fig. 7.20-a,c) and 3 MPa (Fig. 7.20-b,d), the presence of a friction layer was visible. Moreover, other parts were partially covered by loose debris. More in detail, Fig. 7.20-c,d shows part of the samples where this layer covered the whole surface. The presence of this stable protective film explained the mean COF being very stable and not dependent on the temperature change and sliding speed. Moreover, considering the trend of the COF for the single test (Fig. 7.3) that showed a quite stable behaviour, it is believed that a significant friction layer was formed during the first braking cycle. More braking cycles may improve the thickness of the friction film, but this difference did not affect the braking properties. Comparing the friction layers of the samples tested at 1 MPa (Fig. 7.20-c) and 3 MPa

(Fig. 7.20-d), the coverage and thickness of the friction film increased with increasing pressure. With the 3 MPa braking tests, a friction layer, consisting of more than one stacked friction layer was visible. This was the result of more than one follow-up braking cycles. This could explain why the mean COF decreased for more than 0.2 with increasing pressure as observed in the COF trend graphic (Fig. 7.4). Probably this happened because when the braking pressure was high enough to cut the asperities, many asperities were sheared and pulverized by impact and shear action between asperities, and a lot of debris was formed. The debris filled the gaps between peaks and grooves and formed a continuous film on the surface resulting in the decrease of coefficient of friction and friction resistance.

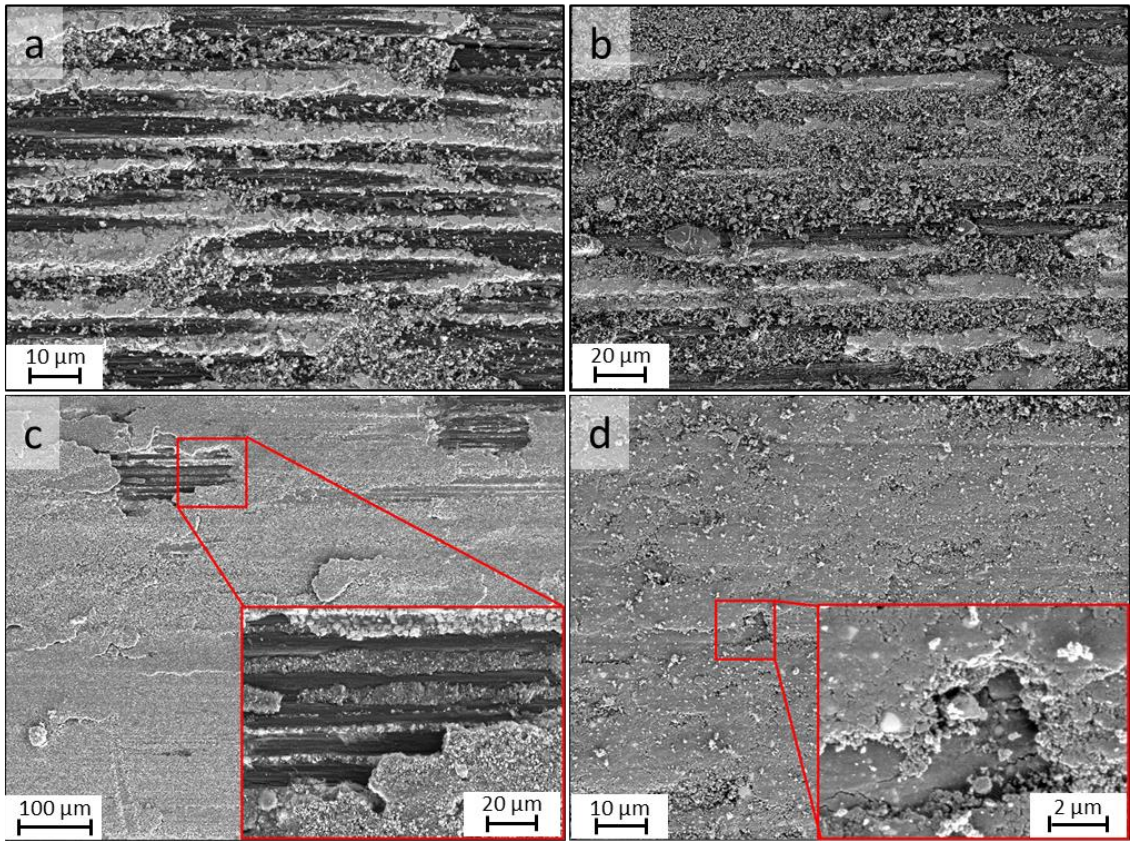

Fig. 7.20: samples ZL tested on C/C-SiC disc at 1 MPa (a, c) and 3 MPa (b, d). The sliding direction is left to right.

7.5.4 ZS pads morphology vs C/C-SiC

For the ZS samples tested with the C/C-SiC disc, a similar behaviour of ZL samples was observed. Also, in this case a friction layer was visible on the tested surface (Fig. 7.21-a) in accordance with the stable trend for the COF (Fig.7.5) for the same reason previously mentioned. The friction film was not homogeneous on the whole surface but

showed parts with a higher thickness and parts with only few debris. In spite of these features, the COF was quite stable, see Fig. 7.5.

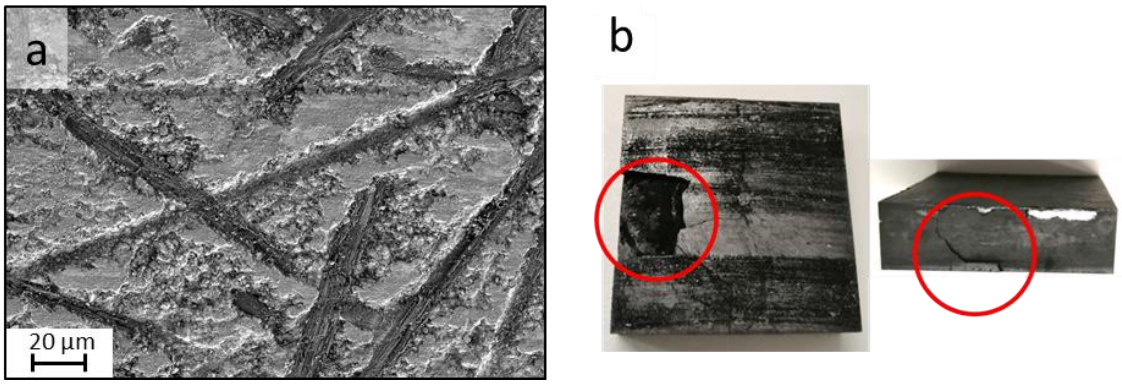

Fig. 7.21: Pad surface of the ZS material with C/C-SiC disc at 1 MPa (a) and broken ZS sample (b) after the break-in period with the C/C-SiC disc at 3 MPa. The sliding direction is left to right therefore a part has broken out at the incoming side.

During the test of the ZS sample, the increase of pressure from 1 MPa to 3 MPa caused a critical failure of the pads (Fig. 7.21-b). The cracks generated and their propagation caused a delamination mechanism combined with interlaminar failure in the z-direction. This problem likely occurred for the lower mechanical properties of ZS pads compared with ZL pads (Table. 7.2). In fact, as previously reported, one of the main problems of the ZrB_2 based ceramics is their low fracture toughness especially for their applicability when vibrations are present [34] and the short carbon fibres reinforcement did not improve the mechanical properties enough for the application in these conditions. Moreover, another reason for cracks generation could be the high COF observed during the braking already with the pressure of 1 MPa ($\mu \approx 0.7$) that exacerbated mechanical stresses on the pads. And finally, due to the thin friction layer, no cushioning effect could take place between the first and second body.

7.5.5 ZL pads morphology vs Steel

In Fig. 7.22 the surfaces of the ZL samples after the tests with the steel disc are reported. For both tests with 1 and 3 MPa an inhomogeneous friction layer was visible. More in detail, some parts of the samples were covered by sparse debris (Fig. 7.22-a,b); other parts were instead completely covered by a continuous layer (Fig. 7.22-c,d). As observed for the C/C-SiC disc, the presence of the friction layer could explain the mean COF being quite stable and not affected by temperature variations, Fig 7.6.

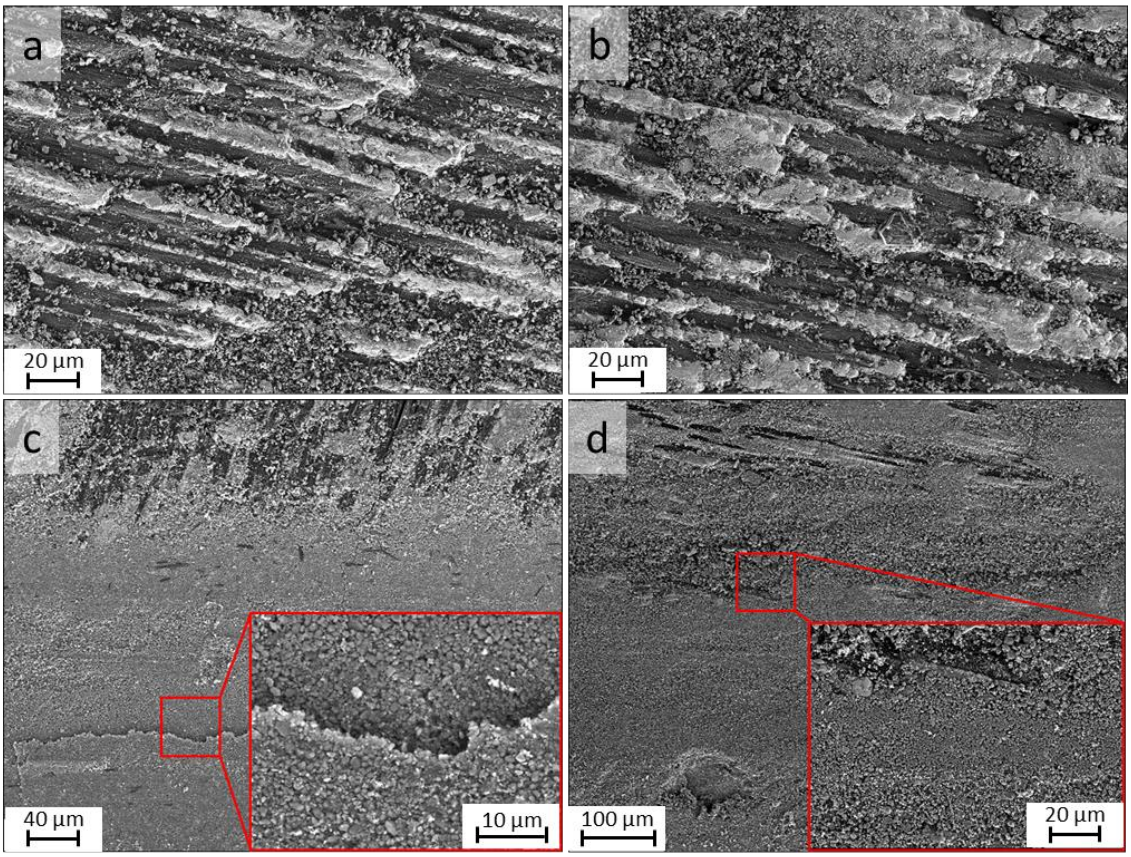

Fig. 7.22: samples ZL tested on steel disc at 1 MPa (a, c) and 3 MPa (b, d). The sliding direction is left to right.

7.5.6 ZS pads morphology vs Steel

For the ZS samples tested against the steel disc, it was also possible to observe a friction layer on the surface. As for the ZL samples, the friction layer was not homogenously distributed on the whole surface. In fact, it was possible to observe that there are parts which are partially covered by a layer (Fig. 7.23-a,b) and other parts completely covered by the layer (Fig. 7.23-c,d) for both pressures. In contrast to the tests discussed before, the partially covered regions showed friction film in direct contact with the disc which was obvious by the braking grooves instead of loose debris. Also, in this case a multi-layer structure was present in both pressure conditions. However, for the ZS samples the coverage increased with the rising pressure. In fact, after the test at 3 MPa, the areas where the fibres were visible after test at 1 MPa, were now fully covered with a smooth layer of debris.

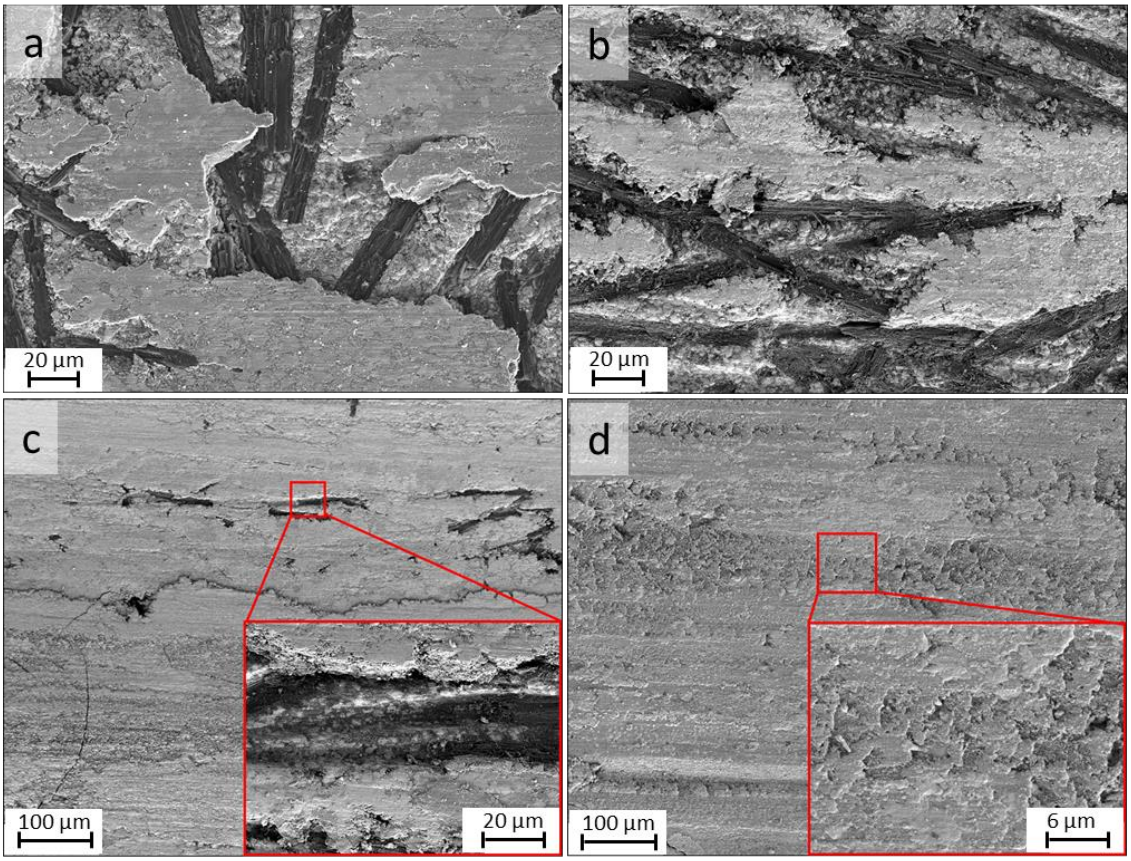

Fig. 7.23: sample ZS tested on steel disc at 1 MPa (a, c) and 3 MPa (b, d). The sliding direction is left to right

Comparing the surface of the samples ZL and ZS after the tests with the steel disc, a different film structure was observed. For the ZL sample the surface was composed of alternating areas. There were sites where the surface maintained the structure of the sample before the test, ZrB_2-SiC matrix and carbon fibres with low damage (Fig. 7.24-a-2). On top of this, there was a layer constituted by sample materials, ZrB_2-SiC-carbon fibres, and iron that came probably from the disc (EDS Fig. 7.24-a-1,3). The iron powder filled the gaps in between ZrB_2-particles and the abraded pitch-based fibres. This layer was composed by grains with a dimension of ≈ 2-5 µm. On the other hand, for the ZS sample, three different surface compositions were observed (Fig. 7.24-b). The first two surfaces presented the same structure observed for the ZL sample. While, the upper layer was constituted by Fe_xO_y which derived from the disc (light grey in Fig. 7.24-b, EDS Fig. 7.24-b-3). In the case of ZS samples, the layer was considerably thinner, with a continuous, smooth, and even surface. The film appeared to be welded out of particles and steel wear dust. For the ZL sample, the film was composed by compacted particles

which resembled an asphalt-like surface, suggesting a welding action in between particles and wear dust.

In conclusion, during the braking with a Steel disc there was a formation of overlapped layers with a different composition. During braking, the surface was ground, and the detached materials were mixed with the iron ground by the disc with the formation of a layer constituted by ZrB_2/ZrO_2-SiC-carbon fibres and Fe. Over this layer, there was the formation of a second layer constituted by Fe_xO_y derived from the abraded disc. The different appearance between the ZL and ZS surface could be attributed to the fibre orientation. In fact, the random distribution of the chopped fibres in the ZS sample improved the amount of debris material held on the surface.

Two mechanisms could contribute to that phenomenon. Firstly, the used pitch-based fibres were easily abraded due to their high carbon orientation as can be seen for example in Fig. 23-b. The fibres were partly abraded and beneath the matrix in z-direction. The friction film could only stay attached to the ceramic matrix surface but not on the fibres. Moreover, less fibre volume content and more homogeneous distribution for ZS samples compared to ZL samples led to more matrix on the surface and therefore more friction film. This was proven by the higher friction film observed on the ZL sample at the fibre sparse crossing areas of the 0° and 90° fibre bundles. The second mechanism, was probably the unknown strength of the influence of fibre orientation, which was known to alter braking performance and friction film development [35–37]. Random fibre orientation usually proved to be optimal for general purpose braking applications [35]. This ability for the ZS material to produce a more stable friction film could explain the reduced wear as seen in Fig. 7.15, as well as the improved COF-stability (compare Fig. 7.6+7.7 and Fig. 7.8+7.9). For sample ZS, wear dust underwent welding on the surface, while for sample ZL it was removed too quickly to form an even surface. The resulting amount of steel on the pad surface was able to produce metal on metal adhesion at low sliding speeds. With adhesion forces, a rapidly rising COF was expected at the end of the braking cycle, as was only oberseved for ZS material in contrast to the ZL sample with lowering COF (compare Fig. 7.6+7.7 and Fig. 7.8+7.9).

In this way, a first homogeneous layer constituted by ZrB_2/ZrO_2-SiC-Cf-Fe was created and a second layer with Fe_xO_y was visible above the first. For the ZL this second Fe_xO_y layer was not visible due to the low amount of debris held on the surface.

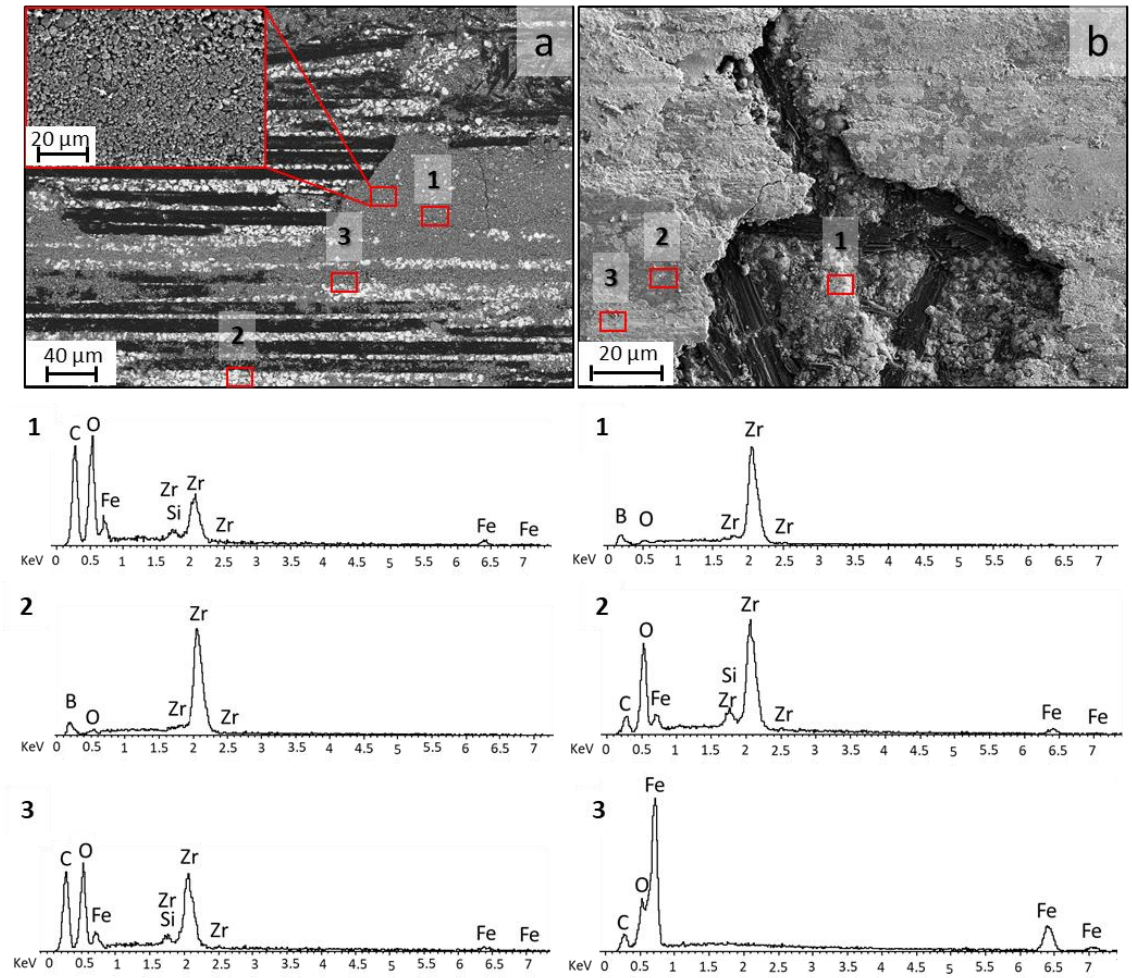

Fig. 7.24: Sample ZL tested on steel disc at 3 MPa (a) and sample ZS tested on steel disc at 3 MPa (b) and EDS analysis.

To investigate more in detail the friction layer, a cross section of the ZS samples was studied (Fig. 7.25). The friction layer presented a thickness ranging from 2 – 10 µm and consisted of two different compositions: a first homogeneous layer constituted by ZrB_2/ZrO_2-SiC-carbon fibre-Fe and a second composed by Fe_xO_y (the high amount of C present in EDS is due to the carbon coating for SEM analysis).

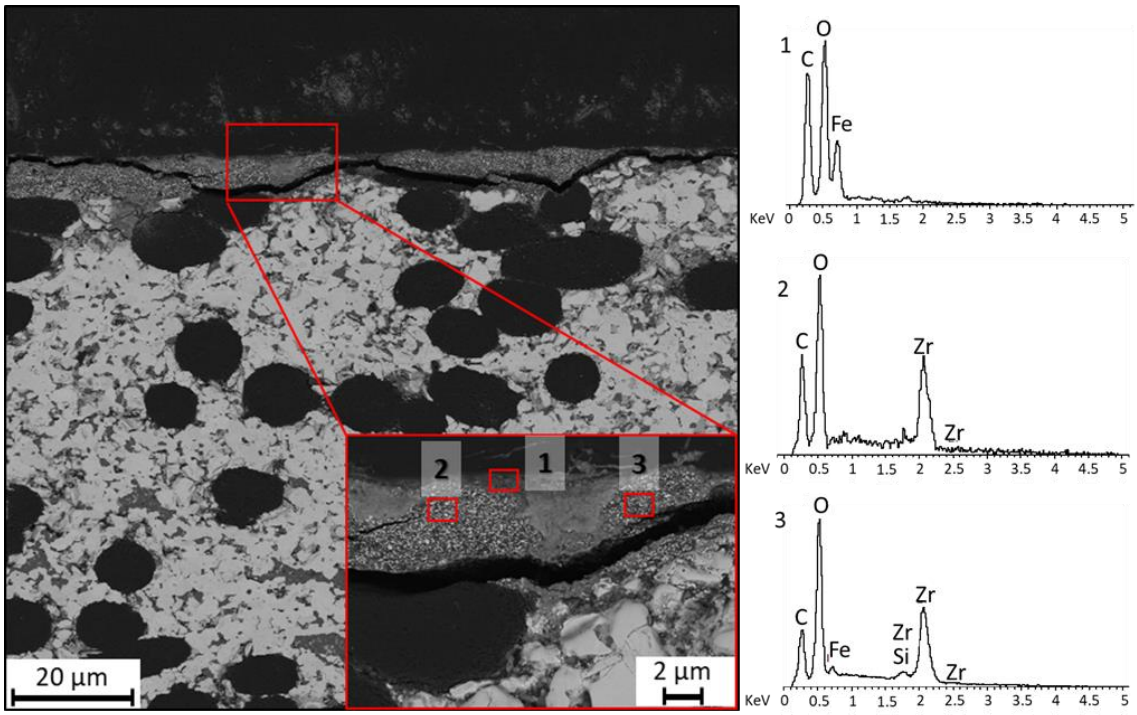

Fig. 7.25: Section of the sample ZS tested on steel disc at 3 MPa and EDS analysis.

7.5.7 ZL pads morphology vs C/C

The surfaces images of the ZL samples after the tests with the C/C disc are reported in Fig. 7.26. For both samples, tested with a pressure of 1 MPa (Fig. 7.26-a,c) and 3 MPa (Fig. 7.26-b,d), the presence of a well visible friction layer was not observed. The surface of the sample after the test at 1 MPa (Fig. 7.26-a,c) had a lustrous appearance. The ceramic matrix had a low superficial roughness and the carbon fibres were covered by a film of carbon which probably come from the C/C disc that polished the surface. The absence of asperities and the presence of a carbon film on the fibres surface could explain the low COF observed during the test (Fig. 7.10). Due to the COF behaviour observed during the test it is hypothesized that the temperature reached a value around ≈ 500 °C with the carbon oxidation. With the 3 MPa braking test, similar behaviour was observed (Fig. 7.26-b,d). The matrix surface in this case resulted completely polished without any asperities or debris due to the higher pressure used. Even in this case the carbon fibre resulted covered by a carbon film but the thickness resulted higher than the previous test and the surface of this layer presented some cracks. So, like the test with 1 MPa of pressure, absence of asperities and the presence of a carbon film on the fibres surface could explain the low COF observed during the test (Fig. 7.11). Due to the higher pressure, the temperature around ≈ 500 °C was reached after the 2nd braking, so the polishing effect started before removing more defects and asperities.

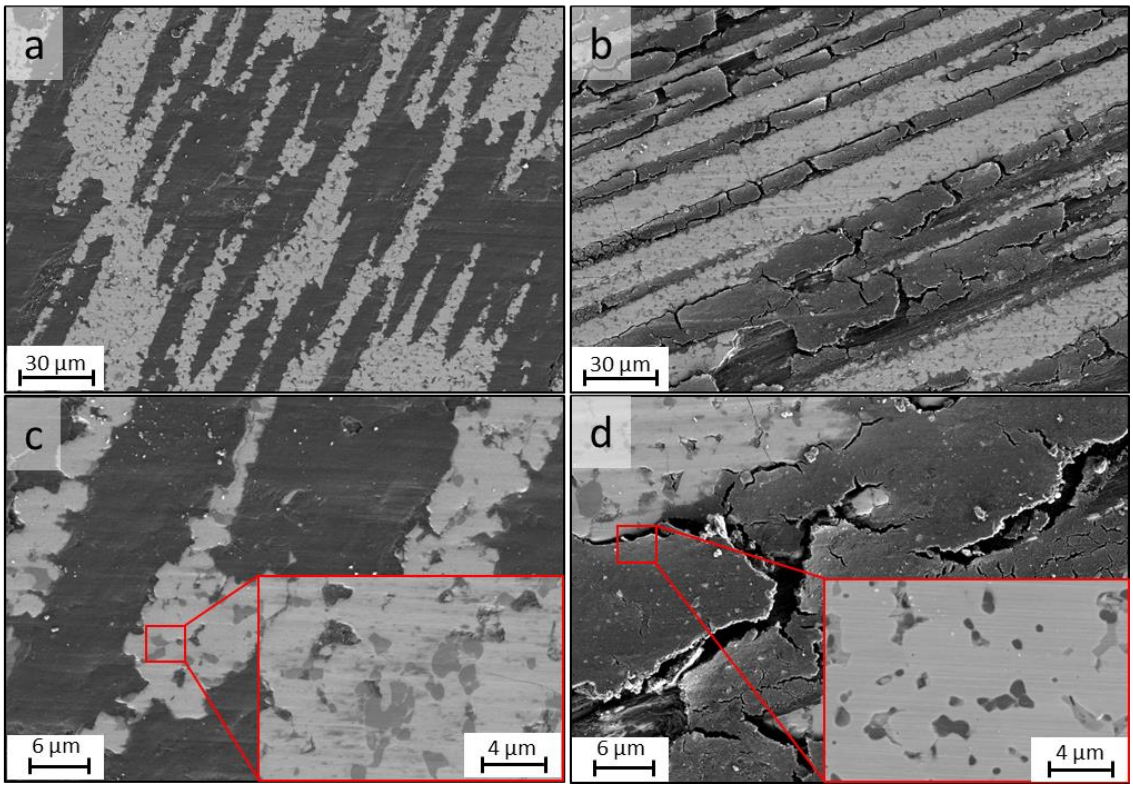

Fig. 7.26: samples ZL tested on C/C disc at 1 MPa (a, c) and 3 MPa (b, d). The sliding direction is right to left.

7.5.8 ZS pads morphology vs C/C

For the ZS samples tested with the C/C disc, the presence of a friction layer was not observed. Similarly, to ZS, sample ZL had a polished appearance. More in detail, after the test at 1 MPa (Fig. 7.27-a,c) the matrix did not present asperities or debris but some scratches were visible around the grains. The carbon fibres in this case were only partially covered by a C/C film that did not affect the COF behaviour which was linear. Moreover, the lower temperature observed during the test < 500 °C did not allow to oxidize the carbon, resulting in a stronger surface and a higher COF compared with the ZL test. With the 3 MPa test, a similar behaviour was observed (Fig. 7.27-b,d). Even in this case the matrix surface was polished, without debris but with some scratches. The surface of the carbon fibres resulted partially covered by a C/C layer probably due to the higher pressure used. Moreover, with a pressure of 3 MPa a temperature higher than 500 °C was reached, resulting in a COF drop due to the carbon oxidation as observed for the ZL samples and demonstrated by the bigger layer oh the carbon fibres.

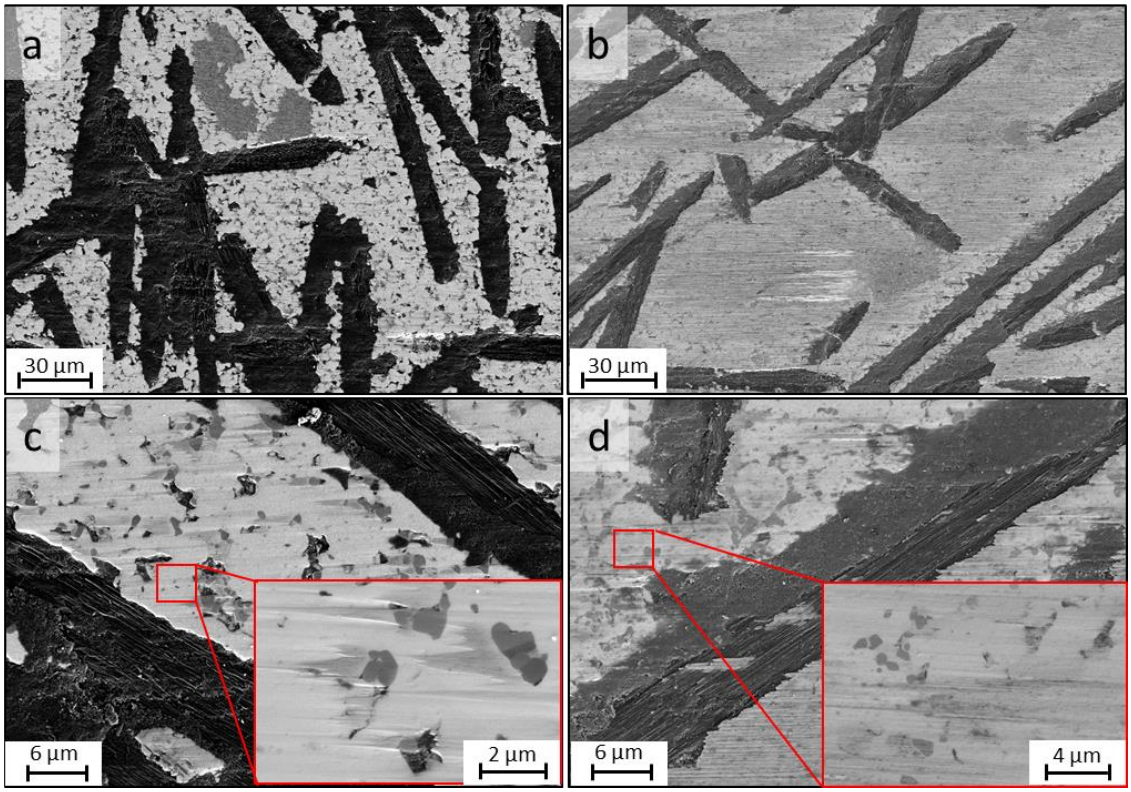

Fig. 7.27: samples ZS tested on C/C disc at 1 MPa (a, c) and 3 MPa (b, d). The sliding direction is right to left.

7.6 XRD analysis

X-Ray diffraction analysis was carried out after testing the samples ZL and ZS with the discs of C/C-SiC, C/C and steel at 3 MPa in order to identify the species that formed on the surface during braking. The two samples, with long and chopped fibres, presented the same characteristics, so only results for the ZS samples were reported here (Fig. 7.28). In the XRD pattern the highest peak was attributed to ZrB_2 (PFF#75-0964), which was the main component of the samples. Moreover, in accordance with the EDS analysis C (PDF#75-0444) and SiC-6H (PD#19-1131) were detected. After the braking tests, for all the discs used, oxidized species were observed in small amount, SiO_2 (PDF#47-1144) and ZrO_2 (PDF#50-1089). This indicates that an oxidation mechanism occurred on the surface due to the temperature and pressure. The EDS analysis identified the presence of Fe on the surface of ZS sample tested with the steel disc (Fig. 24). With the X-Ray diffraction, the presence of Fe was confirmed as Fe_2B species. Fe_2B was formed by the reaction of boron rich compounds on an iron surface. The boron atoms diffuse into the iron substrate between 973-1273 K (700 – 1000 °C) [38]. The highest temperature recorded by thermocouples was around 400-450 °C (Fig. 7.9), too low to obtain Fe_2B.

So, the temperature recorded by thermocouples probably was lower than the real temperature on the sample surface due to the position of the thermocouples located about 60 mm beneath the pads.

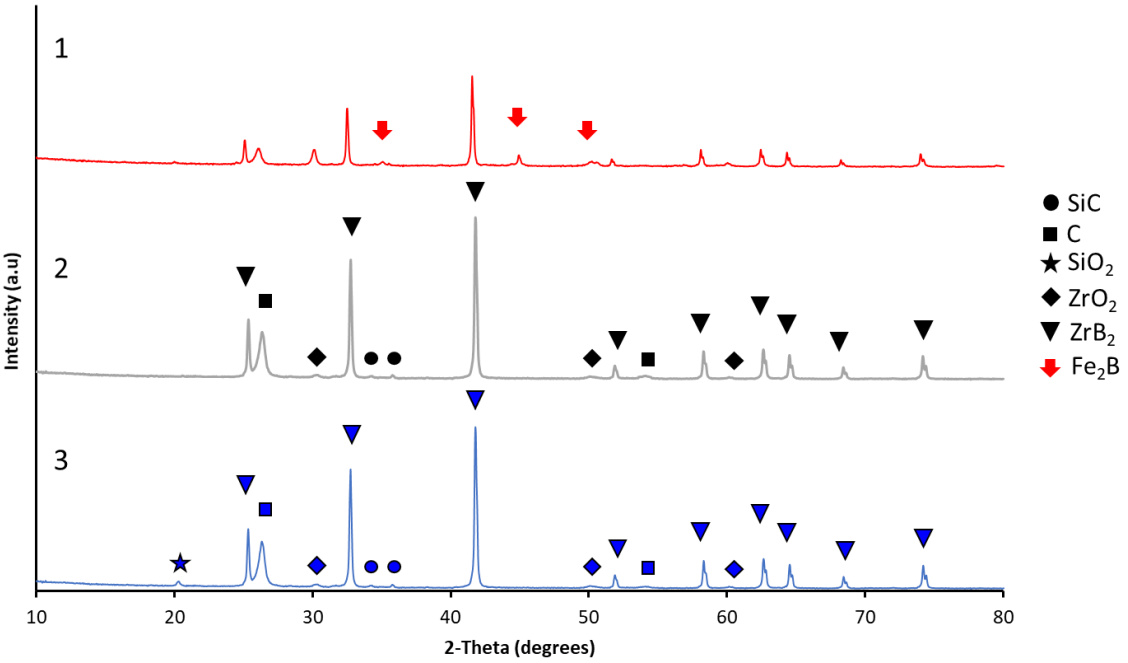

Fig. 7.28: X-Ray diffraction patterns of samples ZS after braking test at 3 MPa with steel disc (1), C/C disc (2) and C/C-SiC disc (3). The main peaks are relative to ZrB_2 (PDF#75-0964). Small peaks are relative to SiC-6H (PDF#19-1131), C (PDF#75-0444), SiO_2 (PDF#47-1144) and ZrO_2 (PDF#50-1089). Presence of Fe_2B was observed for steel disc (PDF#89-1993).

7.7 Conclusions

Two carbon fibre reinforced ZrB_2-10%SiC UHTCMCs (ZL and ZS) have been prepared by hot-pressing with different fibre orientations, 0°/90° and random chopped fibres, respectively. They were tribologically tested on an inertia dynamometer with 1 and 3 MPa on C/C-SiC, steel and C/C discs and their microstructure and friction surface were analysed discovered a two different types of friction film.

The combination with C/C-SiC disc material showed interesting braking behaviour with a stable and independent to temperature COF for both the ZL and ZS sample due to the friction film generated. A film composed by loose debris was observed. The hardness of the disc requires long fibre reinforcement pads like sample ZL because short fibre reinforcement material was severely damaged.

The combination of the different pads with Steel, generated a stable friction film that ensured low wear rate and a temperature-stable COF. The film observed was like smooth film-type, asphalt like film consisting of compressed particles and covering loose debris. Moreover, the smooth film-type observed for the short fibre material with steel showed a stable friction film that reduced the wear and improved the performance during the braking.

The combination of the ZL and ZS pads with C/C disc showed a behaviour strongly dependent on the temperature with a drop of COF after ≈ 500 °C due to the oxidation of the carbon of the disc. However, after an initial drop, the COF became stable. During these tests a friction film was not visible and the matrix had a polished appearance, while the fibre resulted partially or completely covered by a carbon film probably derived from the C/C disc due to the low mass-loss of the pads observed.

Finally, little changes in fibre orientation or fibre volume content can significantly affect the formation and composition of the friction film and therefore change wear and COF performance.

7.9 References

[1] M.M. Opeka, I.G. Talmy, E.J. Wuchina, J.A. Zaykoski, S.J. Causey, Mechanical, Thermal, and Oxidation Properties of Refractory Hafnium and zirconium Compounds, J. Eur. Ceram. Soc. 19 (1999) 2405–2414. https://doi.org/10.1016/s0955-2219(99)00129-6.

[2] D.K. Robinson, Temperature Ceramics Temperature Ceramics Materials for Extreme Environment Applications, 2008.

[3] A.L. Chamberlain, W.G. Fahrenholtz, G.E. Hilmas, D.T. Ellerby, High-strength zirconium diboride-based ceramics, J. Am. Ceram. Soc. 87 (2004) 1170–1172. https://doi.org/10.1111/j.1551-2916.2004.01170.x.

[4] S.R. Levine, E.J. Opila, M.C. Halbig, J.D. Kiser, M. Singh, J.A. Salem, Evaluation of ultra-high temperature ceramics for aeropropulsion use, J. Eur. Ceram. Soc. 22 (2002) 2757–2767. https://doi.org/10.1016/S0955-2219(02)00140-1.

[5] Z. Balak, M. Zakeri, M. Rahimipour, E. Salahi, Taguchi design and hardness optimization of ZrB2-based composites reinforced with chopped carbon fiber and different additives and prepared by SPS, J. Alloys Compd. 639 (2015) 617–625. https://doi.org/10.1016/j.jallcom.2015.03.131.

[6] F. Yang, X. Zhang, J. Han, S. Du, Characterization of hot-pressed short carbon fiber reinforced ZrB2-SiC ultra-high temperature ceramic composites, J. Alloys Compd. 472 (2009) 395–399. https://doi.org/10.1016/j.jallcom.2008.04.092.

[7] Z. Nasiri, M. Mashhadi, A. Abdollahi, Effect of short carbon fiber addition on pressureless densification and mechanical properties of ZrB2-SiC-Csf nanocomposite, Int. J. Refract. Met. Hard Mater. 51 (2015) 216–223. https://doi.org/10.1016/j.ijrmhm.2015.04.005.

[8] S. Tang, J. Deng, S. Wang, W. Liu, Comparison of thermal and ablation behaviors of C/SiC composites and C/ZrB2-SiC composites, Corros. Sci. 51 (2009) 54–61. https://doi.org/10.1016/j.corsci.2008.09.037.

[9] D. Sciti, A. Natali Murri, V. Medri, L. Zoli, Continuous C fibre composites with a porous ZrB2 Matrix, Mater. Des. 85 (2015) 127–134.

https://doi.org/10.1016/j.matdes.2015.06.136.

[10] K. Upadhya, J.M. Yang, W.P. Hoffman, Materials for ultrahigh temperature structural applications, Am. Ceram. Soc. Bull. 76 (1997).

[11] F. Monteverde, A. Bellosi, L. Scatteia, Processing and properties of ultra-high temperature ceramics for space applications, Mater. Sci. Eng. A. 485 (2008) 415–421. https://doi.org/10.1016/j.msea.2007.08.054.

[12] P. Hu, Y. Cheng, P. Wang, X. Guo, C. Ma, Q. Qu, X. Zhang, S. Du, Rolling compacted fabrication of carbon fiber reinforced ultra-high temperature ceramics with highly oriented architectures and exceptional mechanical feedback, Ceram. Int. 44 (2018) 14907–14912. https://doi.org/10.1016/j.ceramint.2018.04.249.

[13] D. Sciti, S. Guicciardi, L. Zoli, S. Failla, C. Melandri, Dry sliding wear behaviour of ZrB2-based ceramics: Self-mated and cross coupling with alumina, J. Eur. Ceram. Soc. 42 (2022) 6335–6346. https://doi.org/10.1016/j.jeurceramsoc.2022.07.022.

[14] J. He, Y. Cao, Z. Li, Y. Wang, Study of tribological properties of polymer derived ZrB2-SiC ceramics, Ceram. Int. 44 (2018) 15627–15630. https://doi.org/10.1016/j.ceramint.2018.05.231.

[15] J.K. Sonber, K. Raju, T.S.R.C. Murthy, K. Sairam, A. Nagaraj, S. Majumdar, V. Kain, Friction and wear properties of zirconium diboride in sliding against WC ball, Int. J. Refract. Met. Hard Mater. 76 (2018) 41–48. https://doi.org/10.1016/j.ijrmhm.2018.05.009.

[16] M. Ivor, D. Medved, M. Vojtko, A. Naughton-Duszova, L. Marciniak, J. Dusza, Nanoindentation and tribology of ZrB2 based luminescent ceramics, J. Eur. Ceram. Soc. 40 (2020) 4901–4908. https://doi.org/10.1016/j.jeurceramsoc.2020.03.021.

[17] M. Mallik, P. Mitra, N. Srivastava, A. Narain, S.G. Dastidar, A. Singh, T.R. Paul, Abrasive wear performance of zirconium diboride based ceramic composite, Int. J. Refract. Met. Hard Mater. 79 (2019) 224–232. https://doi.org/10.1016/j.ijrmhm.2018.12.008.

[18] P. Kumar, V.K. Srivastava, Tribological behaviour of C/C–SiC composites—A review, J. Adv. Ceram. 5 (2016) 1–12. https://doi.org/10.1007/s40145-015-0171-z.

[19] K.H. Breuer, Bert; Bill, Bremsenhandbuch. Grundlagen - Komponenten - Systeme - Fahrdynamik, 5. Aufl, 2017.

[20] S.K. Rhee, M.G. Jacko, P.H.S. Tsang, The role of friction film in friction wear and noise of automotive brakes, Wear. 146 (1991) 89–97. https://doi.org/10.1016/0043-1648(91)90226-k.

[21] Ralph Renz, Entwicklung eines Werkstoff- und Bauweisenkonzepts für keramische Verbundbremsscheiben (Band 14), 2018.

[22] G.Savage, Savage 1993 - Carbon-carbon composites.pdf, Chapman & Hall, 1993.

[23] P. Kumar, V.K. Srivastava, A Review on Wear and Friction Performance of Carbon–Carbon Composites at High Temperature, Int. J. Appl. Ceram. Technol. 13 (2016) 702–710. https://doi.org/10.1111/ijac.12538.

[24] B.H.R.R. W Krenkel, C/C–SiC composites for advanced friction systems, Adv Eng Mater. 4 (2002) 427–436. https://doi.org/10.1002/1527-2648(20020717)4:7<427::aid-adem427>3.0.co.

[25] N. Langhof, M. Rabenstein, J. Rosenlöcher, R. Hackenschmidt, W. Krenkel, F. Rieg, Full-ceramic brake systems for high performance friction applications, J. Eur. Ceram. Soc. 36 (2016) 3823–3832. https://doi.org/10.1016/j.jeurceramsoc.2016.04.040.

[26] N. Langhof, R. Voigt, H. Mucha, W. Krenkel, The Effect of Residual Silicon in CMC Brake Pads on Friction and Wear, 6th Eur. Conf. Braking JEF 2010. (2010) 1–8.

[27] W. Krenkel, C/C–SiC composites for hot structures and advanced friction systems, Proc. 27th Annu. Cocoa Beach Conf. Adv. Ceram. Compos. B Ceram. Eng. Sci. Kriven WM, Lin H-T, Eds. Hoboken, NJ, USA John Wiley Sons, Inc. 24 (2003) 583–592.

[28] S. Fouquet, M. Rollin, R. Pailler, X. Bourrat, Tribological behaviour of

composites made of carbon fibres and ceramic matrix in the Si–C system, Wear. 264 (2008) 850–856. https://doi.org/10.1016/j.wear.2006.12.081.

[29] P. Fournier, P. Reynaud, F. Platon, J. Absi, Tribological behaviour of carbon-fibre-reinforced SiC matrix composites, Proc. IMechE Part J J Eng. Tribol. 214 (2000) 291–306. https://doi.org/10.1243/1350650001543188.

[30] Y. Qian, W. Zhang, M. Ge, X. Wei, Frictional response of a novel C/C-ZrB2-ZrC-SiC composite under simulated braking, J. Adv. Ceram. 2 (2013) 157–161. https://doi.org/10.1007/s40145-013-0055-z.

[31] A. Vinci, L. Zoli, D. Sciti, C. Melandri, S. Guicciardi, Understanding the mechanical properties of novel UHTCMCs through random forest and regression tree analysis, Mater. Des. 145 (2018) 97–107. https://doi.org/10.1016/j.matdes.2018.02.061.

[32] N. Langhof, B. Alber-Laukant, C. Greuel, M. Hilpert, A. Kozub, R. Voigt, W. Krenkel, Fiber Reinforced Ceramic Friction Pads for Automotive Applications – the Dependence of Friction and Wear on Speed and Braking Pressure, Eurobrake 2012. (2012) 1–10.

[33] U. Fischer, Tabellenbuch Metall, Haan-Gruiten Verl. Europa-Lehrmittel Nourney, 2001.

[34] J.J. Sha, J. Li, S.H. Wang, Z.F. Zhang, Y.F. Zu, S. Flauder, W. Krenkel, Improved microstructure and fracture properties of short carbon fiber-toughened ZrB2-based UHTC composites via colloidal process, Int. J. Refract. Met. Hard Mater. 60 (2016) 68–74. https://doi.org/10.1016/j.ijrmhm.2016.07.010.

[35] W. Zhou, M. Meiser, F. Wich, T. Liensdorf, W. Freudenberg, Y. Li, N. Langhof, W. Krenkel, Fiber orientation dependence of tribological behavior of short carbon fiber reinforced ceramic matrix composites, J. Am. Ceram. Soc. 105 (2022) 538–552. https://doi.org/10.1111/JACE.18075.

[36] E. Fitzer, L.M. Manocha, Carbon Reinforcements and Carbon/Carbon Composites, Carbon Reinf. Carbon/Carbon Compos. (1998). https://doi.org/10.1007/978-3-642-58745-0.

[37] T.J. Hutton, D. Johnson, B. McEnaney, Effects of fibre orientation on the tribology of a model carbon-carbon composite, Wear. 249 (2001) 647–655. https://doi.org/10.1016/S0043-1648(01)00689-5.

[38] I. Campos-Silva, M. Ortiz-Domínguez, M. Keddam, N. López-Perrusquia, A. Carmona-Vargas, M. Elías-Espinosa, Kinetics of the formation of Fe2B layers in gray cast iron: Effects of boron concentration and boride incubation time, Appl. Surf. Sci. 255 (2009) 9290–9295. https://doi.org/10.1016/J.APSUSC.2009.07.029.

8. Conclusions and outlook

The theme of this PhD thesis was the fabrication and characterization of short fibre reinforced UHTCMCs. The processes commonly used for the fabrication of short fibre reinforced UHTCMCs and reported in literature, namely the ball milling, the colloidal process and the tape casting, present some problems such as fibres damage, use of organic solvent or the possibility of use only a little amount of fibre as reinforcement. To avoid these problems, the first part of the thesis concerned the development of a novel process for the fabrication of UHTCMCs materials.

In Chapter 4, short carbon fibre reinforced UHTC matrix composites were produced via a new water-based dispersion method with the use of sodium alginate as thickener and binder. This process allowed to obtain UHTCMCs sheets with a high versatility in composition that was overlapped to obtain a "green" sample subsequently sintered by Hot-Pressing. Samples with a different amount of fibres and different fibre length were investigated by microstructural characterisation and mechanical tests. In Chapter 5 the versatility of the UHTCMCs sheets was used to produce samples with a different amount of short carbon fibres, more in detail three layers (0-20-50 vol. %) were made. Samples with different matrix compositions (three types) were fabricated and investigated before and after oxidation tests in air at 1650 °C. In Chapter 6, the flexibility of the sheets was exploited to produce samples with different layers orientation, different shapes and matrix composition. Finally, in Chapter 7, the use of ZrB_2 based UHTCMCs reinforced with short or long carbon fibres as braking materials was investigated. More in detail, three different discs were used as counterparts: C/C-SiC, Steel and C/C. The Coefficient of Friction (COF) was determined during a set of braking tests, wear of discs and pads were then evaluated.

The main results can be summarized in the following points:

- <u>Preparation of short carbon fibre reinforced UHTCMCs</u>

A new organic volatile solvent free route for the fabrication of UHTCMCs reinforced with 3 to 5 mm long carbon fibre was developed. The main steps for this manufacturing process are: the use of sodium alginate as dispersant to obtain a good and homogeneous fibre distribution and the use of the planetary mixer that allows to mix the fibre and the slurry without fibre damage, and removes the bubbles inside the blend. Finally, the hot-

pressing step of the overlapped sheets at 1900 °C and 30 MPa helps to remove the residual defects in the sample.

This process allows to obtain homogeneous, thin (≈ 100 μm) and flexible sheets with the possibility to obtain a large range of composition from 0 to 100 vol. % in fibre volumetric content. Moreover, in this process the carbon fibre was not damaged during the steps as it happens for the ball milling process.

The prepared composites had a composition of ZrB_2 85 vol. % - SiC 10 vol. % - Y_2O_3 5 vol. % and were reinforced with 20-35-50 vol. % of 3- and 5-mm pitch-based carbon fibres. The microstructure showed the benefits of the new process. In fact, the fibre distribution was homogeneous thanks to the mixing method and the interaction between fibre and matrix was low due to the use of sodium alginate as dispersant. Moreover, the fibre surface was not damaged due to the mixing process used. The 4-point flexural strength tests showed a value ranging from 107 MPa for the samples reinforced with 35 vol. % of carbon fibres and 140 MPa for the samples reinforced with 50 vol. % of carbon fibre. This demonstrates the role of the carbon fibre amount in the mechanical properties for the composite materials. A similar behaviour was observed for the work of fracture test, where the values ranging from 108 to 253 J/m^2. A small difference in fibre length (3 to 5 mm) did not affect the mechanical properties in a significant way.

It is possible to conclude that a new method for the production of short carbon fibre reinforced UHTCMCs materials was developed. This method allows to obtain materials without damaging the fibre and with good mechanical properties. Moreover, the feasibility of the process allows to obtain samples with different fibre amount, different matrix and good flexibility, resulting interesting for different applications.

- Versatility of the UHTCMCs sheets

The feasibility of the new process for the short carbon fibre described before - and that allows to obtain samples with different fibre amount and different matrix - was tested in order to investigate the interaction between different compositions and their resistance in severe environments.

Materials composed by three different layers each with an amount of 0-20-50 vol. % of 3 mm pitch-based carbon fibres respectively were made. More in detail, three samples with the reinforcement above described and composed by three different matrices, ZrB_2- 85

vol %, SiC- 10, vol % Y_2O_3- 5 vol % the first ZrB_2- 85 vol % $MoSi_2$- 15 vol % the second and SiC- 95 vol %, Y_2O_3- 5 vol % (SY5 sample) the third, were analysed. To test their resistance in extreme environments, an oxidation tests in air at 1650 °C was made.

All the samples presented a homogeneous fibre distribution and the absence of defects between the different layers. In fact, the matrix resulted continuous without defects. These indicated the absence of CTE mismatch between the layers. However, in all the samples a migration of the liquid phases was observed from the bulk layer to the 20 vol. % reinforced layer. This migration did not produce defects in the interaction area between the layers but increased the chemical reaction between the fibre and the matrix in an area of ≈ 50-100 μm from the interface.

The oxidation tests at 1650 °C in air for 1 min demonstrated that the interaction between the layers in all the samples was good and the CTE mismatch did not cause cracks. For each sample, the different matrix gave different oxidation behaviour. The sample constituted by ZrB_2 and SiC, Y_2O_3 as sintering aid formed a film of ZrO_2-SiO_2-B_2O_3 that covered all the sample surface. This film acted as a barrier against oxygen diffusion, reducing the oxidation damage. The ZrO_2 grains during the oxidation assumed a columnar structure. The sample constituted by ZrB_2 and $MoSi_2$ as sintering aid, after the oxidation was covered by SiO_2 film that also filled the holes left by the oxidized fibres improving the oxidation resistance. A two-region structure was observed composed by an external SiO_2 film that reduced the oxygen diffusivity and an internal ZrO_2 columnar structure that closed the generated defects. The sample constituted by SIC and Y_2O_3 as sintering aid, after oxidation was covered by a thin SiO_2 film that was not sufficient to protect the carbon fibres below, resulting in a porosity increase that could reduce the mechanical properties. sample ZMo15 presented the best oxidation resistance (mass loss ≈ -0.5 mg/cm^2) due to the SiO_2 protective film and the ZrO_2 columnar grains. sample ZSY105 presented also a good oxidation resistance (mass loss ≈ -5 mg/cm^2) due to the formation of B_2O_3 layer and the ZrO_2 lamellar grains. sample SY5 presented the lowest oxidation resistance (mass loss ≈ -7 mg/cm^2) due to the inefficient formation of SiO_2 protective film.

The flexibility of the UHTCMC sheets obtained by the new slurry casting process described before was investigated in order to obtain samples with higher properties or with complex shapes. Four different structures were analysed.

The sample made by ZrB_2-85 vol. %, SiC- 10 vol. %, Y_2O_3-5 vol. % reinforced with 40 vol. % of 3 mm length pitch-based carbon fibres sheets with a vertical orientation was sintered by HP (Z3-40-Z). The fibres were homogeneously distributed, and a sheets bending was visible. This bending improves the mechanical properties (≈ 130MPa) compared with a sample with a horizontal sheet orientation. This demonstrated that the sheets orientation can affect the mechanical properties.

The sample composed by an outer shell of ZrB_2-35 vol. %, SiC- 60 vol. %, Y_2O_3-5 vol. % reinforced with 40 vol. % of 3mm pitch-based carbon fibres (ZSY605) and an internal square composed by ZrB_2-85 vol. %, SiC- 10 vol. %, Y_2O_3-5 vol. % reinforced with 40 vol. % of 3 mm pitch-based carbon fibres (ZSY105) sintered by HP presented good matrix interaction at the interface zone but many defects were visible, resulting in a low value of flexural strength (≈ 45 MPa). This indicated a difficult interaction between UHTCMC sheets without a pressure in the optimal direction during the sintering.

A hollow cylindrical shape composed by vertical sheets of ZrB_2-35 vol. %, SiC- 60 vol. %, Y_2O_3-5 vol. % reinforced with 40 vol. % of 3 mm pitch-based carbon fibres in the internal part and by vertical sheets of ZrB_2-85 vol. %, SiC- 10 vol. %, Y_2O_3-5 vol. % reinforced with 40 vol. % of 3 mm pitch-based carbon fibres with the external part was synthesized by HP. The result presented a good fibre distribution and a good matrix interaction, which is a proof that an unusual shape can be made by HP.

Finally, a cone composed by ZrB_2-85 vol. %, SiC- 10 vol. %, Y_2O_3-5 vol. % reinforced with 40 vol. % of 3 mm pitch-based carbon fibres was obtained by pressure-less sintering of the bending sheets. This sample demonstrated the advantages of the flexibility of the UHTCMC sheet.

- <u>ZrB_2 based UHTCMCs for braking application</u>

The use of ZrB_2 based UHTCMCs reinforced with short or long carbon fibres as friction materials were investigated by the test of two pads consisting of reinforced ZrB_2-10 vol. % SiC reinforced with carbon fabric arranged in 0°/90° orientation (ZL) and reinforced with randomly orientated pitch-based short carbon fibres (ZS).

Tests conducted against a C/C-SiC disc showed stable braking behavior, independent of the temperature due to the generation of a stable friction film composed by loose debris. However, the mechanical stresses are high and can be tolerated only with long carbon

fibre reinforcement (ZL). More in detail, ZL samples showed a mean COF of 0.81 and 0.56 with higher temperature of 350 °C and 450 °C for the tests at 1 MPa and 3 MPa respectively. While ZS samples showed a mean COF of 0.67 with higher temperature of 300 °C for the tests at 1 MPa. The high values of COF and its stability with a wear rate comparable to the state-of-the-art materials (≈ 500mg/MJ) make these materials appealing for automotive brake application.

Tests conducted against a Steel disc showed the formation of a stable friction film that provided a stable COF and a low wear rate. More in detail, ZL samples showed a mean COF of 0.86 and 0.40 with higher temperature of 430 °C and 440 °C for the tests at 1 MPa and 3 MPa respectively. While ZS samples showed a mean COF of 0.56 and 0.43 with higher temperature of 360 °C and 450 °C for the tests at 1 MPa and 3 MPa respectively. The friction film resulted composed by the debris of the Steel disc generating a metal on metal sliding. This coupling reduced the pads wear (≈200mg/MJ) increasing their life time and at the same time generating a little welding effect that could increase the COF at the end of the braking. These characteristics of long life, high and quite stable COF are interesting for everyday brake applications.

Tests conducted against a C/C disc showed a very low but stable coefficient of friction (≈ 0.3) without pads wear and with an operating temperature of the disc surface of ≈ 550 °C. Between the different discs tested, the C/C presented the lowest pads wear (≈ 65-100 mg/MJ) but at the same time the highest wear rate for the disc that was visibly abraded. This combination of UHTCMC and C/C disc is less suitable for everyday brake but opens to the possibility of their use in lubricant field due to their low COF.

In general, it was observed that changes in fibre orientation or fibre amount modified the friction film and therefore change wear and COF.

In conclusion, in this PhD thesis a novel, flexible and versatile process for the fabrication of UHTCMCs reinforced with short fibres was developed. High-performance composites with gradient compositions or fibre contents were consolidated by sintering and successfully tested. Moreover, the application of UHTCMC as friction materials opened to the possibility to use these materials in a higher amount of application fields different from the well-known of aerospace.

Acknowledgments

With this dissertation I have reached one of my most important academic goals up to know, hoping in a future even more successful. Of course, the achievement of this extraordinary objective took its time and during that time many people guided and supported me both directly and indirectly. For this reason, I owe some special thanks to all of them and I would like to dedicate this page to each of them.

The first round of thanks goes to my supervisor Dr. Diletta Sciti, which allowed me in first place to start my PhD in the Structural Ceramics Group at ISSMC- CNR but also whose guidance and support have been fundamental during these last three years. Secondly, I would like to thank my co-supervisor Antonio Vinci which helped me strongly in the making of my research as well as correcting my thesis together with Dr. Sciti and guiding me in the overall realization of this achievement.

Also, thanks go to the other members of the Structural Ceramics Group: Dr. Luca Zoli for his help in the research activity; Dr. Francesca Servadei for her help during research and for providing me with suggestions and tips; Dr. Pietro Galizia for his help, tips and tricks about UHTCMC manufacturing and mechanical testing respectively; Dr. Simone Failla for his technical support in the Sintering Technologies Laboratory but also Dr. Laura Silvestroni and Simone Taraborelli, which together with the rest of team represented my points of reference during the PhD period as well as being my first research group. It is also important to mention all the researchers and technicians for providing technical assistance with the many correlated aspects of this PhD like theoretical discussions, measurements or other aspects. On this matter, I really would like to mention Claudio Capiani for XRD analysis, Mauro Mazzocchi for his help with the scanning electron microscopy and Cesare Melandri for mechanical characterization and investigation using digital microscope.

Since I have been lucky enough to further enrich this experience and this work with a research period in Germany, it is fundamental for me to thank all those people which made this possible. To Dr. Stefan Schafföner and Dr. Nico Langhof for having welcomed me in their Ceramic material engineering research group during my three and a half months stay in the University of Bayreuth. Special thanks also go to Matthias Meiser, my greatest helper during this period and my friend. Not of less importance, is the JECS

Trust, which provided a concrete investment in my career by financially supporting my research in Bayreuth.

A debit of gratitude is also owed to Prof. Enrico Dalcanale, coordinator of this PhD, for his quick and concise answers to questions concerning courses, ECTS and availability of the funds.

And lastly, the most important thanks goes to my family and friends which have been fundamental to reach this achievement. My gratitude goes to my father Egidio, my mother Carla and my brother Luca which were the ones who believed the most. But also, my friend and ex-colleague Federico Saraga for his precious presence over the years. And most importantly, to my best friend and fiancée Maria Rosaria which was and will be always there for me and which also provided me with concrete help during the realization of my thesis as well as supporting me during my ups and downs but that never lost her faith in me.